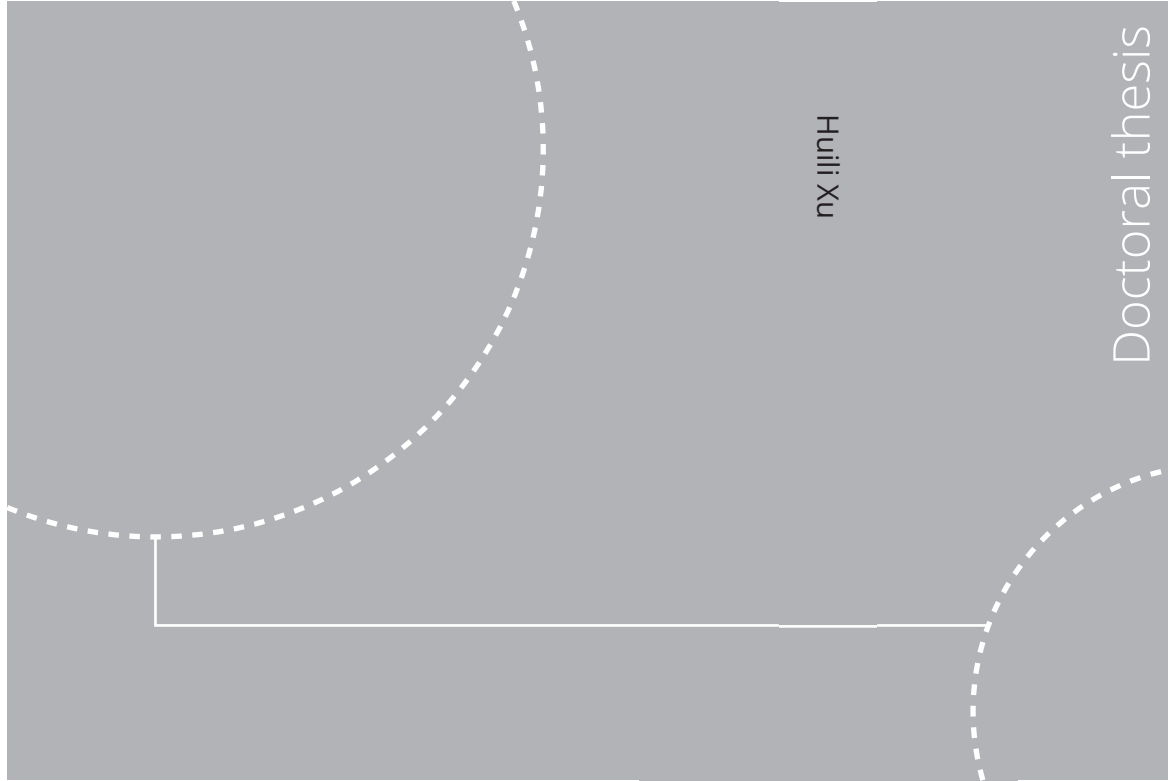


ISBN 978-82-326-6728-4 (printed ver.)  
ISBN 978-82-326-5445-1 (electronic ver.)  
ISSN 1503-8181 (printed ver.)  
ISSN 2703-8084 (electronic ver.)



Doctoral theses at NTNU, 2023:7

Huili Xu

# Fish-Inspired Propulsion Study: Numerical Hydrodynamics of Rigid/Flexible/Morphing Foils and Observations on Real Fish

Doctoral theses at NTNU, 2023:7

**NTNU**  
Norwegian University of  
Science and Technology  
Thesis for the degree of  
Philosophiae Doctor  
Faculty of Engineering  
Department of Marine Technology

 **NTNU**  
Norwegian University of  
Science and Technology

 NTNU

 **NTNU**  
Norwegian University of  
Science and Technology

Huili Xu

# **Fish-Inspired Propulsion Study: Numerical Hydrodynamics of Rigid/Flexible/Morphing Foils and Observations on Real Fish**

Thesis for the degree of Philosophiae Doctor

Trondheim, January 2023

Norwegian University of Science and Technology  
Faculty of Engineering  
Department of Marine Technology



Norwegian University of  
Science and Technology

**NTNU**

Norwegian University of Science and Technology

Thesis for the degree of Philosophiae Doctor

Faculty of Engineering  
Department of Marine Technology

© Huili Xu

ISBN 978-82-326-6728-4 (printed ver.)  
ISBN 978-82-326-5445-1 (electronic ver.)  
ISSN 1503-8181 (printed ver.)  
ISSN 2703-8084 (electronic ver.)

Doctoral theses at NTNU, 2023:7



Printed by Skipnes Kommunikasjon AS

# Abstract

Many swimming fishes in nature have been endowed with high hydrodynamic efficiency and performance, such as low resistance, high speed, and good maneuverability, both when swimming individually and in groups, i.e., using schooling arrangements. The main purpose of the present thesis is to study the fish hydrodynamics through both experimental and numerical investigations, to better understand the physical mechanisms behind high propulsive skills of fish-like bodies, and to build knowledge relevant for the design of greener and more efficient bio-inspired underwater vehicles, which could lead to positive consequences for the environment and the society.

Observational experiments were carried out in swim tunnels under different conditions and examined two fish species using different swimming modes, i.e., a labriform swimmer (shiner perch, *Cymatogaster aggregate*) belonging to median and/or paired fin (MPF) propulsion category, and a sub-carangiform swimmer (Atlantic salmon, *Salmo salar*) belonging to the body and/or caudal fin (BCF) propulsion category. In the experimental investigations performed on the shiner perch, the examined fish were randomly assigned to one of the three experimental scenarios: a solitary fish (Single), a schooling pair of fish (Pair), and a false pair where a single fish swam alongside a video of a conspecific fish (False pair). The swimming behaviours and metabolisms of the fish were analyzed and discussed among different arrangements. The comparisons suggested that schooling confers both hydrodynamic and behavioral advantages over swimming alone for a gregarious fish, but that the relative contribution of the two mechanisms depends on the speed of swimming. In the experiments carried out on Atlantic salmon, the observed results showed that the examined hatchery-reared fish had lower critical swimming speed than biological data of wild fish and fish swimming in larger flumes. The influence of fish body size and swim tunnel boundary walls on the salmon behaviors in the flume was discussed to identify important factors affecting the fish swimming capability. The analysis may provide current velocity threshold for farmed salmon during on-growing phase and give suggestions for experimental set-ups more suited for hydrodynamic and biological studies on fish.

In order to gain deep insights into the propulsive mechanics of swimming fish and to complement experimental studies, a series of hydrodynamic scenarios has been examined by performing two-dimensional CFD simulations within the OpenFOAM open-source platform. Three rigid flapping foils with different fish-like profiles, the tear-shaped semi-circle foil, NACA 0012 foil and NACA 0021 foil, have been studied through systematic numerical simulations to grasp the key propulsion characteristics. The predicted hydrodynamic forces and wake scenarios of the semi-circle foil have

shown good consistency with available experimental data. The critical Strouhal number of the rigid pitching foils at drag-thrust transition is found to be a decreasing function of the Reynolds number, and a universal scaling law of force transition quantifying foil shape effect has been attempted. The analysis of the body-shape influence showed that the forepart of the flapping foil dominates the friction force component, while the trailing edge shape matters for the pressure force. Based on the results of the examined rigid pitching foils, a morphing foil strategy has been proposed to combine the advantages of two rigid foils associated, respectively, with the largest mean thrust and with the lowest mean input power requirement. A parametric analysis of the phase between pitching and morphing motions has been performed and an optimal morphing strategy has been identified. These results can pave the way for the use of morphing strategies to target optimized propulsive behavior and, in a broader context, to overcome limitations of rigid vehicles/devices in marine applications.

The swimming performance of 2D fish-like foils with carangiform propulsion mode has been numerically studied in two different scenarios: one is the fish-like foil, with prescribed undulatory deformations and restrained longitudinal motions, under an incoming uniform stream, and the other one is the fish self-propelling itself in the fluid. In the former case, the computed hydrodynamic loads of the forced swimming foil agreed well with reference data. The influence of body shape and Reynolds number on fish swimming behavior has been examined. The comparisons between two different fish-like foils confirmed that a fish with a blunter body experiences larger drag and has more limited capability to generate thrust compared to a slimmer fish. For the second scenario, a numerical method capable of simulating self-propelled bodies with periodic lateral flexible motions has been proposed. The implemented self-propulsion strategy in OpenFOAM, verified to be numerically accurate and efficient through studying an oscillating elliptic foil case, has been adopted to predict the swimming performance of a carangiform fish-like body under various conditions. The self-propelled swimming scenario allows to examine the effect of recoil. The influence of boundary wall conditions on fish locomotion has also been investigated systematically. The results showed that the forward swimming speed and the propulsive efficiency of the fish dropped significantly with the decrease of swim tunnel width. This analysis provided an indicative minimum swim tunnel width to limit the boundary wall influence on the swimming features.

# Preface

This thesis is submitted to the Norwegian University of Science and Technology (NTNU) for partial fulfilment of the requirements for the degree of philosophiae doctor (PhD).

This doctor work has been carried out at the Center for Autonomous Marine Operations and Systems (AMOS), Department of Marine Technology, NTNU, Trondheim, with Professor Marilena Greco as the main supervisor and with Professor Claudio Lugni from Institute of Marine Engineering, CNR and Professor Odd M. Faltinsen at Department of Marine Technology, NTNU as co-supervisors.

This work was supported by the Research Council of Norway through the Centre of Excellence funding scheme, project number 223254-AMOS. The Norwegian Research Council is acknowledged as the main sponsor of NTNU AMOS.



# Acknowledgements

This work has been carried out under the supervision of Professor Marilena Greco at Department of Marine Technology, and Centre for Autonomous Marine Operations and Systems (AMOS), Norwegian University of Science and Technology (NTNU). I would like to express my sincere gratitude to Prof. Greco for her insightful guidance and continuous encouragement during my PhD study. She has been always available when I was in doubt and in frustration. This work would not have been possible without her professional and enlightening suggestions. Marilena is an energetic person, an excellent supervisor, and a good friend. I am always inspired by her deep passion for scientific research and for life. In addition, I sincerely thank my co-supervisor Prof. Claudio Lugni for his great contribution to this thesis. His immense knowledge of hydrodynamics and experience in experiments benefited me a lot. I have always obtained great help during our many discussions for which I am deeply grateful. I would also like to extend my gratitude to my co-supervisor Prof. Odd M. Faltinsen for his helpful advice and insight. His support has been invaluable in my hydrodynamic study.

It has been a very rewarding experience to have worked with and learned from many dedicated and generous people during the thesis work. I would like to thank Prof. Paolo Domenici, Prof. John F. Steffensen and Prof. Jacob Johansen for providing the valuable fish swimming course in University of Washington. This has been essential for my first fish observation experiments in collaboration with researcher Eleanor Gee and Søs Riber, where we spent a wonderful time in collecting fish, analyzing data, and discussing fish behaviors. I also thank Dr. Eirik Svendsen and Prof. Rolf Erik Olsen in NTNU for providing the great opportunity to collaborate on salmon experiments. I am full of gratitude to Dr. Giuseppina Coliccho and Prof. Babak Ommani for sharing their vast knowledge on numerical computations. I also appreciate the assistance from Dr. Tufan Arslan for the implementation of programs on high-performance computing resources.

I have had the pleasure to work alongside all my fellow colleagues at the Department of Marine Technology. My friend Dr. Yugao Shen and Shaojun Ma have shared a lot of helpful experience and guidance on my PhD study in hydrodynamics. Dr. Mohd Atif Siddiqui has been a great friend and working with him has led to many inspiring discussions and new ideas on program development in OpenFOAM. I appreciate the valuable discussions with Prof. Annette Stahl, Dr. Finn-Christian W. Hanssen, Dr. Jianxun Zhu, Carina Norvik and Eirik Ruben Grimholt Søvik. I am thankful to my friends, Jingxing Cai, Yuan Tian, Xinru Wang, Dr. Fengjian Jiang, Dr. Wei Chai, to name a few who have made my life full of joy. The kind help from the administrative staff is also greatly appreciated.



My deepest gratitude goes to my family in China for their tremendous love and understanding. They are the most wonderful parents and have always provided me the best education and life. Lastly, a special thanks to my husband Zhaolong for his support and encouragement.

# Nomenclature

## General rules

- Only the most used symbols are listed in the following sections
- Meaning of symbols are given when first introduced in the thesis
- Sometimes the same symbol is used to indicate different quantities
- Vectors are represented by bold symbols

## Abbreviations

2D	Two-dimensional
2P	Two vortex pairs shed per oscillation period
2S	Two vortices of opposite sign shed per oscillation period
3D	Three-dimensional
ALE	Arbitrary Lagrangian–Eulerian
ANOVA	Analysis of variance
AOA	Angle of attack
BCF	Body and caudal fin swimming
BG	Background grid
BL	Body length
CFD	Computational fluid dynamics
CN	Crank-Nicolson time scheme
COD	Complex orthogonal decomposition
COT	Cost of transport
DM	Deforming mesh method
DNS	Direct numerical simulation
DOF	Degree of freedom
EBT	Elongated body theory
FFT	Fast fourier transform
GAMC	Generalized added-mass and circulatory
MPF	Median and paired fin swimming
OA	Order of accuracy
OF	OpenFOAM
OG	Overset grid method
PIV	Particle image velocimetry
PTV	Particle tracking velocimetry
RPM	Revolutions per minute
SEM	Standard error of the mean

SMR	Standard metabolic rate
vK	von Kármán

### **Bold Symbols**

<b><math>F</math></b>	Force vector
<b><math>d</math></b>	Motion displacement vector
<b><math>M</math></b>	Inertia matrix of the body
<b><math>u</math></b>	Velocity vector
<b><math>x</math></b>	Position vector
<b><math>\omega</math></b>	Vorticity vector

### **Greek and Mathematical Symbols**

$\Delta t$	Time step
$\Delta x$	Grid spacing in $x$ direction
$\Delta y$	Grid spacing in $y$ direction
$\beta$	swimming speed-to-wave speed ratio
$\delta$	Boundary-layer thickness
$\eta$	Propulsive efficiency
$\theta$	Foil pitch angle
$\theta_0$	Maximum pitch angle
$\lambda$	Wave length
$\mu$	Dynamic viscosity of water
$\nu$	Kinematic viscosity of water
$\omega$	Angular frequency
$\phi$	Phase between foil morphing and pitching motion
$\phi_D$	Phase at maximum drag
$\phi_T$	Phase at maximum thrust
$\rho$	Mass density

### **Roman Letters**

$(u, v, w)$	Velocity of fluid particle
$(x, y, z)$	Motions of the fish-like body
$a$	Foil area / envelope of traveling wave
$a_D$	Amplitude of foil morphing motion
$A$	Amplitude
$A_D$	Flapping amplitude-to-foil thickness ratio
$A_m$	Peak-to-peak amplitude at fish tail
$A_p$	Pectoral fin beat amplitude of fish
$A_w$	Characteristic wake width
$C$	Courant number
$C_{FT1}$	Nondimensional thrust force

---

$C_{PS1}$	Nondimensional swimming power
$C_{Mz}$	Nondimensional hydrodynamic torque
$C_p$	Input power coefficient
$C_x$	Horizontal force coefficient
$C_{x0}$	Horizontal force coefficient of foil at zero angle of attack
$C_{xp}$	Horizontal pressure force coefficient
$C_{xv}$	Horizontal friction force coefficient
$C_y$	Vertical force coefficient
$c$	Foil chord length
$CR$	Foil chord-to-thickness ratio
$D$	Foil thickness
$F_D$	Drag
$F_T$	Thrust
$F_{xp}$	Pressure component of horizontal force
$F_{xv}$	Friction component of horizontal force
$f$	Frequency
$f_p$	Pectoral fin beat frequency of fish
$f_t$	Tail beat frequency of fish
$h_t$	Swim tunnel width
$h_w$	Distance between two vortical rows in the wake
$k$	Wave number / Diffusivity coefficient
$L$	Fish body length or foil characteristic length
$l_w$	Distance between two vortices in the same row of wake
$M$	Dimensionless body mass
$m$	Fish body mass
$M_z$	Hydrodynamic torque
$\dot{M}O_2$	Oxygen consumption rate
$n$	Vortex pair number / Oscillation period number
$\hat{n}$	Normal vector
$O_{xyz}$	Earth-fixed Catesian coordinate system
$P$	Input power
$p$	Pressure
$P_D$	Power required to overcome the horizontal force
$P_S$	Swimming power
$P_T$	Total power
$P_V$	Vorticity impulse
$R$	Radius of a circular cylinder
$r$	Distance between cell center and the specified moving boundary
$r_m$	Background mesh cell size-to-overset grid cell size ratio
$Re$	Reynolds number
$Re_c$	Foil chord based Reynolds number
$Re_L$	Fish length based Reynolds number
$S$	External boundary of fluid volume
$s$	Curvilinear coordinate along fish body

$S_b$	Body boundary
$S_e$	Area of an elliptic foil
$St_r$ ( $St_D$ )	Foil thickness based Strouhal number
$St_A$ ( $St_A$ )	Flapping amplitude based Strouhal number
$St$	Characteristic wake width or fish swimming amplitude based Strouhal number
$St_w$	Wake width based Strouhal number
$T$	Oscillation period
$t$	Time
$U$	Fish swimming speed or free-stream velocity
$U_c$	Current velocity
$U_r$	Relative swimming speed in current
$U_t$	Total swimming speed
$U_{crit}$	Critical swimming speed of fish
$U_{opt}$	Optimal swimming speed of fish
$U_{pc}$	Pectoral-caudal gait transition speed
$V$	Motor voltage / Fluid volume / Wave speed
$y_w$	Local lateral displacement of fish body

### Superscripts

*	Nondimensional value / Critical value
'	Body-fixed coordinate system

### Subscripts

$A$	Flapping amplitude
$b$	Body
$D$	Foil thickness
$e$	Elliptic foil
EBT	Elongated body theory
$f$	Fluid
$max$	Maximum value
$min$	Minimum value
$semi$	Semi-circle foil
SMR	Standard metabolic rate
$p$	Pectoral fin / Pressure force
$pro$	Foil perimeter length
$x$	Horizontal value
$y$	Vertical value
$v$	Friction force

# Contents

<b>Abstract</b> .....	<b>i</b>
<b>Preface</b> .....	<b>iii</b>
<b>Acknowledgements</b> .....	<b>v</b>
<b>Nomenclature</b> .....	<b>vii</b>
<b>Contents</b> .....	<b>xi</b>
<b>Introduction</b> .....	<b>1</b>
1.1    Background and motivation.....	1
1.2    Literature study: State-of-the-art.....	2
1.2.1    Fish swimming behaviour.....	3
1.2.2    Flapping foils.....	7
1.2.3    Underwater bio-inspired vehicles and robots.....	11
1.3    Present work.....	15
1.3.1    Objectives.....	15
1.3.2    Main contributions.....	16
1.3.3    Outline of the thesis.....	18
1.3.4    List of publications.....	19
<b>Part I: Physical Investigations</b> .....	<b>21</b>
<b>Experiments on a labriform swimmer</b> .....	<b>23</b>
2.1    Materials and methods.....	23
2.1.1    Experimental fish and husbandry.....	24
2.1.2    Experimental setup.....	26
2.1.3    Flow velocity calibration.....	28
2.1.4    Experimental protocol.....	28
2.1.5    Kinematic analysis.....	30
2.1.6    Data analysis.....	30
2.2    Results.....	31
2.2.1    Kinematics.....	31
2.2.2    Metabolics.....	35
2.3    Discussion.....	38
2.4    Summary.....	40

<b>Investigations on a sub-carangiform swimmer.....</b>	<b>41</b>
3.1    Materials and methods.....	41
3.1.1    Experimental fish and husbandry.....	42
3.1.2    Experimental setup.....	43
3.1.3    Experimental protocol.....	45
3.1.4    Experimental data analysis.....	46
3.2    Results.....	47
3.3    Discussion.....	49
3.4    Summary.....	52
<b>Main findings from physical investigations.....</b>	<b>53</b>
<b>Part II: Numerical Studies.....</b>	<b>55</b>
<b>Theoretical and numerical methods .....</b>	<b>57</b>
4.1    Governing equations.....	57
4.2    Boundary conditions.....	59
4.3    Numerical solver.....	59
4.4    Dynamic mesh motion.....	61
4.4.1    Deforming mesh method.....	61
4.4.2    Overset grid method.....	62
4.5    Numerical implementation of self-propulsion.....	64
4.5.1    Self-propulsion strategy.....	64
4.5.2    Verification study of an elliptic foil.....	67
4.6    Summary.....	81
<b>Flapping foil studies .....</b>	<b>83</b>
5.1    The models.....	83
5.2    Numerical setup.....	84
5.3    Assessment studies of the semi-circle foil.....	87
5.3.1    Influence of mesh motion methods.....	87
5.3.2    Influence of overset region size.....	90
5.3.3    Influence of mesh ratio between overset and background grids.....	92
5.3.4    Grid convergence analysis.....	93
5.3.5    Influence of time discretization.....	95
5.4    Results and discussion.....	95
5.4.1    Instantaneous thrust and power.....	96
5.4.2    Time-averaged thrust and power and efficiency.....	112

5.4.3	Vorticity and velocity .....	115
5.4.4	Influence of Reynolds number and scaling of drag-thrust transition .....	126
5.4.5	GAMC analysis.....	129
5.5	Summary .....	131
<b>Fish-like swimming foil studies .....</b>		<b>133</b>
6.1	Forced fish-like swimming foil.....	133
6.1.1	Swimming kinematics.....	134
6.1.2	Numerical setup .....	135
6.1.3	Calculation method of swimming forces and efficiency .....	138
6.1.4	Results and discussion.....	141
6.2	Self-propelled fish-like swimming foil.....	159
6.2.1	Self-propelled foil in calm water and current.....	160
6.2.2	Self-propelled foil in a tunnel.....	177
6.3	Summary .....	184
<b>Conclusions and further work.....</b>		<b>187</b>
7.1	Conclusions.....	187
7.1.1	Physical investigations .....	187
7.1.2	Numerical simulations .....	189
7.2	Recommendations for further work .....	192
<b>References .....</b>		<b>195</b>
<b>Appendix A.....</b>		<b>207</b>
<b>Appendix B.....</b>		<b>209</b>
<b>Appendix C .....</b>		<b>213</b>





# Chapter 1

## Introduction

### 1.1 Background and motivation

For hundreds of millions of years, adaptation and evolution have enabled fish to achieve excellent propulsion efficiency and performance (see e.g., Figure 1-1), such as low resistance, high swimming speed and good manoeuvrability. These aquatic animals can be considered as underwater bio vehicles with locally deformable skin and global flexible skeleton, and they propel themselves with many hydrodynamic advantages compared to conventional marine vehicles powered by screw propellers. For instance, fishes can move at high speeds equal to several body lengths per second, reach accelerations much larger than gravity accelerations, introduce little disturbance to the environment, swim with outstanding stealth and obtain various flow sensing abilities to perceive complicated underwater environments (e.g., Williams et al., 2001; Montgomery et al., 1995). They have superior capabilities to produce thrust force by acceleration of water through the movement of their body and body/caudal fins, and they can improve the propulsive and steering performances by controlling the vortex generating and shedding from their body. Simultaneously, they reduce the frictional stresses along their wetted surface by taking advantage of their compliant skin, their mucus, or their skin micro and macro features. In recent years, with the aim of understanding physical mechanisms behind the fish extraordinary performances and transferring them into bio-inspired marine vehicles, the studies of fish hydrodynamics have attracted more and more attention to researchers in the fields of biology, hydrodynamics and engineering.



Figure 1-1. Examples of swimming fishes with high hydrodynamic performance. Left: Atlantic bluefin tuna that can reach maximum speed of  $70\text{km/h}$  ([www.sciencefocus.com](http://www.sciencefocus.com)). Right: Fish shows high acceleration and manoeuvrability to escape from a predator ([www.nature.com](http://www.nature.com))

As an important area of biomimetics, the fish hydrodynamic study should be a multi, strongly interdisciplinary research combining and merging theories and techniques of fluid dynamics with biology. A variety of knowledge is required to reveal the detailed mechanisms of fish hydrodynamics. For example, the fish-physiology study can benefit the comprehension of passive and active fish behaviour as well as control of the surrounding water flow, and then guide towards dedicated physical and numerical investigations on the hydrodynamic field around a fish and on the local and global water-induced loads on a fish. The scientific research inspired by aquatic animals can be traced back to the beginning of the last century, and many scientists have been fascinated to explore the hydrodynamics of swimming from various aspects, such as fish locomotion and manoeuvring, individual fish and schooling fish features, etc. Breder (1926) classified the swimming modes of fishes into two generic categories according to the body part utilization: one is the body and/or caudal fin (BCF) propulsion, and the other one is median and/or paired fin (MPF) propulsion. Through the observation of dolphins, Gray, J. (1936) estimated that their experienced drag power was several times larger than their muscle power, but they could still maintain a high swimming speed. Although the basic premise of Gray's paradox was flawed because of potential errors in estimating the swimming speed and inconsistencies between swimming performance and data on muscle power (Fish and Lauder, 2006), this finding motivated a number of researchers to dig into the mechanisms of fish swimming. Since 1960s, several theoretical studies have been carried out to analyse more accurately the fish propulsion force (eg., Lighthill, 1960; Wu, 1961; Horlock, 1978). In the latest several decades, remarkable progress has been made in the development and design of fish-inspired underwater vehicles (e.g., Yu et al., 2011; Liljebäck and Mills, 2017). Among them, the first and one of the most well-known complete robotic fish systems, named *RoboTuna*, was developed by Massachusetts Institute of Technology (Triantafyllou and Triantafyllou, 1995).

With the increasing requirements of various biomimetic marine applications and underwater missions, the significance of a multi-disciplinary perspective for bio-inspired solutions has been well recognized (e.g., Kovač, 2014). However, still a limited number of the state-of-the-art available studies has built up a strongly interdisciplinary research methodology, dealing with fish physiology, swimming behaviour and related fluid dynamics, to examine fish propulsive performance for guidance towards novel engineering solutions.

The present study aims to investigate the physical mechanisms of fish propulsion and locomotion both experimentally and numerically, and the main motivation is to understand fish hydrodynamics as well as to contribute to the transfer of this knowledge into greener and more efficient bio-inspired underwater vehicles, which could lead to positive consequences for the environment and the society.

## 1.2 Literature study: State-of-the-art

In the present work, the focus is on the understanding of fish hydrodynamics and to provide guidance for the improvement of bio-inspired propulsion. Many documented investigations have been done to observe the fish swimming behaviours, examine the propulsive performance of flapping foils and develop designs of biomimetic underwater vehicles. A review of most

relevant and recent studies on the topic is outlined below, which is not exhaustive but can provide a clear view on the state-of-the-art on this topic.

### 1.2.1 Fish swimming behaviour

In the studies of fish swimming, it is essential to understand how movements of the fish body and/or fins, resulting from muscle contraction, affect the surrounding water in such a way as to move the fish through it (Bone and Moore, 2008). A comprehensive classification and description of the fish swimming modes was developed by Breder (1926) and expanded by Lindsey (1978). As stated in the previous section, the fish swimming modes can be generally categorized into BCF propulsion and MPF propulsion. According to Sfakiotakis et al. (1999), a great majority of fish propel themselves by bending the bodies into a backward-moving propulsive wave that extends to their caudal fin, and these BCF swimmers can produce greater thrust force and accelerations. The BCF mode is suitable for long-term cruising and has been the centre of traditional scientific attention among biologists and mathematicians because of easier experimental investigations and repetitions. The MPF mode, making use of their paired pectoral fins, dorsal fins, or anal fins for swimming, is generally employed at slow speeds but can offer sufficient manoeuvrability. It should be noted that MPF swimmers would switch to the powerful BCF mode at high speeds and burst swimming. Based on whether the propulsion is undulatory or oscillatory and which body parts are used to generate thrust force, the body movements of different fish species have been further divided into the types shown in Figure 1-2 (Sfakiotakis et al., 1999; Li et al., 2022). BCF mode can be classified into anguilliform, subcarangiform, carangiform, thunniform and ostraciiform. Following this order, the fish bodies become more and more rigid, and the body movements are restricted in smaller posterior regions. The most common MPF mode consists of rajiform, diodontiform, labriform, amiiform, gymnotiform, balistiform and tetraodontiform. It is indicated by several reviews that BCF propulsion, especially thunniform and carangiform, is more efficient than MPF propulsion (e.g., Triantafyllou et al., 2004; Bandyopadhyay, 2005).

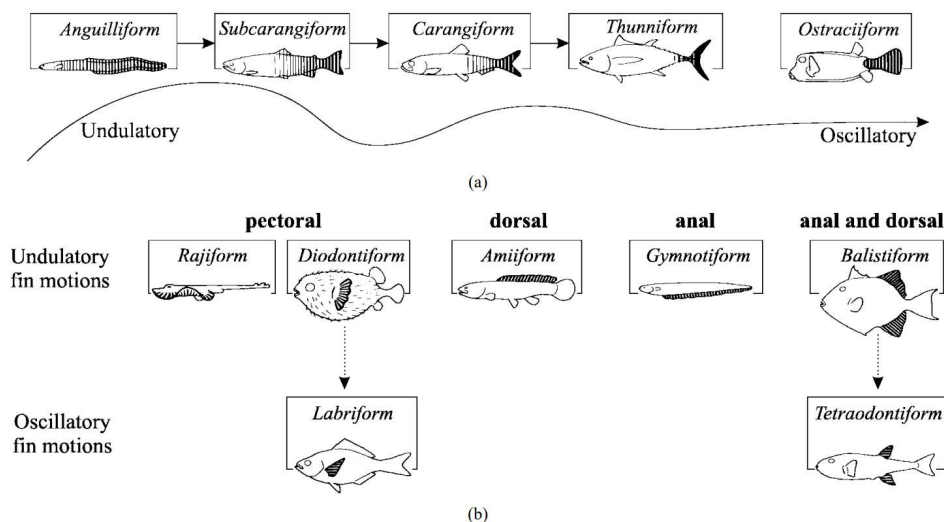


Figure 1-2. Classification of fish swimming modes with (a) BCF and (b) MPF propulsion. Fish shaded areas contribute to thrust generation (Taken from Sfakiotakis et al., 1999)

The distinctive swimming capabilities of BCF fish have attracted many scientists and engineers to study fish-propulsion mechanisms and to design fish-inspired robots. Based on the fish swimming observations from biological research, the midline motion of a BCF fish body during steady locomotion is often described by a travelling wave propagating backward with an increasing amplitude. Videler (1993) analysed the experimental data of several fish species and reported that the midline movement can be modelled by three odd Fourier terms. Lighthill (1960) demonstrated fish-like swimming motions using a sinusoidal wave with an increasing amplitude. Maertens et al. (2017) addressed recoil motions when describing travelling wave kinematics that resemble those observed in fish according to either carangiform or anguilliform swimming. However, this traditional fish-movement description method is not universal because the travelling wave amplitude envelopes can be remarkably different among different BCF fish species (Donley et al., 2004). As an alternative approach to quantify various kinematics of BCF swimmers, Cui et al. (2018) decomposed the midline motions of swimming fish into travelling and standing components through the complex orthogonal decomposition (COD) analysis and adopted the concept of travelling index, i.e., the relative ratio between the magnitudes of the travelling and standing components, to characterize the swimming pattern of BCF fish. The typical biological range of dimensionless wavelength (wavelength  $\lambda$  to fish body length  $L$  ratio), dimensionless wave number (product of the wave number  $k$  and the fish body length  $L$ ) and the travelling index for different BCF categories are documented in Table 1-1.

Table 1-1. Typical swimming parameters and the travelling index of different BCF fish from Cui et al. (2018)

Fish categories	$\lambda/L$	$kL$	Travelling index
Anguilliform	$< 1$	6.28~20	0.70~0.94
Subcarangiform/carangiform	$\approx 1$	6.28	0.42~0.88
thunniform	1~2	3.14~6.28	0.28~0.70

Fish swimming involves the transfer of kinetic energy and momentum from the animal's propulsive movements to the water. Vortex formation and features can contain key components in this fluid-structure interaction problem. Compared to the classical von Kármán wake behind a blunt body in steady current, a swimming fish generates a reverse-von Kármán vortex street, as shown in Figure 1-3, which leads to a thrust instead of a drag force (e.g., Triantafyllou and Triantafyllou, 1995; Sfakiotakis et al., 1999). It is documented by Fish et al. (2014) that for a dolphin swimming forward at constant speed, the total thrust produced by the action of the caudal flukes balances the total resistance encountered by its body. Both biologists and hydrodynamicists have attempted to distinguish drag and thrust of a steady swimming fish in their locomotion studies (e.g., Gray, 1936; Lighthill, 1975), while Schultz and Webb (2002) claimed the dilemma that sources of these two forces are not separable in fish's axial undulatory self-propulsion. Fish et al. (2014) predicted the thrust force by combing the visualization of the dolphin vortices and the Kutta–Joukowski theorem, and the results showed that the dolphin is able to produce high thrust and power without requiring special drag-reducing mechanisms. However, Barrett et al. (1999) found that the fish swimming motion can be drag-reducing as its drag estimate is smaller than that of the corresponding rigid body. On the other hand, some analytical result such as Lighthill (1971) and experimental studies such as Anderson et al. (2001)

indicated that the friction drag increases with the fish swimming motion, and Fish (1993) reported that the pressure component of drag force also increases for swimming dolphins, which suggests a conclusion of drag-increasing. Due to the simultaneous existence of the thrust and drag force, this propulsion mechanism of fish swimming performance remains an important subject that deserves further research.



Figure 1-3. The wake of a swimming fish has reverse-von Kármán vortex street, associated with thrust generation (Taken from Triantafyllou and Triantafyllou, 1995)

It is noted by Lighthill (1969) that all the fastest aquatic animals with BCF propulsion adopted the carangiform swimming mode, i.e., most of their undulatory motions are restricted in the rear half of their body region. To explore the reason, he proposed the elongated body theory and claimed that the thrust is produced only at the tail. Therefore, carangiform swimmers can have more efficient propulsive performance than anguilliform swimmers that undulate the whole body. Borazjani, I., & Sotiropoulos, F. (2010) carried out numerical simulations to examine a more complex scenario. They employed four different self-propelled virtual swimmers to separate the effects of body form and kinematics (only global flexible motion was considered) on the hydrodynamics of fish swimming. Their results showed that anguilliform kinematics reaches higher velocities and efficiency in the viscous and transitional flow regimes, while the carangiform kinematics performs better in the inertial regime. Scientific studies have found that marine animals use vorticity control to enhance swimming performance in manoeuvring and propulsion. For instance, Triantafyllou et al. (2002) provided some of the basic mechanisms employed for controlling vorticity by means of experiments on fish-like robots and on rigid and flexible fins. Fish swimming applies many mechanisms, such as flow-separation elimination, turbulence reduction and energy extraction from oncoming flow, to minimize the energy needed for locomotion (Techet et al., 2003). However, some crucial aspects of fish hydrodynamics have not been investigated, like the influence of local and global flexible fish motion on the swimming efficiency and speed in different flow regimes as well as how to identify the fish features leading to high propulsive performance. Moreover, it should be noted that a wealth of fish swimming data has been provided from biological experiments performed in swim tunnels. Several previous studies have shown that longer and larger swim tunnels can improve fish swimming capability (e.g., Tudorache et al., 2010; Remen et al., 2016). Though it has been well established that the tunnel wall can lead to a boundary-layer effect, it is not trivial the qualitative and quantitative influence on the recoil of a swimming fish with respect to open-water conditions. Therefore, the wall effect of the tunnel on fish swimming behaviours can be an important research topic for more accurate fish hydrodynamic investigations.

In addition, some distinctive features of fishes can also make their performances superior to the manmade marine vessels. Fish and mammals use flippers, body movement, fins, and tails as steering devices. As reported by Triantafyllou et al. (2020), retractable fins are employed by some fish to accommodate both the need for stability of locomotion and the ability to perform tight manoeuvres. The rounded protuberances or tubercles of the humpback whale flipper on the leading edge can reduce the drag and provide lift with less risk of stall at high angles of attack (Miklosovic et al., 2004), which is a kind of passive control of the flow. Meanwhile, the experimental and numerical studies, reported in Fish and Lauder (2006), indicated that swimming fish can use active control through changing fin curvature, displacement, and area. However, demonstrating active flow control is particularly difficult as fins are highly flexible structures and easily deformed by imposed hydrodynamic loads. Triantafyllou et al. (2004) reviewed experimental studies on biomimetic foils and concluded that many functions and details of fish fins remain unexplored. Physical mechanisms of vortical structures formation and force production in unsteadily underwater biomimetic foils need to be further studied. From the previous work, theoretical and numerical studies on fins should be defined carefully as inviscid theory fails when the thrust force is small.

Many species of fish in nature spend their whole life in groups. An emergence of a qualitatively different behavioural pattern from that of the constituent individuals can be caused by the aggregation of fish into a highly integrated supergroup (Pavlov and Kasumyan, 2000). This biological significance of fish schooling behaviour is thus essential to investigate swimming patterns and understand the causal mechanisms. There have been various explanations for the formation of fish schools, and the main reasons can be predator evasion, energy savings or hydrodynamic advantages, migration, foraging, etc. (Parrish and Edelstein-Keshet, 1999). By comparing the tail-beat frequency and oxygen consumption of fish swimming alone and in groups, it is believed by many researchers that one of the most significant benefits of the moving school is a reduction of energy expenditures in swimming compared to that of solitary fish (e.g., Johansen et al., 2010; Shaw, 1978). To reveal the mechanisms of hydrodynamic interrelationships in fish schools, numerous studies have been carried out. Breder (1967) found that fish swimming in a school could maintain the cruising speed 3-5 times longer than solitary individuals under the same conditions. Weihs (1973) proposed a pioneer ‘diamond’ configuration theory of schooling indicating that fish can save energy by taking advantage of adjacent propulsive wakes. Though this analytical model was compelling, there was few evidence from nature supporting such a strict swimming regulation of relative spatial positions (e.g., Partridge and Pitcher, 1979; Katz et al., 2011), which might be caused by potential trade-offs during fish schooling (Abrahams and Colgan, 1987). Marras et al. (2015) carried out experiments on grey mullet *Liza aurata* and demonstrated that every individual in a fish school could reduce swimming cost compared to solitary swimming at the same speed. Dong and Lu (2007) numerically simulated multiple swimming fish in a side-by-side arrangement and their results indicated that the lateral interference is of benefit to save the swimming power in the in-phase case and enhance the forces in the anti-phase case. Besides the hydrodynamic advantages, there can be many behavioral effects in a fish school. For instance, the imitation ability is important for schooling fish as it can help the school retain its unity during rapid and complicated maneuvers when fish are frightened (Verheijen, 1956). It was found that a visual

perception of the partner was able to stimulate "school phenomenon" and increase the fish swimming capability (e.g., Pavlov and Kasumyan, 2000; Sil'va and Saburenkov, 1979). These swimming fish studies prove that schooling can provide not only hydrodynamic advantages but can also have a behavioral impact on the fish. In this context, the relative importance of hydrodynamic and behavioural influence of schooling on the swimming fish is still an open research question.

### 1.2.2 Flapping foils

During fish swimming activities, it is very common for fish to take advantage of the flapping motion of their body and of caudal/pectoral fins to generate propulsive forces. These aquatic animals can often achieve highly effective fluid dynamic performance through the oscillating motion of their foil-like body and/or fins. Inspired by the excellent fish propulsive behaviour, many scientists have been dedicated to getting an insight into these physical phenomena and identifying some crucial principles that can be applied into marine transportation, and herein, numerous experimental and numerical studies have been carried out. Though the kinematics and dynamics of swimming fish are complex, some key features can be grasped from a simplified model of flapping foils. For example, the flapping consisting of a combination of heaving and pitching motions can mimic the tail oscillations of thunniform swimmers (Schouveiler et al., 2005), while the carangiform swimming gait bears some similarity to the oscillating motion of a flexible fin pitching about an axle near its leading edge (Riggs et al., 2010). After flapping foils were reported to be able to generate a thrust force and be an alternative to conventional propellers (Birnbaum, 1924), a great number of studies has been dedicated to investigating the propulsive performance of flapping foils, and a variety of novel marine devices with the utilization of flapping foils have been proposed, such as oscillating wavefoils fixed on a ship that can provide propulsion force and reduce ship resistance and motion (e.g., Shen et al., 2022; Bøckmann and Steen, 2016), ocean energy harvesting devices using flapping foils to extract energy from wind, wave and current (e.g., Bowker et al., 2016; Chen et al., 2017; Xiao and Zhu, 2014) and wave gliders that make use of tandem hydrofoils for thrust generation (e.g., Wang et al., 2019). Till today, the hydrodynamics of flapping foils is still a very popular topic in the field of fluid mechanics.

To study the propulsive performance of flapping foils, as well as of swimming fish, several non-dimensional parameters have been often employed in previous research. Two of the most important ones are the Reynolds number,  $Re$  (defined as the product of the characteristic free-stream velocity and characteristic foil/fish body length divided by the kinematic viscosity of fluid), governing the flow regime (laminar or turbulent) along the fish or foil, and the Strouhal number,  $St$  (defined as the product of the flapping frequency and characteristic wake width divided by the propulsion speed), governing the hydrodynamic features of flapping foil or fish generated wakes and so the flow-induced forces. Experimental and numerical studies have found the optimal propulsive performance incurred by a flapping foil is within a narrow interval  $0.2 < St < 0.4$  (Anderson et al., 1998), which is consistent with the range adopted by many aquatic animals regardless of the sizes and species (Eloy, 2012). It confirms that these native swimmers have been evolved to cruise at an optimal strategy to minimize the energy cost during natural selection.



Flapping foils can lead to the formation of various vortex formation and organization (e.g., Andersen et al., 2017; Schnipper et al., 2009), and observation into the vortex processes is vital for understanding how an oscillating foil generates propulsive forces. With the change of flapping frequencies and amplitudes, different wake scenarios can occur behind flapping foils, for instance, some typical wake types that are often observed in experiments include von Kármán (vK) vortex street in which the vortices engendered at each side of the foil stay on the same side of the symmetry line of the wake in their downstream evolution, aligned wake where vortices of alternating signs align on the symmetry line of the wake, reverse von Kármán (reverse-vK) wake where the vortices shed on one side of the flapping foil organize themselves in the wake on the other side of the wake symmetry line, and asymmetry wake where the vortex street propagates obliquely to one side of the wake symmetry line (Koochesfahani, 1989), as shown in Figure 1-4. Apart from these, many other complicated wake scenarios can also occur with two vortex pairs (2P) or more, say  $n$  ( $nP$ ), shed per oscillation period, combined with/without shedding of single vortices of opposite signs.

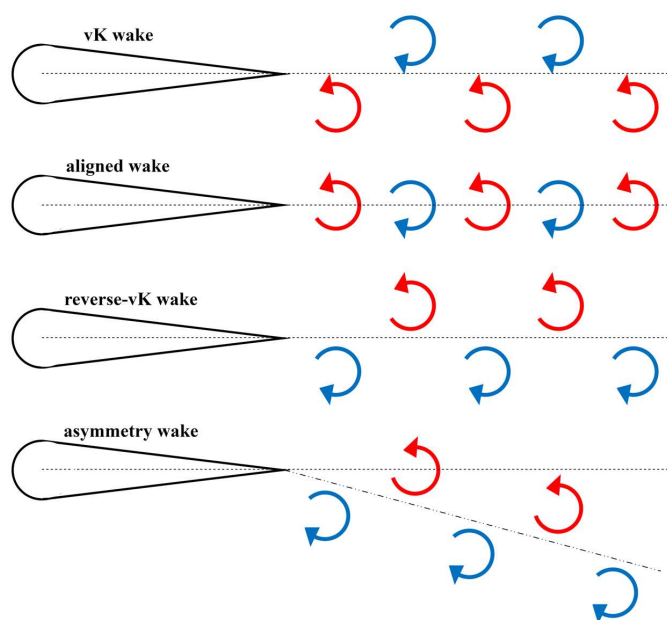


Figure 1-4. Schematic view of some typical types of wake structures

There has been extensive work on flow visualizations pertaining to foils since last century. The observed wake structures were firstly used for theoretical explanation of the force production by von Kármán and Burgers (1943), and then confirmed through wake visualization experiments carried out by Bratt (1950). In the experimental study of Godoy-Diana et al. (2008), the vK-type wakes and the reverse-vK wakes behind a pitching hydrofoil were measured using particle image velocimetry (PIV) techniques, and they reported that a quasi-two-dimensional (quasi-2D) picture of the wake often contains key dynamical elements that are crucial for every flapping foil system, which is closely related to practical engineering problems. The vK / reverse-vK wake transition is considered to occur when the vortices align along the symmetry

line of the wake. The reversed-vK wake plays a significant role in biological locomotion (Triantafyllou et al., 2000). Besides, other complex wakes such as 2P can also be important for swimming of aquatic animals (Muller et al., 2008). Schnipper et al. (2009) used a gravity-driven vertically flowing soap film to visualize a variety of wakes behind a pitching foil with up to 16 vortices per oscillation period, including vK vortex street, inverted-vK vortex street, 2P wake, 2P+2S wake and novel wakes ranging from 4P to 8P. The wake types are mapped out in a phase diagram spanned by the foil-thickness based Strouhal number and the dimensionless flapping amplitude, as shown in Figure 1-5. This Strouhal number is associated to the body geometry rather than the unknown wake width depending on the established regime, and the product of the two axes represents the flapping amplitude based Strouhal number  $St_A = St_D \cdot A_D$ , i.e., the solid lines in the diagram are lines with constant  $St_A$  values. This allows us to investigate the significant wake transition from vK to the reverse-vK by increasing flapping frequency and/or amplitude. Andersen et al. (2017) performed a combined numerical and experimental study of a symmetric foil undergoing pure heaving and pure pitching, and they found that these two modes of the flapping motion are qualitatively similar for their wake maps. Besides, their results about the vK and reversed-vK wake transition as well as drag-thrust transition were in agreements with Godoy-Diana et al. (2008). However, it should be noted that their examined flapping foils were in similar semi-circle shapes (Godoy-Diana et al., 2008; Schnipper et al., 2009; Andersen et al., 2017), and how the foil shape influences the wake scenarios of flapping foils is worth to be considered and investigated.

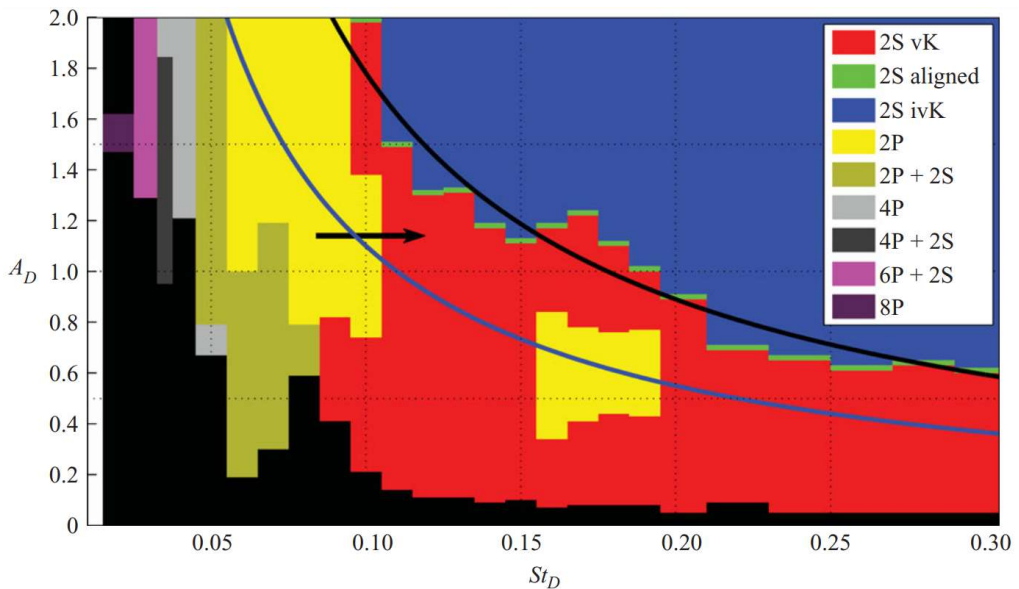


Figure 1-5. Phase diagram of vortex synchronization regions spanned by the foil thickness based Strouhal number and the dimensionless flapping amplitude (Taken from Schnipper et al., 2009). The color shows the type of wake observed. In the legend, ‘vK’ is for von Kármán vortex street and ‘ivK’ is for inverted von Kármán vortex street. ‘S’ represents a single vortex and ‘P’ represents a pair of vortices of opposite signs shed per oscillation period. Along each solid line the flapping amplitude based Strouhal number is constant with the values 0.11 (blue) and 0.18 (black)

The prediction of the hydrodynamic forces acting on the flapping foil is one of the classical problems to understand the propulsion mechanisms. Extensive studies have been conducted both theoretically and experimentally focusing on the measurement of force, moment and propulsion generated by flapping foils (e.g., Katzmayer, 1922; Garrick, 1936). The development of experimental techniques and analytical methods has made it feasible to directly measure or calculate the forces (Mackowski and Williamson, 2015). The forces experienced by the flapping foil depend on the vortex formation and on the consequent features of the fluid-structure interactions, and identifying these links is essential in order to understand the propulsion mechanisms. Many researchers have performed systematic work with respect to the force generation and wake structures of a flapping foil. From the comparison of wake-scenarios phase diagram and measured forces, it is found that the wake transition from vK to reverse-vK vortex street is not exactly consistent with the force transition from drag to thrust (e.g., Godoy-Diana et al., 2008; Schnipper et al., 2009). In the classical inviscid theory, a flapping foil is expected to experience a thrust force when it produces the reverse vK wake, and the boundary between the vK / reverse-vK wake scenarios is also treated as the force transition boundary from drag to thrust. However, in a real fluid, the drag-thrust transition of a flapping foil always takes place in the reverse-vK wake regime and tends to the boundary between the vK/reverse-vK wake scenarios as the Reynolds number increases (e.g., Xu et al., 2021).

Numerous recent studies have provided a wealth of data in terms of flapping motions and wake flow fields at different Reynolds numbers. Experimental data for flapping hydrofoils suggest that fish prefer to swim near a ‘universal’ optimal Strouhal number  $St_A$  because the propulsive efficiency (defined as the ratio of useful power over input power) is maximized (Triantafyllou et al., 2000). However, it is shown for carangiform swimming that the optimal Strouhal number depends strongly on the Reynolds number (Borazjani and Sotiropoulos, 2008). In the work of Chao et al. (2019), the drag-thrust transition of a rigid pitching foil with various chord lengths was studied to find the link between the critical Strouhal number at drag-thrust transition and the Reynolds number. It should be noted that the foil shape in their simulations was changed together with Reynolds number and this effect on the force transition was not well discussed. To understand the hydrodynamics of flapping foils under different conditions, Smits’ research group has carried out many studies with the focus on the scaling law between various kinematic/environmental parameters and hydrodynamic loads acting on a flapping foil (e.g., Dewey et al., 2012; Van Buren et al., 2019; Floryan et al., 2017). Employing the scaling relations as a guide can help to improve the propulsive performance of flapping foils. However, the scaling laws in previous studies were often acquired for one specific foil and were not demonstrated by other foils with different profiles. Therefore, it is still an open research question on proposing a universal scaling law of the thrust-producing strategies that takes the foil shape into account.

In addition to the extensive research and applications by simplifying swimming fish body and fins to rigid foils, the flexible flapping foil studies have also attracted attention to account for the effect of active or passive deformation on the propulsive performance, thus decreasing the discrepancy between the physical findings of rigid foils and real fish. Though both rigid and flexible foils can generate propulsive force by means of flapping motions in water current, it

should be noted that their hydrodynamic behaviours can be quite different, for instance, flexible foils can have larger effective flapping amplitude (Marais et al., 2012) and more complex tail vorticity (Shin et al., 2009). To gain a deep insight into the thrust generation and propulsion efficiency of flexible flapping foils, there have been numerous experimental and numerical studies on such flexible models with pitching motions (e.g., Dewey et al., 2013; Moored et al., 2012), heaving motions (e.g., Quinn et al., 2014; Alben et al., 2012), or a combination of both motions (e.g., Richards and Oshkai, 2015; Liu et al., 2013; Esposito et al., 2012). Katz and Weihs (1978) calculated the hydrodynamic forces of a flexible oscillating foil in an inviscid flow and pointed out that the flexible foil had 20% higher propulsive efficiency than the rigid foil. Dewey et al. (2013) experimentally measured thrust and power acting on flexible pitching foils and found that their thrust production was amplified by 1-2 times while the propulsive efficiency was doubled. However, the detailed understanding of the flexibility effect on the propulsive mechanism of flapping foils remains unclear.

Besides the fluid-structure interaction due to elastic body, a predetermined deformation of the flapping foil has a large potential to provide better control of flow separation and vortex shedding along the flapping body, which leads to greater thrust force and propulsion efficiency. A simplification of biomimetic fish-like motion can be modelled as a combination of flapping motion and morphing motion, and this strategy, combining the advantages of both motions, might be developed into greener and more efficient bio-inspired marine transportation design. Many studies have been carried out for the design and analysis of various morphing concepts with applications to two and three-dimensional foil models. Miao and Ho (2006) investigated the viscous flow over a deformable plunging foil with different flexure amplitudes and found that an enhancement in the propulsive efficiency was observed when the flapping foil has a flexure amplitude of 0.3 of the chord length. Neogi et al. (2022) numerically predicted the wake features and forces of a combined morphing and heaving foil and showed that the thrust generation is closely related to the morphing sections of the body and morphing amplitude. Apart from deformable foils mimicking the fish-like swimming motion, there have been other biomimetic propulsion strategy research involving the change of body volume, which is similar to the shape change of cephalopod, such as squids and octopus, in an escape propulsive behaviour. For example, Weymouth and Triantafyllou (2013) studied the hydrodynamic mechanisms behind the fast start through the shrinking model of a deflating prolate spheroid and pointed out that a flexible collapsing body can have superior propulsion than a rigid-shell jet-propelled body. It was reported by Li et al. (2018) that considerable progress on morphing foils has been made, but the adoption of morphing concepts for routine use on propulsive systems is still scarce. Therefore, based on the understanding of propulsive mechanism behind rigid/flexible oscillating foils, further studies on creating novel morphing foil strategies, combining the advantages of different flapping foils, are crucial to improve the propulsion efficiency and robustness of bio-inspired vehicles and robots.

### **1.2.3 Underwater bio-inspired vehicles and robots**

The ocean covers approximately 70.8% of the earth's surface and has large potential value with respect to the vast amount of water, mineral and aquacultural resources. How to explore and exploit the ocean with safety and efficiency is an essential research topic in the modern

society. For this reason, an increasing attention has been paid to the development of various species and multi-functional marine vehicles working at different environments, from shallow to full ocean depth, with different capabilities like oceanographic observation, underwater mine detection, surveillance, pipeline inspection, gas drilling, water quality monitoring, samplings, rescues, etc (e.g., Cui et al., 2017; Li et al., 2021; Fattah et al., 2016). As aquatic animals have many superior performances compared to conventional marine vessels, such as high propulsion efficiency, outstanding manoeuvrability, low noise and minor disturbance to the flow field, the learning of fish swimming hydrodynamics and the design of biomimetic devices are of great importance for the scientific and engineering research of new-generation underwater bio-inspired vehicles and robots.

In the last decades, researchers have made large progress in understanding fish swimming behaviour and physiology, hydrodynamic physics of rigid and flexible flapping foils (as a simplified model of swimming fish). Meanwhile, tremendous advances in smart materials and actuators and compliant mechanisms have laid the foundation for the soft bionic shape of robotic fish and breathed new life into the bio-inspired underwater vehicle design (e.g., De Greef et al., 2009; Li et al., 2022). Artificial intelligence algorithms, closed-loop control based on onboard sensors, the extraction and analysis of big data have also greatly enhanced the biomimetic device performance, optimization, precise control and information perception capabilities (e.g., Fan et al., 2020; Yu et al., 2018; Xie et al., 2021).

With different purposes of underwater missions, it is necessary to design bio-inspired submersibles with the most appropriate swimming form depending on their application. Similar as the classifications of the fish swimming modes, the fish-inspired vehicles can also be divided into BCF and MPF robots with a series of subcategories (Sun et al., 2022). Figure 1-6 shows several representative fish-inspired robots based on different swimming modes with the description and comparisons of their characteristics. It is obvious that each type of bio-inspired vehicles has its unique features, and the biomechanical efficiency of swimming exhibits large differences for hydrodynamic propulsion, in accordance with their body shape and skeletal structures. Therefore, the corresponding designs of fish-inspired robots should carefully take locomotion modalities and hydrodynamic scenarios into account, and then make trade-offs in these different properties to realize specific targets.

In the practical bio-inspired vehicle design mimicking MPF propulsion, the rajiform class has a variety of robots due to the advantage in stability, manoeuvrability, and efficiency (e.g., Low et al., 2011; Chen et al., 2012), while much less robots belonging to other MPF modes have been made. Although the MPF-based robots often have high manoeuvring capability, there can be a limit in their locomotion speeds. Therefore, it should be noted that the BCF-inspired vehicles are presently still the dominant research interest for high-speed underwater vehicle designs. The robots in anguilliform mode are expected to be highly flexible and perform undulations along the full body, and hyper-redundant design, comprising multiple serially connected links, is usually employed to obtain relatively high manoeuvrability and allow for multiple degrees of freedom (DOF) of robots. Some snake/eel-like robots, such as Eelume (Liljebäck and Mills, 2017), Envirobot (Bayat et al., 2016), LAMPETRA (Stefanini et al., 2012),

*Salamandra robotica* (Crespi and Ijspeert, 2009), belong to this category. However, the pseudo-rigid nature of the links in anguilliform robots may lead to lower manoeuvrability and larger friction force than the mimicked fish. In contrast to the anguilliform type, the subcarangiform and carangiform swimmers are highly similar and their undulatory movements are confined to the aft half or the aft one third part of the body length, respectively, while the rest part of the body remains almost rigid. These two propulsion modes can achieve higher swimming speed than that of the anguilliform but lower manoeuvrability. When mimicking fish of these categories, a multi-joint mechanism is often utilized in the fish-inspired applications. For instance, the G9 fish is a well-known robot using three-link actuation system (Hu et al., 2006). The iSplash-II, employing carangiform swimming, can reach high advancing speed, up to 11.6 body length per second (Clapham and Hu, 2015). A Four-Link Robotic Fish with multiple artificial control surfaces and an embedded vision system is found to have a slightly enhanced cruising speed and a fairly improved turning capability than that of a swimming robot propelled by a single control surface (Yu et al., 2014). To mimic the extremely efficient swimming performance of thunniform fish, the robots in this category are usually very streamlined with a very limited body undulation mainly to the tail area. An early effort toward a corresponding bio-inspired vehicle is the RoboTuna created by Massachusetts Institute of Technology (Triantafyllou and Triantafyllou, 1995), which is also the most famous complete robotic fish system. Thereafter, several other biomimetic robots have been developed. Wen et al. (2012) created a robot mimicking a mackerel named robotic Mackerel. Anderson and Chhabra (2002) utilized experimentally optimized body and tail kinematics from the RoboTuna and developed the Draper Laboratory Vorticity Control Unmanned Undersea Vehicle (VCUUV). Algarín-Pinto et al. (2021) adopted a 3 DOF parallel mechanism with 3UCU-1S (3 universal-cylindrical-universal and 1 spherical joint) as the actuation system of the biomimetic autonomous underwater vehicles (BAUVs) to realize the thunniform locomotion.

Biomimetic marine vehicles have been making rapid progress with the increasing knowledge of biology, hydrodynamics and the development of smart materials and artificial intelligence algorithms. However, most bio-inspired attempts at present are still relatively crude imitations, rarely supported by quantitative and complete hydrodynamic theories, and have difficulties to be optimized (Sun et al., 2022). Fish skills as extraordinary cruising and manoeuvring swimmers can be seldom well employed in current engineered vehicles (Triantafyllou et al., 2016; Fish, 2020). The majority of the existing fish robots are realized as rigid bodies with joint actuations at the tail, with poor locomotion efficiency compared to the biological ones. This emphasises the need for a more fundamental scientific investigation. In addition, flexible body and morphing skins equipped with distributed sensors and actuators can enable engineered vehicles to reduce drag, sense the surrounding environment for energy extraction, and achieve super manoeuvrability. It is expected that the bio-inspired marine vehicles in the future should consider approaches of realizing more flexible deformation and introduce artificially intelligent devices to obtain better hydrodynamic performance.










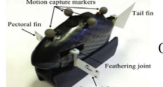
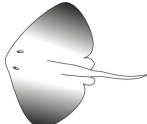


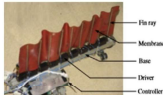


	Fish Subcategories	Representative Robot Fish	Performance description
BCF based fish inspired robots	 Anguilliform	 LAMPETRA (Stefanini et al. 2012)	1) High maneuverability and flexibility 2) Low speed 3) Low hydrodynamic efficiency
	 Subcarangiform & Carangiform	 G9 Fish (Hu et al. 2006)	1) Lower maneuverability than anguilliform 2) Higher speed than anguilliform
	 Thunniform	 MIT RoboTuna (Tolkoff et al. 1999)	1) Lower maneuverability than carangiform 2) Higher speed than carangiform
	 Ostraciiform	 Boxfish-like Robot (Wang et al. 2014)	1) High maneuverability with little flexibility 2) Low speed 3) Low hydrodynamic efficiency
MPF based fish inspired robots	 Labriform	 Flexible Pectoral Fin Joint Labriform Robot (Behbahani et al. 2016)	1) Low maneuverability 2) Low speed
	 Rajiform	 Manta Ray Robot (Gao et al. 2007)	1) Low to medium maneuverability 2) High stability 3) Low speed
	 Amiiform	 RoboGrilos (Hu et al. 2009)	1) High maneuverability 2) Low to medium speed
	 Gymnotiform	 Robotic Knifefish (Curet et al. 2011)	1) High maneuverability 2) Higher speed than labriform

Figure 1-6. Representative fish-inspired robots using different swimming modes (Taken from Sun et al., 2022)

## **1.3 Present work**

### **1.3.1 Objectives**

The state-of-the-art has highlighted many open research questions concerning fish and foils. Those primarily explored in the present thesis are the following:

- What is the relative importance of hydrodynamic and behavioural influence of schooling on the swimming fish?
- How do swim tunnels for biological use affect fish swimming behaviours and propulsion performance?
- Is it possible to identify a universal scaling law between the critical Strouhal number at drag-thrust transition and Reynolds number, which is valid for any foil geometry?
- Can bio-inspired morphing strategies help overcome possible limits in propulsion efficiency and robustness of rigid foils?

In a more general framework, this thesis aims to contribute to the comprehension of fish-like propulsive hydrodynamics. For this analysis, an interdisciplinary approach is used by combing advanced techniques and methods of marine biology and hydrodynamics. Understanding the mechanisms behind high performances of swimming fish as cruising vessels can create new knowledge and will open to innovative solutions for greener and efficient marine transportation, with positive consequences for the environment and the society.

Therefore, the main objective of this study is to perform a systematic research strategy, investigate the fish hydrodynamics using both experimental and numerical methods, and to explore bio-inspired propulsive mechanisms to be transferred in efficient solutions for novel concepts of underwater bio-vehicles. Under the scope of the research, the thesis has two main goals:

- To improve the understanding of the real-fish swimming behaviours under different scenarios by means of experimental observations, and to better identify various important parameters influencing the fish swimming performance, such as hydrodynamic and behavioural advantages in a fish school, fish body geometry, swim tunnel setup, etc.
- To gain deep insights into the propulsive mechanics of fish-like oscillating (flapping or swimming) foils through systematic numerical simulations. Effective and accurate CFD solvers have been developed and validated to study relevant scenarios. The results are analysed with focus on hydrodynamic loads, wake features and locomotion of the foils and to discuss the dependence of propulsive performance on oscillating kinematics, foil shape and boundary wall conditions. In this regard, the present numerical investigations can provide recommendations for bio-vehicle designs and further experimental setups studying fish hydrodynamics.



### 1.3.2 Main contributions

This work has been carried out at the Centre for Autonomous Marine Operations and Systems (NTNU AMOS) and supported by the Research Council of Norway through the Centre of Excellence funding scheme, Project number 223254-AMOS. The simulations were performed under the Project NN9592K: "Unsteady simulations of water-body interaction problems" on resources provided by UNINETT Sigma2 - the National Infrastructure for High Performance Computing and Data Storage in Norway.

The main contributions of the present work consist of experimental and numerical analyses, and the most important aspects and findings from them are summarized below.

#### Experimental work

Experimental investigations were carried out on two fish species using different swimming modes, i.e., one is a labriform swimmer belonging to MPF category, and the other one is a sub-carangiform swimmer belonging to BCF category. The tests were designed and executed following the guidelines of animal care and under the ethics permit. The swimming behaviours of the examined fish were investigated under different conditions. The findings helped to identify important parameters influencing the fish propulsive performance.

- The swimming performance of the shiner perch (*Cymatogaster aggregate*, a labriform swimmer) was investigated in three scenarios: a solitary fish (Single), a schooling pair of fish (Pair), and a false pair where a single fish swims alongside a video of a conspecific fish (False pair). The swimming behaviours and metabolisms were analysed and discussed among different treatments. The comparisons suggested that schooling confers both hydrodynamic and behavioural advantages over swimming alone for a gregarious fish, but that the relative contribution of the two influences depends on the speed of swimming.
- Observation experiments were carried out on Atlantic salmon (*Salmo salar*, a sub-carangiform swimmer). The swimming performance of the fish was investigated at different current velocities. It was found from the tests that the critical swimming speed of the examined hatchery-reared fish was smaller than previous research data.
- The influence of fish body size and swim tunnel boundary walls on the salmon behaviours in the flume was discussed to identify important factors affecting the fish swimming capability. The experimental results indicated that a blunt body shape might lead to larger hydrodynamic loads on a swimming fish. Moreover, the analysis suggested that the real-fish experimental setup should be improved to be suitably large to reveal realistic swimming patterns in nature and to perform more accurate hydrodynamic studies.

#### Numerical work

A series of hydrodynamic scenarios, inspired by the real-fish experiments and by some relevant

open research questions identified through the state-of-the-art, has been examined by performing CFD simulations within the OpenFOAM open-source platform and assuming two-dimensional flow conditions. The numerical predictions serve to complement experimental studies with the aim of better understanding the physical mechanisms behind the fish propulsive performance. Various fish-like foils have been studied in the present work, involving rigid flapping foils, flexible undulatory foils and morphing foils in prescribed-motion scenarios; moreover, self-propelled conditions have also been examined. Herein, flexible and morphing refer to the foil deformation without and with a change of body volume, respectively. The following contributions in this framework are highlighted as follows:

- A numerical method capable of simulating self-propelled rigid and/or flexible bodies with periodic lateral motions has been proposed. The implemented self-propulsion strategy in OpenFOAM is verified to be numerically accurate and efficient by reproducing an oscillating elliptic foil case.
- Three rigid flapping foils with different fish-like profiles have been studied through systematic numerical simulations. The hydrodynamic loads and wake features have been evaluated and compared to understand the influence of body shape on the propulsive performance. It has been found that the forepart of the flapping foil dominates the friction force component, while the trailing edge shape decides the pressure force.
- The numerically predicted phase diagram of wake scenarios with respect to foil-thickness based Strouhal number and dimensionless flapping amplitude of the rigid foil has shown good consistency with previous experimental data, and it is demonstrated that drag-thrust force transition occurred after the transition from the well-known von Kármán (vK) wake to the reversed-vK vortex street.
- The critical flapping-amplitude based Strouhal number of the rigid foil at drag-thrust force transition is found to be a decreasing function of the Reynolds number, and the foil body shape makes a difference on the occurrence of drag-thrust transition, i.e., a thinner streamlined foil with a sharp trailing edge tends to have force transition at lower critical Strouhal number at all Reynolds numbers.
- Based on the numerical investigations of the examined rigid flapping foils, a morphing foil strategy has been proposed to combine the advantages of two rigid foils associated, respectively, with the largest mean thrust and with the lowest mean input power requirement.
- The swimming performance of fish-like foils with carangiform swimming mode has been numerically studied to understand the hydrodynamic mechanisms of their propulsive performance. The forced swimming foil with prescribed undulatory deformations and restrained rigid motions has been examined and agreed well with reference data. A series of simulations has been performed to discuss the influence of body shape and Reynolds number on the propulsive performance. The results indicate

that a fish with a blunter body experiences larger drag and has more limited capability to generate thrust compared to a slimmer fish.

- The swimming performance of a self-propelled fish-like foil free to move in the streamwise direction has been investigated using the developed self-propulsion strategy method. The predicted swimming speed is consistent with the velocity in the drag-thrust force transition case obtained from the forced swimming foils, confirming the employed method is correct and accurate for studying fish swimming motion.
- The locomotion of the self-propelled swimming fish-like foil has been investigated systematically in swim tunnels with different widths. The numerical results showed that the forward swimming speed of the fish significantly decreased in narrower tunnels due to side-wall effect. The force and power computation indicated that fish may swim less efficiently in experimental tanks than in the wild.

The physical and numerical findings from this multi-disciplinary research can help to gain better understanding of fish swimming behaviours and propulsive performance in different scenarios. The knowledge obtained can be transferred to create novel bio-inspired vehicles and robots, improve their propulsion efficiency, as well as provide guidelines for aquaculture industry in offshore fish farms.

### 1.3.3 Outline of the thesis

The thesis comprises of seven chapters and is organized in the following way:

**Chapter 1** introduces the background and motivation of the present thesis, gives an overview of some relevant previous studies, summarizes the main contributions and physical findings, and outlines the thesis structure.

**Chapter 2** presents the experimental investigation on a labriform swimmer. The experimental setup, protocol and analysis methods are introduced in detail. The swimming behaviours and metabolisms are assessed and compared between the solitary fish and schooling fish at different swimming speeds. The analysis on the performance of individual fish with the accompany of a visual fake friend is employed to distinguish the behavioural effect from the hydrodynamic advantages during the fish schooling.

**Chapter 3** documents the observation experiments on a typical sub-carangiform swimmer, Atlantic salmon. The kinematic results of the examined fish are analysed and compared with the previous research on the conspecific fish. Parameters such as fish size, body shape and the swim tunnel size are discussed to understand and explain the swimming behaviours of hatchery-reared salmon in the flume.

**Chapter 4** describes the theoretical and numerical methods adopted to study propulsive performance of fish-like foils. A brief introduction and numerical setup in OpenFOAM are provided. Techniques used to handle moving body motion, the deforming-mesh method and the

overset grid method, are discussed. The numerical implementation of the self-propulsion strategy for simulating a self-propelled body is explained in detail. Verification study of the developed solver is carried out through free heaving elliptic foils. Numerical sensitivity analysis is also performed to examine the influence of using different mesh generation methods, spatial and temporal discretization methods.

**Chapter 5** presents the numerical results of various flapping foils in a uniform current. Validation studies are provided for the semi-circle foil under different pitching conditions. Important parameters in overset grid method are examined. The results of different hydrofoils are compared and discussed in terms of hydrodynamic loads and wake characteristics. A scaling law identifying the relationship between critical Strouhal number at drag-thrust force transition and Reynolds number is explored. A morphing strategy is proposed to combine the advantages of the rigid foils with different shapes, that is, to maximize the mean thrust and efficiency while minimizing the required mean input power during the pitching motion.

**Chapter 6** presents a numerical investigation on fish-like swimming foils in water. Both forced undulating foil and neutrally buoyant self-propelled swimming foil are systematically examined. The results of hydrodynamic loads and flow characteristics under different kinematic and water conditions are discussed. The influence of body shape is investigated by comparison between two fish with different profiles. For the self-propelled swimming fish, the side wall effects on the fish locomotion and wake features are also discussed to help interpret the physical experimental data.

**Chapter 7** provides general conclusions of the present study and gives recommendations for further work.

#### 1.3.4 List of publications

The following papers submitted and published are considered as part of this thesis:

- Xu, H. L., Greco, M., & Lugni, C. (2022, October). Numerical Study Relevant for Proper Design of Experiments on Swimming-fish Hydrodynamics. In: *The 14th International Conference on Hydrodynamics (ICHD 2022), Wuxi, China*.
- Xu, H. L., Greco, M., & Lugni, C. (2022, April). Influence of Rigid/Deformable Foil Shape on the Hydrodynamic Loads and Performance. *The 37th International Workshop on Water Waves and Floating Bodies (IWWF 2022)*.
- Xu, H. L., Greco, M., & Lugni, C. (2021, June). 2D Numerical Study on Wake Scenarios for a Flapping Foil. In *International Conference on Offshore Mechanics and Arctic Engineering (Vol. 85185, p. V008T08A033)*. American Society of Mechanical Engineers.
- Siddiqui, M. A., Xu, H. L., Greco, M., & Colicchio, G. (2020, August). Analysis of Open-Source CFD Tools for Simulating Complex Hydrodynamic Problems. In *International Conference on Offshore Mechanics and Arctic Engineering (Vol. 84409, p. V008T08A036)*. American Society of Mechanical Engineers.

The following co-authored papers are considered as additional background for the thesis:

- Yu, Z., Amdahl, J., Greco, M., & Xu, H. (2019). Hydro-plastic response of beams and stiffened panels subjected to extreme water slamming at small impact angles, part II: Numerical verification and analysis. *Marine Structures*, 65, 114-133.
- Yu, Z., Amdahl, J., Greco, M., & Xu, H. (2019). Hydro-plastic response of beams and stiffened panels subjected to extreme water slamming at small impact angles, Part I: An analytical solution. *Marine Structures*, 65, 53-74.

# **Part I: Physical Investigations**



## Chapter 2

# Experiments on a labriform swimmer

Natural selection has ensured that the mechanical systems employed by fish are highly efficient with respect to the habitat and mode of life for each species. Meanwhile, fish can also enjoy numerous behavioral and hydrodynamic advantages during schooling. In this chapter, shiner perches, labriform swimmers using primarily pectoral fins and assisting with the caudal fin at high speed, are employed for a series of experiments. The experiments are carried out in three scenarios: a solitary fish, a schooling pair of fish, and a false pair where a single fish swims alongside a video of a conspecific fish. For each scenario, the swimming performances of the fish in current with various velocities are recorded and analyzed. The main aim of the experiments is to examine the differences of behaviors and metabolisms between the solitary fish and schooling fish. By comparing the performances of a single fish, a real fish pair, and a fish swimming along with a video of an accompany friend, the hydrodynamic effect could be separated from the behavioral/visual effect for the fish schooling. Therefore, this study can help understand the advantages of schooling not only in terms of hydrodynamic influence but also the behavioral effect.

### 2.1 Materials and methods

Fish swimming modes can be classified into two generic categories based on their locomotion features: one is body and caudal fin swimming (BCF), and the other is median and paired fin swimming (MPF) (see e.g., Breder, 1926; Webb, 1984). By considering the movement of fish fins, MPF swimming mode can be further divided into two types: drag-based and lift-based swimming, respectively. For instance, labriform swimming is a typical style of MPF modes commonly employed by many fish species. It is associated with lift-based pectoral fin locomotion within a wide range of swimming speeds (Walker and Westneat, 1997). However, it is important to mention that labriform swimmers would also use caudal fins at high speeds and to perform burst swimming. This pectoral-caudal fin transition of labriform fish is defined as gait transition (Drucker and Jensen, 1996), which allows them to employ BCF mode for more powerful propulsion.

It is believed by many researchers that fish schooling can provide many benefits for fish, such as saving energy, defending against predators, and increasing foraging success (e.g., Weihs, 1973; Marras et al., 2015). While in a school, labriform swimmers may utilize the vortices created by leading individuals to enjoy significant energetic benefits (Johansen et al., 2010).

To better understand the hydrodynamic advantages of fish schooling, a number of studies have been performed investigating interactions between fish, as well as oxygen consumption under



different conditions. Liao et al. (2003) found that the cost of fish locomotion can be reduced by using vortices. Weihs (1973) proposed a ‘diamond’ configuration theory of schooling indicating that fish can save energy by taking advantage of adjacent propulsive wakes. However, it was pointed out later that some fish do not swim in this pattern (Partridge and Pitcher, 1979), which may be due to potential trade-offs in fish schooling (Abrahams and Colgan, 1987). In fact, there have been suggestions that every individual in a fish school could reduce swimming cost compared to solitary swimming at the same speed (Marras et al., 2015). In the context of energetic benefits, studies have been conducted comparing total oxygen consumption of fish swimming in schools with that of individual fish (Ross et al., 1992; Johansen et al., 2010).

It was hypothesized in a lot of research that the company of a fish would help a real swimming fish increase its maximum speed. Although more and more attention has been paid to the study on the hydrodynamic effect of real fish schools, the influence of behavioral effects has been less studied (Parker, 1973; Klyashtorin and Salikzyanov, 1981; Lefrançois et al., 2009; Nadler et al., 2016). Here, we specifically hypothesize that in addition to the hydrodynamic advantages, swimming in a school is associated with reduced mental stress compared to a lone individual, which can help reduce the cost of transport at a given speed as well as increase the maximum and optimal swimming speed.

The shiner perch (*Cymatogaster aggregate*), a labriform swimmer commonly found in loose schools, are employed in the present study to investigate the kinematic and energetic differences of fish schooling with a visible fake fish and with a real fish. The pectoral fin beat frequency, gait transition and oxygen consumption of the above two fish school trials are evaluated and compared with the reference scenario of solitary swimming fish.

The present research was performed in the advanced course "Fish Swimming: Kinematics, Ecomorphology, Behavior and Environmental Physiology" in University of Washington. The experiments were carried out in collaboration with researcher Eleanor Gee and Søs Riber, and under the guidance from Prof. Paolo Domenici, Prof. John F. Steffensen and Prof. Jacob Johansen in the scientific community of biology. There have been challenges to perform a multi-disciplinary study due to different scientific languages and research perspectives, but this experience can greatly benefit the hydrodynamic investigation of fish swimming performances. In the following sections, many biological concepts have been used; therefore, their descriptions are documented in Table 2-1 together with relevant references for a better understanding.

### 2.1.1 Experimental fish and husbandry

36 shiner surfperch (*Cymatogaster aggregate*) with the body mass =  $20.4 \pm 2.7g$ , standard length =  $9.7 \pm 0.5cm$ , height =  $3.1 \pm 0.3cm$  and width =  $1.1 \pm 0.1cm$  were collected using a beach seine at Jackson Beach ( $48^{\circ}31'N$ ;  $123^{\circ}01'W$ ), San Juan Island, Washington, USA, in July and August 2019. Post captures the fish were transferred to the Friday Harbor Laboratories of the University of Washington, where they were held in  $90cm \times 60cm \times 15cm$  flow-through tanks, which were continuously supplied by natural seawater at the temperature of  $13.0 \pm 2.0^{\circ}C$  and with the salinity of 34ppt. No additional food was provided during husbandry except for the plankton brought in by the seawater. As the postabsorptive state of the

fish could ensure maximal energy for swimming, they were transferred to fasting tanks for at least 24 hours prior to an experimental trial. It should be noted that all the animal care and experimental protocols followed the guidelines of the Institutional Animal Care and Use Committee at the University of Washington (permit number 4238-03).

Table 2-1. List of important biological concepts: descriptions and relevant references

Concept	Description	Reference
Standard length	Fish length measured from the tip of its snout to posterior end of the vertebral column	<a href="http://www.fishbase.se/glossary/Glossary.php?q=standard+length">www.fishbase.se/glossary/Glossary.php?q=standard+length</a>
Fork length	Fish length measured from the tip of the snout to the posterior end of the middle caudal rays	<a href="http://www.fishbase.se/glossary/Glossary.php?q=fork+length&amp;language=english&amp;sc=is">www.fishbase.se/glossary/Glossary.php?q=fork+length&amp;language=english&amp;sc=is</a>
Critical swimming speed	Standard measurement to assess fish swimming capabilities	Brett, J. R. (1964). The respiratory metabolism and swimming performance of young sockeye salmon. <i>Journal of the Fisheries Board of Canada</i> , 21(5), 1183-1226.
Pectoral-caudal gait transition speed	Swimming speed at the transition from exclusively pectoral fin oscillation to combined pectoral and caudal fin propulsion	Drucker, E. G. (1996). The use of gait transition speed in comparative studies of fish locomotion. <i>American Zoologist</i> , 36(6), 555-566.
Optimal swimming speed	Swimming speed that minimizes energy expenditure per unit of travel distance	Claireaux, G., Couturier, C., & Groison, A. L. (2006). Effect of temperature on maximum swimming speed and cost of transport in juvenile European sea bass ( <i>Dicentrarchus labrax</i> ). <i>Journal of Experimental Biology</i> , 209(17), 3420-3428.
Metabolic rate	Fish aerobic metabolism usually measured by the rate of oxygen consumption	<a href="http://www.fishbase.se/manual/fishbasethe_oxygen_table.htm">www.fishbase.se/manual/fishbasethe_oxygen_table.htm</a>
Standard metabolic rate	Minimum metabolic rate required to sustain life	Cech Jr, JJ (1990). Respirometry. <i>Methods for fish biology</i> , 335-362.
Maximum metabolic rate	Maximum rate of aerobic metabolism of an animal	Norin, T., & Clark, T. D. (2016). Measurement and relevance of maximum metabolic rate in fishes. <i>Journal of Fish Biology</i> , 88(1), 122-151.
Cost of transport	Energy efficiency of transporting an animal from one place to another	Tudorache, C., O'Keefe, R. A., & Benfey, T. J. (2011). Optimal swimming speeds reflect preferred swimming speeds of brook charr ( <i>Salvelinus fontinalis</i> Mitchell, 1874). <i>Fish physiology and biochemistry</i> , 37(2), 307-315.

### 2.1.2 Experimental setup

Experiments were conducted in a Steffensen-type swimming tunnel of 5.17L volume (see Methling et al., 2011, for the design schematic of a Steffensen-type swim tunnel). It was situated horizontally and immersed within a larger water tank. The rectangular working section of the swim tunnel has the dimension of  $28\text{cm} \times 7.5\text{cm} \times 7.5\text{cm}$  (length  $\times$  width  $\times$  depth). The water flow inside was redirected by baffles when passing corners and a honeycomb is added at the inlet of the working section to help the flow to be laminar. The solid blocking effect was corrected automatically in AquaResp Swim Software based on the fish length, depth, and width (Bell and Terhune, 1970). The water was circulated from the respirometer system into a sump-bucket where it could be oxygen saturated by an air-tone. A separate cooling circulation was used to maintain the temperature inside the sump-bucket at  $13.8^\circ\text{C}$  by pumping water (with a submersible EHEIM pump) through a cooling coil placed in a cooling tank ( $6^\circ\text{C}$ ) when needed. Then, the water was pumped up through a UV-filter from the sump-bucket and back into the respirometer tank, as shown in Figure 2-1. In this way, the recirculating seawater could be aerated and the temperature inside the swim tunnel was controlled at  $14 \pm 0.1^\circ\text{C}$ . In addition, the swimming chamber was cleaned with a bleach solution regularly (every 2 or 3 days) to remove microbial growth and waste.

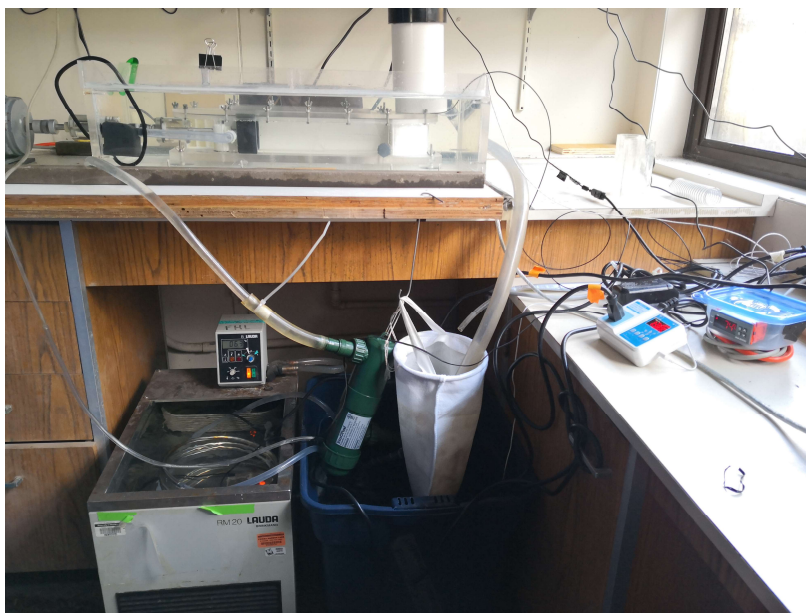


Figure 2-1. Water recirculating and cooling system of the fish experiment

Oxygen calibration was carried out by taking the value of air-saturated seawater as 100% and sodium sulfate as 0%. Measurements of oxygen consumption rate ( $MO_2: \text{mgO}_2 \text{kg}^{-1} \text{h}^{-1}$ , i.e., mg oxygen per kilogram fish per hour) were monitored and logged with AquaResp Swim software for every second during each assessment period which last 10 minutes, including a 240s flush, a 60s calm down phase and a 300s measurement. For each swimming speed of the fish, 3 measurement periods were performed to obtain the average values as well as avoid accidental issues.

A computer monitor with the size of  $37\text{cm} \times 32\text{cm}$  (length  $\times$  height) and the resolution of  $1280 \times 1024$  was situated parallel to the flow direction and next to the working section, as shown in Figure 2-2. Two animations, either of a blank working section or an approximately 8cm long *cymatogaster aggregate* swimming at  $1.5\text{BL/s}$  was shown on the screen depending on the experimental trial.



Figure 2-2. Computer monitor next to the working section of the swim tunnel

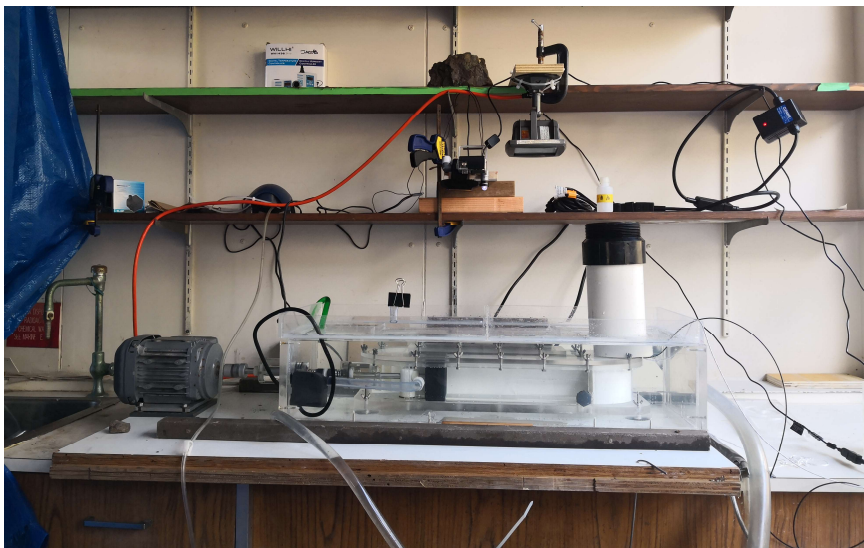


Figure 2-3. Camera and light setup above the swim tunnel

To minimize disturbance during experiments, a big wooden board (73cm × 60cm) was placed on the opposite side of the monitor and also close to the swim tunnel, thus blocking the view of the fish and avoiding experimental fish seeing external stimuli. Above the working section of the swim tunnel, as shown in Figure 2-3, a GoPro HERO 4 and a small LED light was hung solidly to record the dorsal view of the fish swimming behavior throughout the trials at 60fps and 1080 resolution. Besides, a web-camera connected to a working computer was also placed next to the GoPro HERO 4 to inspect the fish condition inside the swim tunnel and help to record fish behavior in case the GoPro HERO 4 did not work normally.

### 2.1.3 Flow velocity calibration

After correct installation of the experimental setups, the flow velocity ( $U_c$ ) was calibrated from 0 to  $125 \pm 10$  cm/s using a digital Hoentszch TAD flow meter. The latter was inserted into the working section of the swim tunnel at three different vertical levels (top, middle and bottom) and three different positions (left, centerline and right) at each level, i.e., 9 locations in total, to measure the flow velocity throughout the working area and allow better understanding of the flow features inside the tunnel. Starting from a static system (i.e., calm water inside the tunnel), the motor voltage ( $V$ ) was increased by small intervals, and the corresponding flow velocities at 9 positions are measured and recorded. The average flow velocity is estimated to be linearly associated with the motor voltage and with its rotational speed (RPM), as shown in Figure 2-4. Therefore, we could derive the mean flow velocity by reading the motor voltage or RPM during experiments without inserting the flow meter again and disturbing the fish inside the tunnel.

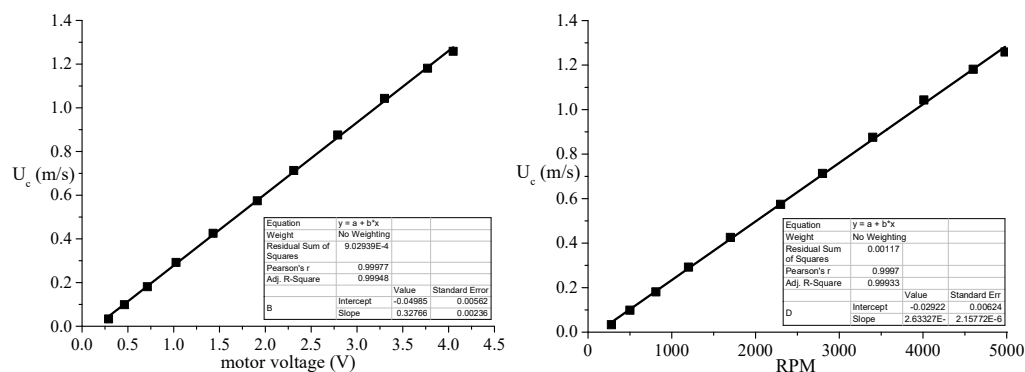


Figure 2-4. Flow calibration results with respect to the motor voltage (left) and rotational speed (right)

### 2.1.4 Experimental protocol

With the aim of investigating the swimming performance of a solitary fish and examining the influence of the fish school from both hydrodynamic and behavioral points of view, fish were randomly assigned to one of the three experimental scenarios, equivalently indicated as treatments, and referred to as “Single”, “Pair” and “False pair”. As illustrated by Figure 2-5, in the Single fish scenario, a solitary fish was released to swim in the current alone with the computer monitor along one side of the tunnel showing an image of the empty flume. The Pair trials involved two real fish swimming in the working section simultaneously, again with an

image of the empty flume displayed on the monitor. In the False pair scenario, a single fish swam in the tunnel with the computer monitor alongside the working section showing a continuous looped video (GIF) of a fish swimming in the flume at  $1.5 BL/s$ . In this way, the real fish in current can see a ‘fake’ companion swimming steadily with it during the trial.

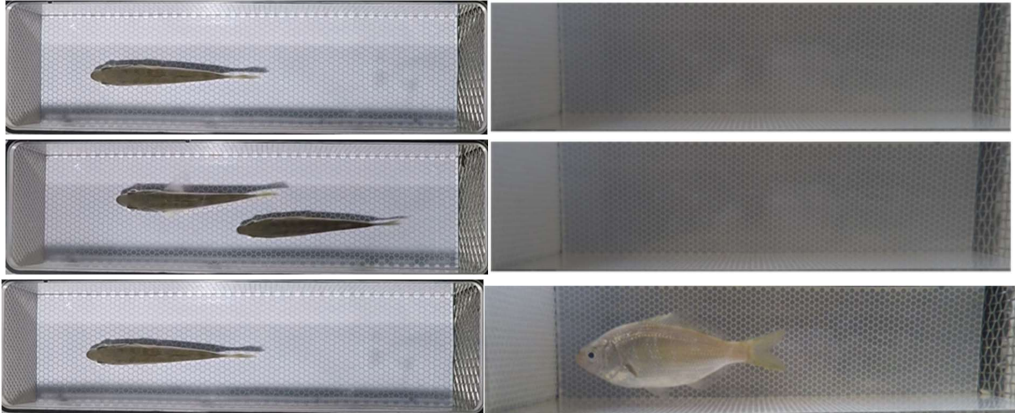


Figure 2-5. The arrangement of fish in working section (left) and the video displayed on the computer monitor along one side of the flume (right) in three treatments: Single (top), Pair (middle) and False pair (bottom)

All the fish used in the experiments were measured in terms of standard length, body width, body depth and weight before they were put into the swim tunnel. The fish were acclimated in the flume for 5-10 hours with the current velocity set as  $0.5 BL/s$  prior to the experimental procedure, to let the effects of handling stress wear off. The fish were considered to have been acclimated when their oxygen consumption decreased to the routine metabolic rate (this corresponds to the metabolism of a fish at feeding, growing, producing sexual products or any other activities, according to Schurmann and Steffensen, 1997) and the changing rate of the measured  $\dot{M}O_2$  was asymptotically zero.

The experiments were carried out following the critical swimming speed ( $U_{crit}$ ) protocol (i.e., increasing speed step by step until fish cannot swim any longer) as described by Brett (1964). In the present trials, the investigations started from current velocity  $0.5 BL/s$  in the flume, and then performed a constant velocity increment of  $1 BL/s$  with a time interval of 30 minutes. The velocity of the current was increased until the point when the fish (the first fish in the case of Pair treatments) were considered to be fatigued, i.e., they could no longer swim unassisted and rested on the downstream grid of the flume for more than 5 seconds during a 30-second time interval. Respirometry was undertaken during each trial, with 3 measurements of  $\dot{M}O_2$  at each 30-minute current velocity interval. For each respirometry measurement, the period last 300 seconds, with a 240-second flushing time and a 60-second waiting time beforehand. At the end of experimental trials, the fish were given 20-30 minutes to recover in the swim tunnel at  $0.5 BL/s$  before they were removed out from the swim tunnel and transferred to a holding tank.

### 2.1.5 Kinematic analysis

In this labriform swimmer experiment, the swimming kinematics (including pectoral fin beat frequency and gait transition) was determined frame-by-frame on the video recordings (GoPro HERO 4) for each individual trial. The pectoral-caudal gait transition speed ( $U_{pc}$ ) was defined as the lowest speed at which the fish tail was employed for propulsion for a minimum of 5 seconds per 30 second interval. The pectoral fin beat frequency of the fish was measured at every swimming speed from  $0.5 BL/s$  up to  $U_{pc}$ . Herein, the fin beat frequency (in *beats/s* or *Hz*) was taken as the average value of the count for three sequences of 10 seconds.

### 2.1.6 Data analysis

Measurements of oxygen consumption rate ( $\dot{M}O_2$ ) at various swimming speeds for each trial were determined as the mean of the 3 measurements during the corresponding periods. At the highest speed of the experiment, the fish might be fatigued and gave up swimming in less than 30 minutes, and therefore  $\dot{M}O_2$  was taken as either the sole measurement at that speed or the average value of the 2 or 3 measurements during the time interval the fish could swim.

To analyze the standard metabolic rate of the fish in each experimental treatment, the  $\dot{M}O_2$  measurement was modeled as a hydrodynamic-based power function of the swimming speed (Videler, 1993):

$$\dot{M}O_2 = aU^b + c \quad (2.1)$$

where  $a$ ,  $b$  and  $c$  are constant parameters calculated for each condition. It should be noted that  $c$  is equal to the theoretical oxygen uptake of the fish at standard metabolic rate (SMR) at zero swimming speed ( $\dot{M}O_{2,SMR}$ ).

According to this relationship, the optimal swimming speed ( $U_{opt}$ ) can be derived.  $U_{opt}$  represents the speed at which the cost of transport (COT) is minimal, with COT defined as the cost of moving a unit mass over a unit distance (Tucker, 1970). In the present work, the equation applied for optimal swimming speed was the following:

$$U_{opt} = \sqrt[b]{\frac{c}{a(b-1)}} \quad (2.2)$$

To better assess the statistical differences in the relationship between  $\dot{M}O_2$  and swimming speed for the different scenarios,  $\dot{M}O_2$  was transformed into a logarithmic function and a linear regression between  $\log(\dot{M}O_2)$  and swimming speed was fitted.

The experimental data, such as fish fin beat frequency, oxygen consumption measurements, fish size and weight, were compared among the three different experimental scenarios by using one-way analysis of variance (one-way ANOVA) method (Brown, 2005). A post-hoc Tukey's HSD test was employed for further analysis when significant differences were discovered (Ullmann et al., 2011).

## 2.2 Results

### 2.2.1 Kinematics

Fish in different experimental scenarios transitioned from a pectoral to a pectoral–caudal swimming gait ( $U_{pc}$ ) at different swimming speeds, and they also experienced different values of the critical swimming speed ( $U_{crit}$ ), the maximum swimming speed that fish can maintain within a certain interval of time (Mu et al., 2019). The results observed from all the experimental trials together with average values and standard error of the mean (SEM, is the sample mean of the standard deviation, see e.g., Altman and Bland, 2005) are documented in Table 2-2 and the values are given in the unit  $BL/s$ . It was found that, even though all the examined fish were of very similar body size and weight,  $U_{pc}$  and  $U_{crit}$  were in general not the same for fish studied in the same experimental scenario due to their individual swimming capabilities.

Table 2-2.  $U_{pc}$  and  $U_{crit}$  of the fish in different experimental trials

Test	Single		Pair		False pair	
	$U_{pc}$	$U_{crit}$	$U_{pc}$	$U_{crit}$	$U_{pc}$	$U_{crit}$
1	4.34	4.84	4.53	5.25	4.57	5.80
2	5.27	6.50	3.70	4.43	4.57	5.43
3	2.64	4.91	4.61	5.44	5.57	5.78
4	4.53	5.97	3.90	5.59	5.50	6.00
5	4.03	5.65	3.63	5.69	2.50	3.90
6	4.50	5.84	4.53	5.92	4.60	6.23
7	4.57	4.67	3.73	4.77	3.50	4.03
8	5.53	6.67	4.70	5.06	3.60	4.04
9	4.27	4.91	3.62	4.87	4.67	6.15
10	–	–	–	–	4.70	6.10
Mean	4.41	5.55	4.11	5.22	4.38	5.35
SEM	0.27	0.25	0.16	0.16	0.30	0.30

Figure 2-6 illustrated the average values of the gait transition speed  $U_{pc}$  and the critical swimming speed  $U_{crit}$  for the fish in the three examined treatments. The calculated mean  $U_{pc}$  value was the highest for fish in Single trials, followed by fish in False pair trials, and then by fish in Pair trials. The examined Single treatment had a slightly larger mean critical swimming speed  $U_{crit}$  than the Pair and False pair trials. However, the one-way ANOVA indicated that the differences in  $U_{pc}$  and in  $U_{crit}$  among the three scenarios were not statistically significant.



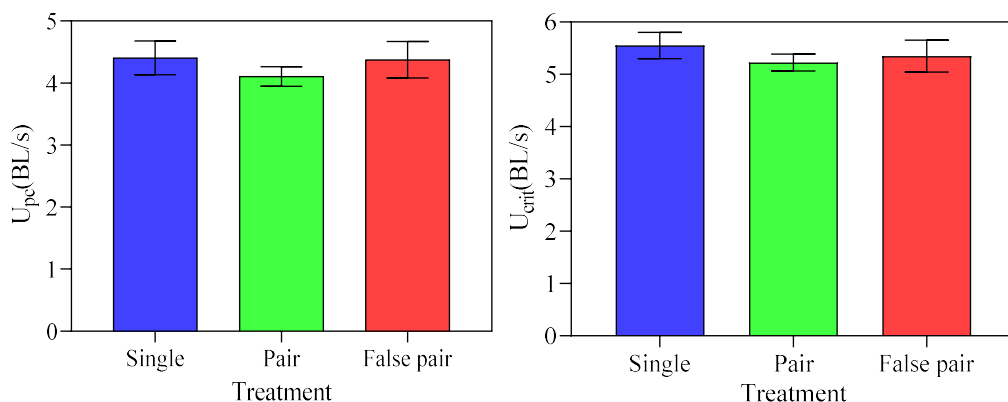


Figure 2-6. Gait transition speed ( $U_{pc}$ ) and critical swimming speed ( $U_{crit}$ ) for the single, pair and false pair treatments. Error bars represent their standard error of the mean (SEM)

Pectoral fin beat frequency ( $f_p$ ) of the fish at various swimming speeds for the three experimental scenarios is shown as lines with symbols in Figure 2-7, while the pure solid lines indicate the percentage of unavailable data, i.e., either the fish fatigued and gave up swimming in high-speed currents or the original videos were broken to provide desired data. It is found that at lower speeds (smaller than  $U_{pc}$ ), when fish used only pectoral fins for propulsion, the fin beat frequencies in the three different treatments were relatively similar, especially at  $U \leq 3.5 BL/s$ . Besides,  $f_p$  increased with swimming speed almost linearly in all scenarios, indicating that the fish consumed more energy to keep up with the increasing inflow velocity. At higher swimming speeds (around  $U_{pc}$ ),  $f_p$  did not change much because in the gait transition region fish used BCF swimming mode for assistance. Due to fish individuality, fish fatigued at different swimming speeds, and only a few fish in the experiments were able to reach a speed of  $6.5 BL/s$ . In False pair case, the fin beat frequencies were similar as those in Single trials, except for a noticeably lower value for fish swimming in a False pair at speed  $4.5 BL/s$ . It indicated that the presence of an accompany fish who remained always steady may calm down the real fish that was struggling to maintain swimming. In the Pair treatments,  $f_p$  of the front fish was quite like that of Single treatments, while the back fish used lower frequencies than the front fish in most of the low-speed cases. This demonstrated that there are hydrodynamic advantages of being the back fish in schooling, and the back fish did not consume as much energy on swimming as if they were alone. At speeds larger than  $U_{pc}$ , the same conclusions cannot be easily drawn because the paired fish in the swim tunnel started to use caudal fins and switch their relative longitudinal positions.

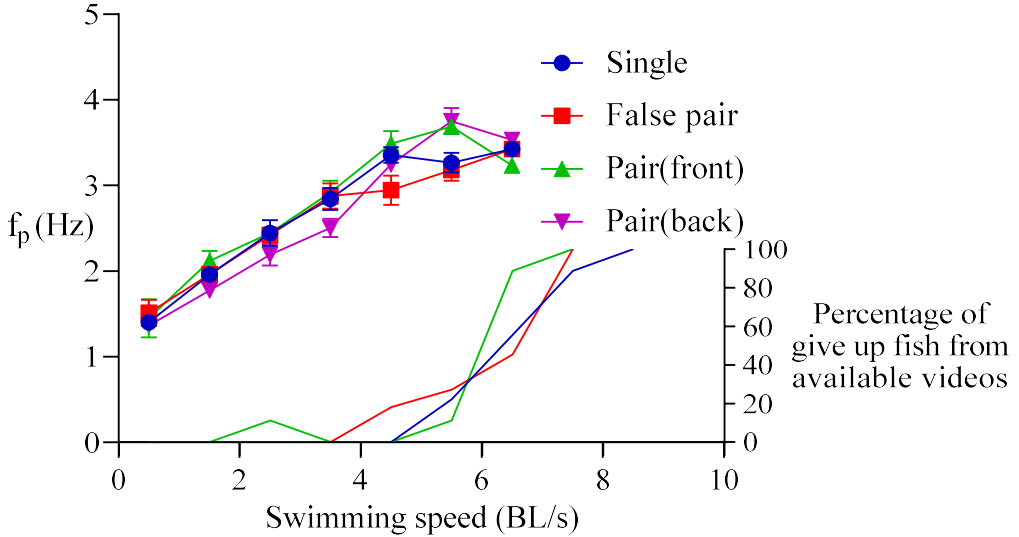


Figure 2-7. Lines with symbols: fin beat frequency ( $f_p$ ) at each speed increment for the single, pair and false pair treatments; lines without symbols: percentage of give up fish from available videos

Figure 2-8 showed the pectoral fin beat amplitude ( $A_p$ ) observed at the fish gait transition speed. Here,  $A_p$  was measured as the angle in degrees formed by the straight line through the body axis of the fish and the leading edge of the fin just before the adduction phase (Mussi et al., 2002). This measurement in the dorsal view represents only an in-plane component of the actual fin beat amplitude, as the fin beat of the examined shiner perch also had a large dorsoventral component. The results showed that the fish in False pair treatment had the largest fin beat amplitude ( $96.7 \pm 2.5^\circ$ ) at the gait-transition speed, followed by the Single fish ( $93.7 \pm 2.1^\circ$ ) and then by the fish in a real Pair ( $90.0 \pm 2.3^\circ$ ).

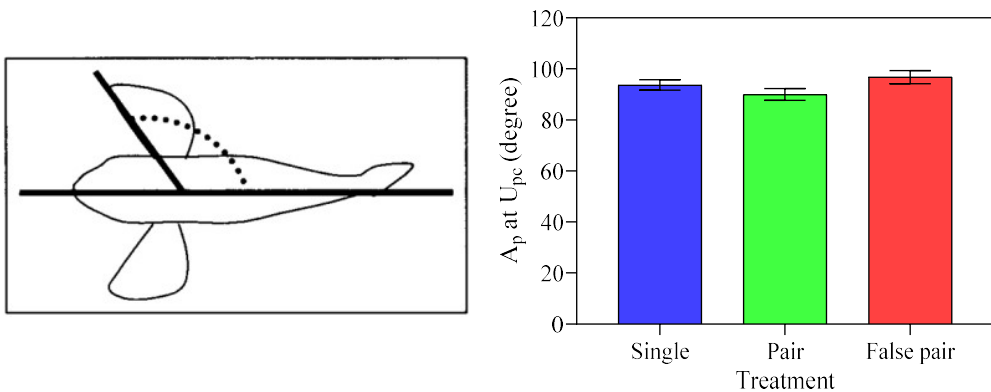


Figure 2-8. Left: Fin beat amplitude ( $A_p$ ) measured as the angle in degrees formed by the straight line through the body axis of the fish and the leading edge of the fin just before the adduction phase (Mussi et al., 2002); Right: Fin beat amplitude ( $A_p$ ) at gait transition speed for the single, pair and false pair treatments

Nine experiments were carried out in total for the Pair treatment, and for each case it was curious to identify whether the fish swimming in the front position or the one in the back would be the first one to give up swimming. Figure 2-9 shows the percentage of time when the first give up fish was in the front position at different swimming speeds. It was found that at small current velocities, the two fish in the flume would like to keep their relative longitudinal positions. However, after the swimming speed was increased above  $4.5 BL/s$ , the fish started bursting into the front and coast to downstream. Accordingly, the percentage go to an intermediate value. It was known from the figure that in 6 out of total 9 cases, the fish that always stayed in the front position gave up earlier than the back fish. This might be because the front fish did not enjoy the hydrodynamic advantages of schooling as the one swimming in the downstream position, therefore it had to consume more energy and felt exhausted earlier.

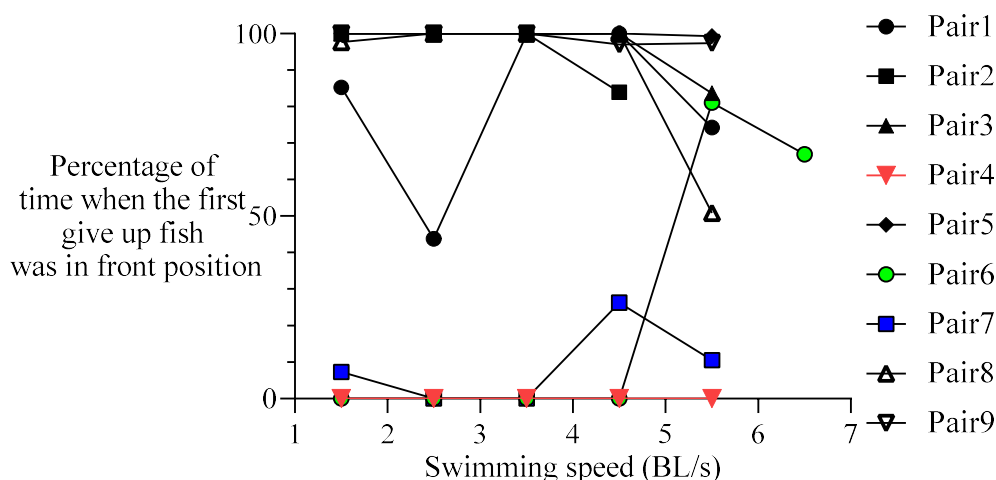


Figure 2-9. Percentage of time when the fish that gave up swimming first in Pair treatments was in the front position. Colors are used for the examined Pair trials where the fish always staying in the downstream position gave up swimming earlier than the fish in the front

Figure 2-10 shows the relative position of the front and back fish in the nine Pair treatments at a time instant during swimming speed  $3.5 BL/s$ , when the two fish in the swim tunnel did not switch their relative longitudinal positions. It should be noted that the Pair fish may change their lateral positions from time to time, and the figure below just gives an indication of their schooling performance. It was found that in most of cases, the front fish tended to swim near the left side wall (the bottom boundary in Figure 2-10, which was next to the computer monitor), while the back fish stayed closer to the tunnel centerline. Due to the boundary layer effect along the tunnel wall, it was suspected that the front fish would like to swim in a region with lower inflow velocity and try to save energy. However, the utilization of the fish left pectoral fin was also restricted when swimming close to the swim tunnel side wall.

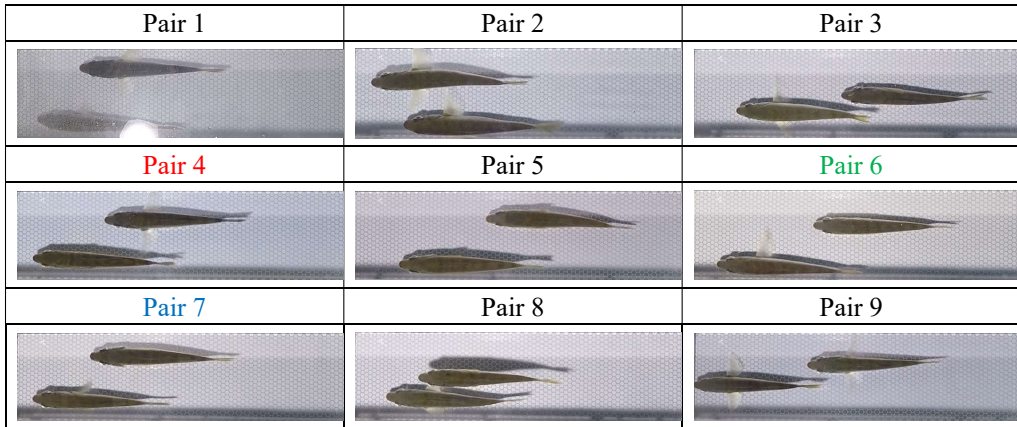


Figure 2-10. Relative position of the front and back fish in the Pair treatments at an instant of swimming speed  $3.5 BL/s$

### 2.2.2 Metabolics

For each individual experiment, the hydrodynamic-based power function describing the relationship between  $\dot{M}O_2$  and the swimming speed had unique values of coefficients. The three parameters involved in Eq. (2.1) for all the trials are documented in Table 2-3.

Table 2-3. Estimated coefficients in Eq. (2.1) for the  $\dot{M}O_2$ -swimming speed relationship estimated in all trials

Test	Single			Pair			False pair		
	<i>a</i>	<i>b</i>	<i>c</i>	<i>a</i>	<i>b</i>	<i>c</i>	<i>a</i>	<i>b</i>	<i>c</i>
1	16.38	2.14	118.10	4.65	2.76	130.96	1.03	3.27	237.67
2	11.41	2.11	121.44	17.44	2.35	113.90	31.52	1.53	217.57
3	6.42	2.98	166.77	4.84	2.66	123.43	7.39	2.33	149.08
4	27.47	1.67	152.83	3.67	2.86	184.70	3.09	2.69	158.66
5	4.03	2.87	184.88	11.60	2.18	143.66	46.26	1.58	130.10
6	12.73	2.05	167.15	12.77	2.13	145.83	5.47	2.46	193.21
7	69.04	1.12	116.76	15.07	1.94	126.09	19.50	1.79	131.48
8	6.15	2.39	197.75	8.32	2.43	166.53	6.79	2.98	151.68
9	5.98	2.68	149.70	15.67	1.93	143.30	12.29	2.06	171.44
10	–	–	–	–	–	–	4.97	2.48	269.84

From the  $\dot{M}O_2$  measurement results at each swimming speed, the optimal swimming speed ( $U_{opt}$ ) was calculated using Eq. (2.2) and thus obtaining the corresponding minimum cost of transport ( $COT_{min}$ ) of the fish. Figure 2-11 illustrates the average values of  $U_{opt}$  and  $COT_{min}$  for the three different treatments. The optimal swimming speed was the lowest for the fish in Pair ( $2.87 \pm 0.13 BL/s$ ), followed by the fish in Single ( $3.18 \pm 0.23 BL/s$ ) and then by the fish in False Pair ( $3.47 \pm 0.20 BL/s$ ) trials. The  $COT_{min}$  followed the same tendency as  $U_{opt}$ : the lowest average value was for the fish in Pair treatment ( $0.0266 \pm 0.001 mgO_2/kg/BL$ ), followed by the Single fish ( $0.0244 \pm 0.001 mgO_2/kg/BL$ ) and then by the fish in False Pair ( $0.0269 \pm 0.002 mgO_2/kg/BL$ ).

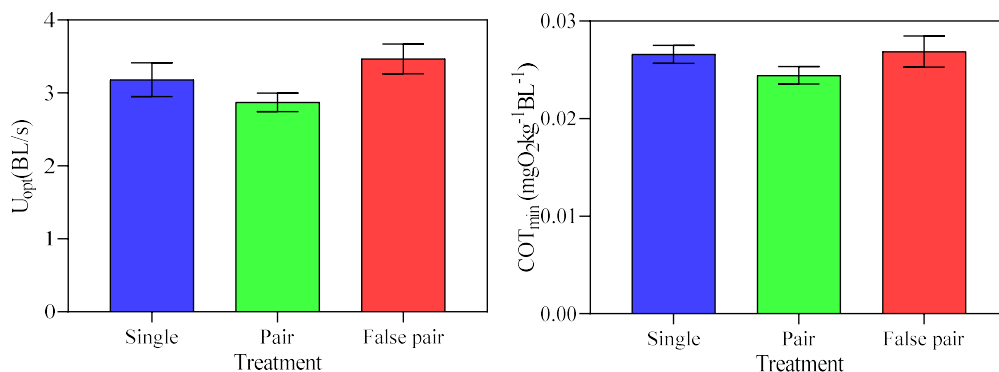


Figure 2-11. Optimal swimming speed ( $U_{opt}$ ) and minimum cost of transport ( $COT_{min}$ ) for the single, pair and false pair treatments. Error bars represent their standard error of the mean (SEM)

Other important biological variables of interest are the standard metabolic rate (SMR), representing the minimal amount of oxygen needed by a fish to support its aerobic metabolic rate (Chabot et al., 2016), and the maximum metabolic rate, corresponding to the maximum rate of oxygen consumption ( $\dot{M}O_{2max}$ ) that the fish achieved in the experiments (Norin and Clark, 2016). These two metabolic parameters for the three examined scenarios are shown in Figure 2-12. The average SMR values of the fish in Single, Pair and False pair treatments were  $152.82 \pm 9.82 mgO_2/kg/h$ ,  $142.04 \pm 7.41 mgO_2/kg/h$ , and  $181.07 \pm 14.95 mgO_2/kg/h$ , respectively. Therefore, SMR was the highest for False pair, followed by Single fish and then by Pair treatments. The maximum metabolic rate of the fish in Single trials was the highest ( $717.22 \pm 29.08 mgO_2/kg/h$ ), followed by the value for fish in False pair ( $682.94 \pm 35.61 mgO_2/kg/h$ ) and then by that of the Pair scenarios ( $618.23 \pm 35.56 mgO_2/kg/h$ ).

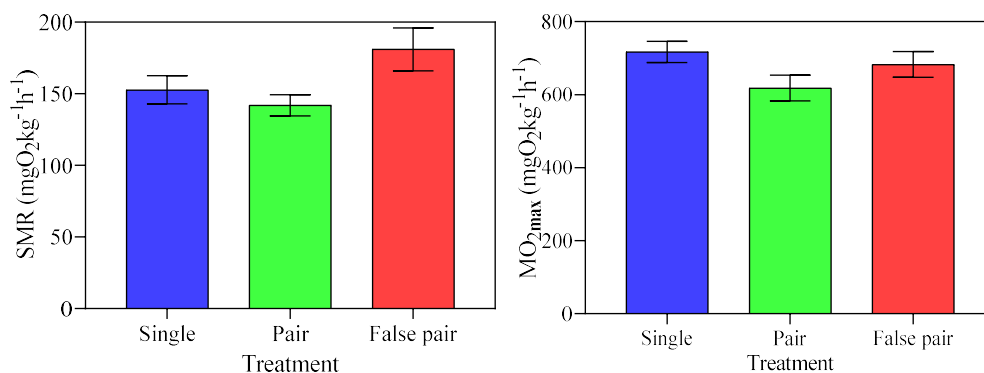


Figure 2-12. Standard metabolic rate (SMR) and maximum metabolic rate ( $\dot{M}O_{2max}$ ) for the single, pair and false pair treatments. Error bars represent their standard error of the mean (SEM)

Figure 2-13 gives the  $\log(\dot{M}O_2)$  from the measurements and its linear fitted model as a function of swimming speed for the three different treatments. The statistical information about these fitted relationships is documented in Table 2-4. From the results, all the three regressions

relating  $\log(\dot{M}O_2)$  to the swimming speed had a high goodness of fit. The slopes of the relationships for different treatments were significantly different, and the 95% confidence intervals for the slope of the False pair relationship did not overlap those of the slope of the Pair.

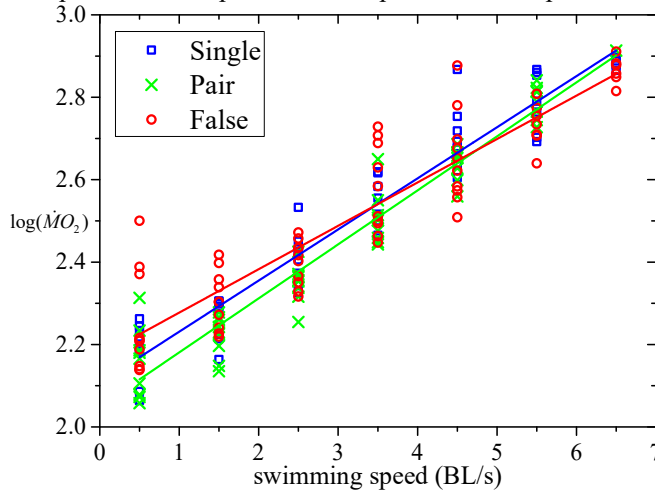


Figure 2-13. Measured and modelled oxygen consumption ( $\log(\dot{M}O_2)$ ) as a function of the fish swimming speed for the single, pair and false pair treatments

Table 2-4. Linear regressions for each treatment fitted to  $\log(\dot{M}O_2)$  as a function of swimming speed

Treatment	Single	Pair	False
<b>Best-fit values</b>			
Slope	$0.124 \pm 0.005$	$0.131 \pm 0.005$	$0.105 \pm 0.006$
Y-intercept	$2.107 \pm 0.017$	$2.050 \pm 0.016$	$2.172 \pm 0.022$
X-intercept	-16.99	-15.64	-20.63
<b>95% Confidence Intervals</b>			
Slope	0.115 to 0.133	0.122 to 0.141	0.093 to 0.117
Y-intercept	2.073 to 2.141	2.017 to 2.083	2.128 to 2.216
X-intercept	-18.63 to -15.58	-17.10 to -14.38	-23.66 to -18.20
<b>Goodness of Fit</b>			
R square	0.930	0.938	0.838
Sy.x	0.064	0.060	0.089
<b>Is slope significantly non-zero?</b>			
F	717.3	774.2	314.3
DFn, DFd	1, 54	1, 51	1, 61
P value	<0.0001	<0.0001	<0.0001
Deviation from zero?	Significant	Significant	Significant
<b>Data</b>			
Number of X values	56	53	63
Maximum number of Y replicates	1	1	1
Number of missing values	12	13	7
Number of missing values	12	13	7

## 2.3 Discussion

Through the experimental data obtained in Single, Pair and False pair treatments, we demonstrate the importance of real/visual accompany fish in a fish school. Comparing the results from False pair treatment with those from Pair scenario helps to disentangle the hydrodynamic effects of schooling from the behavioral effects, while comparison of these two treatments with the results from Single fish provides a guide as to the overall kinematic and metabolic differences between individual swimming and swimming in a school.

The kinematic analysis showed that the fish in a False pair tended to use a higher pectoral fin beat frequency than the fish in Single trials at swimming speed  $0.5 BL/s$ . Between speed  $1.5 BL/s$  and  $3.5 BL/s$ , the pectoral fin beat frequency employed by the fish in False pair treatment was approximately the same as that of the Single fish. However, at higher speeds, i.e.,  $4.5 BL/s$  and  $5.5 BL/s$ , the False pair had a noticeable lower fin beat frequency than the fish in other treatments. This may be because the “fake friend” on the computer monitor displayed steady swimming performance at  $1.5 BL/s$  and therefore showed a pectoral fin beat frequency consistent with that swimming speed, while the fish in the swim tunnel kept increasing swimming speed every 30 minutes. The results suggest that at the lowest inflow speed ( $0.5 BL/s$ ) the real fish of the False pair in the flume used more energy in order to mimic the behavior of “faster” swimming “fake friend”, and that at high speeds (i.e., larger than gait transition speed) the “fake friend” calmed the real fish down with respect to the fish in Single treatment at the same swimming speed. This finding indicates that the fish in the experiments were sensitive to the visual stimuli and were aware of their surroundings even when swimming at high speeds, and that there might be a calming effect of swimming together with another steady individual when high speeds were involved. The observation also indicates that a fish swimming with a lower fin beat frequency may influence the neighboring fish to increase fin beat amplitude and lower its fin beat frequency. Mussi et al. (2002) observed that *Cymatogaster aggregata* had a higher  $U_{pc}$  than two other MPF swimming species because of the preference of the *Cymatogaster aggregata* to use larger fin beat amplitude rather than higher frequency at  $U_{pc}$ .

Comparison of pectoral fin beat frequency between the front and the back fish in Pair treatment showed that the back fish had a lower fin beat frequency when swimming speed  $\leq 4.5 BL/s$ . Besides, it was found that from  $1.5 BL/s$  to  $3.5 BL/s$ ,  $f_p$  of the back fish was also much lower than that of the fish in Single and False pair treatments, while the front fish in a real Pair used a slightly higher fin beat frequency than the fish in Single and False pair treatments. This demonstrates that there are hydrodynamic advantages in being the back fish in a swimming school, and that the back fish does not use as much energy for swimming as the front fish does or as it would if it was alone. This finding concurs with Johansen et al. (2010) who found that in a swimming school of MPF fish, the rear fish used about 15% lower fin beat frequency than the front one, and the back fish were estimated to have a 25% reduction in oxygen consumption. They further estimated that schooling would be energetically advantageous if more than 78% of individuals occupied trailing positions in the school; this was a commonly observed phenomenon for that fish species. Wiwchar et al. (2018) similarly concluded that schooling

provides advantages in swimming performance, finding that  $U_{crit}$  was higher in zebrafish tested in groups of three, five, or ten, than those tested individually. However, contrary to these studies, Hvas et al. (2019) found that schooling did not improve  $U_{crit}$  of salmon, and thus the effect might be species specific.

The semi-log linear regression of the relationship between  $\dot{M}O_2$  and swimming speed basically concurred with the fin beat frequency results. It points to a behavioral advantage of swimming with an accompany friend at high speeds, with the  $\dot{M}O_2$  of the fish in False pair being the lowest among the three treatments for swimming speed higher than approximately  $4.5 BL/s$ . By contrast, the standard metabolic rate (SMR) of the False pair treatment was higher than that for the Single and for Paired fish. One possible explanation for this is that the active and steady swimming of the “fake fish” on the computer monitor kept the fish in the swim tunnel more active than it would otherwise have been. Nadler et al. (2016) found that there was a calming effect of shoaling on gregarious fish that depressed their overall metabolic demand, and it was highly variable between individuals, for example, the reduction of SMR was in the range [5%, 60%]. Assume that such calming effect also occurred in the examined fish species, *Cymatogaster aggregate*, and did not vary much with activity level, then this effect would be of the order 9 – 15% for the maximum metabolic rate, which would likely be within the range of error in the observations. This may explain why the analysis of  $\dot{M}O_{2max}$  measurement did not show statistically significant difference among Single, Pair and False pair treatments.

It should be noted that the present experimental study had some limitations. In particular,  $U_{crit}$  trials for the fish in Pair treatment were terminated when the first fish fatigued and could no longer keep swimming. This skewed downward the measure of  $U_{crit}$  for the Pair treatment in a way that did not reflect the effect of schooling on fish maximum swimming speed. Figure 2-9 presented the percentage of time the fish that gave up swimming first was in the forward position. Only in 3 out of 9 trials, it was the trailing fish who gave up first, while in most of the cases (66.6%), it was the leading fish that fatigued faster. It can be because the front fish cannot experience the hydrodynamic advantages of schooling as does the back fish, therefore it must consume relatively more energy and feels exhausted earlier. In addition, the measurements of oxygen consumption for the fish in Pair treatments were necessarily an average of the consumption of the two individuals, and thus the metabolic cost of swimming cannot be equally apportioned between the front and back fish. However, all the metabolic results suggested that the oxygen consumption level of the fish in Pair treatments was lower than that of the Single fish at every swimming speed. This could therefore indicate that the trailing fish uses less energy than the front one and there is a hydrodynamic advantage of fish schooling.

In addition, the maximum swimming speed reached by the fish was different due to individuality. Figure 2-7 showed the percentage of fish that insisted on swimming at each swimming speed alongside the fin beat frequency observations. It can be seen from this figure that  $U_{crit}$  in the experiments was typically between  $5.0 BL/s$  and  $6.0 BL/s$ , therefore, the differences between the fin beat frequencies at speeds of  $5.5 BL/s$  and  $6.5 BL/s$  may be spurious as few fish were able to swim at those high speeds.



From the video observations, fish in most of the treatments had the tendency to swim near the side wall, which was next to the computer monitor, especially at low swimming speeds. It was possibly because the animation displayed on the monitor next to the swim tunnel gave the illusion to the fish in flume that the tunnel was twice as wide as its actual width. This fact also reflects that fish benefited from slower inflow velocity in the boundary layer of this wall, but also that they may have been hampered by the inability to fully extend the pectoral fin on the wall side. This swimming behavior meant that the measured fish kinematic data might be larger than that of the fish in nature. Besides, other measurements such as  $U_{crit}$  should also be interpreted cautiously. However, as this behavior of swimming against the wall at low speeds was observed in almost all the examined fish and evenly amongst treatments, it did not affect the interpretation of the inter-treatment observations.

Despite the above findings of the fish swimming alone (Single), in a Pair, or in a False pair, the present preliminary statistical analysis did not reveal significant relationships in the gross measures of metabolic and kinematic performance during swimming. The trends in the experimental data suggest that a more thorough investigation is required for further understanding. In particular, the significantly different slopes in the fitted  $\dot{M}O_2$  to swimming speed models indicate that at high speeds the metabolic rate in fish with companions could be lower due to the calming effect of swimming in a school. By contrast, at lower swimming speeds, the pectoral fin beat frequency of the back fish in a pair was smaller compared to the front fish or the fish in Single and False pair treatments, suggesting that hydrodynamic advantages of schooling are dominant over behavioral effects.

## 2.4 Summary

In this chapter, a series of experimental studies performed on shiner perch (*Cymatogaster aggregate*), a labriform swimmer, were described and discussed to investigate the hydrodynamic and behavioral advantages during fish schooling. The main results were compared in terms of swimming speed, pectoral fin beat frequency and oxygen consumption among three different scenarios: Single treatment with a solitary fish in swim tunnel, Pair treatment with a schooling pair of fish and False pair treatment with one real fish swam alongside a looped video of a conspecific fish on the computer monitor next to the swim tunnel. It was found that pectoral fin beat frequencies of the back fish swimming in pair were apparently lower before gait transition speed than the front fish and the ones in other groups.

Besides, the fish with fake friend had lower oxygen consumption relative to the single fish from 3.5  $BL/s$  and onwards, while the average metabolic cost of the real fish school was always smaller than the single fish. The present results suggest that schooling confers both hydrodynamic and behavioral advantages over swimming alone for a gregarious fish, but that the relative contribution of the two influences depends on the speed of swimming. At low speeds hydrodynamic effects outweigh behavioral effects, but at high speeds when an individual may start to struggle with the effort required to maintain swimming, the presence of another fish who remains calm may have a calming effect on the fish that is struggling.

## Chapter 3

# Investigations on a sub-carangiform swimmer

As a typical sub-carangiform swimmer, the Atlantic salmon has been extensively studied due to conservation concerns and its economic importance in aquaculture industry. In this chapter, observation experiments were performed on Atlantic salmon *Salmo salar* post-smolts in a Blazka-type swim tunnel in which the current velocity was controlled to increase incrementally at prescribed values and keep constant within prescribed time intervals until fish fatigue. The main aim of the experiments is to investigate the salmon swimming behavior over the entire range of examined current velocities in the flume. The critical swimming speed, a standard measurement to assess fish swimming capabilities, was calculated for the hatchery-reared salmon in this confined flow domain. The kinematic performance of the fish was recorded and analyzed with respect to the swimming speed, body size and water environment. The experimental results may provide current velocity guidance for farmed salmon during on-growing phase with proper consideration. The observed data could be used to calibrate numerical models of salmon swimming motion and support the development of underwater robotic fish. The analysis on the boundary wall effect of swim tunnel suggested that fish swimming performance could be compromised in restricted water space. Therefore, the fish experimental setup in the future should be designed to be suitably large for more accurate hydrodynamic studies.

### 3.1 Materials and methods

Carangiform and sub-carangiform swimming are modes of BCF propulsion in which the large amplitude of the undulations is mostly restricted to the one-half or even one-third posterior part of the body and increases sharply in the caudal area (Lindsey, 1978). These modes of swimming are used by many fishes such as the Atlantic salmon and rainbow trout in the Salmonidae family. The fishes employing this mode can often achieve high swimming speeds and possess high swimming efficiency.

Many researchers have been inspired by the astonishing swimming abilities of fish to better understand the mechanisms behind their high performance (Childress, 1981; Lighthill, 1975). In the recent decades, an increasing number of studies have been carried out on biomimicking such underwater swimmers with the aim of creating greener and efficient marine vehicles. Several types of aquatic man-made robotic systems have been developed and are being improved now, such as the best-known *RoboTuna* built at Massachusetts Institute of Technology (Triantafyllou and Triantafyllou, 1995; Zhu et al., 2002; Triantafyllou et al., 2000) and the

Eelume conceptualized at NTNU (Liljebäck and Mills, 2017; Engebretsen et al., 2019). As the body undulations of sub-carangiform and carangiform swimming modes are localized in the posterior portion and the rest body part can remain almost rigid, the robots in these categories seem to be more convenient for engineering realization compared to anguilliform swimmers, and thus have been selected by many scientists as the prototype of their robot fish. For instance, Nagoya University in Japan developed a micro robotic fish using ICPF Actuators (Yu et al., 2004), while University of Essex designed a kind of carangiform robotic fish named *iSplash-II* (Clapham and Hu, 2015; Liu and Hu, 2004). In order to thoroughly explore the carangiform/sub-carangiform propulsive mechanisms and transfer the knowledge to novel underwater vehicle design, it is of great significance to investigate the real fish swimming performance under different conditions, and experimental study is an essential method to realize this objective.

As a typical sub-carangiform swimmer, Atlantic salmon has been an extensively studied fish species because of its economic importance in aquaculture and for conservation concerns from declining natural populations (Horreo et al, 2011). The Norwegian aquaculture industry of Atlantic salmon *Salmo salar* is currently expanding to more exposed farming sites (Bjelland et al., 2015). It is important to identify the limit of fish swimming capability and provide acceptable environment for fish farming. Therefore, the real salmon fish experiments were carried out to quantify the fish swimming behavior at various current velocities.

This research was approved under the ethics permit 19/279843 and abided to Norwegian procedures and legislations of animal usage in scientific research. The experiments were carried out in collaboration with researcher Eirik Svendsen and Prof. Rolf Erik Olsen in NTNU. They have qualifications of animal care in Norway and performed necessary animal treatments in the actual experiments.

### 3.1.1 Experimental fish and husbandry

The experiments were performed on Atlantic salmon (*Salmo salar*) reared at NTNU SeaLab in Trondheim, Norway, between April and May 2020. After smoltification, fish were transferred and held in large square tanks (length  $\times$  width  $\times$  water depth was approximately  $2m \times 2m \times 1.6m$ ) since fish mean weight  $100g$ . The tanks were continuously supplied with flow-through seawater (salinity  $34ppt$ ), which was pumped and filtered from Trondheimsfjorden at  $70m$  depth to avoid the introduction of parasites and pathogens as well as to ensure the water quality in the tanks. Consequently, tank water properties were consistent with the ambient conditions in the sea, i.e., water temperatures varied with season from  $5^{\circ}C$  in the spring to  $10^{\circ}C$  in the summer; the maintained ambient oxygen levels were between 80% and 85% saturation. The fish were fed every 24 hours with standard commercial diets (Skretting Spirit Trout 300-40A,  $4.5mm$  pellet size: [www.skretting.com](http://www.skretting.com)) through automatic feeding devices, with each meal consisting of 1.5 – 2.0% of the tank biomass. Besides, the fish were subjected to a continuous light condition to facilitate growth. All fish were allowed to habituate in the tanks for a minimum of 4 weeks prior to experimental trials. The experimental fish were selected randomly from tanks and equipped with tags. It should be noted that in the COVID-19 situation, the experiments had to be suspended several times due to the quarantine policy or fish grown too

big for trials, resulting in 5 examined fish in total. Their bodies were weighted and measured according to Figure 3-1, and the information is documented in Table 3-1.

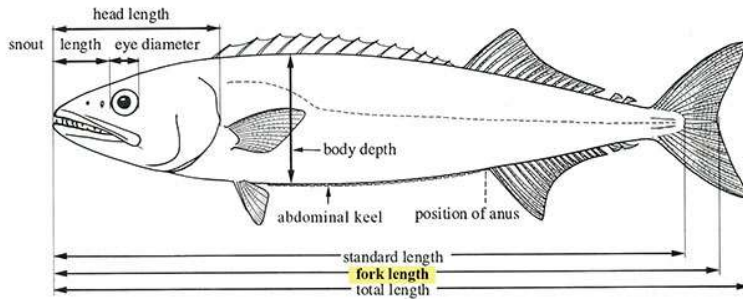


Figure 3-1. Schematic view of fish body measurements (Taken from [www.fishbase.se](http://www.fishbase.se))

Table 3-1. Information about the tagged individuals in the experimental trials

Test	Fork length (cm)	Body width (cm)	Body depth (cm)	Body mass (g)
1	43.5	6.5	11.5	1153.6
2	43.0	6.0	10.5	1127.5
3	37.0	3.2	7.3	570.0
4	42.1	4.0	9.0	932.0
5	29.0	2.5	6.2	319.5

### 3.1.2 Experimental setup

Experiments were conducted in a Blazka-type swim tunnel of approximately 58.9L volume (Van Den Thillart et al., 2004), as shown in Figure 3-2. The cylindrical swim tunnel consists of two concentric perspex tubes with length of 120cm and two PVC endcaps. The inner and outer diameters of the swim tunnel are 16.5cm and 25cm, respectively. A propeller with three blades was driven by an electromotor to suck water out from the inner tube and push it into the outer ring. After correction of wall thickness, the surface area of the inner tube cross section was equal to the surface area of the outer ring, thus allowing the same current velocity in both compartments. The power was controlled by a Boston Gear (Model VES 3) digital motor controller. A laser tachometer (Model AT-6L) was equipped for independent RPM measurements. At the front end of the swim tunnel a PVC flow streamer was placed inside the inner tube to help the flow become laminar and at the propeller end, a shorter flow streamer was placed to protect fish from crashing into the propeller. The water inlet was connected to the tunnel endcap, providing the swim tunnel with fully aerated seawater at a flow rate of 5.5 L/min when the controlling magnetic valve was open.



Figure 3-2. Cylindrical swim tunnel with details of the fish experiment

The relation between the rotational speed of the motor and the water velocity inside the inner tube of the swim tunnel was determined by particle tracking velocimetry (PTV) method. The revolutions per min (RPM) of the motor were tested in the range of 0~1500RPM with an interval of 100RPM. Figure 3-3 illustrates that the relationship between the measured flow velocity and RPM values appeared to be a linear function. Therefore, the mean flow velocity could be calculated from the motor RPM according to this law during experiments. Herein, the grey symbols represent the measured velocity values, and the blue symbols are the average of the measured values for each RPM.

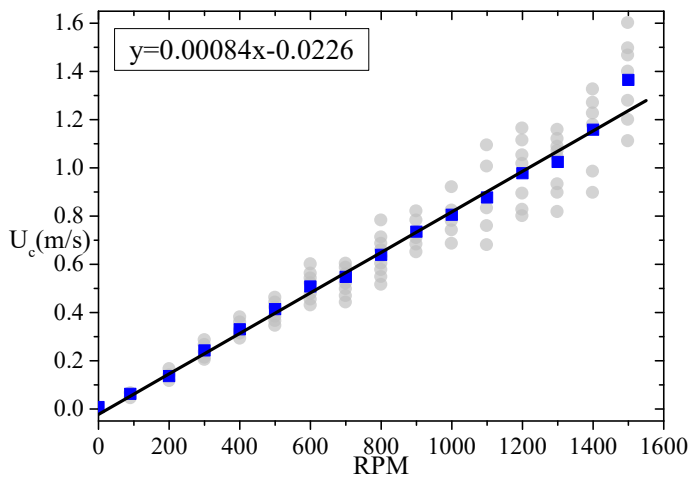


Figure 3-3. Flow calibration results with respect to the motor rotational speed. Grey symbols represent the measured values, and the blue symbols are the average of measures values at each RPM

To minimize visual disturbance to the fish, the entire experimental setup was shielded by a large white curtain, and the swim tunnel was partially covered in black plastic sheets. The view of fish was blocked from seeing external stimuli and thus helping fish to calm down in the swim tunnel. A rigid square frame, fixed to the swim tunnel platform, was used to support a Blackfly GigE camera system, and it was always orthogonal to the tunnel, as shown in Figure 3-4. The

camera mounted on the top beam of the frame was employed to record the dorsal view of the fish swimming behavior throughout the trials at frame rate approximately  $50fps$  and with resolution  $1920 \times 720$ . Moreover, two other cameras fixed to the side beam recorded side views of the fish at lower frame rate, around  $25fps$ . These cameras were connected to a working computer behind the curtain, so that the fish state in the swim tunnel could be continuously remotely monitored.



Figure 3-4. Camera setup of the fish experiment

### 3.1.3 Experimental protocol

Due to the cylindrical geometric feature of the swim tunnel, both top and side views of the fish inside were highly distorted, leading to difficulties in identifying actual fish swimming state during video analysis. To help solve this problem, as well as accurately measure the undulatory motion of fish midline, four red perforated beads (with length  $4mm$  and diameter  $5mm$ ) were tagged along the centerline of fish back. The positions of 4 beads were respectively at head, ahead of the dorsal fin, behind the dorsal fin and at the caudal peduncle, as shown in Figure 3-5. The beads were in sharp contrast color to be tracked by cameras. Every bead tagging was started by gently capturing a random fish from tanks using a knotless dip net and immediately transferring it to an anaesthetic bath (Finquel,  $60mg/L$ ). After the fish totally lost its equilibrium, it was carefully placed on a V-shaped surgical table with its dorsal side up and its head immersed in water. A hose circulating anaesthetic (Finquel,  $30mg/L$ ) was used to irrigate the fish gills throughout the whole procedure. The four red tags were attached to the corresponding positions along fish back using a single interrupted suture per bead, which cost less than 3 minutes in total. Then, the fish was transferred to a recovery tank with circulating seawater and kept till regaining consciousness. The fish should be recovered and monitored for a minimum of 48 hours before it is ready for experiments.



Figure 3-5. Tags on the experimental fish

Each experimental fish was introduced into the swim tunnel from the holding tank, where it was slightly sedated (Finquel,  $15 \text{ mg/L}$ ) in order to minimize sampling stress. Before transferring into the swimming tube, the fish fork length, body width and depth were measured. After consciousness was regained, the current velocity was set as  $0.5 \text{ BL/s}$  and the fish was left to acclimate in the flume for 5 hours or overnight (for fish no. 4 and 5) prior to the experimental trial. The effects of anaesthesia and handling stress on swimming performance were considered to be negligible after this recovery period (Hayashida et al., 2013).

The experiments were carried out following the critical swimming speed ( $U_{crit}$ ) protocol as described by Brett (1964). The  $U_{crit}$  measurements started from current velocity  $0.5 \text{ BL/s}$  in the swim tunnel, and then the current increments of  $0.5 \text{ BL/s}$  were carried out every 10 minutes. Some fish were able to hold station against the current by lying on the wall of inner tube at the lowest speeds, but eventually, steady swimming was initiated. The experiments had to be interrupted when the fish were fatigued, which was defined as it could not swim continuously and rested on the downstream side against the rear grid for at least 15s. During the tests, fish swimming behavior was remotely monitored on a computer screen to avoid stimulating the fish, and data were continuously collected by cameras.

Once the experiment was completed, the fatigued fish were rapidly taken out of the swim tunnel and transferred to a bucket with an overdose of anaesthetic (Finquel  $> 500 \text{ mg/L}$ ). Afterwards, the fish was killed with a blow to the head and its weight measurement was recorded.

### 3.1.4 Experimental data analysis

In the present Atlantic salmon experiment, the swimming kinematics was determined through frame-by-frame of the video recordings for each individual trial. The critical swimming speed  $U_{crit}$  was calculated according to Brett (1964). The tail beat frequency of the fish was estimated directly from the videos at every swimming speed from  $0.5 \text{ BL/s}$  up to its maximum speed, and the value was taken as the average of the tail beat frequency count for three sequences of 10 seconds.

In addition, a machine deep learning model, for object identification and segmentation, has been used to convert the videos of the salmon experiments into digital datasets. It can recognize the fish profile from images, extract the midline points of fish body, and provide the needed data to analyze fish locomotion features, e.g., fish swimming frequencies, amplitude envelopes of the

fish midline motion. In the present study, it was used to estimate the fish tail beat amplitude. The main elements of this identification strategy are outlined by Figure 3-6, more details can be found in Søvik (2022).

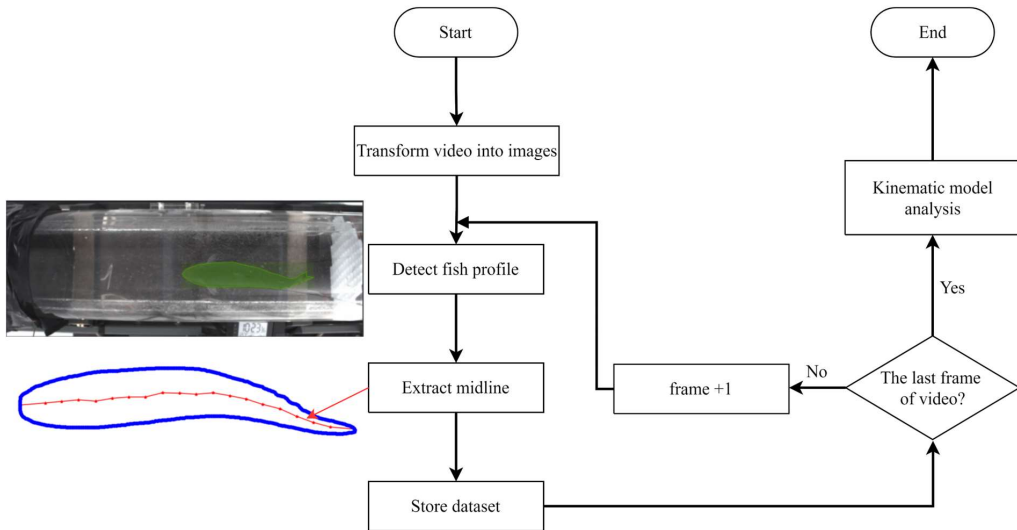


Figure 3-6. Flow chart depicting main elements of fish midline extraction and fish locomotion analysis

## 3.2 Results

The critical swimming speed ( $U_{crit}$ ) performed by the Atlantic salmon in the experiments is illustrated in Figure 3-7. It was found that the calculated  $U_{crit}$  (expressed in the unit  $BL/s$ ) was smaller for fish with larger fork length. To be more precise, the smallest fish had the highest  $U_{crit}$  value ( $2.05 BL/s$ ), while the four larger fish had similar smaller  $U_{crit}$ , between  $1.0 BL/s$  and  $1.3 BL/s$ .

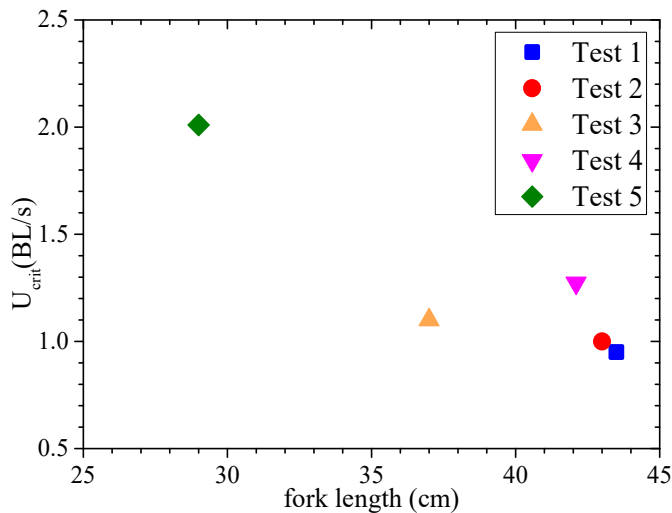


Figure 3-7. Critical swimming speed ( $U_{crit}$ ) versus fish fork length



The tail beat frequency ( $f_t$ ) of the fish (estimated directly from the videos) at each swimming speed for the five experimental trails is shown in Figure 3-8. At lower swimming speeds ( $\leq 1.0 BL/s$ ), fish generally preferred to hold station against the current by leaning on the inner tube, and they were found to switch between swimming and resting from time to time. At the highest swimming speed reached, the fish were observed to fall back to the rear grid a few times before they became fatigued. The frequencies shown in the plot were identified in the time intervals when the fish showed a continuous swimming performance. It was found that the tail beat frequency  $f_t$  increased almost linearly with the swimming speed in all tests, indicating that the fish consumed more energy to swim against larger inflow current. In addition, the results showed that the  $f_t$  value of the smallest fish (Test 5) was the highest at all the examined swimming speeds, followed by the medium size fish (Test 3), and then by the fish in Test 1, 2 and 4. This suggested that smaller individual fish need larger oscillation frequencies to achieve desired swimming speeds than larger fish.

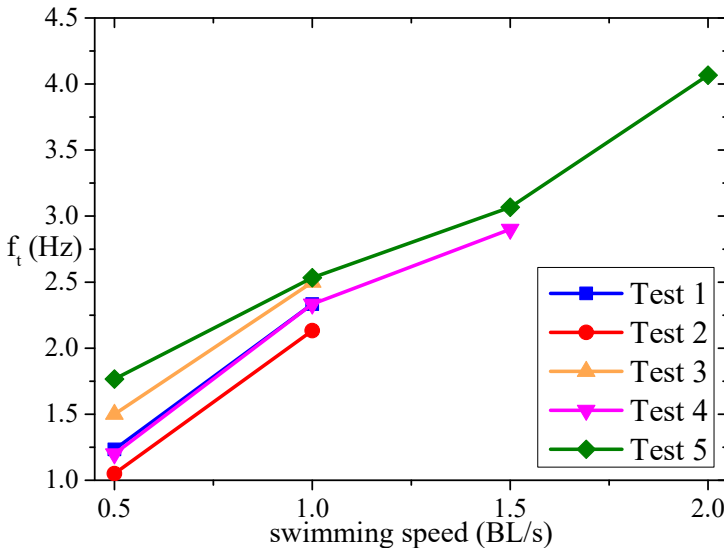


Figure 3-8. Tail beat frequency of the fish at each speed increment estimated directly from the videos

The fish tail beat amplitude under different swimming speeds has been analyzed for the smallest salmon in Test 5, the only one that could reach  $2.0 BL/s$  during experiments. Figure 3-9 shows the results of nondimensional tail beat amplitude ( $A_t/BL$ ). Here,  $A_t$  was taken as the averaged value within the examined time interval when the fish exhibited a steady swimming behavior at the corresponding swimming speed. For the lowest current velocity  $0.5 BL/s$ , the fish was resting on the wall of inner tube from time to time, implying that steady-state swimming was not satisfactorily performed in this condition; therefore, the tail beat amplitude at this swimming speed was not examined. From  $1.0 BL/s$  to  $2.0 BL/s$ , the fish tail beat amplitude becomes slightly larger with the increase of swimming speed. The larger fish studied in the experiments achieved steady-state locomotion scenarios only at one or two speed levels, which is not sufficient to make a conclusion about the functional dependence of the fish tail beat amplitude on the speed. As the experimental data from one single fish test can barely show the tendency of fish swimming behaviors, more real-fish experiments should be carried out to collect data at

different swimming speeds and to gain a deep insight into the scaling law of fish swimming amplitude. The estimated tail beat frequencies and amplitudes of the fish in Test 5 correspond to a Strouhal number 0.2143 at 1.0 BL/s, 0.184 at 1.5 BL/s, and 0.2076 at 2.0 BL/s. These values are within the Strouhal number range often employed by fish in nature and are near the lower limit of the range (0.2; 0.4) for optimal flapping foil propulsive performance.

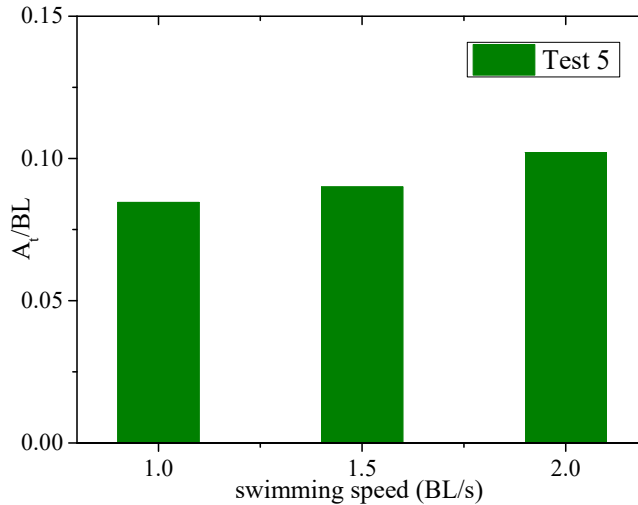


Figure 3-9. Nondimensional tail beat amplitude ( $A_t/BL$ ) of the fish in Test 5 at different swimming speeds

### 3.3 Discussion

The swimming behavior of the Atlantic Salmon was investigated at different flow velocities in the experiments, and the data obtained can be further analyzed to calibrate numerical models of fish undulatory performance. As observed from the videos, the swimming mode of the fish remained essentially unchanged throughout the experimental test, i.e., it used the body and caudal fin for propulsion over the entire range of examined velocities. The results demonstrate that the fish employs higher oscillating frequency to reach higher swimming speed and indicate that the tail beat frequency increases almost linearly with the swimming speed. This finding is in agreement with the behavior performed by most of carangiform and subcarangiform swimming species (Bainbridge, 1958; Tytler, 1969; Hunter & Zweifel, 1971). For instance, Herskin and Steffensen (1998) reported that the tail beat frequency of solitary swimming sea bass was correlated linearly with swimming speed.

Besides, the tail beat frequency appeared to decrease with the increase of fish size at various swimming speeds in the experiments, as illustrated in Figure 3-8. This relationship between  $f_t$  and body mass also exists in other aquatic animals like bony fish and shark (Watanabe et al., 2012). It indicated that smaller fish became more challenged than larger fish to reach the desired swimming speed, and that the fish with small size might require more energy in the corresponding swimming performance. A qualitative check of the videos suggested that a relatively higher tail beat amplitude might be employed by a larger fish to compensate for the

lower tail beat frequency than a smaller fish, though the oscillation amplitudes of the larger fishes have not been estimated quantitatively within this study as the larger fish only achieved steady-state swimming at one or two speeds. An in-depth study on tail beat frequency and amplitude, as well as on the corresponding consumed energy, needs more data on different fish sizes and swimming speeds and this is left as a recommendation for future work.

The results show that the critical swimming speed ( $U_{crit}$ ) of the smallest fish was significantly (about 83%) higher than that of the larger fish. Despite of statistical error due to fish individuality,  $U_{crit}$  tends to be inversely associated with the fish size, and this relationship is found to be typical for fish (Beamish, 1978). As documented by Webb et al (1984), the critical swimming speed of rainbow trout could be described by a decreasing function with respect to fish total length.

It should be noted that the critical swimming speeds reached by the experimental fish in the swim tunnel were apparently lower than expected. The maximum value of  $U_{crit}$  in the experiments was only slightly larger than  $2.0 BL/s$ , and  $U_{crit}$  of the other four fish were all lower than  $1.3 BL/s$ . However, the Atlantic salmon of similar size should be able to achieve much larger swimming speed than observed in the experiments based on previous biological research. As reported by Booth et al. (1997), the critical swimming speed of wild adult Atlantic salmon ( $50 - 60cm$ ) was above  $3.3 BL/s$  at  $18^{\circ}C$  and above  $2.8 BL/s$  at  $12^{\circ}C$ . In the experiments carried out by Hvas et al. (2017),  $U_{crit}$  of Atlantic salmon post-smolts increased with temperature in the range of  $3 - 18^{\circ}C$ , and the fish with fork length  $36.9 \pm 0.5cm$  reached  $U_{crit} \approx 2.3 BL/s$  at  $8^{\circ}C$  in a large Brett-type swim tunnel. Therefore,  $U_{crit}$  of our examined fish was relatively low compared to the data normally observed in the wild and many previous experiments.

One possible reason could be that the hatchery-reared fish had grown out of shape and could not properly adapt to high current condition. From video recordings and measurements of fish size, it was easily found that the body thickness and the body mass were larger than the normal salmon (Kane, 1988; Sutton et al., 2000). The water velocity in the tanks, where the experimental fish were held since small (around  $100g$ ), was very low. The fish did not get trained for cruising at large swimming speed, and this led to their bodies to become too blunt for swimming motion. The effect of body shape on the propulsion performance will be numerically discuss in chapter 5 and 6.

The limited volume of the swim tunnel could also account for the low critical swimming speed of the salmon fish in the experiments. Several previous studies have shown that longer and larger swim tunnels improved  $U_{crit}$  in many species. For instance,  $U_{crit}$  of brook charr *Salvelinus fontinalis* improved by 12% when flume length was increased from 2.9 to 6.2BL (Tudorache et al., 2010), and  $U_{crit}$  of shortnose sturgeon *Acipenser brevirostrum* was 22% higher in a flume with length of 10.5BL than in a half-length flume (Deslauriers and Kieffer, 2011). In the experiments of Remen et al. (2016),  $U_{crit}$  of large Atlantic salmon post-smolts (around  $300g$ ) was increased by 37% in a large flume of 252L compared to a small tunnel of 10.2L. These research indicated that the flume size could play an important role on the fish

swimming performance. The *Salmo salar* was found to perform more vigorous burst swimming in a larger tunnel, while the fish was observed to collide with the upstream front end of the swimming section when carrying out powerful bursts in a small tunnel (Hvas and Oppedal, 2019). In the present experimental setup, the swim tunnel length was less than  $4BL$  of the examined salmon, and the inner flume diameter was not larger than 6.6 times of fish body width, which was considered to be a narrow space with respect to the fish size, and thus it was likely that the natural swimming behaviors, such as tail beat amplitudes and swimming locomotion, of the tested fish were compromised in our experimental setup. Besides, the burst and coast swimming in the tests was only observed in the small length fish, while unsteady swimming seemed to be inhibited for the large fish. Therefore, it was not surprising that  $U_{crit}$  was significantly lower than normal on condition that the swimming motion was restricted due to the limit of space.

In addition, the wall effect of the swim tunnel should be taken in account when analyzing the fish swimming behavior. In a water flume, a boundary layer was generated along the boundary walls due to fluid viscosity. Its thickness is reversely related to current velocity according to boundary layer theory (Schlichting and Gersten, 2015). The fish was able to and preferred to find locations with lower water velocities in the swim tunnel, especially at smaller swimming speeds. In the steelhead trout *Oncorhynchus mykiss* studies of Webb (1993), it was concluded that a fish work less hard when swimming near a solid wall. The interaction between the vortex shedding from the fish body and the boundary layer along the flume walls could cause more challenges for fish propulsion. The critical swimming speed  $U_{crit}$  was often proved to be lower for fish swimming in narrow space, and this suggested that the obtained  $U_{crit}$  values of the examined salmon fish were also underestimated in the small swim tunnel. Therefore, the present results are not recommended to be used directly for aquaculture industry as the maximum current velocity tolerance threshold, and the actual value of upper current velocity limit can be determined to be considerably higher.

From the video observations, the undulatory movements of the fish body under different swimming conditions can be cautiously analyzed to validate the kinematic model of swimming fish. For instance, some key kinematic parameters for the fish in Test 5 at swimming speed  $1.5 BL/s$  have been calculated and discussed by Søvik (2022). Here his proposed strategy has been applied to estimate the swimming amplitude for the smallest examined fish as a function of swimming speed. The improvement on the digitalized swimming model will reduce errors in numerical predictions of fish performance. This experimental study contributes to understand the swimming behavior and hydrodynamics of the Atlantic salmon. Besides, the investigated values could help to calibrate the data obtained by biosensor implants (Svendsen et al., 2021; Føre et al., 2021). It is known that the observed transitions in the salmon swimming behaviors can serve as early indicators of changed environment around fish, such as current velocity, predators, hypoxia etc. The findings from experiments could be referred as a guide for necessary infrastructure and ensure welfare of the fish in aquaculture industry.

### 3.4 Summary

In this chapter, experimental studies were carried out on Atlantic salmon *Salmo salar* post-smolts in a Blazka-type swim tunnel with the focus on investigating fish behavior and kinematics at different swimming speeds. Individual swimming salmon in this tunnel produced a significantly lower critical swimming speed compared to biological data of wild fish and fish swimming in larger flumes. The tail beat frequency of the fish increased almost linearly with the swimming speed. Both  $U_{crit}$  and  $f_t$  of the examined salmon tended to decrease with the fish size. One possible reason for these observations could be the blunt body shape of the hatchery-reared fish, which caused larger hydrodynamic loads acting on the fish body. The side-wall effect of the swim tunnel should be another important reason to explain these behaviors of fish. The hydrodynamic interaction between fish swimming motion and boundary walls in a narrow swim tunnel may lead to the underestimate of  $U_{crit}$ . The fish swimming data obtained from videos can be further analyzed to calibrate kinematic models of Atlantic salmon undulatory motions at various swimming speeds, which could provide as background and theoretical support for numerical predictions of fish propulsive performance. In general, the experimental results should be discussed with proper considerations and then can be used as guidelines in the aquaculture industry for peak current velocity thresholds and animal welfare. The analysis of boundary layer effect in swim tunnel can help to better understand the experimental data in respirometry systems and make accurate predictions of fish swimming behavior in the future.

# Main findings from physical investigations

To gain more knowledge on real-fish swimming behaviours and better understand the fish propulsion performances, observation experiments have been carried out on two different fish species under various conditions in the present work. Distinctive findings are listed as follows:

- From the labriform swimmer tests: Fish schooling confers both hydrodynamic and behavioural advantages, but their relative contributions are swimming-speed dependent.
- From the sub-carangiform swimmer tests: Swimming capability of the examined salmon was relatively low compared to biological data. Possible reasons could be that 1) the hatchery-reared fish had grown out of shape and 2) the swim tunnel provided limited swimming space. One should note that, despite the lower achieved speeds, the Strouhal number was still within the normal range (though near the lower limit).

These experiments have a primary value as they allow to observe and learn from real fish swimming in labs. On the other end, they present challenges in connection with, e.g., test permission, costs, duration, and repetitions. Therefore, numerical simulations, representing another valuable way to study fish hydrodynamics, are complementary to answer research questions inspired by the real-fish experiments.

Major content of the following numerical part is dedicated to pitching-foil investigations, partially inspired by the state-of-the-art and our labriform swimmer tests, and to fish-like swimming studies, partially inspired by the state-of-the-art and our sub-carangiform swimmer tests. With varying Strouhal number and Reynolds number, the flow features and hydrodynamic loads of different fish-like foils are systematically analysed to identify the parameter range for optimal fish propulsion performance. The links between the fish propulsion and the body shape, as well as between the fish locomotion and swim tunnel size, are investigated numerically in sections 6.2.1 and 6.2.2.



## **Part II: Numerical Studies**





## Chapter 4

# Theoretical and numerical methods

The objective of the present numerical studies is to understand the mechanisms behind high performances of fish and provide innovative solutions for greener and efficient marine transportation. A series of hydrodynamic scenarios has been numerically examined in this thesis, where the fish-like body is modelled as a rigid or deforming foil interacting with a current or advancing in otherwise calm water without the presence of a free surface. Therefore, the following description considers for convenience a foil as body geometry to mimic the sub-carangiform fishes without appendages, which are of secondary importance for cruising.

In this chapter, the theoretical and numerical research methods used for the fish-like hydrodynamic studies of chapters 5 and 6 are introduced, starting with the equations of motion for a viscous incompressible fluid. A Computational Fluid Dynamics (CFD) code, the open-source platform OpenFOAM (OF), has been selected. To deal with the motion of the foil, two dynamic mesh motion methods are described in detail, including the deforming mesh method and the overset grid method.

In addition, easy implementation of user-defined routines makes OF very valuable for developers and researchers. A self-propulsion function for both rigid and flexible bodies with periodic lateral motions has been implemented within the OF library and is outlined here. A self-propelled foil undergoing forced harmonic heave motions in still water has been considered to verify the capability of the present method.

All the abbreviations and variables used in connection with the numerical studies have been defined in the Nomenclature.

### 4.1 Governing equations

The numerical investigation in the present thesis is comprised of various rigid and morphing foils with oscillatory forced motions in current, a flexible foil with a prescribed traveling wave motion in current and a self-propelled fish-like swimming foil. The fish-like body is assumed fully surrounded by water and the latter is modelled as a viscous fluid with incompressible flow and the temperature is assumed constant and known. We define a Cartesian rectangular coordinate system  $(x, y, z)$  and the body is assumed at  $z = 0$  for convenience in two-dimensional simulations. The  $x$ -axis coincides with the equilibrium position of the fish-like foil. The current flows towards positive  $x$  direction. A top view of the generic problem of interest is illustrated in Figure 4-1.

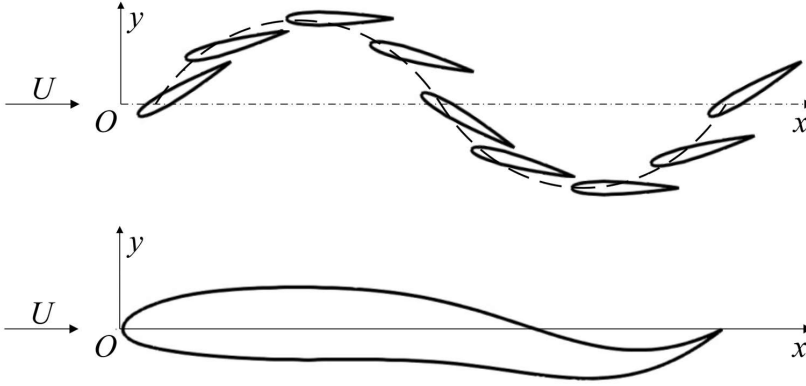


Figure 4-1. Schematics showing a rigid flapping foil and a flexible undulatory foil

Under these assumptions the governing equations are the continuity and Navier-Stokes equations, which can be written as:

$$\nabla \cdot \mathbf{u} = 0 \quad (4.1)$$

$$\frac{\partial \mathbf{u}}{\partial t} + (\mathbf{u} \cdot \nabla) \mathbf{u} = -\frac{1}{\rho} \nabla p + \nu \nabla^2 \mathbf{u} + \frac{1}{\rho} \mathbf{F} \quad (4.2)$$

where  $\mathbf{u}(\mathbf{x}, t) = (u, v, w)$  represents the velocity vector of the fluid particle, which is a function of location  $\mathbf{x} = (x, y, z)$  and time  $t$  in the Cartesian coordinate system fixed in space. Other physical parameters  $p$ ,  $\rho$  and  $\nu = \mu/\rho$ ,  $\mu$  stand for the pressure, fluid density, the kinematic viscosity coefficient and dynamic viscosity coefficient, respectively, and  $\mathbf{F}$  is the external body force acting on the fluid. Both  $\rho$  and  $\nu$  are assumed to be uniform and constant. When the flow is assumed to be essentially two-dimensional (2D), the dependence of these variables in the  $z$  direction is omitted.

The Navier-Stokes equation of (4.2) consists of three nonlinear partial differential equations that depend on both time and space. This coupled system leads to the difficulty of solving this mathematical problem, and only have analytical solutions for a few very simple geometrical configurations where the nonlinear convective accelerations terms  $(\mathbf{u} \cdot \nabla) \mathbf{u}$  can be assumed to vanish. In most of the cases, the governing equations need to be complemented by initial and boundary conditions.

For the numerical investigations in the present study, a thoroughly validated finite-volume-based numerical code in the OpenFOAM platform is used to directly solve the governing equations without introducing any turbulent models, as presented in Chen et al. (2019) and Siddiqui et al. (2020). In this finite volume method, the Eqs. (4.1) and (4.2) are actually written in their integral form through the integration over a control volume  $V$ , bounded internally by a solid surface  $S_b$  and externally by a surface  $S$ . Besides, the external body force in Eq. (4.2) is neglected during the integration, since there is no external force applying to the fluid volume in all the simulations in this work.

## 4.2 Boundary conditions

The complete mathematical problem of finding the solution to the governing equations has to include the relevant boundary conditions. In addition, it is also necessary to distinguish different flow problems by imposing appropriate physical conditions on the boundaries of the fluid domain.

The body boundary condition acting on a solid boundary expresses that the fluid velocity equals the velocity of the body, because in the viscous fluid theory, the existence of a shear stress requires both the normal and tangential velocity components of the fluid and the boundary to be equal. This is named the no-slip boundary condition, and it is often applied on the body and walls during numerical simulations.

The conditions for the external surface  $S$  bounding the fluid volume should represent the physical problem as precisely as possible. In the instances of a body placed in a current, the velocity of the inflow needs to be imposed on the inlet boundary, and a fixed-value pressure condition  $p = 0$  is often applied on the outlet, as presented in Figure 4-2.

For 2D flow assumptions, the governing equations will not be solved in the  $z$  direction. In the OpenFOAM solver, the geometries are always generated in 3D, but it can be instructed to solve in 2 dimensions by specifying a special "empty" condition on the surfaces whose plane is normal to the third dimension where no solution is required. Hence, for the front and back boundaries parallel to the  $xOy$  plane in the present work, the conditions are set to be empty for all variables.

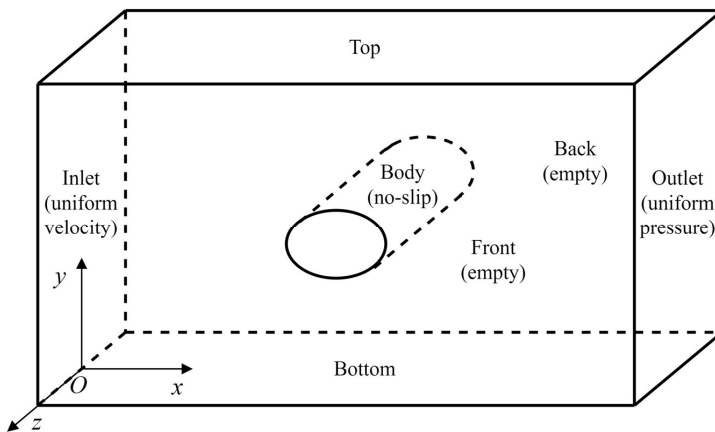


Figure 4-2. Schematic view of some typical boundary conditions

## 4.3 Numerical solver

OpenFOAM (OF) platform is a popular open-source code implemented in C++ toolbox to simulate various complex fluid dynamic problems. It is particularly advantageous due to the

availability of large number and type of utilities for pre-processing (grid generator, converters, manipulators, case setup), post-processing (using OpenSource Paraview) and many specialized CFD solvers of real-flow problems. The features in OpenFOAM are comparable to what is available in the major commercial CFD codes. Some of the more specialized features that are included in OpenFOAM are: sliding grid, moving meshes, two-phase flow (Langrange, VOF, Euler-Euler) and fluid-structure interaction. The strength of OpenFOAM is however the object-oriented approach to generating specialized solvers, utilities and libraries, using a flexible set of C++ modules (see e.g., Salehi et al., 2021; Jasak, 2009b). OpenFOAM runs in parallel using automatic/manual domain decomposition, and the parallelism is integrated at a low level so that solvers can generally be developed without the need for any parallel-specific coding.

Due to the distribution as an OpenSource code, it is possible to gain control over the exact implementations of different features, which is essential in research work. It also makes development and tailoring of the code for the specific application possible. In the recent years, numerous solvers and numerical schemes have been developed and added into the OF environment. With the objective of realizing specific functions due to the physics of the phenomena, this open-source code is relatively easy for modification and parallelization. Therefore, OpenFOAM in versions 1806/1812 has been employed in the present numerical studies.

The governing equations of the hydrodynamic problem in this work are discretized on a three-dimensional collocated Cartesian grid based on the finite volume method. Fluid dynamic quantities are centered on the discrete control volume centroids. The Eulerian algorithms are widely used in fluid dynamics. The Eulerian mesh is fixed, and the fluid continuum moves with respect to the grid (Donea et al., 2004). If any Eulerian material moves outside the Eulerian mesh, it is lost from the simulation, which causes the expense of precise interface definition and the resolution of flow details. To overcome the shortcomings of purely Eulerian descriptions, a technique, known as the arbitrary Lagrangian–Eulerian (ALE) method, has then been developed by combining the best features of both the Lagrangian and the Eulerian approaches to a certain extent. In the ALE algorithm, the nodes of the computational mesh may be moved with the fluid continuum in normal Lagrangian fashion, or be held fixed in Eulerian manner, or in some arbitrarily specified way to give a continuous rezoning capability (Miller et al., 2014). Hence, the ALE method is adopted in the present numerical studies.

In simulating the flow past a moving fish-like body under the assumption of viscous flow, the PIMPLE algorithm is employed for solving the incompressible Navier-Stokes equations, which is a combination of PISO (Pressure Implicit with Splitting of Operator) and SIMPLE (Semi-Implicit Method for Pressure Linked Equations) algorithms (Versteeg and Malalasekera, 2007). The inner (pressure correction for SIMPLE) and outer (pressure correction for PISO) iterations are set to 2 for all simulations as they give converged results. A second order Gauss-linear scheme is used for the space discretization (Bayraktar et al., 2012). Various time schemes including first order implicit Euler scheme, second order implicit backward scheme and second order Crank-Nicholson scheme have been adopted in the simulations to examine the effect of different time-evolution schemes (see e.g., Siddiqui et al., 2020; Xu et al., 2021). The stability

of the iterative algorithm is guaranteed by adjusting the time step and ensuring the Courant number to be less than 0.9 throughout the whole computational domain. The Courant number is defined as  $C = \frac{|u|\Delta t}{\Delta x}$ , where  $|u|$  is the velocity magnitude,  $\Delta t$  is the time step and  $\Delta x$  is the cell size of the mesh. It is a necessary condition for convergence while solving NS equations. Performing 2D simulations in OpenFOAM implies that the 2D grid is extruded one single cell thick in the third direction (z-axis in this work) and fluid properties are not solved in this dimension.

Additionally, all simulations in this study are run on NTNU supercomputer VILJE nodes (Intel Xeon E5-2670) using 2 nodes (32 cores) per simulation and FRAM nodes (Intel E5-2683v4 2.1 GHz) with 1 node (32 cores).

## 4.4 Dynamic mesh motion

Many examples of hydrodynamic problems in computational fluid dynamics involve moving boundaries, ranging from prescribed oscillating motion of foils to a six degree-of-freedom flow-dependent solid body motion of ship hulls and even more general cases of flow-induced body motion and boundary deformation. In this numerical study, the fish-like body will perform rigid oscillatory motions or flexible undulatory motions fixed in a current or advancing in otherwise calm water. The motion amplitude involved can be comparable to the characteristic length of the body, as will be presented in cases of chapters 5 and 6. With the objective of producing reasonable simulation results, it is important to support basic mesh motion and handle mesh deformation in a robust and reliable manner.

In the OpenFOAM library, various strategies under the Arbitrary Lagrangian Eulerian (ALE) method have been employed and implemented to allow for mesh motion and deformation. These dynamic mesh motion strategies can be applied to any CFD solver. Herein, two categories are introduced and examined: deforming mesh and overset grid techniques. Both strategies preserve the topology of the mesh, i.e., the number or connectivity of points, faces, and cells in the mesh remains unchanged. In the deforming mesh method, referred as DM in this work, the computational mesh is moved to follow the changing shape or motion of the boundary by moving its points in every step of the transient simulation. In the overset grid method, referred as OG, multiple grid systems are used, and the meshes are able to move rigidly with the body and keep good quality during dynamic simulations.

### 4.4.1 Deforming mesh method

The detailed analysis of various deforming mesh techniques and their implementation in OF is provided by Jasak and Tukovic (2006), and the main features relevant for the present work are given here.

The *displacementLaplacian* solver in the class of the *dynamicMotionSolverFvMesh* is selected for handling the dynamic mesh motion. The mesh motion for the entire domain is handled by solving the equation  $\nabla \cdot (k\nabla \mathbf{d}) = 0$ . Here,  $k$  is a diffusivity coefficient and  $\mathbf{d}$  is the motion

displacement vector for each cell. The body motion acts as a boundary condition and determines the position of mesh points. An extra file named *pointDisplacement* is required to give the starting point displacements as the initial condition.

The mesh spacing and quality for each time step is controlled by variable diffusivity. Changing the diffusivity implies applying different diffusion laws to define the movements of mesh points. The diffusivity models can be classified into two categories: quality-based methods and distance-based methods. In the quality-based method, the diffusion field is a function of a cell quantity measure. For example, the mesh manipulation of the *uniform* model is done uniformly for the moving boundary by stretching or squeezing with the same ratio for all cells, and the cell diffusivity of the *inverseDistance* model is based on inverse of the distance from the boundary. The distance-based methods are used together with the quality-based methods and their diffusion field will be a function of the inverse distance to the nearest selected boundary. A quadratic distance-based diffusivity coefficient ( $k = 1/r^2$ ) is employed in this study, with  $r$  the cell-center distance from the specified moving boundary. This implies that as we go far away from the moving body, less deformation occurs for the cells, as illustrated in Figure 4-3.

However, when the moving boundary undergoes large motions, it can lead to large distortion of the cells and in some cases make it impossible to preserve mesh quality and solution accuracy, together with the risk of substantial increase in the computational time or of numerical instability. Therefore, it is suggested to avoid directly using this method to large motions. The detailed analysis of this approach will be discussed in section 5.3.

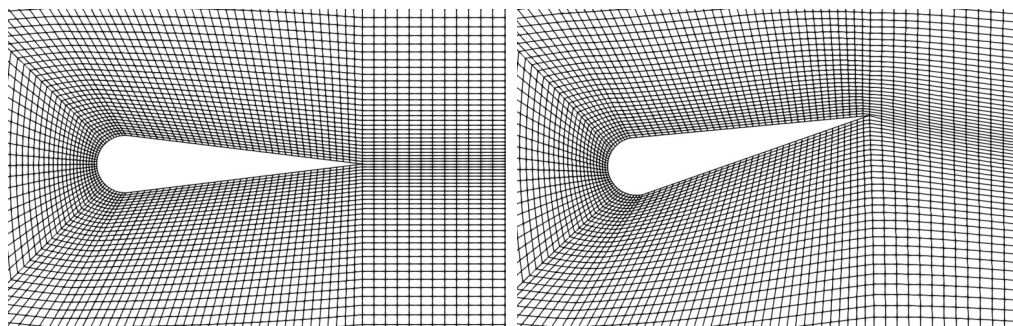


Figure 4-3. An example of mesh at initial time and under large motion conditions using deforming mesh method

#### 4.4.2 Overset grid method

The problems of severe mesh deformation following large boundary motions can be overcome by using overset (i.e., overlapping) grid (OG) method. In the overset grid method, two separate grids are defined, which may arbitrarily overlay each other: an Earth-fixed grid is used as background mesh, while a body-fitted (i.e., fitted to the body shape) and body-fixed (i.e., fixed to the body and moving rigidly with it) grid is used near the moving body (see Figure 4-4). The former often adopts Cartesian grid, and the latter is named as overset grid. In this scenario with two grid systems, the internally static grids can retain their original structure and quality but can move relative to each other without restrictions (e.g., Chen et al., 2019; Miller et al., 2014).

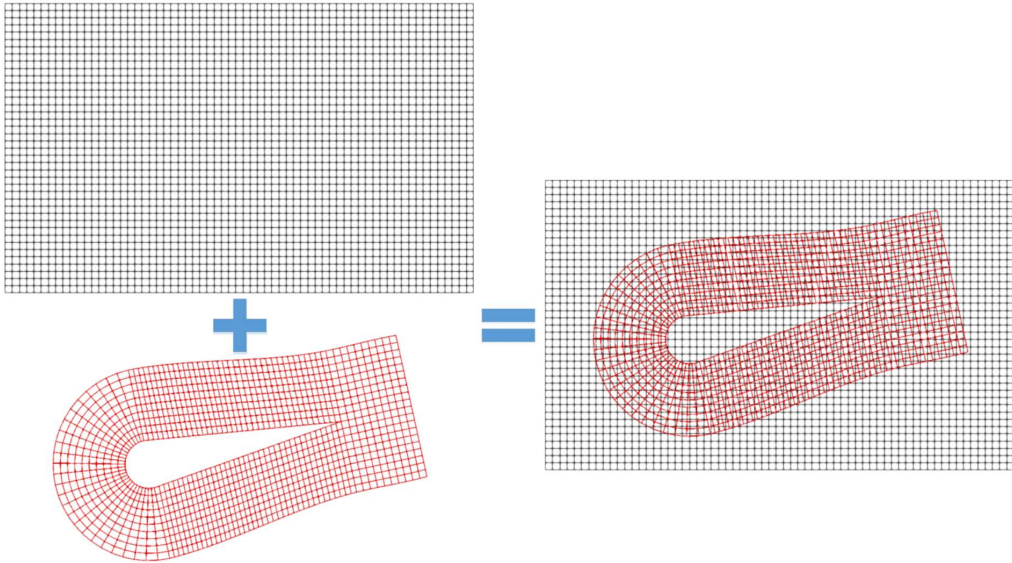


Figure 4-4. Schematic of overset grid method. Black line: background mesh; red line: overset mesh

The governing equations are solved on both grids, and in order to pass information between the two disconnected grids, interpolation must be performed. The overset method implemented in OpenFOAM library does the linear interpolation within values. Thus, it is recommended to make the cell sizes of background mesh comparable to those of overset grid for proper exchange of information between grids so to ensure accuracy. In practice, their size ratio is often adjusted to smaller than 2.

The overset grid method can be divided into the following four sequential steps, to be performed at every time step in dynamic simulations:

1) *Identification of hole cells.* They belong to the background mesh and are located inside the area occupied by the moving body. These cells are marked and blanked out during the simulation process. This region is considered as empty, i.e., no fluid equations should be solved here.

2) *Identification of fringe cells.* They are used as boundary cells in the calculation procedure, with boundary values determined through solution interpolation. In the background grid, these cells locate at the border with the moving body and are adjacent to hole cells, while in the body-fitted grid, the fringe cells are at the outer boundary. The former ones provide information from the overset grid to the background mesh, and the latter ones give the exchange information from the background mesh to overset grid.

3) *Identification of donor cells.* They are cells providing information for the fringe cells in the other mesh sufficiently close to them.

4) *Interpolation between fringe and donor cells.* The interpolation function takes the correct values from donor cells and then does the linear interpolation to provide information for fringe cells.



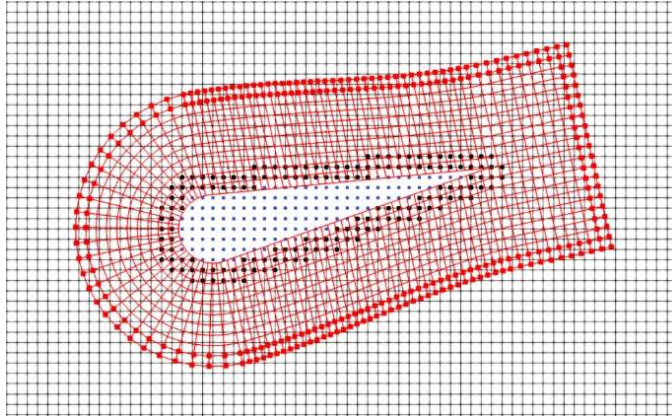


Figure 4-5. Illustration of overset grid method. Black line: background mesh; red line: body-fitted mesh; blue points: hole cells; black and red points: fringe cells. The overset grid donor cells are those near the black points and the background grid donor cells are those near the red points

Figure 4-5 shows the cells for information exchange between the grids. Note that the hole, fringe and donor cells have to be updated at each time step in the computation. This additional process results in the increase of computational time for overset grid method as compared to the deforming mesh method. The detailed analysis using the above two dynamic mesh motion solvers is described in section 5.3, where the influence of various numerical parameters on the simulation results are examined. Moreover, to examine the effectiveness of the overset grid method, a numerical simulation has been performed for a stationary airfoil case, as documented in Appendix A.

## 4.5 Numerical implementation of self-propulsion

OpenFOAM is distributed with a large number of applications, but researchers continuously develop new numerical features and libraries connected with their special needs. The interest of our numerical investigations is to study the kinematic and dynamic behaviours of a fish-like body, which can propel itself. In this section, we present the strategy for implementing the self-propelled motion of a lateral moving body within OpenFOAM library. Then, numerical simulation of an oscillating elliptic foil has been performed for verification of the proposed method.

### 4.5.1 Self-propulsion strategy

In many flapping foil and robotic fish studies, the body is placed in a steady stream with a prescribed lateral oscillation while its movement in the streamwise direction is prohibited. However, the conditions in these studies can be different from those in self-propelled bio-locomotion. In other words, the body velocity in real bio-locomotion is allowed to change in response to the variation of the forward force.

Motivated by the quest to understand the hydrodynamic performance of a self-propelled body, the self-propulsion technique has been developed and implemented in OpenFOAM toolbox. It

can automatically integrate hydrodynamic forces acting on the body and then returns the next position of the body patch.

For the more traditional foil studies, the body is forced to flap in a sinusoidal fashion or swim in an undulatory motion with a fixed pivot point in current. However, for the hydrodynamic scenarios studied herein, the fish-like body will also experience a locomotion in addition to the prescribed lateral motion, which is often defined in the form of a wave traveling in the streamwise direction (e.g., Maertens et al., 2017):

$$y(x, t) = A(x) \sin(2\pi(x/\lambda - ft) + \phi) + B(x, t) \quad (4.3)$$

where  $A(x)$  is the amplitude function of the body deformation,  $\lambda$  is the wavelength,  $f$  is the frequency, and  $B(x, t)$  can stand for the recoil or the lateral position of the body. Then, the self-propelled foil is free to move horizontally due to the results of the fluid-body interactions. The locomotion of the body in the horizontal direction is governed by Newton's law:

$$\mathbf{M} \frac{d\mathbf{u}_b}{dt} = \mathbf{F}_b \quad (4.4)$$

where  $\mathbf{M}$  represents the inertia matrix of the body,  $\mathbf{u}_b$  is the six-degree-of-freedom (6 DoF) velocity vector (3 translational velocities and 3 rotational velocities) and  $\mathbf{F}_b$  is the generalized force/torque vector estimated from the solution of Eqs. (4.1) and (4.2) by integrating on the surface of the fish-like body. As explained previously, all the variables in the third direction are not solved in 2D simulations. Moreover, the degree of freedom along  $x$ -axis is free and other motions are constrained in the verification case presented in the next section.

Though there is no such application where the body can have both prescribed motions in some directions and the free motion coupled with fluid around in other directions, the idea of realizing this strategy can be inspired by an existing library, named *sixDoFRigidBodyMotion*. It is used to solve the translational and rotational movement of a solid body caused by the forces acting on it due to the interaction with the surrounding fluid, and therefore we can for instance predict the transient behavior of a ship hull with accuracy, as reported by Jasak (2009a). Moreover, the *sixDoFRigidBodyMotion*, a library solving dynamic mesh motions, can be called by many fluid solvers such as *pimpleFoam* and *overPimpleDyMFoam*, which provides convenience for our code implementation since these solvers are the ones adopted in the numerical simulations here.

To implement the free locomotion of the body with the prescribed motion, the *forces* library is necessary to be introduced into the new application. The *forces* class calculates the forces and moments by integrating the pressure and shear forces over the desired boundaries. Forces and moments comprise normal pressure and tangential viscous contributions are computed in the Earth-fixed Cartesian coordinate system by default. In order to obtain the transient motion of the body, the accelerations need to be calculated by solving Eq. (4.4) for every time instant, and then we can get to know the velocity and displacement of the moving body by integrations. The updated state of motion will be applied to the subsequent time step and coupled with the corresponding prescribed motion. The starting motion state of the body is often given by the initial conditions of the case setup. The simulation procedure of a self-propelled body in OpenFOAM is shown in Figure 4-6, in which the detail of the implemented self-propulsion

strategy is provided.

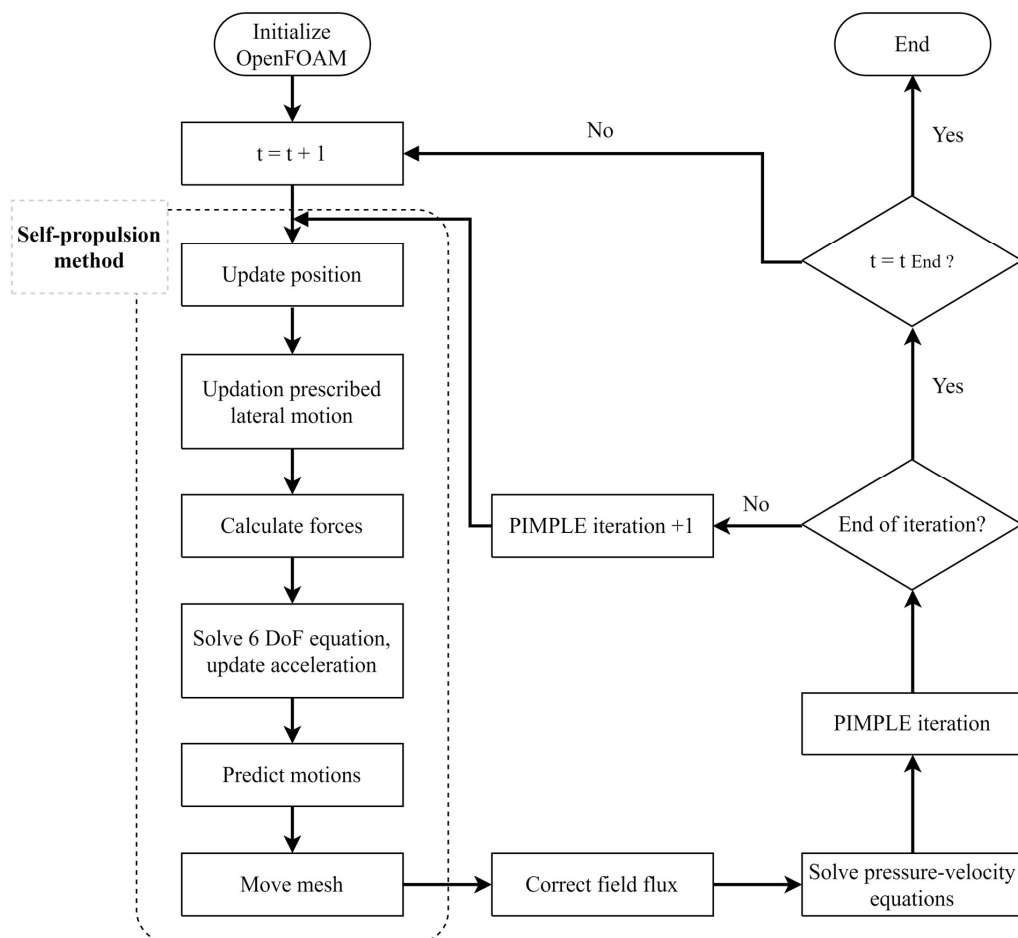


Figure 4-6. Flow chart depicting computation procedure in OpenFOAM using the self-propulsion strategy

The implementation of the new function in OpenFOAM can be split into the following steps:

- 1) store the motion state at the beginning of each time step.
- 2) compute the forces on the desired patch, i.e., moving body boundary surface. A boundary is generally broken up into a set of patches in OF.
- 3) extract the updated mass centre position at the new time step by solving the 6 DoF motion equation (4.4).
- 4) move the body boundary to the new positions according to the calculated displacement. Here, the mesh surrounding the body should also be moved together in order to maintain its good quality. Various mesh motion solvers can be employed by user to handle the mesh motion and deformation.
- 5) output the new values of desired variables.

The complete development of the self-propulsion strategy should finally include the compilation of the new library and some verification/validation studies.

### 4.5.2 Verification study of an elliptic foil

The kinematic and dynamic behaviors of a free flapping foil is presented as a numerical verification of the implemented self-propulsion strategy to examine the effectiveness and accuracy of this approach. The simulation results are compared against the two-dimensional numerical work of Zhang et al. (2009) for verification, where an in-house Navier–Stokes solver using modified SIMPLEC pressure-correction scheme on moving unstructured Chimera grid was applied.

In this study, the elliptic foil of chord length  $c$  and thickness  $D$  is forced to flap up and down in an incompressible fluid and free to move horizontally along  $x$  direction. The forced vertical motion of the foil is prescribed as a sinusoidal oscillation:

$$y_b = A \sin(\omega t) \quad (4.5)$$

where  $A$  represents the heaving amplitude of the foil and  $\omega$  is the angular frequency. One oscillation period is denoted as  $T$ . The characteristic length, velocity, and time used for nondimensionalization are  $c$ ,  $A\omega$ , and  $c/(A\omega)$ , respectively.

The horizontal force acting on the foil results in a free movement in the  $x$  direction according to the Newton's second law, and the dimensionless mass of the foil is defined as:

$$M = \frac{\rho_b S_e}{\rho_f c^2} \quad (4.6)$$

where  $\rho_b$  and  $\rho_f$  are the density of the foil and the fluid, respectively, assumed uniform and  $S_e$  is the area of the elliptic foil.

In the present verification study, the effect of geometric shape on the hydrodynamics is considered herein to understand the relation between the morphology of wings (fins) and their hydrodynamic performance in terms of velocity history and wake pattern, and thus the chord-thickness ratio of the elliptic foil  $CR = c/D$  is varied from 1:1 to 15:1 in the numerical simulations.

The Reynolds number is based on the foil flapping amplitude and frequency  $Re_e = A\omega c/\nu$ . Other important dimensionless parameters in the present problem are the density ratio  $\rho_b/\rho_f$  and the nondimensional heaving amplitude  $A/c$ . In the following numerical simulations, the parameters of  $Re_e = 200$ ,  $\rho_b/\rho_f = 4$  and  $A/c = 0.4$  are used to be consistent with reference study, and thus verifying the self-propulsion strategy implemented in OpenFOAM.

Since the horizontal motion of the elliptic foil can be hardly foreseen and it is likely to perform large locomotion, the overset grid method introduced in section 4.5.2 is an efficient approach for this verification study. It gives the flexibility to allow for numerical simulations of arbitrary foil motions relative to the Earth-fixed background grid.

A schematic representation of the computational domain in the present problem is given in Figure 4-7. The length and height of this domain size are set to be  $60c$  and  $10c$ , respectively,

same as that done in the reference work. The elliptic foil is placed at the center of computational domain as the starting position. Zero horizontal velocity is given to the foil by default, but in some cases, the effect of initial perturbation is examined by imposing a small initial horizontal velocity. On the four boundaries of the domain and the surface of the flapping foil, the no-slip boundary conditions are applied, which is also consistent with the reference simulations. As the overset grid method is employed for simulation and information should be exchanged between grids, the boundary condition named “overset” in OF solver is used on the internal boundary of the overset mesh. For 2D computations here, the direction in the plane of the paper is only one cell thick, i.e., all variables are not solved in the  $z$  direction and boundary conditions are set to be empty.

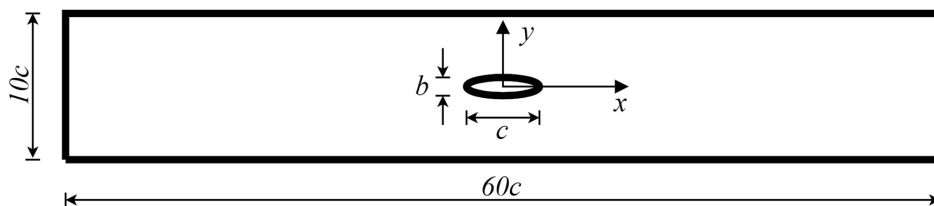


Figure 4-7. A schematic representation of the computational domain.  $c$  is the chord length of the foil and  $b$  is the thickness

Both structured and unstructured meshes can be used to discretize the fluid domain. The background grid of the overset grid method often uses a Cartesian structured hexahedral (hex) mesh created by the *blockMesh* utility included in the OpenFOAM platform. This is quite simple to apply and only requires definition of corners forming the hexahedral block together with the number of divisions in each of the three dimensions. For simple body shapes, this technique can also be used. But for complex body shapes, *snappyHexMesh* utility can be an appropriate option to generate unstructured meshes. Before applying this method, a computational domain larger than the size of the body in all directions has to be created firstly to provide a starting mesh, and the body geometry should be given as an input in the form of a stereolithography format. Then, the *snappyHexMesh* utility conforms the mesh approximately to the surface by iteratively refining the starting mesh and morphing the resulting split-hex mesh to the surface, i.e., all the cells inside the body surface are removed and the cell vertex points close to the surface will be moved onto surface geometry to remove the jagged castellated surface from the mesh. Generally, this process involves refinement of cells near the body surface and cannot be performed with hexahedral blocks alone due to arbitrary shapes and curvatures of the body. Therefore, unstructured meshes including prism and tetrahedral cells are often generated for refinement, as shown in Figure 4-8. The *snappyHexMesh* automatically generates a 3D mesh, and another utility named *extrudeMesh* can be applied to extrude the mesh from an existing surface patch into a 2D mesh. In this mesh generation method, some important parameters can be defined by users in order to obtain a suitable mesh with good quality, such as the region of refinement zones, size of maximum cells relative to the starting mesh, and number of prismatic layers close to the body surface. However, for a more exquisite mesh, it is suggested to employ some advanced mesh generation utilities or software. For example, the spacing between nodes along and around the body surface can be specified by many bunching laws or adjusted manually in the commercial software ICEM (ANSYS, 2005).

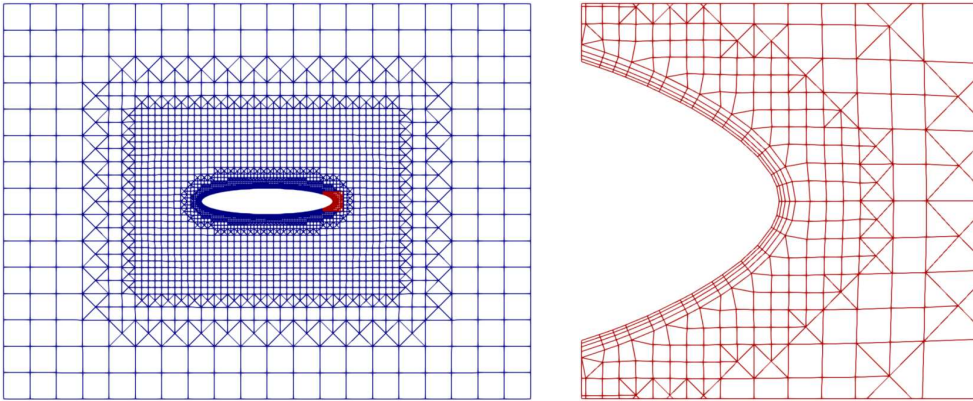


Figure 4-8. Unstructured mesh generated by *snappyHexMesh* in the overset region for the case of  $CR = 5$  with details near the boundary surface (red)

Both structured and unstructured grids can be generated by ICEM. The unstructured grid can be created with tetra/prism mesh automatically after giving the maximum cell size as well as mesh parameters around boundaries, and the structured one must be generated with more manual intervention. The structured grids are able to provide more flexible control of the mesh generation, especially the refinement in specific regions where large flow gradients are expected to happen. In most of the cases, the structured mesh can provide a more efficient computation as compared to an unstructured mesh, since the unstructured one generally owns larger number of cells (due to automatic refinement near boundary surface). However, for the elliptic body with very large chord-thickness ratio, the unstructured mesh can have better mesh quality than the structure one in terms of the metrics such as skewness and non-orthogonality. Figure 4-9 shows an example of structured and unstructured O-type grids for the 2D elliptic foil of  $CR = 5$ .

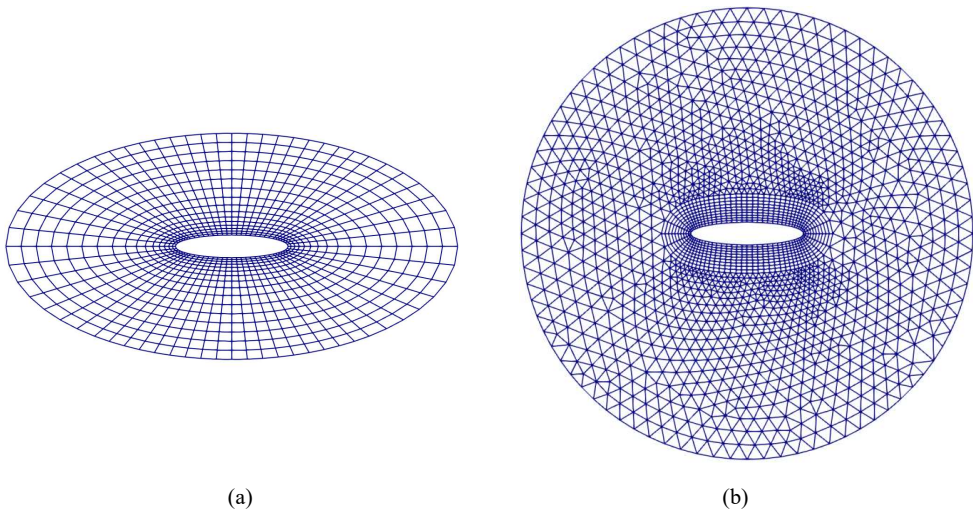


Figure 4-9. A schematic view of meshes generated by ICEM in the overset region for the case of  $CR = 5$ . (a) Structured mesh; (b) Unstructured mesh

Due to the linear interpolation algorithm of the overset mesh method, the overset mesh is often constructed so that the outermost layer of the moving mesh has the same cell size as the background grid. Note that though both overset and background grids are extruded one single cell thick in the third direction for 2D simulations, we should always remember to set their mesh thickness along  $z$  direction equal.

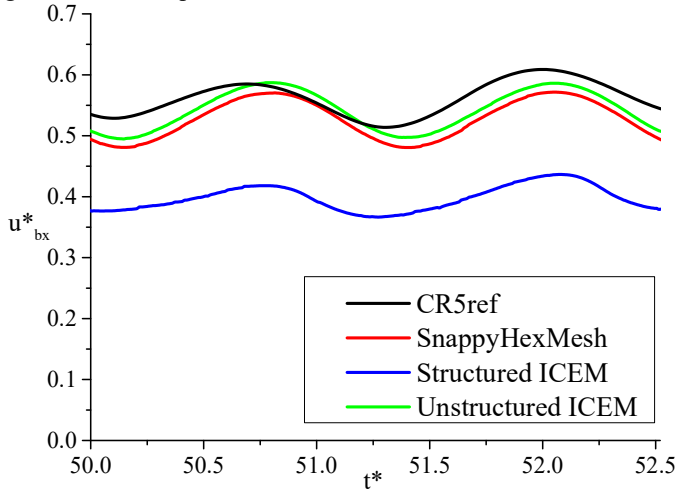


Figure 4-10. Nondimensional horizontal velocity for the elliptic foil with  $CR = 5$  using different mesh methods

The OpenFOAM results obtained using the three mesh approaches in Figures 4-8 and 4-9 are compared against the reference results for the case of an elliptic foil with  $CR = 5$  because it is expected to have a unidirectional locomotion. As reported by Zhang et al. (2009), after an initial transient phase in this case, the foil achieves a quasi-steady-state phase with a unidirectional locomotion. Figure 4-10 examines the latter phase showing the dimensionless horizontal velocity of the foil from the three simulations. One should note that the same background grids with cell size  $0.2c$  are employed by the *snappyHexMesh* (red) and the structured mesh (blue), and the unstructured mesh generated by ICEM (green) adopted a finer background grid of size  $0.125c$  since the outermost layer of its overset grid is smaller. It is found that the unstructured mesh generated by *snappyHexMesh* can predict similar kinematic results as the one by ICEM, which might be because both meshes have fine cells within the refinement region around the foil. Moreover, the results from the two unstructured meshes agree much better with the reference solution than the structure mesh result. The disability of the structured mesh in this case may be due to the overset mesh is quite coarse and many cells are skewed, thus it didn't capture well the flow features close to the foil and also lost accuracy during information interpolation between grids. With the increase of the chord-thickness ratio  $CR$  in this hydrodynamic problem, it becomes even challenging to generate a body-fitted O-type structured mesh with better quality than the unstructured mesh. There will be more and more cells clustering around sharp corners for increasing  $CR$ , and as a result, the aspect ratio of these cells for the structured mesh will be too large. It is also difficult to control the prismatic layers covering the entire body surface using the *snappyHexMesh* utility for large  $CR$  foils. Therefore, the unstructured mesh generated by means of the available software ICEM is employed for the overset grid attached to the elliptic foil with different  $CR$  values in the present study.

For better comparison against the reference solutions, it is performed a numerical convergence analysis of the OpenFOAM results. The case of elliptic foil with  $CR = 5$  is used again to this scope. Due to the symmetric setup of the studied foil, it is expected that the grids can have a huge influence on the predicted results. According to Prandtl's boundary-layer theory (Schlichting and Gersten, 2015), the boundary-layer thickness  $\delta$  in a two-dimensional incompressible laminar flow satisfies the following trend:

$$\frac{\delta}{L} \sim \frac{1}{\sqrt{R_n}} = \sqrt{\frac{\nu}{UL}} \quad (4.7)$$

where  $L$  represents the characteristic length of the body,  $U$  is the free-stream velocity (true or seen in a reference frame moving with the body), and  $R_n$  denotes the Reynolds number defined in a general sense:  $R_n = \frac{UL}{\nu}$ . A simple example of its application is the boundary-layer along a 2D circular cylinder of radius  $R$  in a current parallel to the  $x$ -axis, and the thickness around maximum  $y$  point is estimated to be  $\delta \approx \frac{2\sqrt{2}}{\sqrt{R_n}}R$ . Here the diameter of the cylinder is taken as the characteristic length  $L$  for Reynolds number. The present elliptic foil case follows this law for a rough estimation by considering  $R = c/2$ , the maximum thickness is approximately around  $0.1c$ . Therefore, the number of mesh points within this boundary-layer region should be determined so that the body boundary layer is well resolved, which is important to predict accurately the fluid-body interactions.

As mentioned above, the unstructured mesh strategy from ICEM is adopted to discretize the overset region with different values of the first off-wall cell height (the distance from the first off-wall point to the body surface along surface normal direction), the height ratio as well as the number of prismatic layers. The maximum cell size of the overset mesh in all the cases is  $0.15c$ . The names of the generated grids and details of grid parameters are given in Table 4-1.

Table 4-1. Grid details for  $CR = 5$ 

Grid	First cell height ( $\times c$ )	Height ratio	Number of layers	Nodes on foil
G1	0.02	1.05	10	72
G2	0.019	1.1	10	72
G3	0.015	1.15	10	68
G4	0.012	1.2	10	72
G5	0.02	1.1	10	72
G6	0.012	1.1	14	68
G7	0.005	1.1	21	68
G8	0.02	1.1	10	68
G9	0.005	1.1	21	68
G10	0.02	1.1	10	116
G11	0.005	1.1	21	116

The cases from G1 to G7 have asymmetric unstructured mesh, and the height ratios in G5-G7 are kept the same. For the cases G8-G11, the unstructured mesh is generated for a quarter of the



foil and mirrored twice for the whole overset domain and thus they are symmetric with respect to the  $x$  and  $y$  axes defined in the sketch of Figure 4-7. In these numerical cases, the Euler scheme is selected for time discretization and the time step is  $0.005s$  to ensure that the maximum Courant number is less than 1 for all simulations. The foil horizontal velocity, predicted in quasi-steady-state conditions by using the G1-G11 grids, is documented in Figure 4-11.

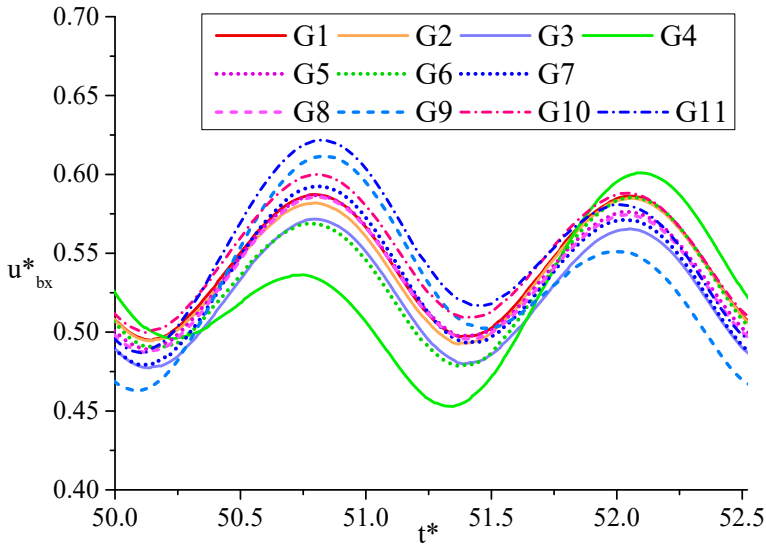


Figure 4-11. Nondimensional horizontal velocity for the elliptic foil with  $CR = 5$  using grids G1-G11

From the results of G1-G4, it can be seen the velocity history of G4 is obviously deviated from G1-G4 even though it had a finer mesh in the first off-wall layer. The deviation could be due to the higher value of the cell height ratio. For G5-G8, the height ratio is 1.1 and the numbers of layers are adjusted so that the boundary layer from the body is well resolved. By comparing the results of G1 and G5 where the first layer thicknesses are the same, we find that the velocity time history from G5 almost coincides with that from G1 except that G5, with a larger prismatic layer region, can capture better the frequency content associated with the time history of horizontal velocity for  $CR = 5$ , as documented in Figure 4-11. The maxima and minima of the horizontal velocity from G6 and G7 agree well but they have half-period phase difference. It may be due to the symmetric setup of the numerical simulation and the vorticity shedding occurred half-period later. In the symmetric meshes studies of G8-G11, the results from G8 coincide with those from G5, but those from G9 have larger oscillation amplitude than the results from G7. Moreover, there are more nodes along the foil in G10 and G11. The results from G5 and G10 are similar while the finer mesh G10 documents larger velocity discrepancies. The mesh G11 results in higher horizontal speed of the foil. Overall, this elliptic foil case is very sensitive to the mesh because of its symmetric geometry and symmetric computational domain. From this analysis, it is found that too small first off-wall cell size and too large cell height ratio can lead to the risk of increasing numerical errors for simulations. The meshes with first cell height  $0.02c$  and height ratio 1.1 are generally stable for simulation. The symmetric mesh G10 can give reasonable results for the horizontal velocity of the body, and it is selected

as a base mesh for the following time scheme analysis, as shown in Figure 4-12. Besides, the strategy associated with the mesh G10 is adopted to generate grids for other  $CR$  values examined in this verification study.

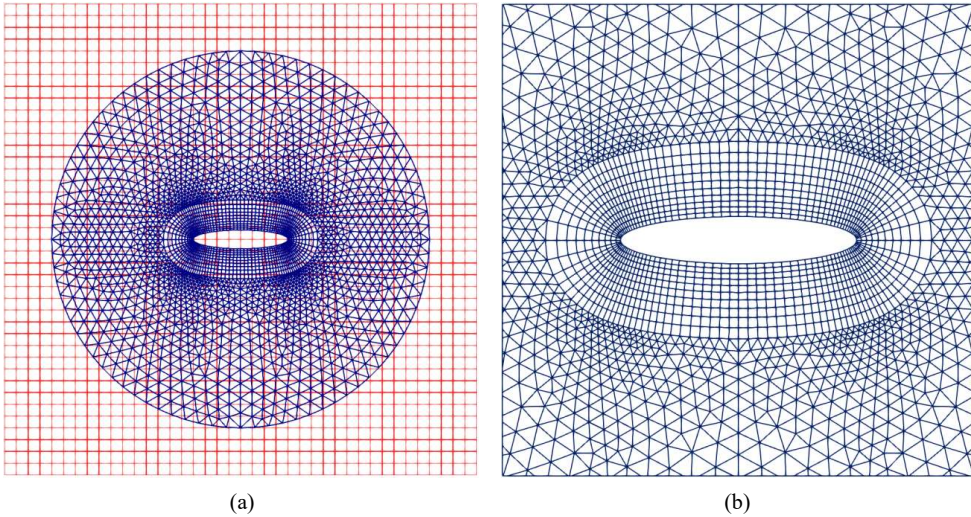


Figure 4-12. Meshes for the case of  $CR = 5$ . (a) Meshes near the overset region (red line: background mesh; blue line: moving mesh); (b) local mesh around the foil surface where rectangular cells are used to capture the flow features in the boundary layer

In addition, the effect of time evolution schemes has been examined since it is also one of the most important factors controlling numerical diffusion in hydrodynamic problems. The first-order Euler implicit time scheme and the second-order Crank-Nicolson method with under-relaxation values of 0.7 and 0.9 (CN 0.7 and CN 0.9) are adopted for the elliptic case of  $CR = 5$  with the mesh shown in Figure 4-12.

The velocity histories of the elliptic foil  $CR = 5$  using these time schemes are plotted in Figure 4-13. To make a quantitative comparison between the numerical schemes, the maxima and mean values in the quasi-steady-state region for two oscillation periods are considered and documented in Table 4-2. From the results, the CN 0.7 scheme is observed to present a lower horizontal velocity, with a difference of 1.5% for the mean velocity when compared with CN 0.9 scheme. In general, the under-relaxation value of 0.9 is considered as a good compromise between accuracy and robustness for CFD simulations. But the maximum velocity predicted by CN 0.9 in this case is smaller than the value predicted using the Euler scheme, and another disadvantage is that it increases the computational time by about 30%. The comparison between Euler and CN schemes is reasonable and thus the Euler scheme is chosen as the base scheme for all studied elliptic foil cases with different chord-thickness ratios.

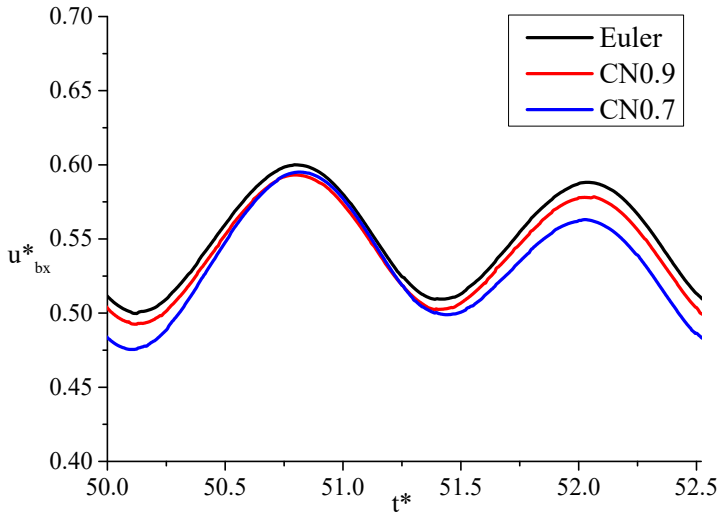
Figure 4-13. Nondimensional horizontal velocity for the elliptic foil with  $CR = 5$  using different time schemes

Table 4-2. Horizontal velocity results of different time schemes

Time scheme	Maxima	Mean	Computational time (s)
Euler	0.600	0.550	2541
CN 0.9	0.593	0.543	3137
CN 0.7	0.596	0.535	3237

For the cases with other  $CR$ s, the number of mesh points that are deployed on the surface of the foil is adjusted to its shape accordingly. For example, we can decrease nodes number to 60 for  $CR = 3$  and increase it for  $CR = 15$ . The extra grid points are clustered near the leading and trailing edges where larger gradients of flow quantities are expected.

After establishing these numerical setups and convergence criteria, the simulation results are verified against the reference solutions. The comparisons are performed in terms of the horizontal velocity histories of the foil and the corresponding vortex-shedding features. This is important to analyze the effectiveness of the self-propulsion strategy implemented in OpenFOAM library for predicting the body locomotion and the hydrodynamic forces acting on the moving body. The time histories of the simulated horizontal velocity for  $CR = 1, 3, 5,$  and  $15$  are plotted in comparison with the reference data in Figure 4-14. From this figure, it is seen that three different scenarios can be identified, namely, no symmetry breaking ( $CR = 1$ ), chaotic motion ( $CR = 3$ ), and unidirectional locomotion ( $CR = 5$  and  $15$ ).

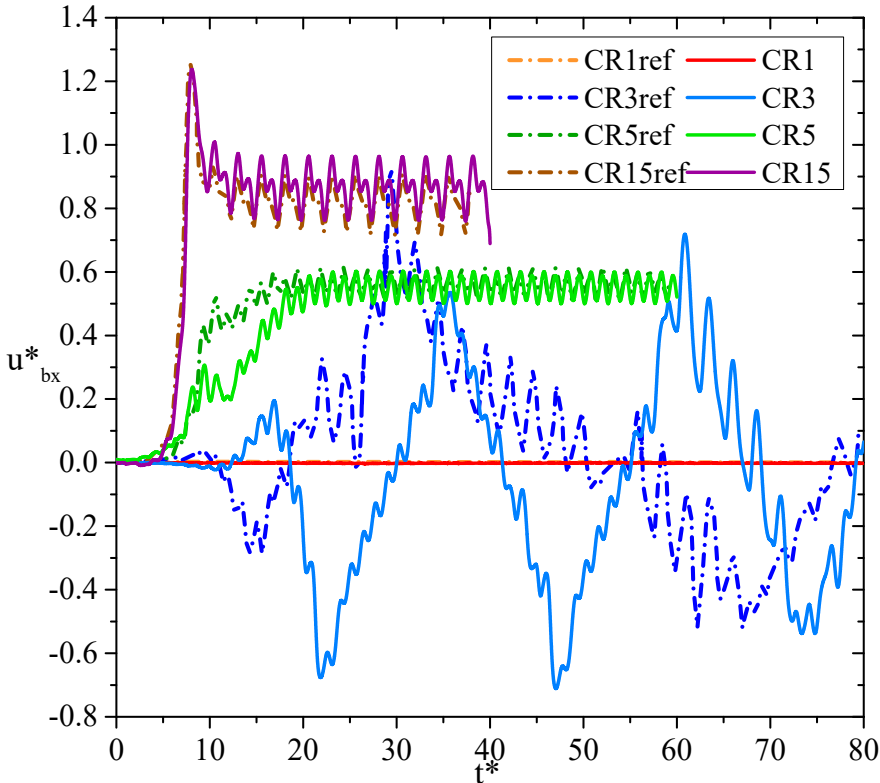


Figure 4-14. The comparison of the horizontal velocity histories between numerical simulations (dash line) and reference solutions (solid line) for elliptic foils at various  $CR$ s

The results from the developed self-propulsion strategy and those from the reference numerical solution are in good agreement for the case with  $CR = 1$ , where the foil is actually a circular cylinder. No effective locomotion is triggered by the adopted method and this left-right symmetric pattern is very stable in the investigation period even with a large initial perturbation of the foil horizontal velocity. The simulated horizontal velocity is not strictly zero after a long time of simulation due to error accumulation, but its magnitude remains smaller than  $10^{-3}$  after 30 oscillation periods as presented.

To figure out the reason of cylinder's zero locomotion behaviour and further explore the effectiveness of the implemented self-propulsion method, the flow field of the above scenario is thus illustrated here. Figure 4-15 shows the comparison of the vorticity contours when the foil is at the equilibrium position. The vorticity field around the circular foil can maintain the left-right symmetric pattern for a long time, despite a negligible deviation from its initial body horizontal position at the centre of the computational domain. Besides, good agreement is confirmed between the present simulations and the reference results.

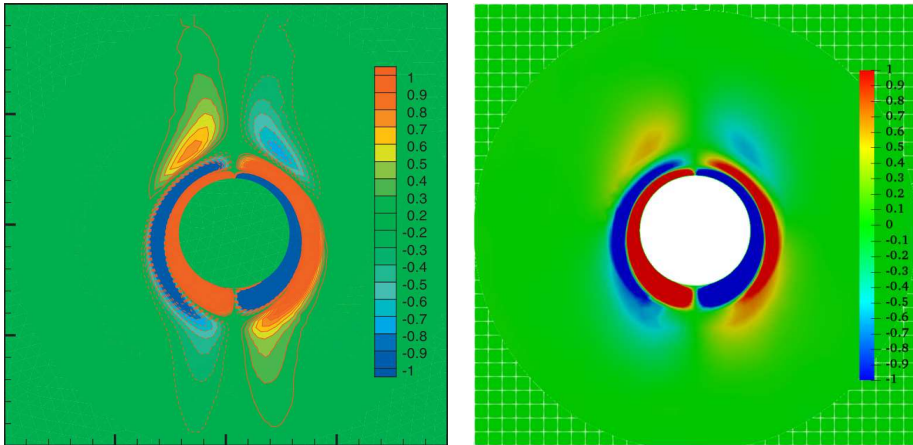


Figure 4-15. Vorticity contours of the elliptic foil  $CR = 1$  at equilibrium position from the reference solution (left) and OpenFOAM simulations (right)

In the case of  $CR = 3$ , it is apparent from Figure 4-14 that the horizontal motion experienced by the elliptic foil is different from the reference solution. However, it should be noted that the foil moves back and forth in a chaotic manner and no unidirectional locomotion is achieved after a long time of simulation for this scenario, which is consistent with the chaotic-motion scenario predicted by the reference solution. The zero horizontal velocity is soon broke during the foil evolution and the time averaged velocity after ten periods of foil oscillations, for minimizing the influence of initial disturbance, is relatively small (approximately 0.03). Moreover, a minor numerical perturbation, such as machine error or mesh asymmetry, will lead to a quite different foil locomotion. But no matter what the velocity history is, the foil always keeps the chaotic behavior and has a very small time-averaged velocity, which are consistent with the reference numerical work, indicating the implemented method is effective in studying this problem.

Figure 4-16 displays the instantaneous vorticity field of the elliptic foil  $CR = 3$  from the reference and OpenFOAM results, and the direction of the foil instantaneous velocity is indicated by the black arrow. In this chaotic scenario, the symmetric pattern of the flow field is lost soon after the foil oscillation, and the vorticities begin to emerge at one end of the foil. Then the foil is accelerated by the non-zero horizontal force toward one direction, depending on the initial conditions and the consequent arrangement of the vortices. It seems that the foil cannot easily shake off the vortices that are shed during the previous strokes. These asymmetric vortices tend to circulate around the body and give rise to complicated interactions among them. Although the instantaneous horizontal velocity and locomotion of the foil predicted by the present numerical method is different from the reference solution, it is seen that the foil moves back and forth within a certain range for a long time in both studies.

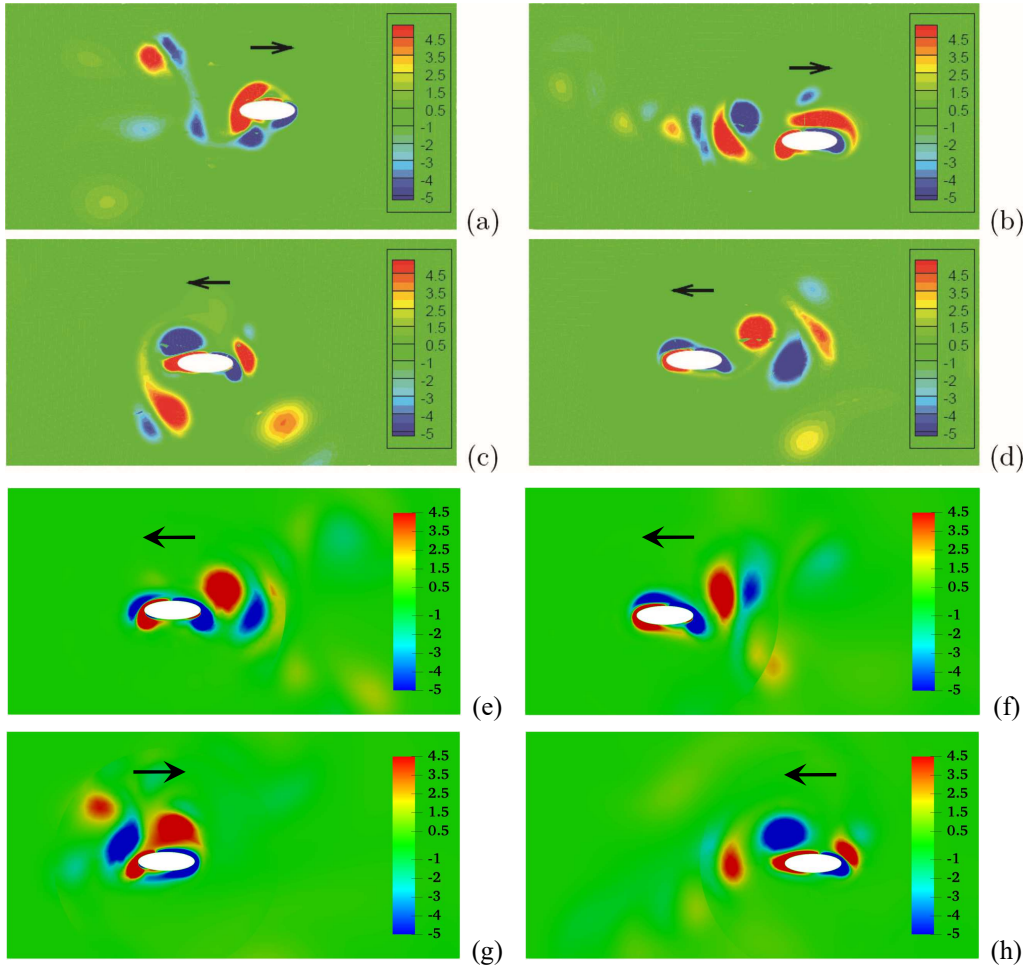


Figure 4-16. Instantaneous vorticity contours of the elliptic foil  $CR = 3$  at  $t^* = 30, 50, 60,$  and  $70$  from the reference solution (a-d) and OpenFOAM simulations (e-h)

In the cases of  $CR = 5$  and  $15$ , the elliptic foils can perform a unidirectional locomotion, and the agreements between present results and reference data are quite reasonable. The nondimensional averaged terminal velocities after the periodic quasi steady states are reached for the two cases are estimated as  $0.55$  and  $0.86$ , respectively. The corresponding values from the reference solution are  $0.56$  and  $0.82$ , and the differences between OF and reference results are about  $1.8\%$  and  $4.9\%$ , respectively. Thus, the present numerical method can be considered satisfactory in predicting foil kinematics with effectiveness and accuracy.

For the elliptic foil  $CR = 5$ , a unidirectional locomotion is achieved soon after the symmetry breaking of the vorticity field. Large vortical structures propagate almost horizontally to the left and thus the foil moves toward the right, and this direction selection can be affected by the initial conditions. From the vorticity contours shown in Figure 4-17, it is found the vortical structures behind the foil propagate to different sides about the center line in the two cases, and

this could be due to the numerical perturbations such as machine error and mesh asymmetry (used in the reference work). Besides, this vortical structure is the reversed von Kármán vortex street, which is often related with the thrust force of the foil.

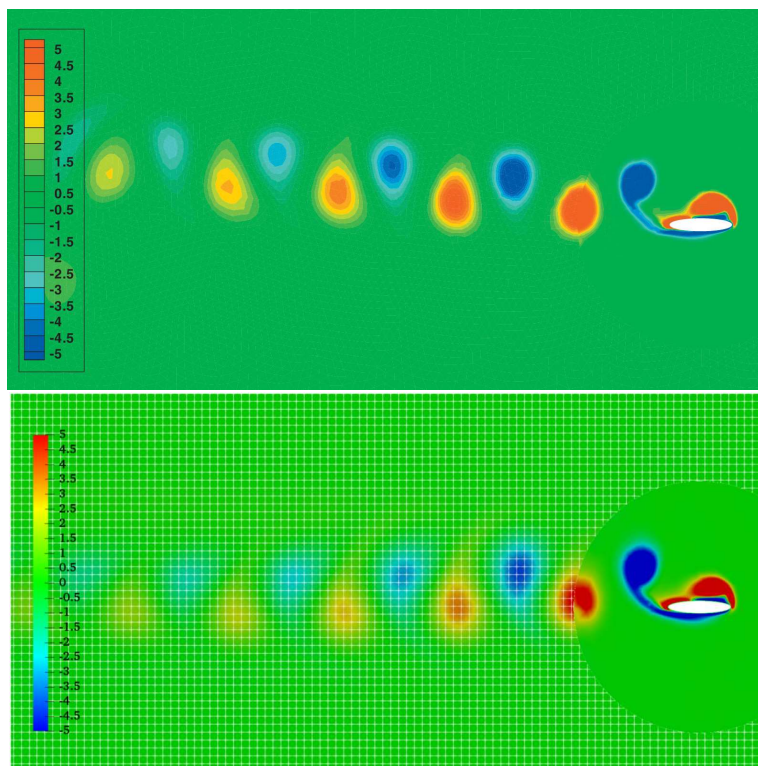


Figure 4-17. The reversed von Kármán vortex street behind the elliptic foil of  $CR = 5$  from the reference solution (top) and OpenFOAM simulations (bottom)

The unidirectional locomotion and the qualitative nature of the vortex structure in the case of  $CR = 15$  are similar to those of  $CR = 5$ , but the vortical structures propagating to the left are oblique (downwards in the present study) as the foil moves toward the right, as illustrated in Figure 4-18. Here, the OpenFOAM simulation results are in satisfactory agreement with results from the reference paper.

Figure 4-19 gives the nondimensional velocity histories of  $CR = 5$  and 15 within one oscillation period  $T$  during quasi steady state. Though the sinusoidal heaving motion of the elliptic foil is symmetric, the maxima and minima values are different in the two consecutive half periods.

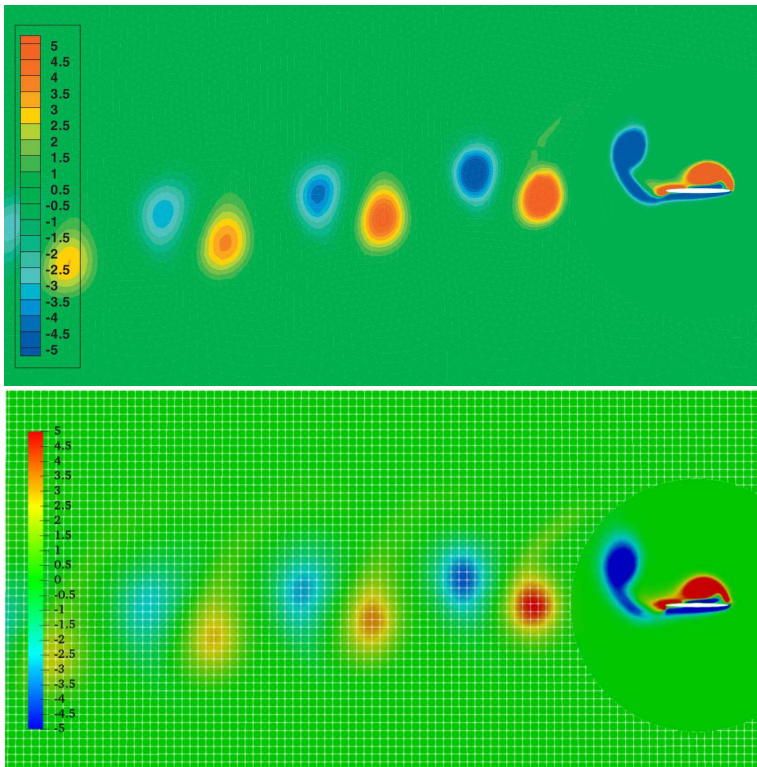


Figure 4-18. The reversed von Kármán vortex street behind the elliptic foil of  $CR = 15$  from the reference solution (top) and OpenFOAM simulations (bottom)

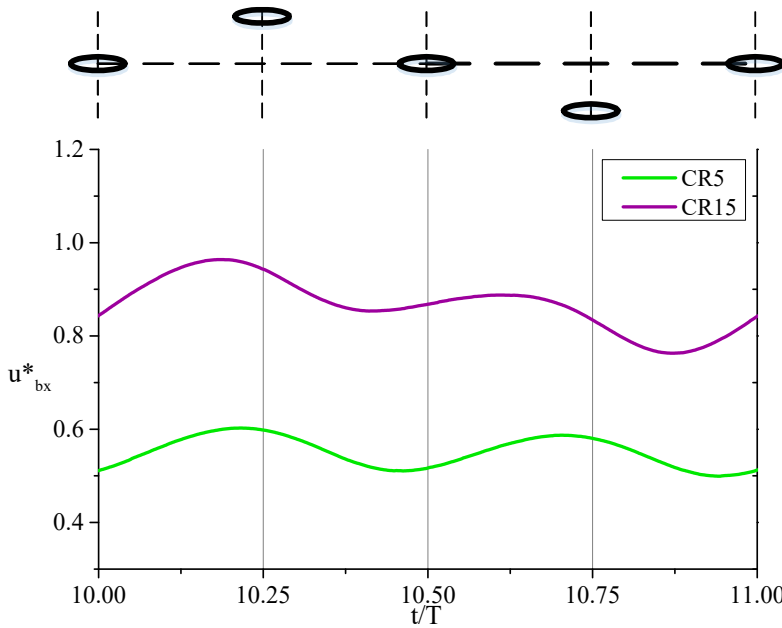


Figure 4-19. The horizontal velocities within one oscillation period at quasi steady state



A Fast Fourier Transform (FFT) technique is used to examine the time variation of the nondimensional horizontal velocity. A time interval of 5 oscillation periods during the quasi-steady-state region is analyzed and the results are shown in Figure 4-20. The nondimensional frequency of the foil heave motion is 1, and the dimensionless frequency of the oscillatory drag force caused by the alternate vortex shedding is expected to be 2. However, both foils are found to have another apparent frequency 1.

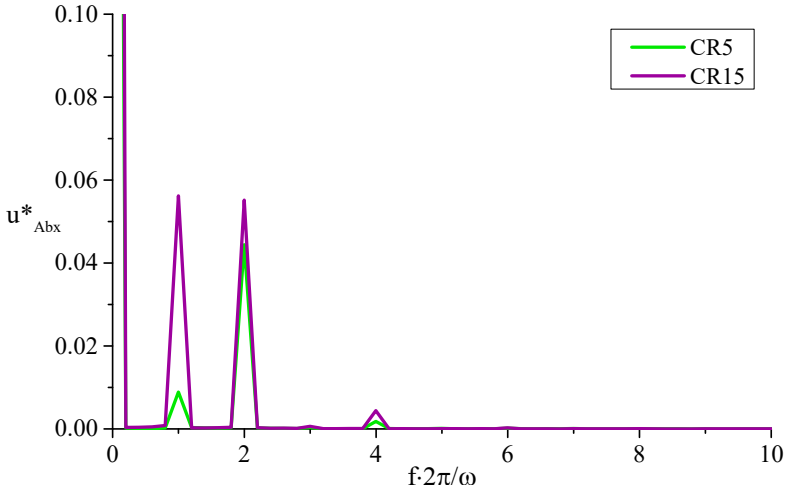


Figure 4-20. Fourier horizontal velocity amplitude spectra at quasi steady state

The multiple frequency content associated with the horizontal velocity history may be resulted from the asymmetric vortex shedding behind the foil. Figure 4-21 displays the instantaneous vorticity field of the elliptic foil  $CR = 15$  at four different states during one oscillation period illustrated in Figure 4-19.

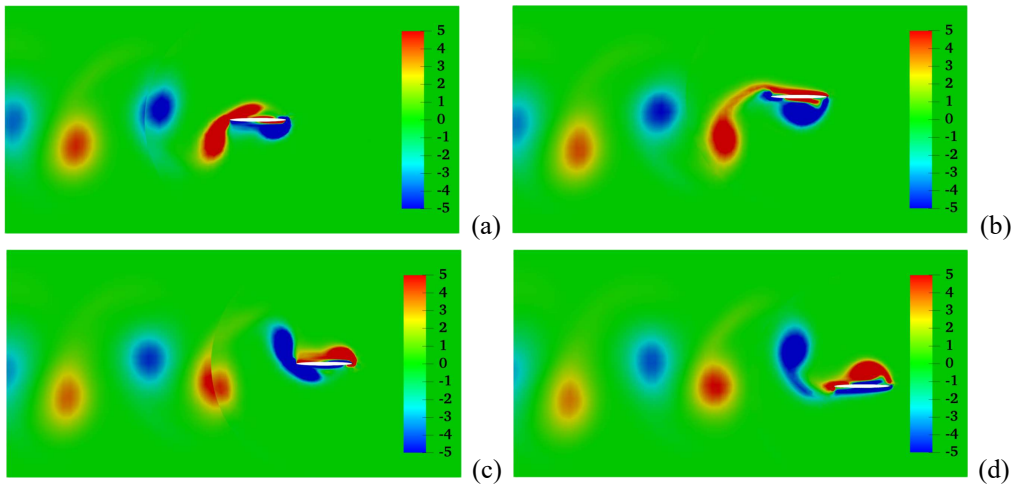


Figure 4-21. Instantaneous vorticity contours of the elliptic foil  $CR = 15$  at different positions during one oscillation period. (a)  $t/T = 10$ , (b)  $t/T = 10.25$ , (c)  $t/T = 10.5$ , (d)  $t/T = 10.75$

The overall consistency between numerical simulations and reference solutions demonstrate that the self-propulsion strategy implemented in OpenFOAM library is an effective method for studying body locomotion and the corresponding hydrodynamic forces acting on it. The comparisons in terms of velocity history and vortical structures indicate that the present method is able to capture the hydrodynamic details around the moving body with satisfactory accuracy and efficiency. In addition, the advantage and disadvantage of different types of grids (structured and unstructured mesh) have been discussed and it is suggested to choose a suitable one depending on specific cases. Various spatial and temporal discretization schemes have been examined in this verification case, and this can help in determining optimum solver settings for the further studies in chapter 6.

## 4.6 Summary

In this chapter, key aspects for numerical simulation methods have been introduced, with particular focus on numerical schemes adopted in OpenFOAM library as well as various dynamic mesh motion methods.

A numerical implementation to study self-propelled fish-like foil has been proposed. The strategy of the self-propulsion application is described in detail. The verification study case of an oscillating elliptic foil gives reasonable results and demonstrates the effectiveness of the proposed strategy. Herein, different mesh generation methods have been described and compared. The effect of different spatial and temporal discretization mesh has also been analyzed in the present verification study.

The theoretical and numerical methods introduced here are used as basis for the numerical investigations of the hydrodynamic problems in the following chapters.



## Chapter 5

# Flapping foil studies

The basis source of locomotion and manoeuvring forces of many swimming fishes is the control of vortices produced by their oscillating bodies and fins. In this chapter we are interested in the study of the propulsive performances of various flapping foils with different fish-like profiles: the tear-shaped foil introduced in chapter 4, two NACA geometries and a series of deformable NACA foils. Systematic numerical simulations are carried out in a uniform current under two-dimensional conditions, since the experimental studies performed by previous researchers reveal that a quasi-2D mechanism often contains key dynamical elements of most flapping foil systems. The results of the semi-circle foil are validated against reference experimental data, and the effect of various numerical setup parameters are also examined. Detailed investigations of the foils with different fish-like profiles are presented in terms of thrust force, propulsion efficiency and wake features. The critical Strouhal number at the drag-thrust transition at different Reynolds numbers is documented to explore the relationship between them. In addition, a morphing strategy is proposed to combine the advantages of the rigid foils with different shapes, that is, to maximize the mean thrust and efficiency while minimizing the required mean input power during the pitching motion.

As last note, the acronyms introduced in the previous chapter are directly used without explicit definition.

### 5.1 The models

For the flapping systems, either natural or man-made, a dimensionless parameter, the Strouhal number, defined as the product of the flapping frequency  $f$  and characteristic wake width  $A_w$  divided by the cruising speed  $U$ , i.e.,  $St_w = fA_w/U$ , is often employed to characterize the features of fish-like body generated wake and so the flow-induced force, with attention to the capability of thrust production. Laboratory and theoretical studies suggest the optimal propulsive efficiency of a flapping foil peaks within a narrow interval  $0.2 < St_w < 0.4$  (Read et al., 2003 and Anderson et al., 1998). Data collected by Taylor et al. (2003) indicate that this interval is consistent with the range adopted by many aquatic animals regardless of the sizes and species. However, it is apparent that foils with different profiles can perform oscillating motions with the same Strouhal number as long as their flapping configurations being the same. Less clear is the influence of the body shape on the flapping performance, their associated vortex signature in the wake, and the optimal choice for the configuration of foil kinematic and shape for efficient thrust generation.

In order to better understand the flapping performances of foils with different profiles in a

proper manner, three symmetric hydrofoils with the same chord length  $c$  are examined, as shown in Figure 5-1, and considered to experience forced pitching motions with the same pivot point (approximately  $0.11c$  behind the leading edge). The tear-shaped foil with a semicircular leading edge and a triangular section in the aft is adopted from the experiments performed by Godoy-Diana et al. (2008), as represented by the black line. The trailing edge of NACA 0012 foil is as sharp as the semi-circle foil, but its maximum thickness  $D$  is much smaller. In contrast, we selected NACA 0021 foil that has the same maximum thickness as the semi-circle foil, but it is thicker in the aft part.

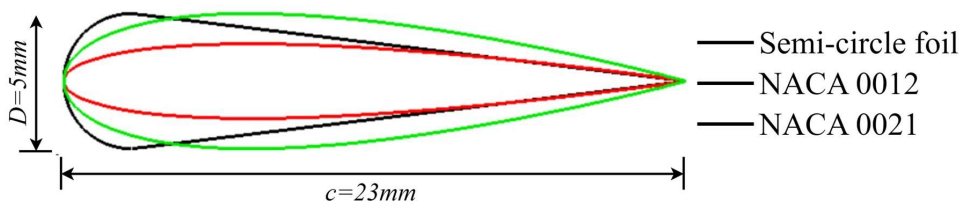


Figure 5-1. Schematic view of the examined fish-like foil profiles

The details of the three foil parameters are given in Table 5-1.

Table 5-1. Foil profile details

Foil	Semi-circle	NACA 0012	NACA 0021
chord length (mm)	23	23	23
maximum thickness (mm)	5	2.76	5
perimeter (mm)	49.16	46.9	48.38
cross-sectional area (mm <sup>2</sup> )	61	43	78

## 5.2 Numerical setup

Taking the semi-circle foil as an example, Figure 5-2 depicts the present hydrodynamic problem through the schematic of the foil motion and flow configuration. This numerical study is based on the pitching foil experiments carried out by Godoy-Diana et al. (2008) in a hydrodynamic tunnel, used here as reference data. The two-dimensional foil is placed in the uniform current with constant inflow speed  $U_c$  in the horizontal direction parallel to the  $x$ -axis. The flapping hydrofoil is forced to perform pitching motions in a sinusoidal pattern (about  $O$  and  $z$ -axis), and the angular motions are described by:

$$\theta(t) = \theta_0 \sin(\omega t) \quad (5.1)$$

Here  $\omega = 2\pi f = 2\pi/T$  is the foil forced-oscillation angular frequency, and  $\theta_0$  is the maximum pitching angle. The solid line of the foil in Figure 5-2 represents its equilibrium position, while the dashed lines represent the positions at the maximum rotation angles. The pivot center for the three foils keeps the same.

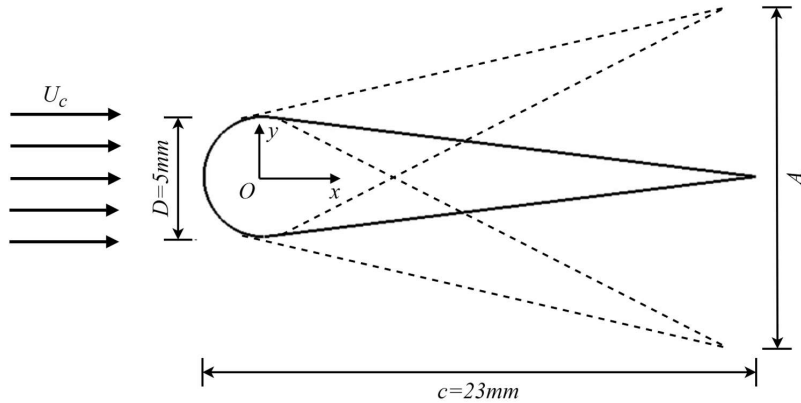


Figure 5-2. Schematic view of foil motion and flow configuration using the semi-circle foil

Defining the Reynolds number based on foil chord length, i.e.,  $Re_c = U_c c / \nu$ , its value was 1173 in the reference experiments (Godoy-Diana et al., 2008). Firstly, a set of numerical investigations is performed at this Reynolds number to be validated against the experimental results, and then, the kinematic viscosity of fluid is varied to change  $Re_c$  from 500 to about 4000 in order to study its influence on the optimal flapping characteristics and on the performance.

Other important parameters introduced here are the nondimensional flapping amplitude and a sort of Strouhal number defined by Godoy-Diana et al. (2008), respectively, as  $A_D = A/D$  and  $Sr = fD/U_c$ , with  $A$  the prescribed peak-to-peak amplitude (see sketch in Figure 5-2). In the following, the pitching hydrofoils are studied in the parameter region of  $0.1 < Sr < 0.5$  and  $0.36 < A_D < 2.14$ , covering the wake scenarios from von Kármán (vK) wake, reverse von Kármán (reverse-vK) wake to asymmetry wake regimes. As noted earlier in the text, flapping foils creating the optimal propulsive efficiency and a wide range of cruising fishes are discovered to lie in a narrow interval  $0.2 < Sr_A = fA/U_c < 0.4$  by laboratory and theoretical studies. This region will also be the focused part in our investigations.

Within these parameter regimes, previous studies (eg., Godoy-Diana et al., 2008; Deng and Caulfield, 2015) found that although three-dimensionality can be important in many cases, a quasi-two-dimensional (quasi-2D) picture of the wake often contains key dynamical elements that are crucial for every flapping foil system, which is closely related to practical engineering problems. In addition, the forces acting on the 2D hydrofoils indicate that they are comparable to those on three-dimensional (3D) foils in terms of values and evolutions at low Reynolds number (Morange et al., 2016). Therefore, 2D simulations are carried out in the present flapping foil simulations to explore the mechanisms of wake transitions and propulsive forces, which are also consistent with the reference experimental study by Godoy-Diana et al. (2008).

The numerical methods described in chapter 4 are used here with the assumption of viscous flow, without turbulence-flow model and in two-dimensional conditions. The resulting model

corresponds to a direct numerical simulation (DNS) for laminar flow if the used discretization can capture the physics of the problem. For the examined foil case, the flow is laminar close to the body while transition to turbulence can happen in the far field. In this context, one should note that turbulence leads, in a real environment, to three-dimensional features. It means that, even though we were able to capture the small scale of the turbulence in the far field, we would not be able to capture its evolution in proper way (direct energy cascade in 3D, inverse energy cascade in 2D), so including a turbulent-flow model within a 2D-flow assumption would not lead to an improvement. Besides, far-field turbulence induces an additional viscosity (eddy viscosity) which could be included in the fluid to emulate the diffusion effects. The comparison against the experiments (in terms of local and global quantities) can help in quantifying the importance of this possible error source in the numerical model.

The 2D computational domain around the flapping foil is defined by a rectangle extending 5.2 chords upstream and 6.5 chords downstream. The domain transverse dimension (i.e., in the  $y$  direction) is set to  $-3.26c < y < 3.26c$ , which is the same as the tunnel width in experiments. Numerical simulations illustrated that such dimensions are sufficient to have negligible boundary effects on the foil wake and flow-induced loads. Boundary conditions and the reference system for this hydrodynamic problem are shown in Figure 5-3. A no-slip condition is enforced along the flapping foil. Slip conditions are applied to the top and bottom domain boundaries, i.e., only velocity in the  $y$ -direction is enforced to be zero along these boundaries. A uniform inflow condition is enforced at the inlet while a uniform pressure condition is used at the outlet. Herein, to avoid a break-down at the beginning of the numerical simulations, we adopted a sinusoidal ramp function within the first second starting from zero to a desired constant velocity ( $U_c = 51\text{mm/s}$  in the study reproducing the experiments by Godoy-Diana et al., 2008) for the inlet. The boundary conditions in the third direction ( $z$  direction) for all variables are set to be empty as none of them are solved consistently with the two-dimensional flow assumption. For the interpolation layer in the overset mesh, an additional boundary condition named “overset” is provided in the OF solver.

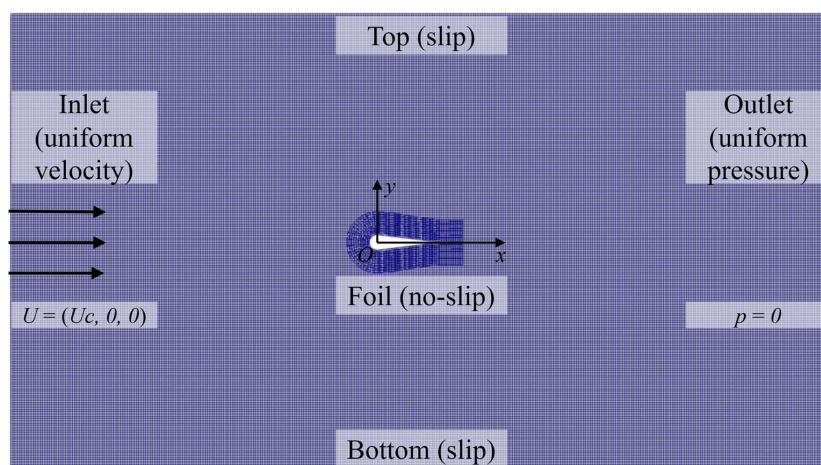


Figure 5-3. Schematic view of computational domain with reference system and parameters definition. An example of the two grids (body-fixed and background grids) of the overset strategy are also shown

### 5.3 Assessment studies of the semi-circle foil

The semi-circle pitching foil is simulated at  $Re_c = 1173$ ,  $Sr = 0.22$  and  $A_D = 0.36, 0.71, 1.07, 1.77$  to validate the numerical model adopted. Here, the simulation results are compared against the reference experiments (Godoy-Diana et al., 2008) in terms of instantaneous spanwise vorticity fields, mean flow near the semi-circle foil and hydrodynamic force coefficients.

In addition to the comparison with physical experiments, we also put focus on studying the effect of various numerical parameters on local and global phenomena of the pitching foil. The dynamic mesh and overset grid methods introduced in chapter 4 are discussed for this basis case. The effects of time schemes, grid resolution, overset region size and mesh ratio between overset and background mesh are documented for the overset grid technique. Cost-benefit analysis is also discussed, wherever necessary, in terms of error with respect to the experiments, computational effort/time required, complexity in mesh generation, etc.

#### 5.3.1 Influence of mesh motion methods

The structured grid is employed for both deforming mesh method (DM) and overset grid method (OG) grids as, based on the gained experience, it often brings about a better force prediction and captures wake features better than the unstructured mesh in this flapping foil study. A C-type grid is generated by means of the commercial software ICEM around the hydrofoil for the morphing mesh case. In the OG case, the two-dimensional grid used to discretize the flow domain close to the flapping foil (overset grid) is also generated by ICEM and the background grid by the corresponding library included in the OpenFOAM platform. Due to the use of a linear interpolation between grids, the overset mesh is constructed so that the outermost layer of the moving mesh has comparable cell size as the background (BG) grid. Figure 5-4 illustrates the C-type DM grid and the body-fitted overset grid applied for the semi-circle foil.

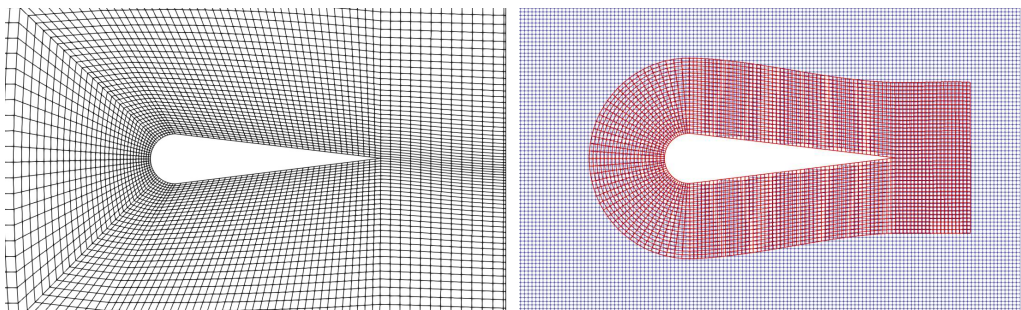


Figure 5-4. Local structured grids generated by ICEM for the flapping foil. Left: DM; Right: OG

To better investigate the effect of different mesh motion strategies on simulation results, a similar discretization size should be used for the C-grid close to the foil and for the overset mesh. In this way, a mesh with 22800 structured hexahedral cells is selected for the DM case, meanwhile, the OG case has 3640 hexahedral cells in the overset region and 288000 structured cells for the background mesh ( $\Delta x = \Delta y = 0.0163c$ ).



Figure 5-5 presents the qualitative comparisons for instantaneous vorticity field and time-averaged flow velocity between the OF simulations with OG and the experiments for the case performed at  $Re_c = 1173$ ,  $Sr = 0.22$  and  $A_D = 0.71$ , corresponding to an intermediate oscillation amplitude among those examined. The contour legends represent the vorticity intensity and velocity magnitude, respectively, in the top and bottom figures. Euler method is used as temporal scheme and the ratio of outermost cell size of the overset grid to the background grid size (i.e., the mesh ratio) is 1. The time step is  $0.0025s$  to ensure that the maximum Courant number is less than 1 for these dynamic simulations. In this case, the oscillating foil should lead to a scenario where vortices of alternating signs align on the symmetry line of the wake (aligned wake) and to a time-averaged drag force on the foil according to the experiments (Godoy-Diana et al., 2008). We observe a reasonably similar behavior from the figures. The numerical simulation can capture the aligned vortex street and the time-averaged velocity field quite well. The intensities of vortices in the downstream of the physical foil are slightly smaller than the experimental data. It may be due to the time/space discretization causing diffusion or because of the linear interpolation scheme between overset and background grids. The mean horizontal velocity behind the foil is lower than the inlet velocity  $U_c$  in this case and leads to a mean drag force, which is consistent with the experiments.

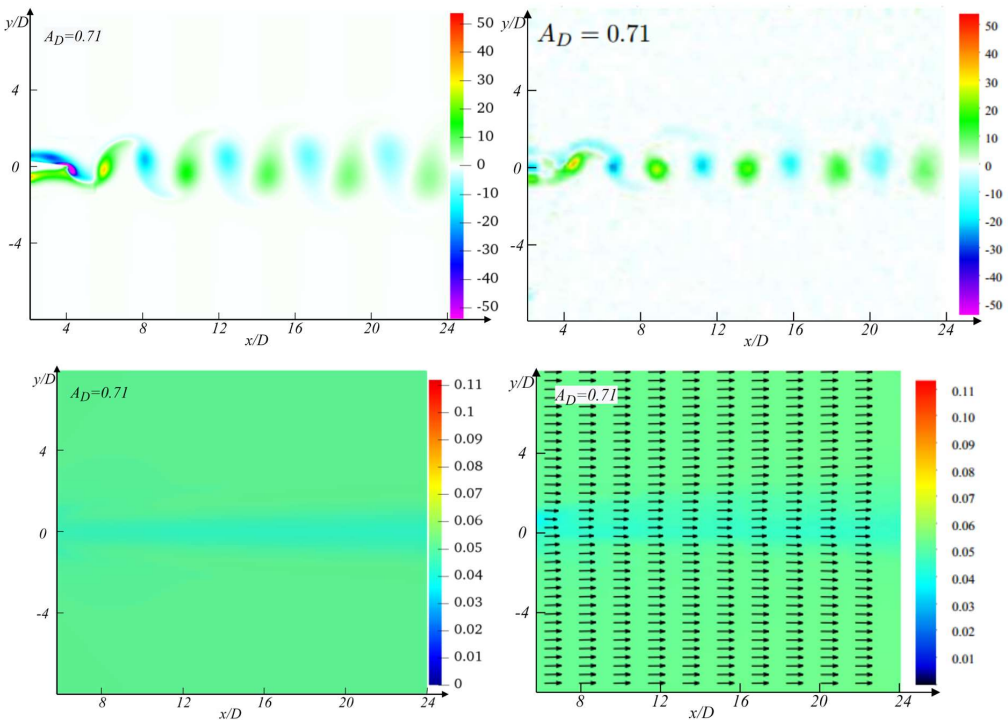


Figure 5-5. Instantaneous spanwise vorticity fields at the instant  $t = 20.5s$  (top) and time-averaged flow velocity (bottom) of the semi-circle foil at  $Re_c = 1173$ ,  $Sr = 0.22$  and  $A_D = 0.71$  from OF with OG (left) and experiments (right)

Figure 5-6 shows the instantaneous spanwise vorticity fields for the same case using DM and OG techniques, respectively, with the same scale of the vorticity contour levels. There is nearly a discontinuity for the overset grid near the outermost cell layer because of the interpolation between the overset and background grid, which can be found around the foil and the latest shedding vorticity from the trailing edge. From comparisons between DM and OG at the equilibrium pitching state, we find that their behaviors are similar, but the intensity of vorticity is apparently lower for the deforming mesh, especially close to the foil. In addition, due to mesh deformation, the detailed vortex structure for the DM case is not as well captured as for the overset case, indicating that the deforming mesh method may lead to numerical diffusion. The mean velocity fields show that the velocity deficit in the wake profile is almost completely erased in the DM case while we can still see the mean velocity along the centerline is slightly reduced in the OG case and the experiments in Figure 5-5. It confirms again that higher diffusion occurs for the DM case.

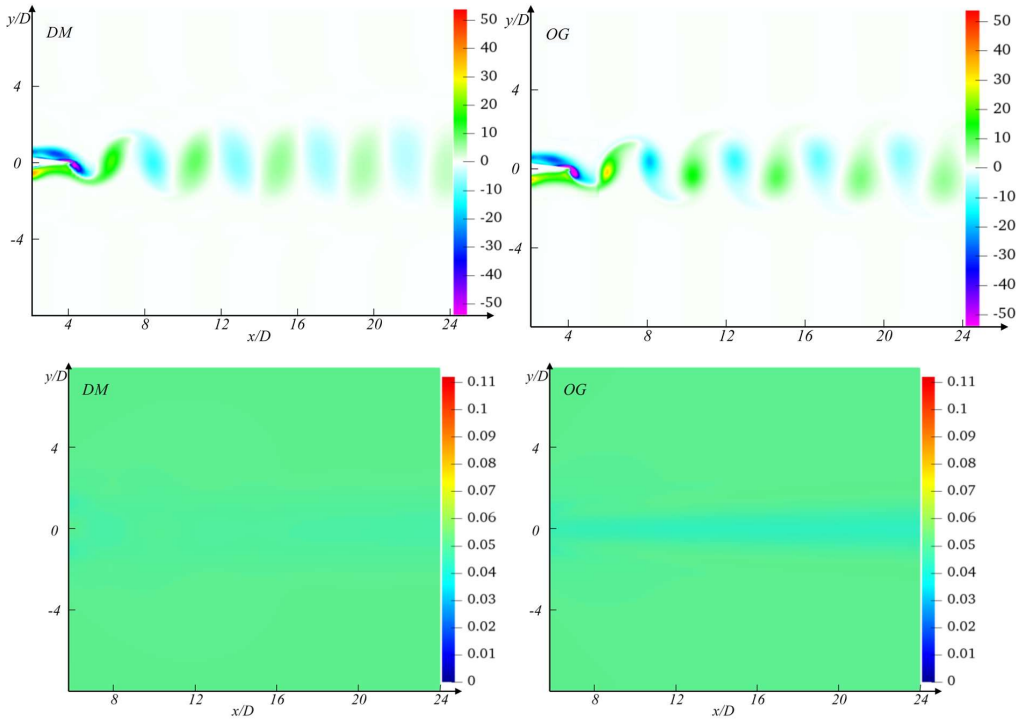


Figure 5-6. OF vorticity field at the instant  $t = 20.5s$  and time-average velocity of the semi-circle foil at  $Re_c = 1173$ ,  $Sr = 0.22$  and  $A_D = 0.71$  with DM and OG methods

The global effect of these mesh motion strategies is then examined for this case in terms of the horizontal and vertical force coefficients. The two coefficients are defined by the following equations, respectively:

$$C_x = \frac{F_x}{\frac{1}{2}\rho U_c^2 c} \quad (5.2)$$

$$C_y = \frac{F_y}{\frac{1}{2}\rho U_\infty^2 c} \quad (5.3)$$

Here  $\rho$  is the density of the fluid. Based on this definition and the reference system introduced in Figure 5-3, the foil experiences thrust when  $C_x < 0$  and drag when  $C_x > 0$ .

Figure 5-7 shows the results for the two mesh motion types with Euler temporal scheme and same time steps. As expected, the  $C_x$  frequency is twice the  $C_y$  frequency  $f$ . DM gives a much smoother behavior. One reason can be that the linear interpolation between grids in OG requires a smaller time step. Also, the crests have slightly larger values for OG, which might be due to finer mesh in the wake region or less diffusion effect in the OG method. The time-averaged value of  $C_x$  for the DM and OG cases are 0.115 and 0.119, respectively. The experimental value extracted from the reference paper (Godoy-Diana et al., 2008) is about 0.119, and the estimation method used will be explained in section 5.4.2. Therefore, the OG method is considered to give more accurate results.

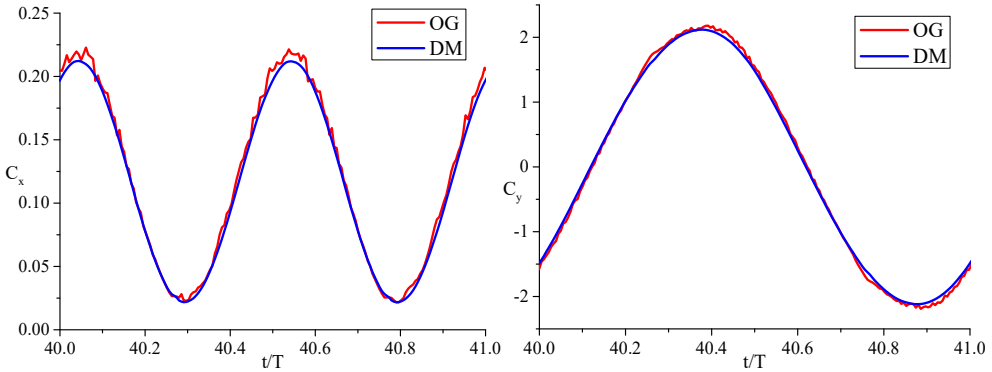


Figure 5-7. Horizontal (left) and vertical (right) force coefficients of the semi-circle foil at  $Re_c = 1173$ ,  $Sr = 0.22$  and  $A_D = 0.71$  vs time for DM and OG methods

Since the OG method can capture more localized wake features and its predicted hydrodynamic forces are consistent with the DM approach, it is selected for the rest of numerical simulations, including foils with larger flapping motions where OG is able to avoid severe mesh deformation problems.

### 5.3.2 Influence of overset region size

The size of the foil-fitted overset grid region could also affect the local and integrated predictions. Here, the dependence of the simulation results on the overset domain size has been assessed in the semi-circle foil case. The distance from the foil profile to the overset boundary is set to three different values:  $0.20c$  (labelled as small region),  $0.33c$  (labelled as medium region) and  $0.72c$  (labelled as large region), as shown in Figure 5-8. Although the overset domain size varies, the mesh size in these three cases remains the same, meaning that the cell number of the overset region increases with the expansion of the domain size. Therefore, the elements number and size within the background grid ( $\Delta x = \Delta y = 0.0326c$ ) keep the same in the simulations.

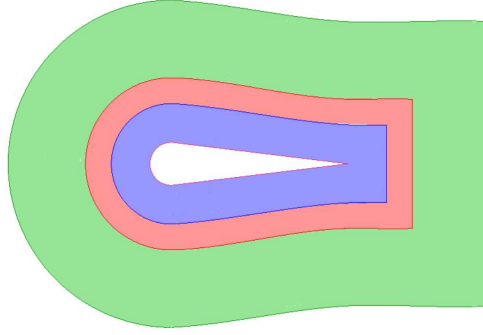


Figure 5-8. Schematic view of three overset grids with different extensions

In the following validation studies of section 5.3, the semi-circle pitching foil oscillating at  $Re_c = 1173$ ,  $Sr = 0.22$  and  $A_D = 1.77$  is examined (herein named as basis case) because it is expected to experience the largest variation of hydrodynamic loads during the pitching motion. The time histories of the horizontal force coefficient for the flapping foil from the three simulations are shown in Figure 5-9. It is found that the results obtained using the small oveset domain (small region) case are not as smooth as the others, but the mean values agree well.

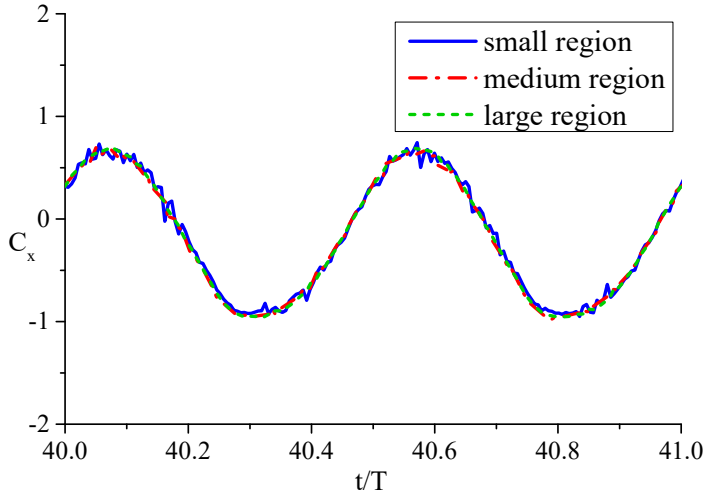


Figure 5-9. Basis case: horizontal force coefficient vs. time for three overset domain sizes

The latter can be estimated as time-averaged values of the horizontal force; similarly one can do for the mean values of the force coefficient, i.e., as:

$$\bar{F}_x = \frac{1}{nT} \int_{t_0}^{t_0+nT} F_x(t) dt \quad (5.4)$$

$$\bar{C}_x = \frac{1}{nT} \int_{t_0}^{t_0+nT} C_x(t) dt \quad (5.5)$$

Here  $T$  is the foil oscillation period, as previously defined,  $n$  is a positive integer, and the initial time instant  $t_0$  is chosen as a time instant after the numerical results reached nearly steady-state conditions.

The time-averaged horizontal force coefficient during ten flapping periods ( $n = 10$ ) and the computational time for a simulation of 20s (about 45 periods) for the three cases are documented in Table 5-2. Following these numerical tests, unexpectedly the medium size of overset region costs the least time. A possible reason could be that in the examined small-region case the fringe and donor cells from the background mesh to the overset mesh, and vice versa, would get very close, thus leading to interpolation issues. Because the medium size of overset region also gives predictions comparable to the case with thicker overset domain, it is applied in the following for the rest of simulations after the cost-benefit analysis.

Table 5-2. Basis case: horizontal force coefficient and computational time for a simulation of 20s ( $= 44.88T$ ) as a function of the overset region size

Overset-domain size	0.20c	0.33c	0.72c
$\overline{C_x}$	-0.168	-0.177	-0.181
Computational time (s)	1920	1902	1924

### 5.3.3 Influence of mesh ratio between overset and background grids

The ratio of cell size between background ( $\Delta x$ ) and overset ( $\Delta x'$ ) grids also plays a role in affecting the accuracy of numerical results. The mesh ratio is defined as:

$$r_m = \frac{\Delta x}{\Delta x'} \tag{5.6}$$

In the analysis of the mesh-ratio effect in terms of  $C_x$ , the Euler scheme is used for temporal discretization and the results are presented in Figure 5-10 and Table 5-3. Because OF allows only linear interpolation between grids in OG, it is important to keep the interpolation layer of the overset grid with very similar size as the background grid. This may lead to high computational costs and mesh generation issues sometimes but seems to give the most reliable results.

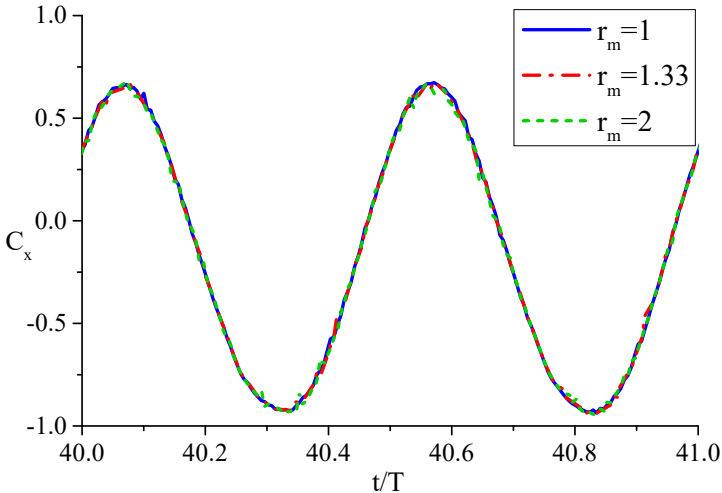


Figure 5-10. Basis case: horizontal force coefficient for three mesh ratios

Table 5-3. Basis case: horizontal force coefficients and computational time for a simulation of 20s (= 44.88T) as a function of the mesh ratio

$r_m$	$\bar{C}_x$	Computational time (s)
1	-0.172	10603
1.33	-0.174	4975
2	-0.177	2135

### 5.3.4 Grid convergence analysis

To confirm the spatial convergence of the overset grid method for the examined case, an extensive analysis on grid resolutions with the corresponding boundary conditions has been performed. In particular, Figure 5-11 shows the time-dependent horizontal force coefficient for the flapping foil in the basis case and using three discretizations labelled as Grid 1 to 3.

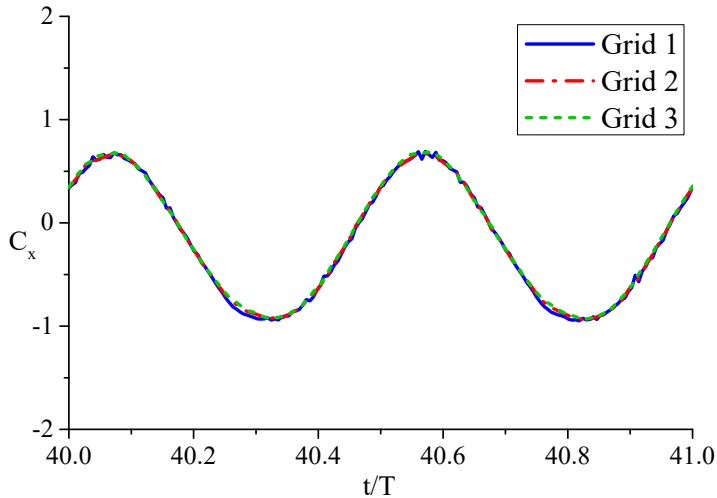


Figure 5-11. Basis case: horizontal force coefficient vs. time for three different grid resolutions

They are made of structured hexahedral cells and are defined in Table 5-4. The results obtained by the examined grid sizes agree well with each other except for slight differences between the results from Grid 1 and those from the other grids around minimum values.

Table 5-4. Basis case: three grid resolutions for the flapping foil

	Grid 1	Grid 2	Grid 3
Nodes along foil	120	142	164
Cells in BG grid	162,000	288,000	450,000

The time-averaged horizontal force coefficients and the dimensionless time-averaged streamwise velocity ( $\bar{u}/U$ ) along the wake centerline at  $x/D = 6$  obtained with the three discretizations are documented in Table 5-5.

Table 5-5. Basis case: time-averaged horizontal force coefficients and velocity along wake centerline for the flapping foil for the grids defined in Table 5-4

Discretization	Grid 1	Grid 2	Grid 3
$\overline{C_x}$	-0.182	-0.172	-0.164
$\overline{u}/U$ at $x/D = 6$	1.878	1.967	1.968

The corresponding flow structures have been also carefully studied. Figure 5-12 illustrates the instantaneous vorticity contours at  $t = 20.6s$  ( $t/T = 46.226$ , i.e., about to reach the extreme inclined positions) for the three grid discretizations. The peak values of the vorticities in the wake are labelled to show the convergence. As the second-order spatial discretization is employed in the present simulations, the order of accuracy (OA) of the numerical results is expected to be two. From the results in Figure 5-12, the order of accuracy for the negative and positive vorticity intensities are estimated as 1.7 and 3.5, respectively, according to the procedure documented for instance by Colicchio et al. (2005). Based on these results, as compromise between local accuracy and efficiency, Grid 2 is employed for all the further simulations discussed in the present study.

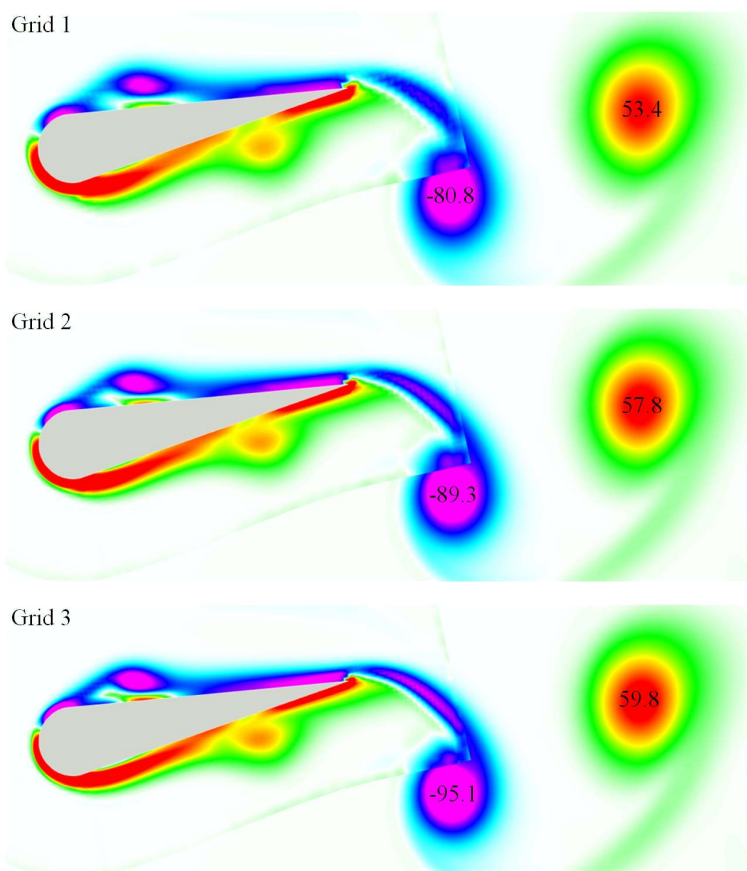


Figure 5-12. Basis case: instantaneous vorticity contour for three grids at  $t = 20.6s$ . The red and purple colors stand for positive and negative vorticities, respectively. Peak values of the vorticities in the wake are marked

### 5.3.5 Influence of time discretization

In the present simulations, a first order implicit Euler scheme, a second order implicit backward scheme and a second order Crank-Nicolson scheme have been adopted to examine the effect of different time-evolution schemes. The time step is  $0.0025s$  and the maximum Courant number is less than 1 for all the cases. The comparisons of the numerical results obtained using different time schemes are shown in Figure 5-13. It is obvious that the Crank Nicolson (CN) method with an under-relaxation value of 0.7 produces some spikes both in  $C_x$  and  $C_y$  in this flapping foil case. The backward scheme is closer to the Euler method and both are much smoother compared to CN method.

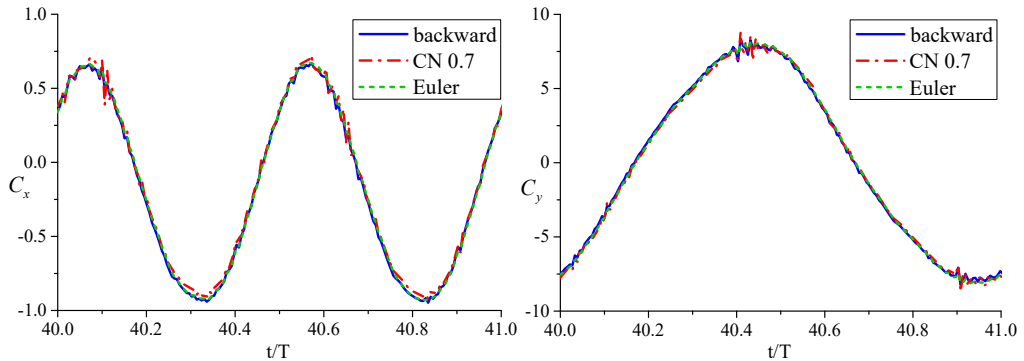


Figure 5-13. Basis case: horizontal (left) and vertical (right) force coefficients for different time discretization schemes

Table 5-6 discusses the average values of  $C_x$ , i.e.,  $\overline{C_x}$ , during ten oscillation periods and the computational time for a simulation of  $20s$  ( $t/T = 44.88$ ) obtained using different numerical time schemes. Negative value of  $\overline{C_x}$  indicates thrust, which was the aim of the flapping foil studies. In general, all cases show similar results for  $\overline{C_x}$ . The computational times show more variation and a difference of 23% (with respect to the result of CN 0.7) is observed. As compromise between local accuracy and efficiency, the Euler scheme is employed for all the rest of simulations in this chapter. This validation study is useful to identify the solution sensitivity to the numerical parameters for a submerged foil case. Though, it may not be applicable to all cases in general.

Table 5-6. Basis case: horizontal force coefficients and computational time versus time schemes

Time scheme	$\overline{C_x}$	Computational time (s)
backward	-0.180	9933
CN 0.7	-0.159	12863
Euler	-0.172	10603

## 5.4 Results and discussion

The validation studies performed in the previous section are used as basis for the discretization and mesh strategy of the three hydrofoil models defined in section 5.1, which are examined



comparatively in the following. The flapping amplitude and Strouhal number are varied so to characterize the vorticity regimes in the foil-generated wake at different Reynolds numbers.

### 5.4.1 Instantaneous thrust and power

During the forced pitching motion, the hydrofoil is aligned with the inflow at  $\omega t = n\pi$  and reaches the extreme inclined positions at  $\omega t = n\pi + \pi/2$  (maximum rotation to the top) and  $n\pi + 3\pi/2$  (maximum rotation to the bottom). In order to investigate in which phase of the prescribed motion the hydrofoil generates the maximum thrust force and in which phase it requires the highest power input, as well as checking any possible link between these two phases, the instantaneous horizontal force and power must be estimated as a part of the analysis. Both direct integration (DI) method and conversation of fluid momentum (CFM) method can be employed for predicting hydrodynamic forces. Their comparison is documented in Appendix B for the foil cases and identifies challenges for the CFM method when using overset grid strategy in OpenFOAM. Considering the computation accuracy and efficiency, the numerical results presented in the following sections are obtained by DI method.

The mechanical power required to activate the foil, or input power  $P$ , in the pitching foil case is calculated by Eqs. (5.7) and (5.8):

$$P = M_z \dot{\theta} \quad (5.7)$$

$$\dot{\theta}(t) = \omega \theta_0 \cos(\omega t) \quad (5.8)$$

where  $M_z$  is the torque experienced by the hydrofoil. We then define the input power coefficient  $C_p$  as

$$C_p = \frac{P}{\frac{1}{2}\rho U^3 c} \quad (5.9)$$

Based on this definition, the foil requires input power when  $C_p < 0$  and conversely when  $C_p > 0$ .

With the objective of understanding the relationship between flapping kinematics ( $A_D$  and  $Sr$ ) and the hydrodynamic force, the prediction of the instantaneous force is firstly examined by four cases with varying  $A_D$  at  $Re_c = 1173$  and  $Sr = 0.22$ , as documented in Table 5-7, which are the flapping conditions of the experiments carried out by Godoy-Diana et al. (2008).

Table 5-7. Same flapping frequency cases for the semi-circle foil

	$Sr$	$A_D$	$Sr_A$
Case 1	0.22	0.36	0.0792
Case 2	0.22	0.71	0.1562
Case 3	0.22	1.07	0.2354
Case 4	0.22	1.77	0.3894

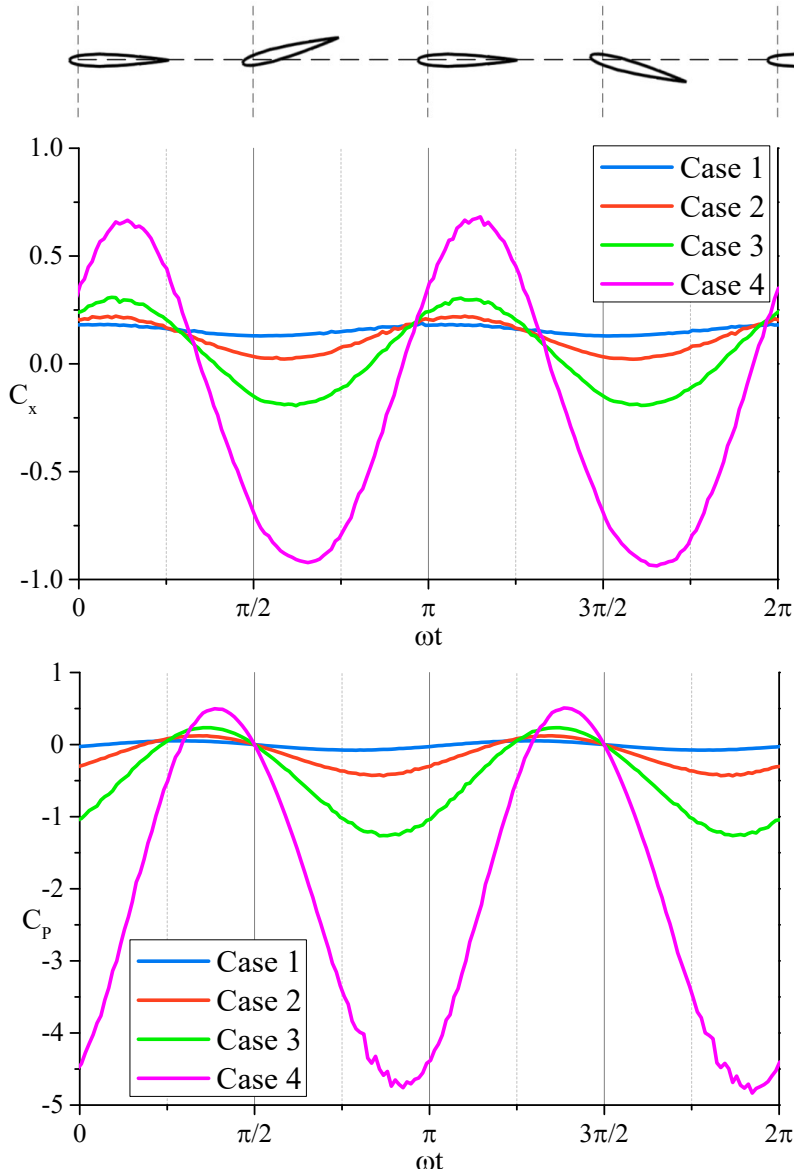


Figure 5-14. Instantaneous horizontal force coefficient and input power coefficient for the semi-circle foil in same flapping frequency cases. Case 1-3: drag; Case 4: thrust

Figure 5-14 shows the time histories of the horizontal force coefficient (as defined in Eq. (5.2)) and power coefficient within one complete oscillation period for the above cases. Their  $C_x$  and  $C_p$  are periodic with a period half of the pitching period. This is expected for the horizontal force as in steady-state conditions: due to the symmetry of the foil and of the rotation with respect to the  $x$ -axis, it is not sensitive if the foil is at a positive or negative rotation angle. When the semi-circle foil moves from the mean to the extreme top position, as presented in Figure 5-14, both  $C_x$  and  $C_p$  experience an increasing trend and reach the first maximum

around  $\pi/8$  and  $3\pi/8$ , respectively. With the increase of the  $A_D$ , the oscillation amplitude of  $C_x$  increases monotonously. For Case 1 and 2, the values of horizontal force are always positive and thus leading to drag force during the whole pitching period.  $C_x$  of Case 3 starts to have negative value but it remains positive for the most of period. In Case 4, the horizontal force becomes negative for more than half of the period and its absolute value of minimum  $C_x$  is obviously larger than the maximum value. Therefore, the mean horizontal force corresponds to a thrust only in Case 4. The details of the time-averaged forces and comparison with experiments can be found in section 5.4.2 and in Xu et al. (2022). The same tendency can be observed for the  $C_p$  with  $A_D$ : as the foil flapping amplitude increases,  $C_p$  experiences larger oscillation amplitude. The semi-circle foil needs very little input power in Case 1 and 2, and it requires more and more power to perform the large pitching motion in Case 3 and 4. However, the positive value of  $C_p$  also increases with  $A_D$ , which means that more power can be extracted by that foil when performing larger flapping motion within the corresponding time interval. In general, both the horizontal force and input power have larger oscillation amplitude when the Strouhal number  $Sr_A$  ( $A_D$ ) increases. The force transits from drag-type to thrust-type and more mechanical power is needed at higher  $Sr_A$  ( $A_D$ ).

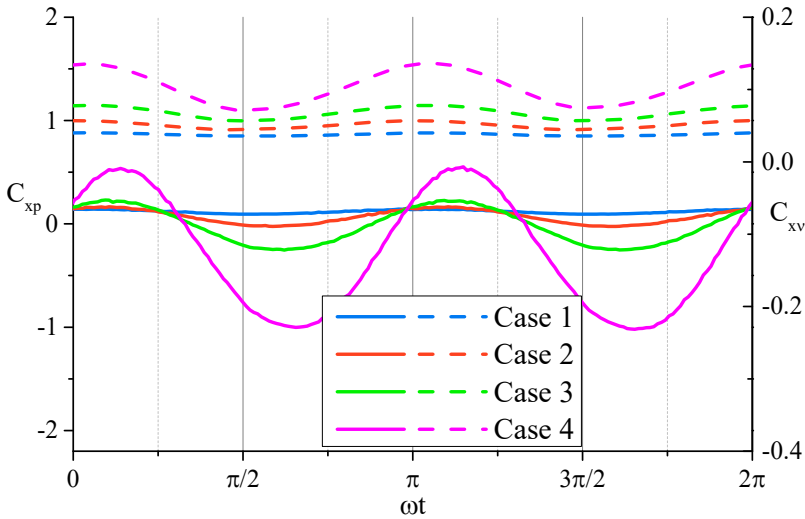


Figure 5-15. Instantaneous pressure (solid line) and friction (dash line) components of the non-dimensional horizontal force for the semi-circle foil in the same flapping frequency cases. Case 1-3: drag; Case 4: thrust

The horizontal force experienced by the hydrofoil can be divided into the pressure component and friction component,

$$F_x = F_{xp} + F_{xv} \quad (5.10)$$

where  $F_{xp}$  and  $F_{xv}$  are the pressure and friction horizontal forces, respectively. Figure 5-15 shows these two components of the horizontal force in terms of coefficients  $C_{xp} = F_{xp}/0.5\rho U^2 c$  and  $C_{xv} = F_{xv}/0.5\rho U^2 c$  for the four examined cases of the semi-circle foil. The two components experience larger oscillation amplitudes with the increasing  $A_D$ , consistently with the time history of the total force  $C_x$ . As expected, the friction force  $C_{xv}$

(dash line) is always positive during the pitching motion despite the varying  $A_D$ . The pressure force  $C_{xp}$  remains all the time positive for Case 1 and 2, and then has negative values in Case 3 and 4. These negative pressure forces counteract with the positive  $C_{xp}$  and  $C_{xv}$ , and are the main contributions to the time-averaged thrust force experienced by the foil.

It should be noted that the flapping frequencies are the same in the above examined cases. In order to investigate the hydrodynamic loads of the semi-circle foil with various  $Sr$  and  $A_D$ , and identify if they can possess any similar load behavior under totally different kinematic conditions, three representative cases at  $Re_c = 1173$ , as documented in Table 5-8, are examined. Here case 5 and case 6 correspond to drag generation and thrust generation, respectively, and the case 7 corresponds to the drag-thrust transition.

Table 5-8. Representative cases for the semi-circle foil

	$Sr$	$A_D$	$Sr_A$
Case 5	0.15	1.07	0.1605
Case 6	0.22	1.25	0.275
Case 7	0.30	1.42	0.426

Figure 5-16 shows the time histories of the horizontal force coefficient and power coefficient within one complete oscillation period for the semi-circle foil in three representative cases. It is found that despite the different pitching frequency and amplitude, when the semi-circle foil moves from the mean to the extreme top position, both  $C_x$  and  $C_p$  experience an increasing trend and reach the first maximum around  $\pi/8$  and  $3\pi/8$ , respectively. Alam and Muhammad (2020) and Andersen et al. (2017) presented  $C_x$  histories for various Strouhal numbers and pitching amplitudes at  $Re_c = 920$  and  $2640$ , respectively. Their numerical simulations also show that the thrust is minimum when  $\omega t \approx \pi/8$  and maximum at  $\omega t \approx 5\pi/8$ , which are consistent with the present results.

$C_p$  is positive for  $\omega t = (\pi/4 : \pi/2)$ , indicating that the foil does not require power for movement during this time interval. According to the time history of the input power coefficient, an increasing power is needed to move the foil from the extreme top position toward the mean position, i.e., within  $\omega t = (\pi/2 : 7\pi/8)$ . This behavior of the pitching foil is quite different from that of the same foil at rest in its extreme position, which is suddenly released while interacting with the steady inflow. In the latter case, the foil is expected to move towards the mean position without requiring any power. This suggests that dynamic and memory effects connected with vortex shedding are quite important in the examined scenarios. In addition, for the pitching foil, it is estimated that the maximum power is required immediately after  $\omega t = 7\pi/8$ , i.e., just before reaching the mean position. After that the foil requires less and less power until  $\omega t \approx 11\pi/8$ , i.e., just before the extreme bottom position.

The comparison between the instantaneous force and power coefficients reveals that there is a relationship between  $C_x$  and  $C_p$ . The inflection point of the  $C_p$  curve, near  $\omega t = 5\pi/8$ , synchronizes with the maximum thrust force, i.e., minimum  $C_x$ . The inflection point of the  $C_p$  curve near  $\omega t = 9\pi/8$  is simultaneous with the maximum  $C_x$ , which is also consistent with

the experimental and numerical work of Andersen et al. (2017) and Alam and Muhammad (2020).

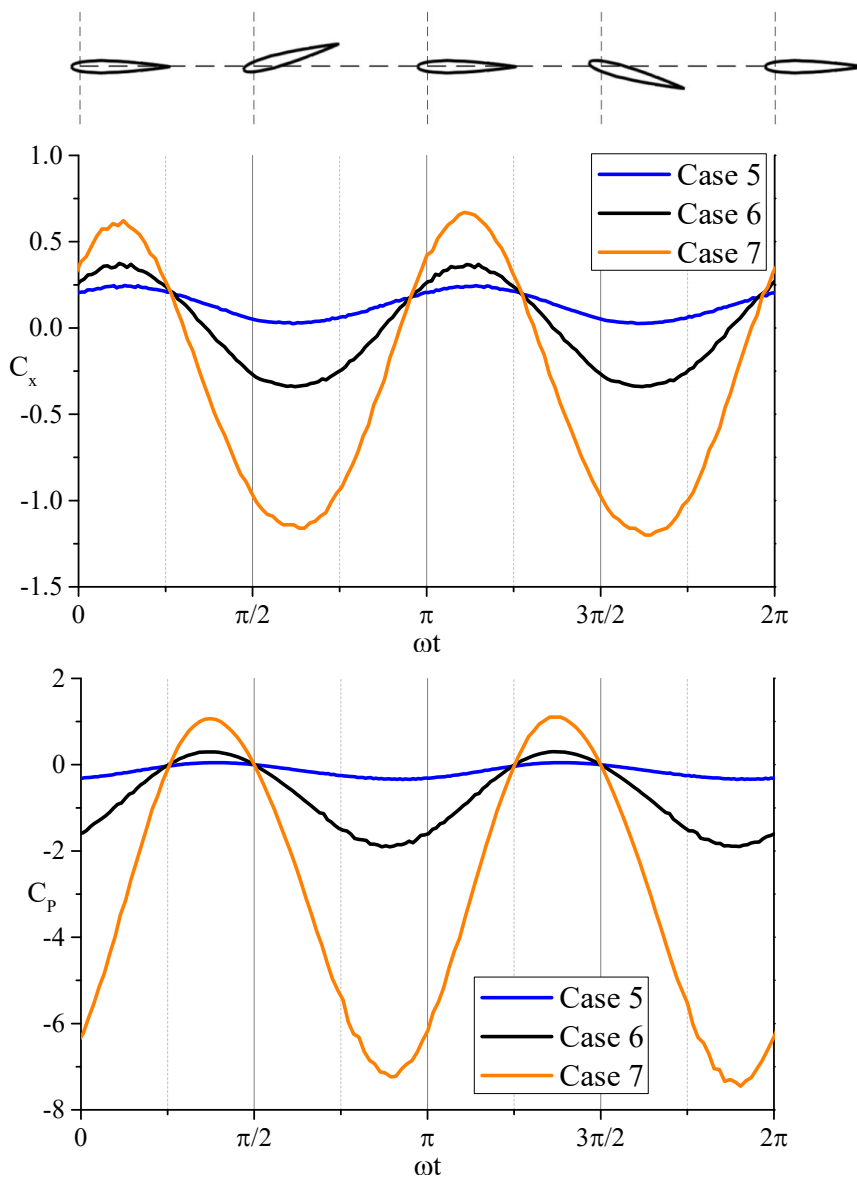


Figure 5-16. Instantaneous foil configuration (top), horizontal force coefficient (middle) and input power coefficient (bottom) for the semi-circle foil in three representative cases. Case 5: drag; Case 6: drag-thrust transition; Case 7: thrust

Figure 5-17 shows the pressure and friction components of the horizontal force coefficient, i.e.,  $C_{xp}$  and  $C_{xv}$ , for the three examined cases of the semi-circle foil. The horizontal pink solid and dash lines represent, respectively,  $C_{xp} = 0.138$  and  $C_{xv} = 0.028$  for the stationary semi-

circle foil at zero angle of attack in steady-state conditions, and their corresponding  $C_x$  is 0.166. The  $C_{xp}$  and  $C_{xv}$  of the stationary foil are provided as the baseline to compare with those of the pitching foils. The oscillatory foil leads to a higher magnitude of the time-averaged  $C_{xv}$  than the stationary one, and  $C_{xv}$  is positive for the whole cycle in all the present cases. Besides, both the extreme value and the oscillation amplitude of  $C_{xv}$  become larger with the increase of  $Sr_A$ . In case 5, the magnitudes of the extreme values of  $C_{xp}$  are small, and its time-averaged value,  $\overline{C_{xp}} = 0.086$ , is smaller than the value of the stationary foil. But it is still positive, thus leading to a drag force when summed up with the contribution  $\overline{C_{xv}} = 0.047$ . For case 6, the pressure force coefficient becomes negative,  $\overline{C_{xp}} = -0.076$ , and counteracts the friction force component  $\overline{C_{xv}} = 0.076$ . It indicates the occurrence of the drag-thrust transition for the semi-circle foil. In case 7 where the values of  $Sr$  and  $A_D$  are the largest,  $C_{xp}$  and  $C_{xv}$  are, respectively, more negative and more positive, and their amplitudes of oscillation enlarge compared to those for case 6.  $\overline{C_{xp}}$  overcomes  $\overline{C_{xv}}$  and thus results in a thrust force  $\overline{C_x} = -0.316$ . In addition, it is found that  $C_{xp}$  is not in the same phase as  $C_{xv}$  for the three cases.  $C_{xp}$  is estimated to be  $\pi/4$  lagging behind  $C_{xv}$ .

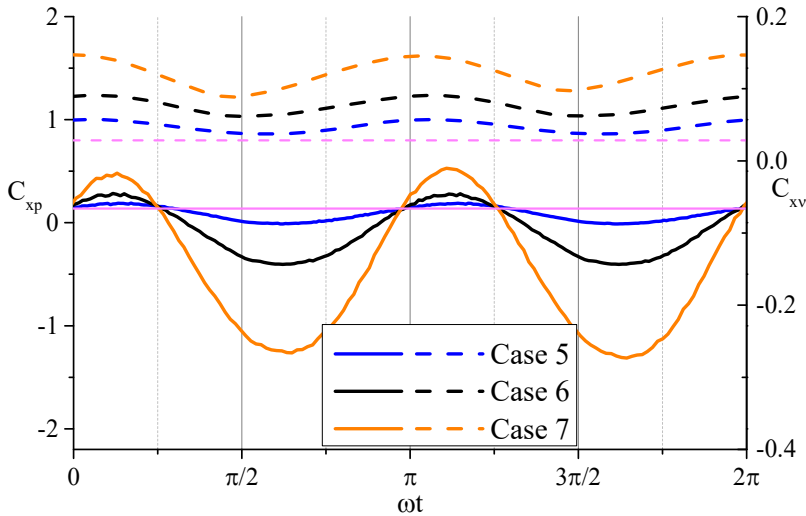


Figure 5-17. Instantaneous pressure (solid line) and friction (dash line) components of the non-dimensional horizontal force for the semi-circle foil in three representative cases. Case 5: drag; Case 6: drag-thrust transition; Case 7: thrust. Pink solid and dash lines represent  $C_{xp}$  and  $C_{xv}$  of the stationary foil at zero angle of attack, respectively

Based on the above three representative cases of the semi-circle foil, the requirement of the input power ( $C_p < 0$ ) is found to be maximum at  $\omega t = 7\pi/8$  and minimum at  $\omega t = 11\pi/8$ . The friction force coefficient ( $C_{xv}$ ) is the largest around the mean position and the lowest around the extreme position, which is somehow intuitively reasonable as the tangential projection of the inflow velocity along the foil is largest when the foil is in its mean position and so largest

shear stresses are expected in the boundary layer. On the other hand, the  $C_x$  and  $C_{xp}$  have the same characteristics, both being minimum at  $\omega t = 5\pi/8$  (maximum thrust) and maximum at  $\omega t = 9\pi/8$  (maximum drag). This scenario is different from the intuitively expectation that the largest thrust and drag force would occur right at instants when the foil reaches the mean and extreme positions.

The steady-state behaviors of horizontal force and power coefficients within one complete oscillation period for the three hydrofoils defined in Figure 5-1 are given in Figure 5-18. They are studied with the following parameters coinciding with those of case 6 of the semi-circle foil:  $f = 2.244 \text{ s}^{-1}$  and  $\theta_0 = 0.153 \text{ rad}$  ( $A = 6.25 \text{ mm}$ ). Under these conditions, the NACA 0012 foil and NACA 0021 foil are associated with thrust generation and drag generation, respectively, and the semi-circle foil is at the drag-thrust transition. With this choice of parameters, the values of  $Sr$  and  $A_D$  are different for the three foils ( $Sr = 0.22$  and  $A_D = 1.25$  for the semi-circle foil), but the corresponding values of the amplitude based Strouhal number  $Sr_A = Sr \times A_D$  coincide, i.e., 0.275. This would suggest that  $Sr_A$  is not the only parameter governing the drag-thrust transition in general scenarios.

Figure 5-18 shows that both  $C_x$  and  $C_p$  have the same characteristics as for the semi-circle foil during the pitching motion. In particular, their extreme values occur nearly at the same phases  $\omega t$  (this is exactly true for  $C_p$ , slightly less for  $C_x$ ) and the correspondence between the inflection points of the  $C_p$  curve and the extremes of the  $C_x$  curve is practically confirmed.

On the other hand, there are obvious differences among the results of the three foils. The  $C_x$  curves for the NACA 0012 and semi-circle foils have similar oscillation amplitude (half of the difference between maximum and minimum values), i.e., 0.356 and 0.349, respectively, while the one for the NACA 0021 foil has a slightly smaller value (0.332); this indicates that the force oscillation amplitude is dominated by mechanisms connected with the trailing edge and increases for sharper/thinner geometries (compare sketches in Figure 5-1). Considering the relative strength of the vortex generated at the leading and trailing edge, the vK-reverse vK wake transition occurs at a smaller  $A_D$  for the NACA 0012 foil than for the other two, and therefore it is also expected that its drag-thrust transition would occur firstly. The NACA 0021 and semi-circle foils experience similar maximum drag, occurring slightly after the foil has passed its mean position, while the NACA 0012 foil has a smaller maximum drag; this confirms the primary role of the maximum thickness in the forward part of the foil for this variable. The  $C_x$  curve for the NACA 0012 appears to be shifted of about 0.057 overall towards the negative values, i.e., towards thrust production, with respect to the corresponding curve for the semi-circle foil. This leads to the corresponding maximum drag force (at  $\omega t = 9\pi/8$ ) and maximum thrust force ( $C_x < 0$ , at  $\omega t = 5\pi/8$ ), respectively, smaller and larger, than those of the semi-circle foil. This shifting effect is documented also for the  $C_x$  curve of NACA 0012 with respect to that of the NACA 0021 in the zone of  $C_x > 0$ , i.e., for limited foil rotation, while the NACA 0021 produces much smaller negative values (i.e., smaller thrust production) at large foil rotation angles. These two aspects suggest that the maximum thickness affects the mean value of  $C_x$  uniformly during the oscillation period, while the trailing-edge geometry plays a role at sufficiently high oscillation angles, and this agrees with the findings by Schnipper et al. (2009).

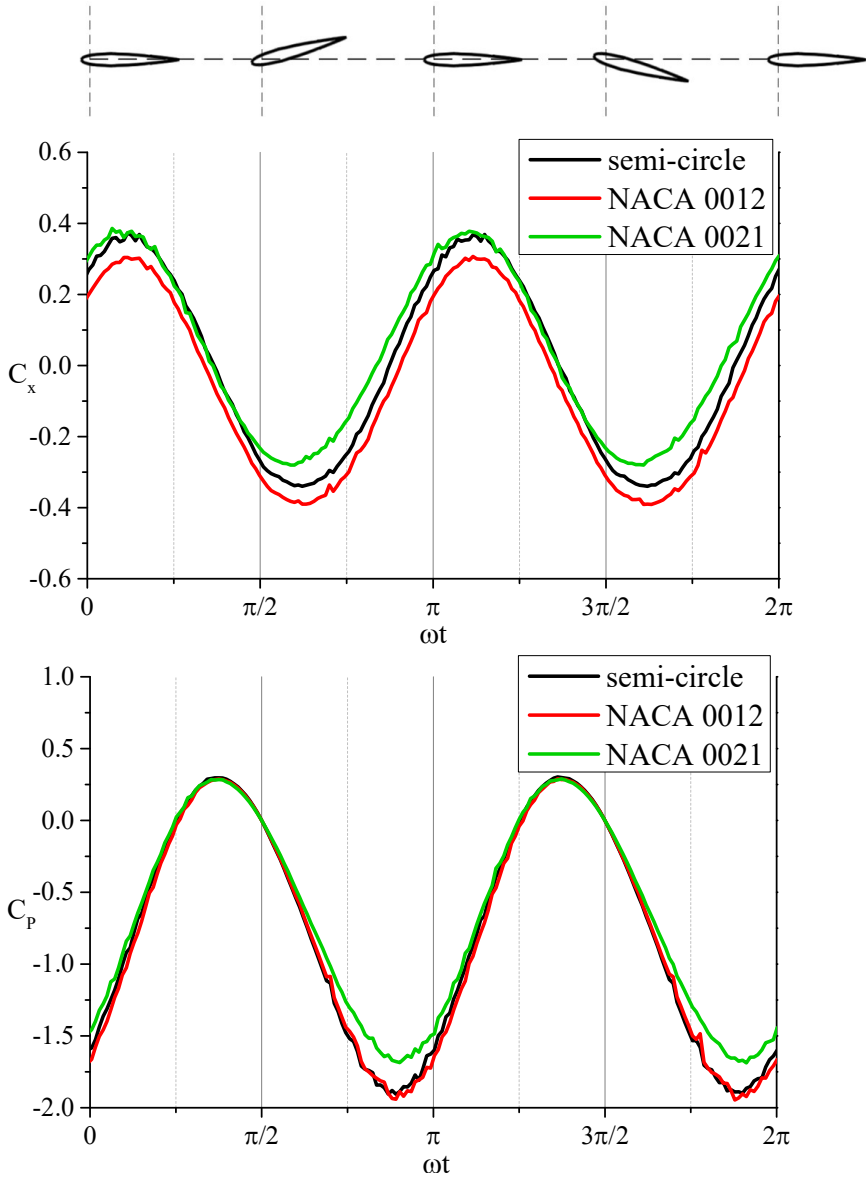


Figure 5-18. Instantaneous horizontal force coefficient and input power coefficient for three hydrofoils at  $f = 2.244s^{-1}$  and  $A = 6.25mm$

From the bottom plot of Figure 5-18, the  $C_p$  histories of the semi-circle foil and NACA 0012 foil practically coincide. In fact, these two foils have the same geometry near the trailing edge, confirming the relevance of this part for the torque due to the larger distance of the trailing edge from the center of rotation. The NACA 0021 foil has the same maximum  $C_p$ , but its absolute value of the minimum  $C_p$  at  $\omega t = 7\pi/8$  is smaller than the value documented by the other two foils. Since the pitching frequency and amplitude make no difference, the only reason is their torque experienced by the hydrofoils. The results made nondimensional by  $\frac{1}{2}\rho U^2 c^2$  are



shown in Figure 5-19. When the foils move from the mean positions to the extreme positions, the torques of the three foils agree well. However, when the foils pitch from the extreme positions to the mean positions, the results of NACA 0021 foil become different from the other two foils. This confirms again the importance of the shape of foils' trailing edge and that the less sharp/thicker trailing edge leads to lower input power requirement for the NACA 0021 foil.

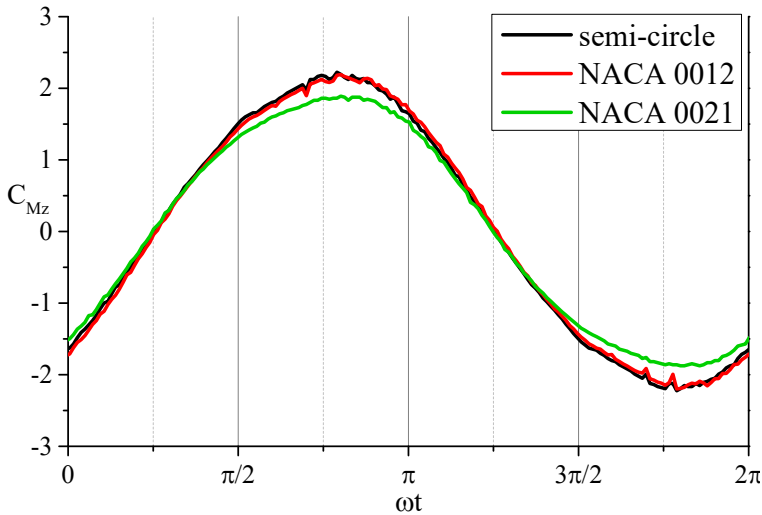


Figure 5-19. Evolution of the dimensionless torque for three hydrofoils during a complete oscillation period at  $f = 2.244s^{-1}$  and  $A = 6.25mm$

Figure 5-20 shows the pressure and friction components,  $C_{xp}$  and  $C_{xv}$ , of the horizontal force coefficient for the three foils. One should note that the two coefficients here are defined using the foil chord length (same as  $C_x$ ). From the results, the tendencies of  $C_{xp}$  for the three foils are very similar and their values are relatively close, confirming the importance of the vortex shedding at the sharp trailing edge for this force component. The curves show however some differences. The NACA 0021 and semi-circle foils are associated with very similar  $C_{xp}$  while the NACA 0012 has a shift toward the negative values. This appears reasonable as the first two foils have the same maximum thickness, which is larger than for the third foil, and the pressure-loss force contribution is affected by the frontal area experienced by the pitching foils. Consistently with this, such force component is associated with the largest oscillation amplitudes, as the rotations can affect greatly the pressure along the foil. Things are different for the  $C_{xv}$  results, indicating much more limited oscillation amplitudes and the largest values for the NACA 0021 foil, followed by the NACA 0012 foil and then by the semi-circle foil. This rotation motion has less effect on the shear stresses along the foil than the pressure loads. It is reasonable that the NACA 0021 foil experiences the largest values for this non-dimensional force contribution because the latter is affected by the foil-profile length, which is largest for this foil. However, the semi-circle foil has values smaller than the NACA 0012 foil, despite the latter has the lowest foil-profile length. The comparisons between the simulation results of the semi-circle and NACA 0012 foil show that  $C_{xv}$  of the semi-circle foil is about 0.034 smaller, but  $C_{xp}$  is 0.091 larger than NACA 0012 foil during the whole pitching period, which leads to

a smaller thrust force of the semi-circle foil. The  $C_{xp}$  of the NACA 0021 foil is comparable to that of the semi-circle foil, and it also experiences the highest  $C_{xv}$ .

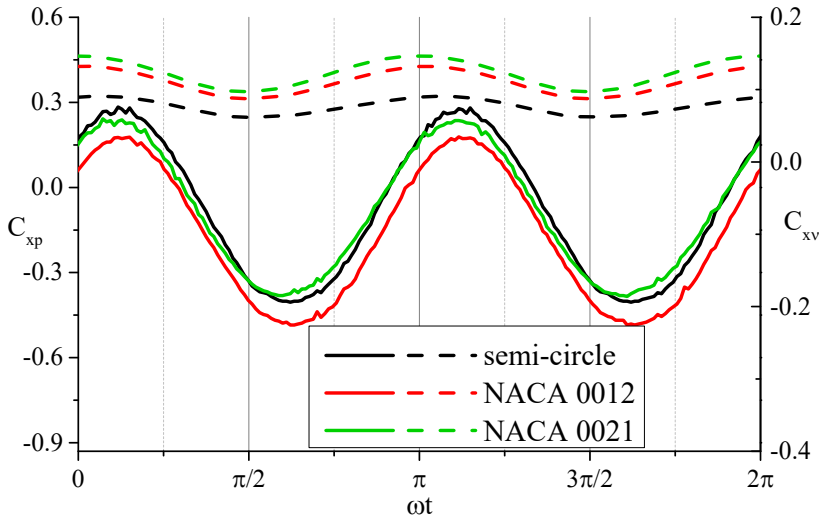


Figure 5-20. Instantaneous pressure (solid line) and friction (dash line) components of the horizontal force for three hydrofoils at  $f = 2.244s^{-1}$  and  $A = 6.25mm$

In the following discussion and in Figure 5-21 the force coefficients are defined using more appropriate characteristic lengths so to identify better the role played by the foil geometry. The maximum foil thickness is used as a relevant characteristic length for the pressure-force component (i.e.,  $C_{xp_D} = F_{xp}/0.5\rho U^2 D$ ) and the foil profile length is considered for the friction-force component (i.e.,  $C_{xv_{pro}} = F_{xv}/0.5\rho U^2 L_{pro}$ , where  $L_{pro}$  is the perimeter of the foil profile). The results of  $C_{xv_{pro}}$  are consistent with the  $C_{xv}$  results, with the largest values for the NACA 0021 foil, but now closer to the results for the NACA 0012 foil, and the smallest values for the semi-circle foil. This confirms limited effects of the rotations on the shear stresses along the foils and main role played by the foils' profiles. More in detail, the NACA 0012 has smaller thickness than the NACA 0021 and therefore it is expected to experience less flow acceleration along its profile, and averagely smaller shear stresses; this could explain the slightly lower value for its  $C_{xv_{pro}}$ . The NACA 0021 has the maximum thickness more downstream than the semi-circle foil, therefore the flow is expected to remain attached along a larger part of the body while the flow separates immediately after the circular leading part for the semi-circle foil. This might reduce the tangential flow velocity and therefore the shear stresses along the semi-circle foil more substantially than for the NACA 0012 foil, explaining the smallest values (among the three examined foils) for its  $C_{xv_{pro}}$ . These aspects will be shown in the later section 5.4.3 through the local flow features around the foils. Concerning the pressure-force coefficient, the NACA 0021 and semi-circle foils have similar  $C_{xp_D}$  while the NACA 0012 has similar maximum value and much larger negative values. This confirms the effect of the frontal area near the mean foil configuration (i.e., at low pitch angles) and the importance of the trailing-edge sharpness at large pitching angle (i.e., when vortex shedding at the trailing edge occurs more easily). Overall, the friction-force component depends highly on

the forepart of foil profile and the possible vortex shedding occurring in the upstream part of the foil; the main features of the pressure-force component depend on the trailing-edge shape and the resulting shedding vortex, while the leading part of the foil has a more limited (yet not always negligible) effect when vortex shedding occurs there leading to increase in pressure-loss drag.

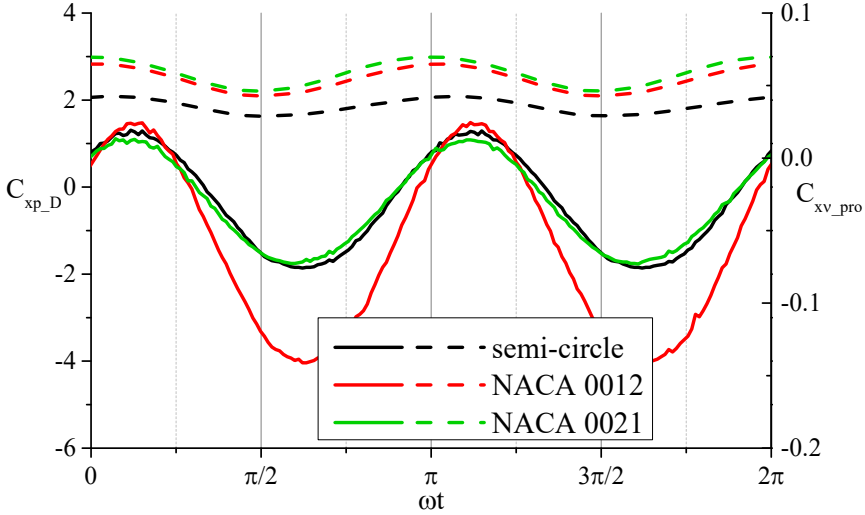


Figure 5-21. Instantaneous pressure (solid line) and friction (dash line) components of the horizontal force for three hydrofoils at  $f = 2.244s^{-1}$  and  $A = 6.25mm$

The present analysis showed that the NACA 0012 foil is associated to the largest thrust, but it also experiences the largest hydrodynamic torque, which might lead to possible issues for structural integrity. This poses the following research question: *based on the influence of the foil geometrical features, can we identify a morphing-foil strategy so to generate a thrust similar to that of the NACA 0012 foil while reducing the hydrodynamic torque to a level comparable to that of the NACA 0021 foil?*

From the numerical predictions of the three hydrofoils with different profiles, we have found that NACA 0012 foil can generate the largest thrust force ( $C_x$  and  $C_{xp}$  being the minimum) at  $\omega t = 5\pi/8$ , but NACA 0021 requires the minimum input power for the pitching motion at  $\omega t = 7\pi/8$ . A first attempt to combine these advantages within a foil morphing strategy is to enforce that the foil becomes thicker when close to the mean position and thinner when close to the extreme positions. Therefore, the thickness of the foil profile is forced to change in time according to the law:

$$D(t, x) = D_0(x) + a_D D_0(x) (\cos(2\omega t + \phi) - 1) = D_{mean}(x) + a_D D_0(x) \cos(2\omega t + \phi) \quad (5.11)$$

with  $D_0(x)$  the local maximum value,  $D_{mean}(x)$  the local mean value, and  $a_D D_0(x)$  the local amplitude of the oscillatory part, which has a period half of the pitching period and a phase  $\phi$  with respect to the pitching motion of the foil. To pursue our scope,  $D_0(x)$  coincides with the local thickness of the NACA 0021 foil, and  $a_D$  is defined as  $a_D = \frac{1}{2} \left( 1 - \frac{D_{NACA0012}}{D_{NACA0021}} \right) =$

0.224 to ensure the foil profile is morphed between NACA 0021 (with  $D_{NACA\ 0021}$  the maximum thickness) and NACA 0012 (with  $D_{NACA\ 0012}$  the maximum thickness) foil geometries, as illustrated in Figure 5-22. In this first attempt,  $\phi = 0\ rad$  is chosen.

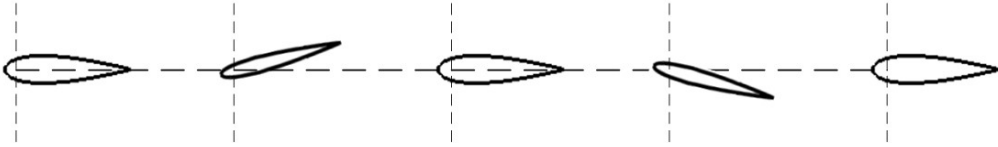


Figure 5-22. Schematic showing foil morphing between NACA 0012 and 0021 during one pitching period

This deformable NACA foil is studied under the same pitching motion condition as examined above ( $f = 2.244\ s^{-1}$  and  $\theta_0 = 0.153\ rad$ ) to investigate whether it can achieve our aim. Figure 5-23 gives the force and power results for the rigid and deformable NACA foils. The time histories of the input power coefficient  $C_P$  prove that the deformable NACA foil requires as less power as NACA 0021 foil to perform the prescribed pitching motion. From the instantaneous plots of  $C_x$ , it is obvious that the horizontal force for the deformable NACA foil is not in phase with those for the rigid foils and therefore the morphing foil experiences drag and thrust forces at phases different from those of the rigid foils. When it moves from the mean to the extreme position,  $C_x$  firstly decreases, reaching the minimum at  $\pi/2$  (the extreme position), and then it increases till the maximum value reached a little behind  $7\pi/8$ . The rate of the increase is steeper for  $\omega t = (\pi/2 : 7\pi/8)$  and the rate of the decrease is milder for  $\omega t = (7\pi/8 : 3\pi/2)$ . The results illustrate that the deformable NACA foil generates the maximum thrust force at the extreme positions and experiences the largest drag just before reaching the mean positions. The comparison of  $C_x$  among the three NACA foils shows that the minimum  $C_x$  value of deformable NACA foil is the same as the blunt NACA 0021 foil, however, its maximum  $C_x$  value is even smaller than the streamlined NACA 0012 foil. Therefore, the deformable NACA foil generates a time-averaged thrust force of  $\overline{C_x} = -0.043$ , while NACA 0012 experiences a mean thrust of  $\overline{C_x} = -0.058$  and NACA 0021 foil suffers a mean drag of  $\overline{C_x} = 0.038$ .

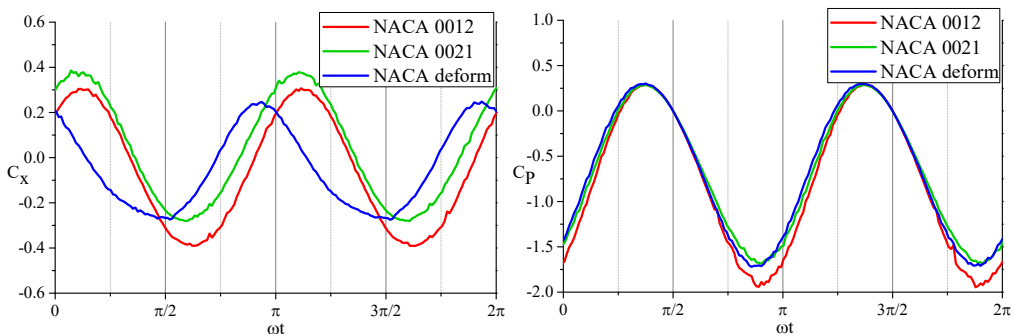


Figure 5-23. Instantaneous horizontal force and input power coefficients for rigid and deformable NACA foils at  $f = 2.244s^{-1}$  and  $A = 6.25mm$

The instantaneous pressure and friction components defined in two ways,  $C_{xp}$  and  $C_{xv}$ ,  $C_{xp,D}$  and  $C_{xv,pro}$ , of the horizontal force coefficient for the rigid and deformable NACA foils are shown in Figure 5-24. Apparently, both  $C_{xp}$  and  $C_{xv}$  are not in phase with the corresponding components of the NACA 0012 and 0021 foils. Due to the morphing profile, the amplitude of oscillation of  $C_{xv}$  for the deformable NACA foil is larger than those of the rigid foils. However, since the friction component makes less contribution to the total horizontal force, the pressure force still plays the leading role. In terms of the pressure force coefficient, the previous analysis has proved the important effect of the frontal area experienced by the pitching foils, thus  $C_{xp,D}$  is used for the following discussion. The maximum value of  $C_{xp,D}$  for the deformable NACA foil is smaller than that of the other two foils, but the absolute value of minimum  $C_{xp,D}$  for the deformable NACA foil is larger than that of NACA 0021 foil. It indicates that its pressure force gives more contribution to the thrust generation around the extreme pitching positions. Overall, the deformable NACA foil has smaller oscillation amplitude of the instantaneous horizontal force than that of the NACA 0012 foil, and it can generate much smaller drag force than NACA 0021 foil. Its time-averaged thrust is larger than NACA 0021 while it requires as less input power as this foil. This finding might inspire the design of underwater bio vehicles for greener propulsion.

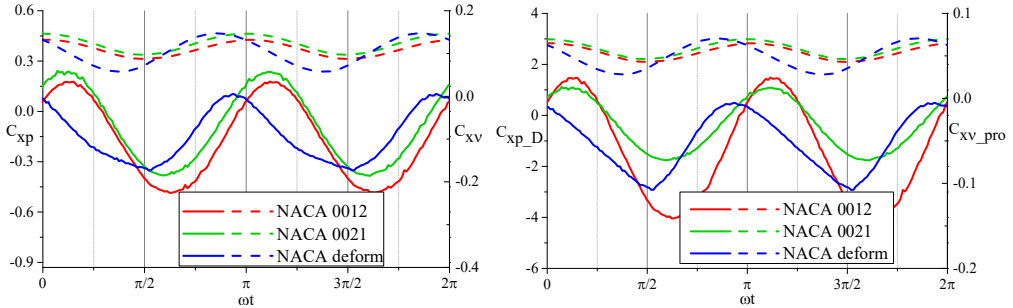


Figure 5-24. Instantaneous pressure (solid line) and friction (dash line) components of the horizontal force for rigid and deformable NACA foils at  $f = 2.244s^{-1}$  and  $A = 6.25mm$

The first attempt has shown that the answer to our research question is yes, i.e., a morphing strategy can serve to the scope. This brings to the next research question: *is it possible to identify an optimized morphing strategy so to maximize the mean thrust (toward the reference rigid-foil value, i.e., in our case the NACA 0012) and efficiency while minimizing the required mean input power (toward the reference rigid-foil value, i.e., in our case the NACA 0021)?*

To obtain the answer to this question, the morphing phase  $\phi$  is varied between 0 and  $2\pi$  with an interval of  $\pi/8$ . This leads to the definition of 16 deformable foils in D1-D16. Table 5-9 documents the results of  $\overline{C_x}$ ,  $\overline{C_p}$ ,  $\eta$  and the time instants within one complete oscillation period when the hydrofoil experiences the maximum thrust  $\phi_T$  and maximum drag  $\phi_D$  for all the examined deformable NACA foils compared with the three rigid foils illustrated in Figure 5-1. Here, the time-averaged power coefficient  $\overline{C_p}$  has been estimated similarly as done for the force, i.e. (see section 5.3.2 for the definitions of  $n$  and  $t_0$ ):

$$\overline{C_p} = \frac{1}{nT} \int_{t_0}^{t_0+nT} C_p(t) dt \quad (5.12)$$

The propulsive efficiency,  $\eta$ , is defined to be the ratio of useful power over input power, as:

$$\eta = \frac{\overline{F_x}U}{\overline{P}} = \frac{\overline{C_x}}{\overline{C_p}} \quad (5.13)$$

The top three performances are marked in red, green and blue, respectively, i.e., the NACA 0012 foil generates the largest mean thrust and has the highest efficiency, while the deformable NACA foil with  $\phi = \pi/8$  needs the minimum input power. The worst performance is marked in yellow.

Table 5-9. Phase influence tests for deformable NACA foils at  $f = 2.244s^{-1}$  and  $A = 6.25mm$

case	$\phi$	$\overline{C_x}$	$\phi_T$	$\phi_D$	$\overline{C_p}$	$\eta$
Semi-circle	–	-0.0002	$5\pi/8$	$9\pi/8$	-0.7710	0.0003
NACA 0012	–	-0.0568	$5\pi/8$	$9\pi/8$	-0.7881	0.0721
NACA 0021	–	0.0378	$5\pi/8$	$9\pi/8$	-0.6843	-0.0552
D1	0	-0.0428	$\pi/2$	$15\pi/16$	-0.6749	0.0634
D2	$\pi/8$	-0.0364	$\pi/2$	$7\pi/8$	-0.6746	0.0539
D3	$\pi/4$	-0.0289	$7\pi/16$	$5\pi/4$	-0.6824	0.0424
D4	$3\pi/8$	-0.0209	$7\pi/8$	$5\pi/4$	-0.7004	0.0299
D5	$\pi/2$	-0.0147	$13\pi/16$	$5\pi/4$	-0.7259	0.0203
D6	$5\pi/8$	-0.0110	$25\pi/32$	$49\pi/40$	-0.7530	0.0146
D7	$3\pi/4$	-0.0104	$23\pi/32$	$39\pi/32$	-0.7796	0.0133
D8	$7\pi/8$	-0.0114	$11\pi/16$	$29\pi/24$	-0.8003	0.0143
D9	$\pi$	-0.0148	$2\pi/3$	$19\pi/16$	-0.8138	0.0182
D10	$9\pi/8$	-0.0214	$5\pi/8$	$7\pi/6$	-0.8156	0.0262
D11	$5\pi/4$	-0.0297	$7\pi/12$	$9\pi/8$	-0.8053	0.0369
D12	$11\pi/8$	-0.0384	$9\pi/16$	$13\pi/12$	-0.7843	0.0490
D13	$3\pi/2$	-0.0455	$17\pi/32$	$17\pi/16$	-0.7576	0.0601
D14	$13\pi/8$	-0.0496	$\pi/2$	$25\pi/24$	-0.7281	0.0681
D15	$7\pi/4$	-0.0503	$15\pi/32$	$\pi$	-0.7024	0.0716
D16	$15\pi/8$	-0.0473	$11\pi/24$	$23\pi/24$	-0.6848	0.0691

Figure 5-25 shows the instantaneous horizontal force coefficients for all the deformable NACA foils defined in Table 5-9. They achieve the extreme values at different phases. Besides, when the foil can generate larger maximum thrust, it also tends to experience larger maximum drag force.

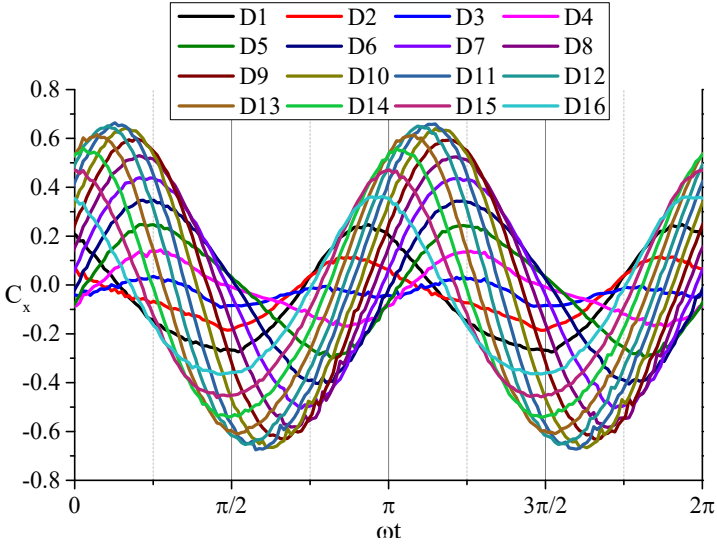


Figure 5-25. Instantaneous horizontal force coefficient for the examined deformable NACA foils at  $f = 2.244s^{-1}$  and  $A = 6.25mm$

Figure 5-26 presents the time-averaged horizontal force, input power coefficients and the efficiency for all the examined deformable NACA foils. It illustrates that the morphing foil with  $\phi = 7\pi/4$  (D15) experiences the maximum time-averaged thrust force and the maximum efficiency with respect to the parameter  $\phi$ , but requires relatively low input power compared to the maximum value required by the morphing foil with  $\phi = 9\pi/8$ .

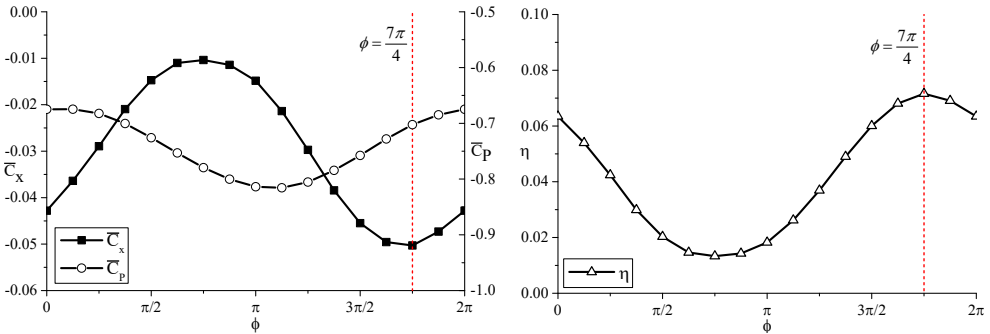


Figure 5-26. Time-averaged horizontal force coefficient, input power coefficient and efficiency for the examined deformable NACA foils at  $f = 2.244s^{-1}$  and  $A = 6.25mm$

The morphing and pitching motion for the deformable NACA foil with  $\phi = 7\pi/4$  is illustrated in Figure 5-27. The occurrences of the maximum and minimum  $C_x$  and  $C_p$  are also marked in the schematic.

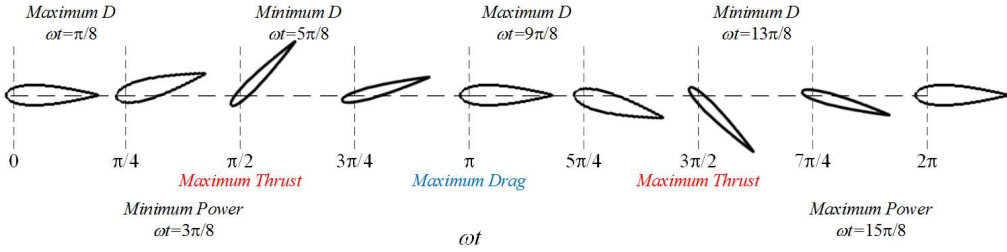


Figure 5-27. Schematic showing foil morphing (D15) and the corresponding occurrences of maximum and minimum drag, thrust and power

Figure 5-28 shows the instantaneous force and power coefficients for the rigid NACA foils and for the deformable NACA foil D15. The latter requires less power, similar as the NACA 0021 foil, around the mean positions, and it outputs a little more power before reaching the extreme positions. From the time history of  $C_x$ , this deformable NACA foil experiences maximum thrust (minimum  $C_x$ ) close to the extreme positions. Though the maximum drag of the deformable foil is larger than the rigid NACA 0021 foil, it generates even larger thrust than the NACA 0012 foil, and therefore, the time-averaged horizontal force for this deformable NACA foil is a thrust of  $\overline{C_x} = -0.050$ , which is slightly less than that of the NACA 0012 foil ( $\overline{C_x} = -0.058$ ).

This simplified analysis indicated that there is a challenge in identifying a morphing strategy that targets the optimization of  $\overline{C_x}$ ,  $\overline{C_p}$  and  $\eta$ . However, we were able to identify a deformable foil law (D15) with maximum thrust and efficiency (with respect to the examined parameter  $\phi$ ) and that requires less input power than the original rigid foil NACA 0012. Therefore, it can offer a compromise to let the foil have less torque and be robust as NACA 0021 foil while retaining the capability to create large propulsion force.

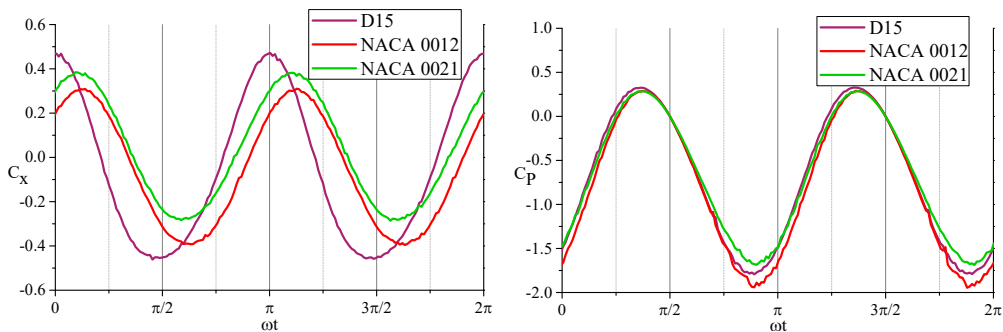


Figure 5-28. Instantaneous horizontal force and input power coefficients for rigid NACA foils and deformable NACA foil D15 at  $f = 2.244s^{-1}$  and  $A = 6.25mm$

In this section, the different foils were examined at a specific Strouhal number and oscillation amplitude. In the following section, their influence on the loads and wake scenarios is examined in a systematic way.



### 5.4.2 Time-averaged thrust and power and efficiency

In the present section, the semi-circle foil case is used to examine the time-average force and power, as well as the efficiency as a function of the Strouhal number ( $Str$ ) and of the oscillation amplitude ( $A_D$ ). This can enable us to identify the drag-thrust transition and possible optimal conditions for the foil efficiency.

Since the foil profile and the flapping motion are up-and-down symmetric, the side force varies symmetrically about zero in such a way that the time-averaged value of  $\overline{F}_y$  and therefore the force coefficient  $\overline{C}_y$  are approximately zero. In order to identify when the transition from drag to thrust occurs, the mean horizontal force on the flapping foil is estimated by OpenFOAM force library based on normal pressure and shear stress integration. This force prediction method is firstly examined for Cases 1-4 with different  $A_D$  at  $Re_c = 1173$  and  $Str = 0.22$ , which are provided in experimental work of Godoy-Diana et al (2008). The simulation results of the flapping foil are documented in Table 5-10.

Table 5-10. Time-averaged horizontal force coefficients for the semi-circle foil

$A_D$	0.36	0.71	1.07	1.77
$\overline{C}_x$	0.156	0.119	0.047	-0.172

Figure 5-29 shows the map of horizontal force coefficients estimated in the reference paper (Godoy-Diana et al., 2008) through momentum conservation equation by using experimental mean velocity fields.  $\overline{C}_{x0}$ , defined as the horizontal force coefficient for a non-flapping foil at zero angle of attack (AOA), is applied for normalization. Its actual value is not provided in the reference but using the corresponding predicted value from OpenFOAM leads to numerical estimates quite different from the corresponding experimental values. In order to avoid a possible error in the value of  $\overline{C}_{x0}$ , the following approach was used. In Figure 5-29, it is found that the point (0.22, 0.30) lies on the contour line  $\overline{C}_x/\overline{C}_{x0} = 0.6$ . Assuming that the experimental value  $\overline{C}_x$  coincides with the corresponding numerical estimates,  $\overline{C}_{x0}$  is estimated as  $\overline{C}_{x0} = 0.27$  and this value is used to estimate  $\overline{C}_x/\overline{C}_{x0}$  for all other numerical cases. As an example, Table 5-11 provides the predicted normalized time-averaged horizontal force coefficients for the above four cases.

Table 5-11. Predicted normalized time-averaged horizontal force coefficients for the semi-circle foil

$A_D$	0.36	0.71	1.07	1.77
$\overline{C}_x/\overline{C}_{x0}$	0.578	0.444	0.175	-0.638

These numerical results have been included in Figure 5-29 as solid red circles labelled with their  $\overline{C}_x/\overline{C}_{x0}$  value, confirming a satisfactory consistency with the experiments.

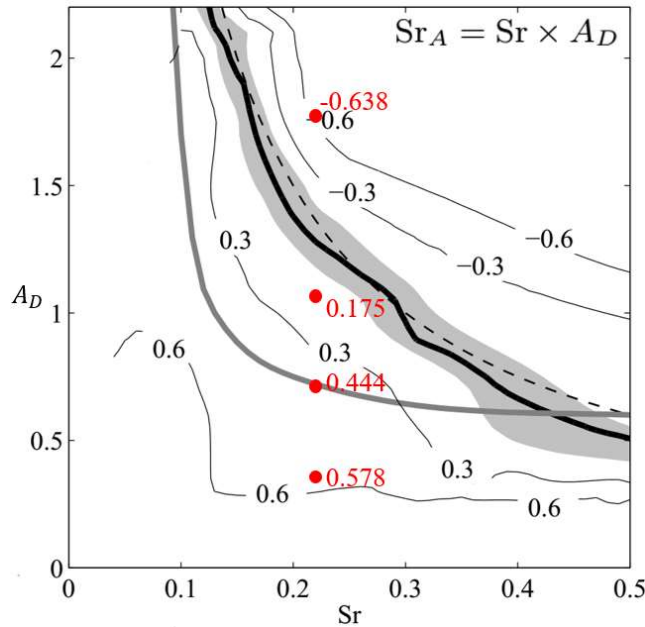


Figure 5-29. Contours of the mean horizontal force coefficient  $\overline{C_x}/\overline{C_{x0}}$  ( $\overline{C_{x0}}$  is the force coefficient for a static foil at AOA=0) estimated from time-averaged velocity fields of experiments. The black line corresponds to  $\overline{C_x} = 0$ ; the shaded area represents the estimated error for the force transition curve; the gray line is the wake transition from vK to reverse vK; the dashed line corresponds to  $Sr_A = 0.3$ . The solid red circles are numerical results, labelled with their  $\overline{C_x}/\overline{C_{x0}}$  values

Figure 5-30 shows the contour plots of  $\overline{C_x}$ ,  $\overline{C_p}$  and  $\eta$  as functions of  $Sr$  and  $A_D$ . The solid lines are the  $Sr_A$  lines labelled with values.  $\overline{C_p}$  decreases with increasing  $Sr$  and  $A_D$ .  $\overline{C_T}$  is positive for small  $Sr$  and  $A_D$ , primarily the lower left region of the contour, and it becomes negative when  $Sr$  and  $A_D$  are sufficiently high. The dashed line represents the boundary between the positive and negative  $\overline{C_x}$ , i.e., the drag-thrust transition. Accordingly, the efficiency  $\eta$  has the same boundary between positive and negative values as  $\overline{C_x}$ . It is observed that the growth of  $\eta$  is rapid from  $\eta = -0.16$  to  $0.02$  with  $Sr_A$  changing from  $0.25$  to  $0.30$  in the plot. On the other hand, the growth is relatively slow from  $\eta = 0.02$  to  $0.08$  with the same increase of  $Sr_A$  (from  $0.30$  to  $0.35$ ). By further increasing  $Sr_A$ , the efficiency  $\eta$  continues to grow and it reaches the maximum value within  $Sr_A = 0.60 - 0.70$ . The contour lines of these parameters ( $\overline{C_x}$ ,  $\overline{C_p}$  and  $\eta$ ) follow the same trends as those of  $Sr_A$ , which indicates strong dependence of these coefficients with respect to  $Sr_A$ . In the present simulations performed at  $Re_c = 1173$  for the semi-circle foil, the optimum efficiency occurs around  $Sr = 0.30$  and  $A_D = 2.14$ . It is known in the literature that a wide range of flying and swimming animals converge to the same narrow range of Strouhal number during cruising. For example, it is reported by Triantafyllou et al. (1993) that many different species of fish and cetaceans flap their tail at Strouhal number ( $Sr_A$ ) in the range  $0.25-0.35$  to achieve a maximum efficiency. Taylor et al. (2003) also pointed out that dolphins, sharks and bony fish swim at Strouhal number ( $Sr_A$ ) in the range  $0.2-0.4$ . Since this  $Sr_A$  region is of particular interest for natural propulsion, a close observation is performed for the  $\overline{C_x}$  and  $\overline{C_p}$  plots of Figure 5-30.

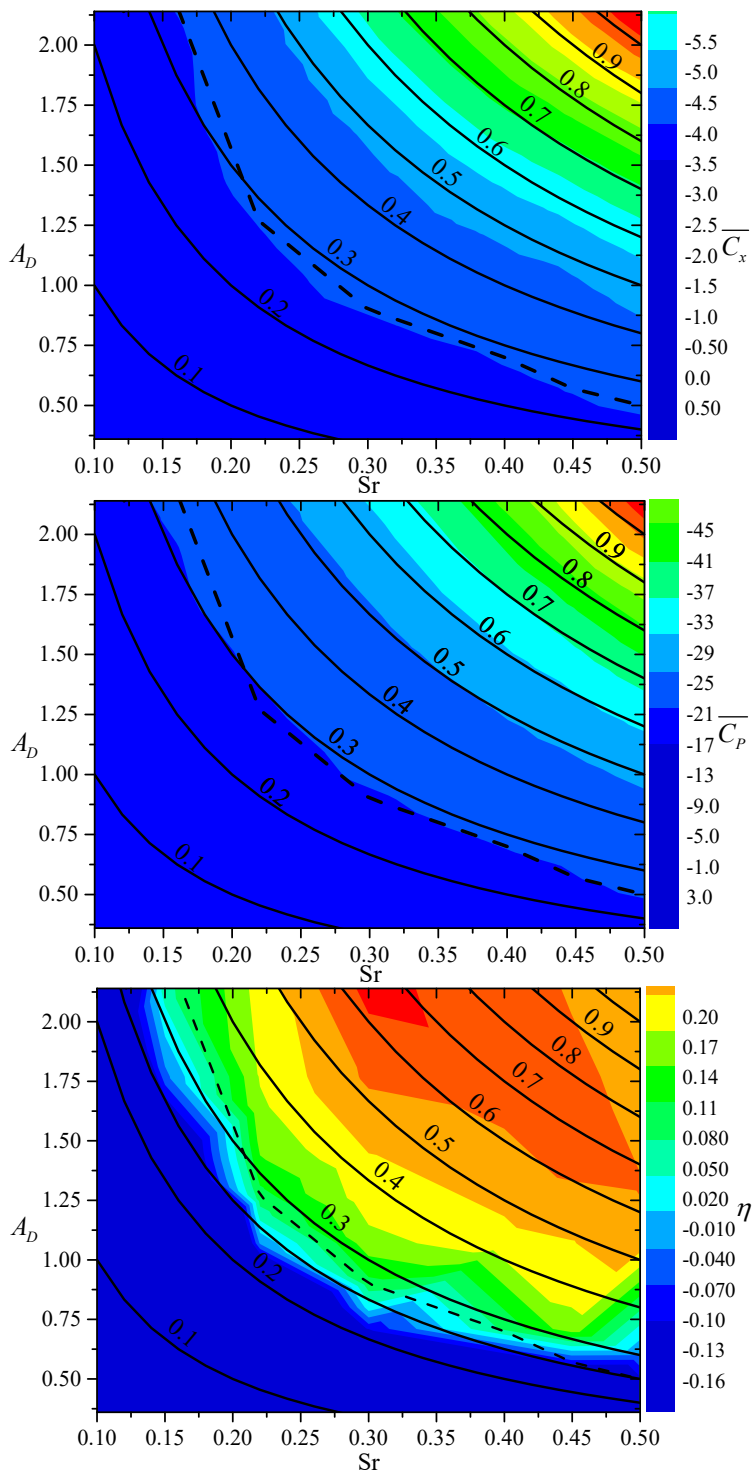


Figure 5-30. Time-averaged horizontal force coefficient, input power coefficient and propulsive efficiency maps for the semi-circle foil

By investigating the contour change for  $A_D = 1.07$  from  $Sr = 0.20$  to  $0.40$ , it is estimated that the decrease in  $\overline{C_x}$  with  $Sr$  is slightly slower in the range  $Sr = 0.20 - 0.30$  (from about  $0.07$  to  $-0.09$ ) than in the range  $Sr = 0.30 - 0.34$  (from about  $-0.09$  to  $-0.34$ ), but the  $\overline{C_p}$  declines much slower in the range  $Sr = 0.20 - 0.30$  (from about  $-0.40$  to  $-1.35$ ) than in the range  $Sr = 0.30 - 0.40$  (from  $-1.35$  to  $-3.37$ ). As the contours of  $\overline{C_x}$  and  $\overline{C_p}$  are following those of  $Sr_A$ , this decreasing tendency also exists for different  $Sr$  and  $A_D$ . In other words, the decreasing rate of  $d\overline{C_x}/d\overline{C_p}$  would become large for  $Sr > 0.30$ . This finding suggests that an optimum condition could be selected to increase the thrust force (negative  $\overline{C_x}$ ) while avoiding the rapid growth of input power (negative  $\overline{C_p}$ ).

### 5.4.3 Vorticity and velocity

Here, the wake regimes associated with the different examined foils are analyzed as a function of the Strouhal number and of the oscillation amplitude. This can allow to identify the transition between different regimes and their connection with drag-to-thrust transition and foil efficiency.

Visualizations of instantaneous spanwise vorticity fields and mean flow near the semi-circle foil at  $Re_c = 1173$  and  $Sr = 0.22$  (Cases 1-4) are provided in the experimental work of Godoy-Diana et al. (2008), documenting mainly two-dimensional flow in the main wake of the foil at this Reynolds number. The corresponding simulation results of the semi-circle foil are shown and compared against the experiments in Figure 5-31 and Figure 5-32, respectively.

From the plots we can find that the predicted flow features by the adopted method agree satisfactorily with results obtained from the experiments, especially for the cases with small flapping amplitudes. At the largest examined  $A_D = 1.77$  case, the vortices, however, start to break up in the downstream of the physical foil and the coherence of vortical structures in the horizontal mid-plane where the experimental observations were performed does not prevail for more than two cycles. This effect is not captured in our numerical simulations. It may be because that the quasi-two-dimensional nature of the flow is lost in this experiment owing to the large flapping amplitude. The mean horizontal velocity behind the foil is higher than the inlet velocity  $U_c$  in this case and leads to a jet-flow profile, which is consistent with the experiments. Whereas the experimental velocity field shows a larger diffusion and smaller advection with respect to the numerical results, indicating that the applied 2D numerical method has a limitation to predict accurately high-amplitude-pitching case where the turbulence may become relevant in the wake and may be not properly handled by the adopted discretization combined with 2D-flow assumption. However, for this pitching foil study, the applied model can still give predictions physically correct in terms of hydrodynamic loads and flow features near the moving foil.

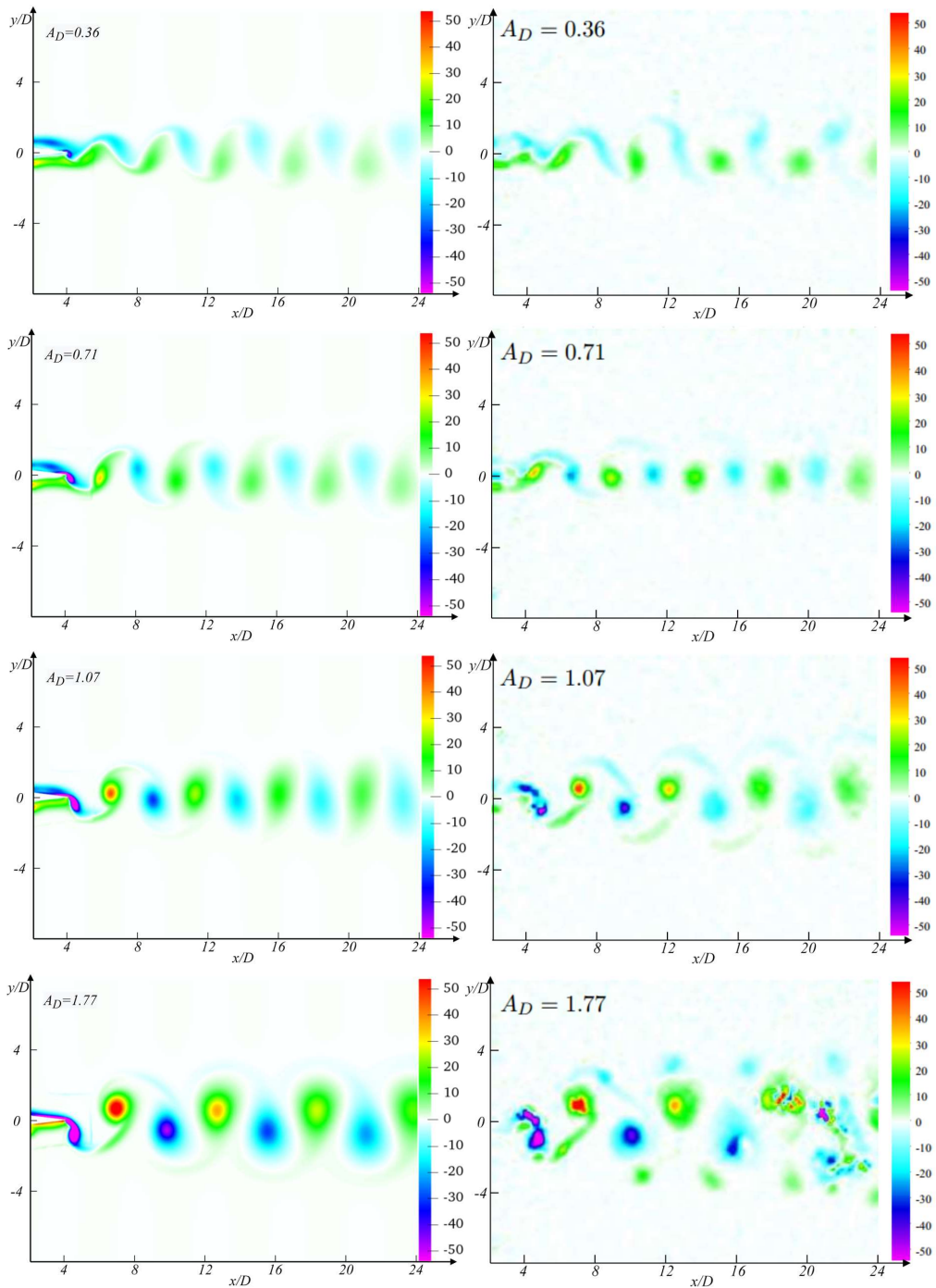


Figure 5-31.  $Re_c = 1173$ ,  $Sr = 0.22$  for the semi-circle foil. From top to bottom:  $A_D=0.36$ ,  $0.71$ ,  $1.07$ ,  $1.77$ . Instantaneous spanwise vorticity fields from OpenFOAM simulations (left) and experiments (right)

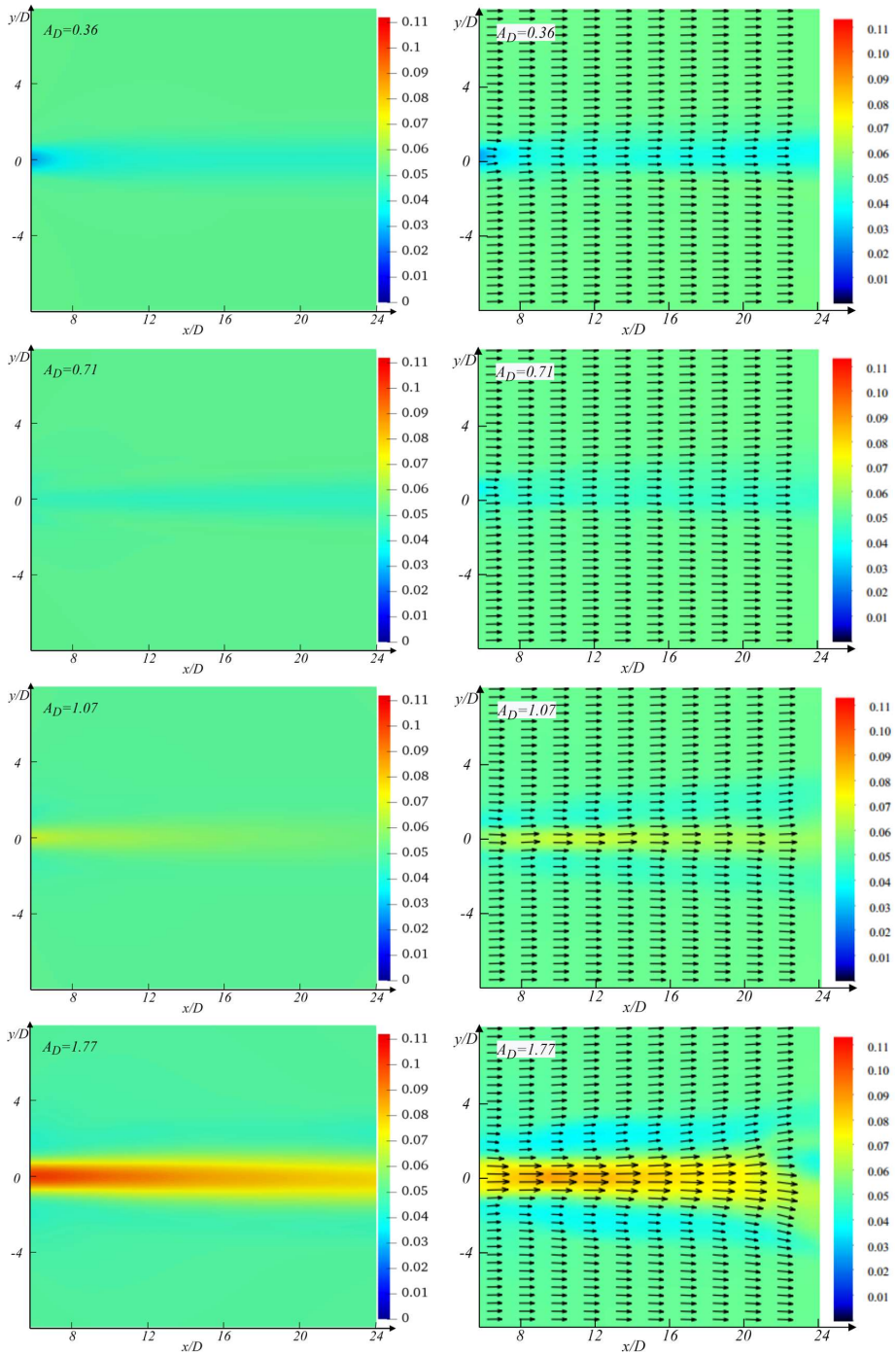


Figure 5-32.  $Re_c = 1173$ ,  $Sr = 0.22$  for the semi-circle foil. From top to bottom:  $A_D=0.36$ , 0.71, 1.07, 1.77. Time-averaged flow velocity from OpenFOAM simulations (left) and experiments (right)

From these comparisons, it is found that by increasing the pitching amplitude, the vK vortex street gives way firstly to the aligned wake, then transforms into a reverse-vK wake. According to Schnipper et al. (2009), the transition from the vK to reverse-vK wake occurs when the vortex at the trailing edge has larger strength than the one generated at the leading edge. Accordingly, the mean horizontal velocity behind the foil is lower than  $U$  at the smallest  $A_D$  but increases with  $A_D$ , and then it becomes higher than  $U$  at the largest  $A_D$ , leading to a jet-flow profile. Figure 5-33 shows the mean horizontal velocity along the wake centerline at  $x/D = 6$  estimated from numerical simulations and from the reference experiments in Godoy-Diana et al. (2008). The error bars connected with the latter quantify the human error in extracting the contour-plot data from the original paper. The mean horizontal velocity increases practically linearly with  $A_D$ , in the examined range of  $A_D$ , and agrees well with experimental data at small flapping amplitudes. The time-averaged velocity in the largest amplitude case is overestimated by OpenFOAM due to the laminar 2D model.

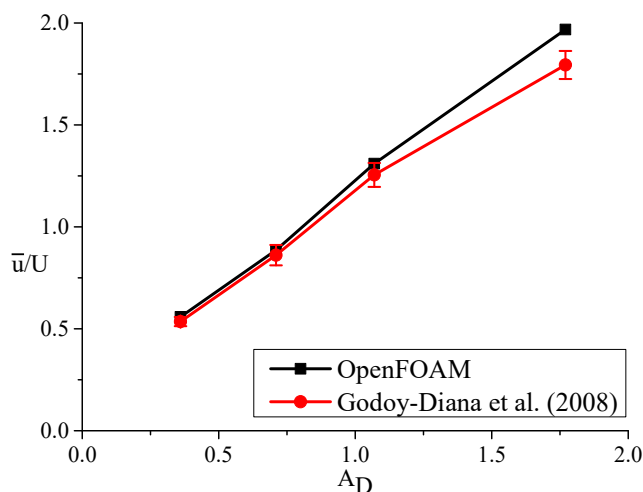


Figure 5-33. The non-dimensional mean horizontal velocity behind the semi-circle foil along the wake centerline at  $x/D = 6$  vs.  $A_D$  for the semi-circle foil at  $Sr = 0.22$

Figure 5-34 shows the simulation results of instantaneous vorticity field and time-averaged velocity field for Cases 5-7 studied in section 5.4.1. It confirms again that the vortices organized in the form of von Kármán wake lead to a drag force, and that the drag-thrust transition occurs in the scenario of reverse-vK wake, i.e., after the wake transition. The foil generates a time-average thrust force in Case 7, and the reverse-vK wake and the mean jet velocity field in the downstream start to propagate in an asymmetric manner.

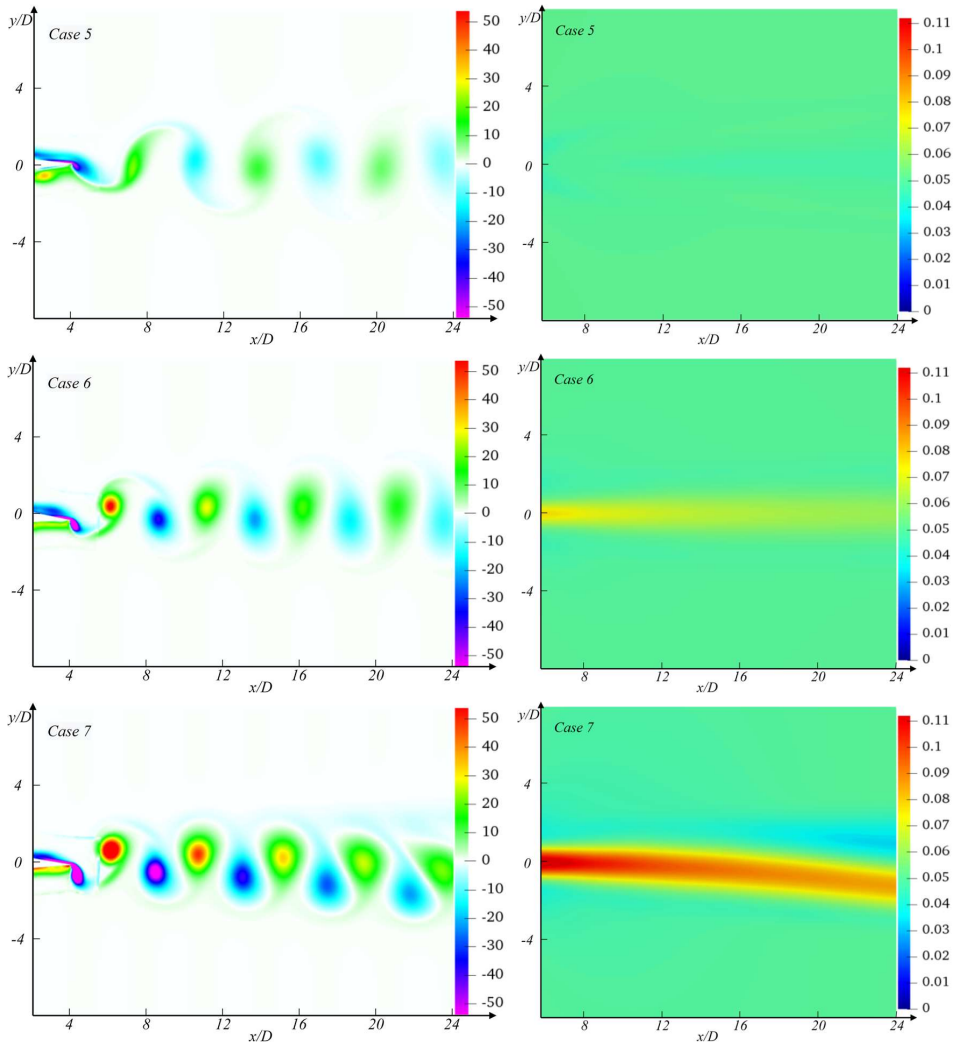


Figure 5-34. Three representative cases for the semi-circle foil. Case 5:  $Sr = 0.15$  and  $A_D = 1.07$ ; Case 6:  $Sr = 0.22$  and  $A_D = 1.25$ ; Case 7:  $Sr = 0.30$  and  $A_D = 1.42$ . Instantaneous spanwise vorticity fields (left) and time-averaged flow velocity (right)

The systematic variation of Strouhal number and non-dimensional flapping amplitude can provide an existence plane of the wake scenarios experienced by this tear-shaped foil geometry. The latter involve vK-type, reverse vK-type and asymmetric wake regimes. Figure 5-35 shows both numerical and experimental  $A_D$  vs.  $Sr$  phase diagram, different symbols represent different types of wakes. It is observed that when the flapping amplitude is fixed and the Strouhal number is varied, the transition from vK-type to reverse vK-type wake can also occur with the increase of  $Sr$ . The vK-type wake occupies primarily the lower left region of the existence plane but extends to higher Strouhal numbers for the lowest amplitude tested.



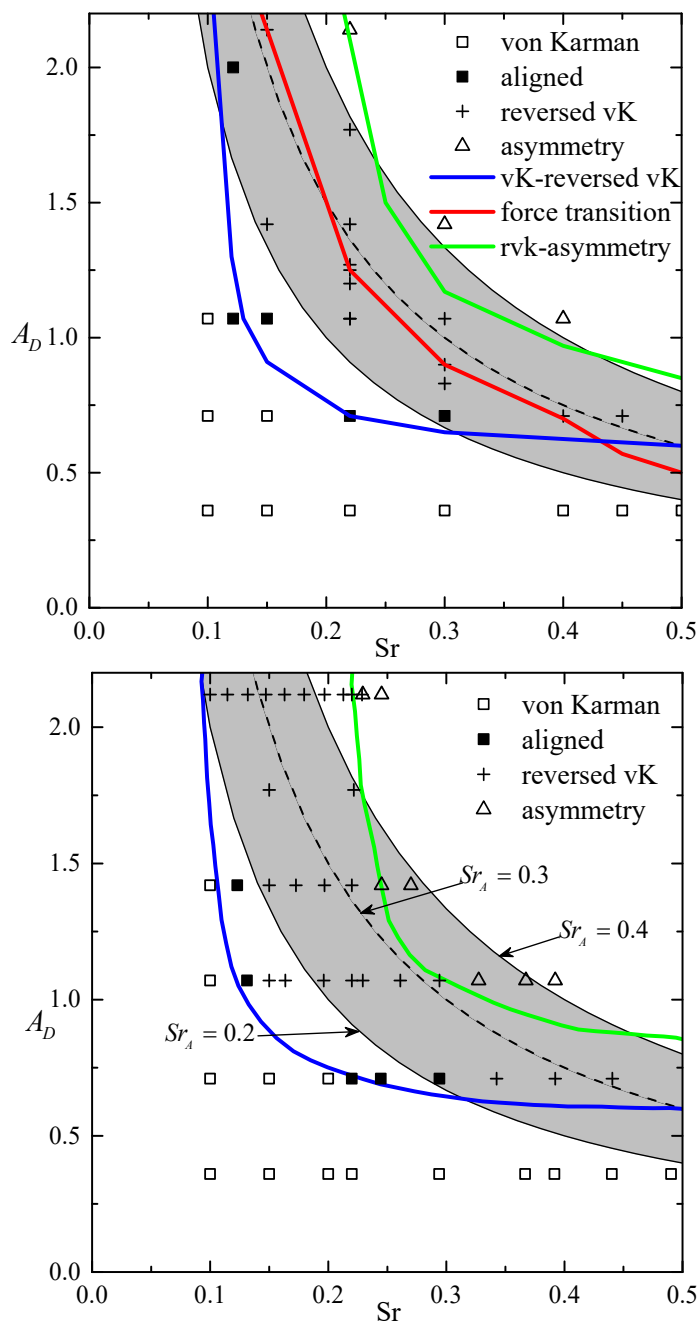


Figure 5-35.  $A_D$  vs.  $Sr$  map of the semi-circle foil at  $Re_c = 1173$ . Top: OpenFOAM simulations; bottom: experiments (Godoy-Diana et al., 2008).  $\square$ : vK wake;  $\blacksquare$ : aligned vortices (2S wake);  $+$ : reverse vK wake;  $\triangle$ : deflected rever-vK street resulting in an asymmetric wake. Blue line: transition between vK-reverse vK. Green line: transition between reverse vK and asymmetry regimes. Red line: predicted curve with  $\overline{C_x} = 0$  where the estimated drag-thrust transition occurs. The grey region corresponds to the  $Sr_A = 0.3 \pm 0.1$  interval

With increase of  $Sr$  and  $A_D$ , the vortex structures behind the pitching foil evolve from the vK regime to the reverse-vK regime (marked by the blue line in Figure 5-35), which can be univocally defined in the existence plane when the position of vorticity maxima, at any given time and horizontal position, cross the symmetry axis of the wake. It illustrates that the transition line tends to an asymptotic value of  $A_D \approx 0.6$  for  $Sr > 0.4$  so that a threshold non-dimensional amplitude value exists to produce a reverse vortex street. The reverse-vK region is bounded on the other side by the transition to asymmetric regimes represented by the green line. Besides, this map also agrees well with the experiments carried out by Schnipper et al. (2009).

The result of (0.22, 0.71) point in Figure 5-35 (the lowest-left solid black square) indicates that the vortices of alternating signs align on the symmetry line of the wake, but the force calculation in Table 5-11 reveals that the foil pitching at this frequency and amplitude still generates a drag force. In fact, the horizontal force turns into a thrust force at a much higher amplitude, i.e., larger than  $A_D = 1.07$ . Moreover, the red line in the top of Figure 5-35 marks the estimated force transition from drag to propulsive regimes for the pitching foil, which is in good agreement with the reference experimental observation. It is noted that the transition from vK to reverse-vK vorticity regime does not coincide with the drag-thrust transition. In most of the cases, the drag-thrust transition occurs after the vK–reverse vK wake transition has occurred but before the vortices evolve into an asymmetric wake. This is not expected from inviscid-flow theory, but it agrees with many experiments. The comparison of the existence plane in Figure 5-35 with the efficiency plane in Figure 5-30 indicates that, within the examined parameters, the efficiency is largest for the foil at point (0.30, 2.14) operating in asymmetric wake. Its instantaneous vorticity field, horizontal force and input power coefficients are shown in Figure 5-36. A strong dipolar structure is formed in each pitching cycle and propagates obliquely to one side of the symmetry line of the wake, while a much weaker single vortex is shed on the other side. Compared to the vK-wake cases as discussed in section 5.4.1, the horizontal force coefficient loses the symmetry and it generates drag for only one time in one cycle but still have positive power twice around the extreme pitching angles in a period. One should note that the numerically predicted wake scenario and the thrust level for this case are qualitatively consistent with the model tests, however in this wake regime three-dimensional effects were relevant in the reference experiments and they should be considered to confirm this efficiency behavior.

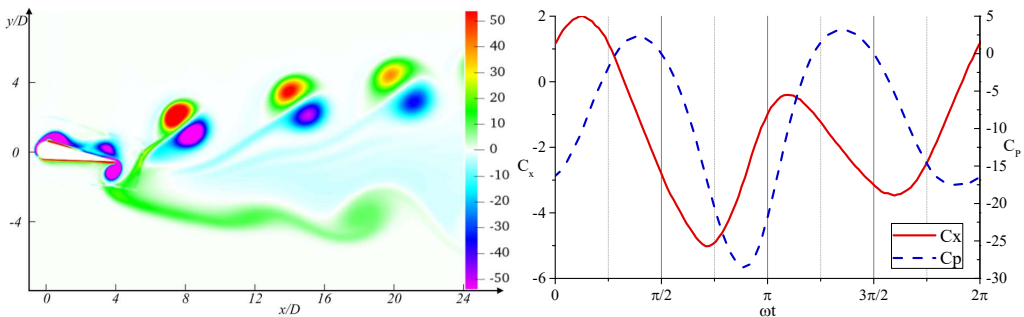


Figure 5-36. Instantaneous vorticity field at  $t = 15s$  (left, corresponding to  $\omega t = 9\pi/5$ ), the instantaneous horizontal force and input power coefficient (right) for the semi-circle foil at  $Sr = 0.30$  and  $A_D = 2.14$

The wake scenarios of NACA 0012 and NACA 0021 foils are studied in the same ranges of Strouhal number and flapping amplitude at  $Re_c = 1173$  as the semi-circle foil, employing the validated method. The diagrams of the three hydrofoils are plotted in Figure 5-37. Similarly as for the semi-circle foil, the wake structures of NACA 0012 and 0021 foils are vK-type wakes at small  $Sr$  and  $A_D$ , then evolve into aligned wakes with the increase of  $Sr$  and  $A_D$ , and enter the reverse-vK regime at sufficiently large  $Sr$  and  $A_D$ . However, there are apparent differences of the wake scenario transitions among the three foils. When the  $Sr$  is fixed and the  $A_D$  is varied, taking the  $Sr = 0.22$  as an example, it is found that the NACA 0012 foil undergoes the vK–reverse vK wake transition at lower non-dimensional flapping amplitude than the semi-circle foil, and the NACA 0021 foil is the last one to experience this wake transition. This is also the case for the drag–thrust transition. At the present Reynolds number, the NACA 0012 foil can generate thrust force at  $Sr_A > 0.23$ , the semi-circle foil around  $Sr_A > 0.28$  and the NACA 0021 foil higher than  $Sr_A > 0.31$ .

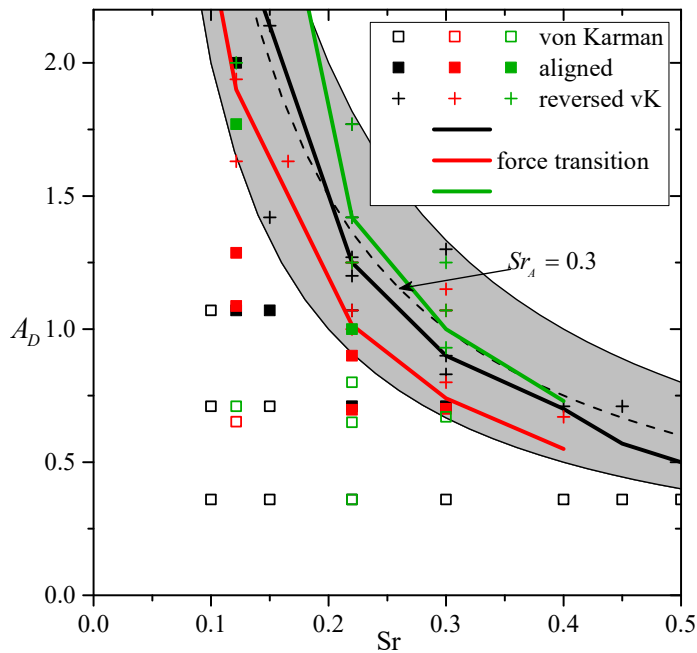
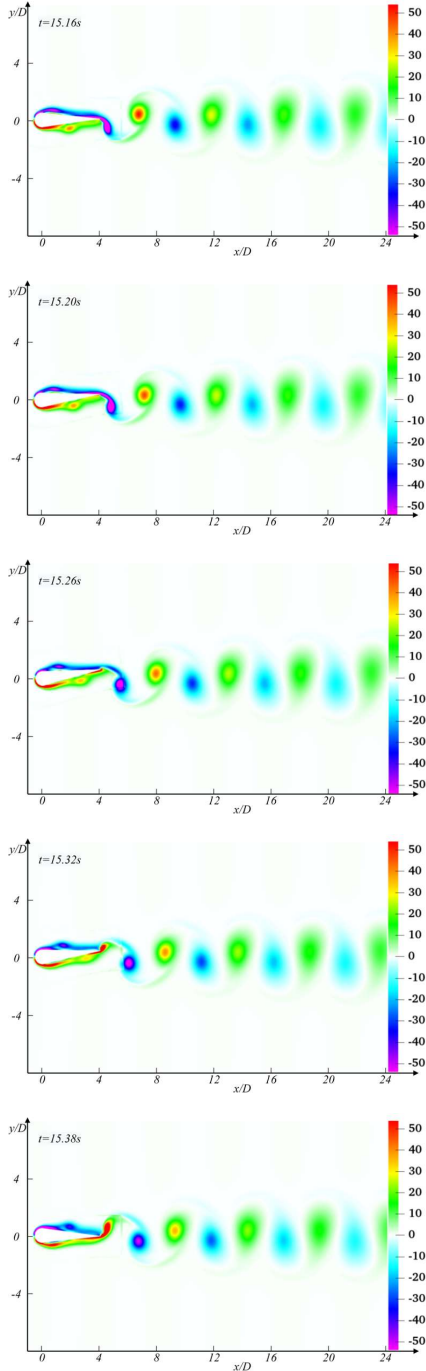


Figure 5-37.  $A_D$  vs.  $Sr$  map for the semi-circle foil (black scatter), NACA 0012 foil (red scatter) and NACA 0021 foil (green scatter) at  $Re_c = 1173$ .  $\square$ : vK wake;  $\blacksquare$ : aligned vortices (2S wake);  $+$ : reverse vK wake. Black, red and green solid lines: predicted curves with  $\overline{C_x} = 0$  where the estimated drag-thrust transition occurs for the semi-circle, NACA 0012 and 0021 foils, respectively. The grey region is the  $Sr_A = 0.3 \pm 0.1$  interval

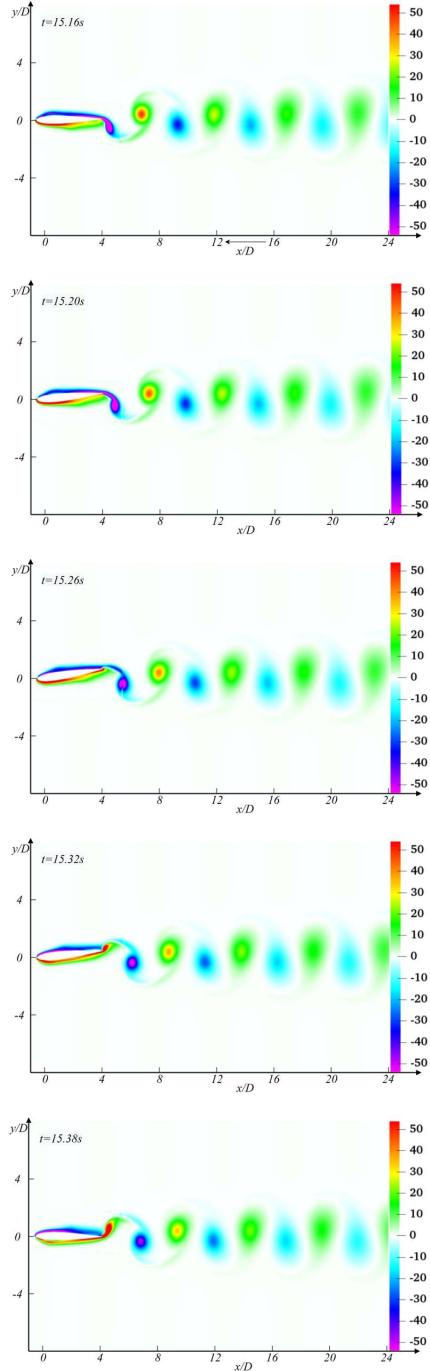
Lagopoulos et al. (2019) suggested a cycle-averaged swept trajectory length of the foil chord line to connect the vK–reverse vK wake development to the chosen kinematics. However, the foil profiles were not considered in their proposed universal scaling law of the drag-to-thrust wake transition. In our present simulations, the three hydrofoils with different shapes share the same time-averaged swept trajectory during the pitching motion, indicating that the influence of foil profile plays an important role to identify a self-similar characterization of flapping foil propulsion.

In the following, the vorticity fields for the semi-circle foil, NACA 0012, NACA 0021 and NACA deformable (D15) hydrofoils are compared at one of the conditions examined for the semi-circle foil, i.e.,  $Re_c = 1173$ ,  $f = 2.244 \text{ s}^{-1}$  and  $\theta_0 = 0.153 \text{ rad}$  ( $A = 6.25 \text{ mm}$ ), corresponding to  $Sr = 0.22$ ,  $A_D = 1.25$  and  $Sr_A = 0.275$  for the semi-circle foil.

(a)



(b)



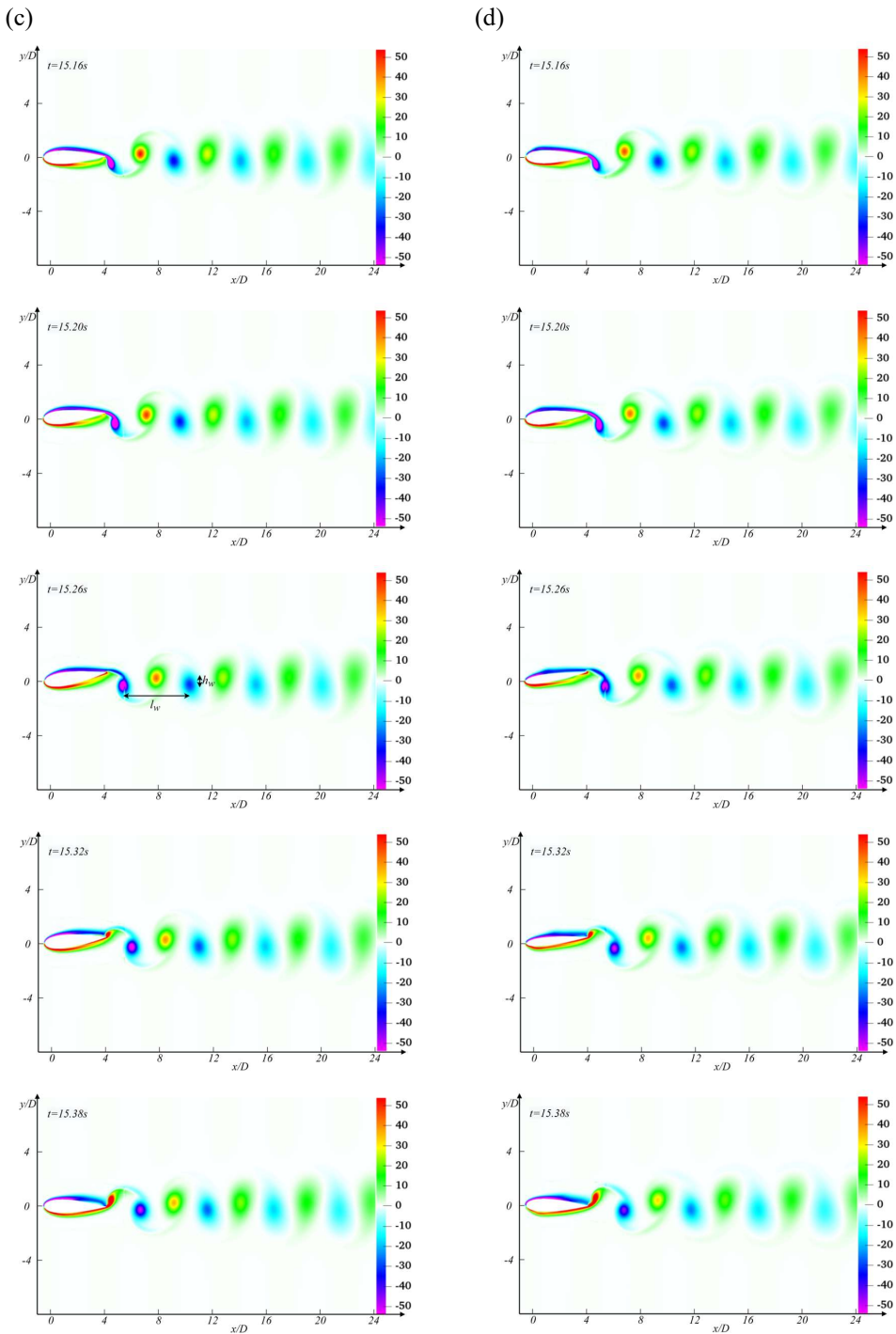


Figure 5-38. Instantaneous spanwise vorticity contours for (a) the semi-circle foil, (b) NACA 0012 foil, (c) NACA 0021 foil and (d) deformable NACA D15 foil in a half oscillation period at  $f = 2.244s^{-1}$  and  $A = 6.25mm$ .

From top to bottom:  $\omega t \approx 0, \frac{\pi}{4}, \frac{\pi}{2}, \frac{3\pi}{4}, \pi$

From the vorticity contours, we find that the flow tends to follow the profiles of three NACA foils and the flow separation occurs in the aft part of the foils, while it is difficult for the flow around the semi-circle foil to remain attached to the body. It confirms our explanation of the lowest shear stress for the semi-circle foil. However, it is not obvious to identify the differences among the wake structures behind these examined foils. A detailed estimation of the wake features for the examined foils is documented in Table 5-12, including the maximum vorticity intensity inside the latest shed negative and positive vorticities at instant  $t = 15.26s$  ( $\omega t \approx \pi/2$ ), the distance between two vortices in the same row ( $l_w$ , as shown in the third contour of Figure 5-38(c)), the distance between the two vortical rows ( $h_w$ ) as well as the dimensionless time-averaged streamwise velocity ( $\bar{u}/U$ ) along the wake centerline at  $x/D_{semi} = 6$ . The analysis of the vorticity field near the foils indicates that the intensity and relative locations of the vortex pair closest to the trailing edge are different. Even though the NACA 0012 and semi-circle foils have similar sharp trailing edges, it is quite surprising that the absolute extreme intensity values within the vortices of the NACA 0012 foil are much smaller than those of the semi-circle foil, while the values of NACA 0021 foil are comparable to the semi-circle foil. The deformable NACA foil generates vortices with the lowest absolute extreme values. There are not big differences in terms of  $l_w$  for all the examined foils, but apparently the wake width ( $h_w$ ) of the NACA 0021 foil is the smallest. The NACA 0012 and deformable D15 foil have the largest  $h_w$ , and it may be the reason why they can generate the maximum thrust force. The time-averaged streamwise velocity ( $\bar{u}/U$ ) along the wake centerline is the minimum for the NACA 0021 foil, followed by the semi-circle foil and then NACA 0012 foil. It indicates that the higher velocity exceedance behind the foil is not necessarily linked with stronger vorticities but may depend on the arrangements of two parallel vortical rows. Another surprise is that the deformable NACA foil (D15) has an even larger time-averaged mean velocity field than that of the NACA 0012 foil, though its time-averaged thrust force is slightly smaller. By recalling the instantaneous force coefficient in Figure 5-28, the deformable NACA foil is found to experience the largest instantaneous thrust and drag among all the examined foils. Besides, the top plot in Figure 5-18 shows that there is an approximately shift effect for the three rigid foils, i.e., their curves seldomly intersect. The above discussions suggest that to some extent, the value of time-averaged velocity exceedance behind the foil can represent the hydrodynamic forces acting on the foil for rigid flapping foils, but more attention should be paid when comparing with the deformable foils. Although the wake patterns are all reverse von Kármán and seem similar, there are distinctions in flow field details and its accumulation results in the significant differences of total forces, which can be seen in section 5.4.5.

Table 5-12. Wake features for the examined rigid foils at  $f = 2.244s^{-1}$  and  $A = 6.25mm$ 

Foil	Semi-circle	NACA 0012	NACA 0021	NACA deform D15
1st negative vorticity	-78.094	-68.203	-85.376	-67.026
1st positive vorticity	43.492	40.950	43.665	38.959
$l_w$ (m)	0.0250	0.0251	0.0248	0.0251
$h_w$ (m)	0.0038	0.0039	0.0029	0.0039
$\bar{u}/U$ at $x/D_{semi} = 6$	1.4542	1.5122	1.4447	1.5370

#### 5.4.4 Influence of Reynolds number and scaling of drag-thrust transition

To systematically quantify the effect of governing parameters on the forces and associated flow patterns of a flapping foil, numerical simulations have been carried out for various  $Re_c$  and  $Sr_A = Sr \times A_D$ . In particular, the kinematic viscosity of fluid was varied to ensure that only one parameter,  $Re_c$ , is changed during the study trying to identify a clear relationship between Strouhal number and Reynolds number.

Viscous-flow simulations, without turbulence model, have been performed for the NACA 0012, NACA 0021 and semi-circle foils from  $Re_c=500$  to about 4000, and the  $Sr_A$  is increased systematically from 0.1 in small increments until the time-averaged net force acting on the foil crosses zero and becomes negative. Zero net force identifies the critical  $Sr_A$  for drag-thrust transition for each examined  $Re_c$ .

The time-dependent horizontal force coefficients for the flapping semi-circle foil at  $Re_c = 3910$ ,  $A_D = 0.71$  and  $Sr = 0.22$  obtained with the three grid resolutions in Figure 5-39 confirm the results are converged in the 2D simulations.

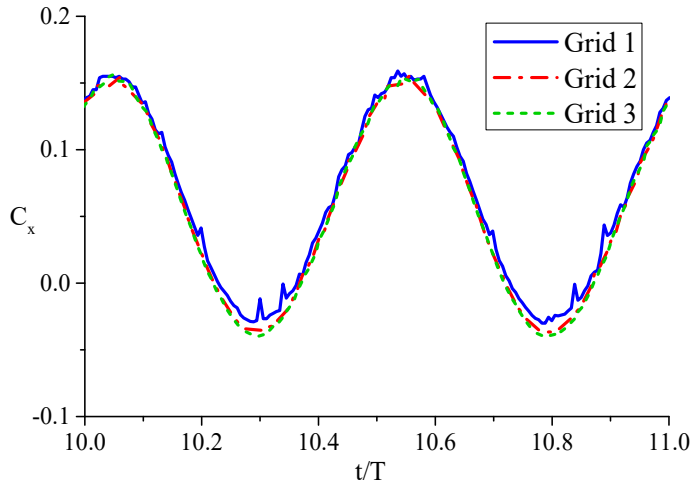


Figure 5-39. Horizontal force coefficient vs. time for three grid resolutions of the semi-circle foil at  $Re_c = 3910$ ,  $A_D = 0.71$  and  $Sr = 0.22$

In general, the hydrodynamic flow features and forces on the foils at different  $Re_c$  have the same trends as those shown in Figure 5-35 except that the lower left region of the phase diagram with  $0 < Sr < 0.1$  in some cases contains other types of wakes, for example more than two vortices could be shed from the foil per oscillation period.

The critical Strouhal number  $Sr_A^*$  at which the net horizontal force changes sign is not universal but depends on  $Re_c$ , as shown in Figure 5-40. This confirms that the hydrodynamic forces acting on the pitching foil have strong dependence on the chord-based Reynolds number  $Re_c$ . It is found from the figure that at the drag-thrust transition curve, the amplitude-based Strouhal number  $Sr_A^*$  is inversely related to  $Re_c$  in the present simulations. This finding is consistent with fish swimming studies by Borazjani and Sotiropoulos (2008) as well as those

on undulatory swimmers in nature reported by Lauder and Tytell (2005), documenting that the swimming  $Sr_A$  increases with decreasing swimming speed (i.e., decreasing the Reynolds number). It reveals that the drag-thrust transition of the foil pitching at the forced oscillations would become closer to the vk-reverse vK wake transition curve for increasing  $Re_c$ . As the thickness-based Reynolds number  $Re_D = UD/\nu$  is proportional to  $Re_c$ , it also indicates that the drag-thrust transition curve is strongly linked to the foil thickness-based Reynolds number  $Re_D$ . As last note, as the Reynolds number increases, the curves for the vk-to-reverse-vK wake transition and for the drag-thrust transition get closer and the  $Sr_A^*$  tends to be less affected by  $Re_c$ . This would suggest that at sufficiently large Reynolds number the inviscid theory can provide reliable results for the drag-thrust transition and that, therefore, rotational-flow effects dominate on viscous-flow effects. However, at this stage we cannot make a strong statement on these aspects. In fact, an attempt has been made to predict the hydrodynamic force on the pitching foil in nearly inviscid flow. To practically study this, a free-slip boundary condition has been implemented in OpenFOAM library and tested by studying two foil scenarios at the highest Reynolds number for reliable results in OF ( $Re_c \sim 10^6$ , see e.g., Reid and Hunsaker, 2017). The results of this effort are documented in Appendix C. Though they are promising, the comparison against reference results does not provide a full verification, therefore the simulation results employing this user-defined boundary condition are not presented here.

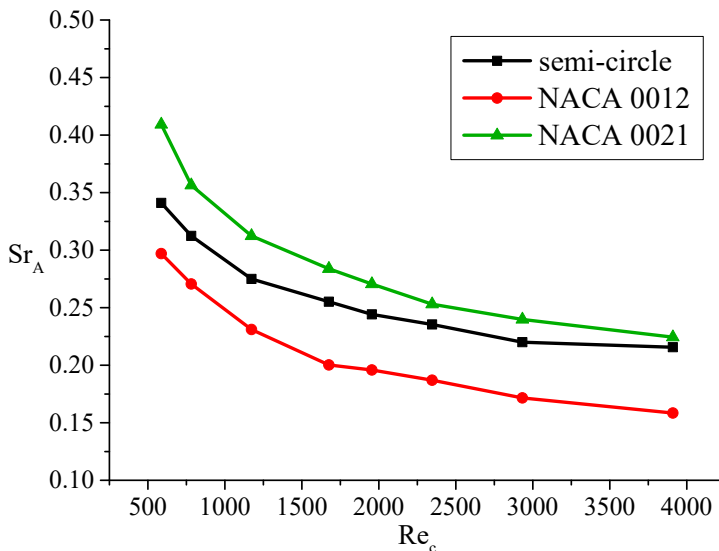


Figure 5-40. Strouhal number vs. Reynolds number for three pitching foils at drag-thrust transition condition

Though the drag-thrust transition  $Sr_A^*$  is inversely related to  $Re_c$  for all the three foils, the values of the  $Sr_A^*$  are obviously different. Fundamentally, the foil generates thrust force by displacing and accelerating fluid out of its path as it performs prescribed motion in the current. The quantity of fluid displaced by a pitching foil is expected to be dependent on the profiles of the foil over one period of oscillation, which may lead to the drag-transition difference among the three foils. Thus, a proper interpretation of the foil's drag-thrust transition should reflect the profile of the foil.



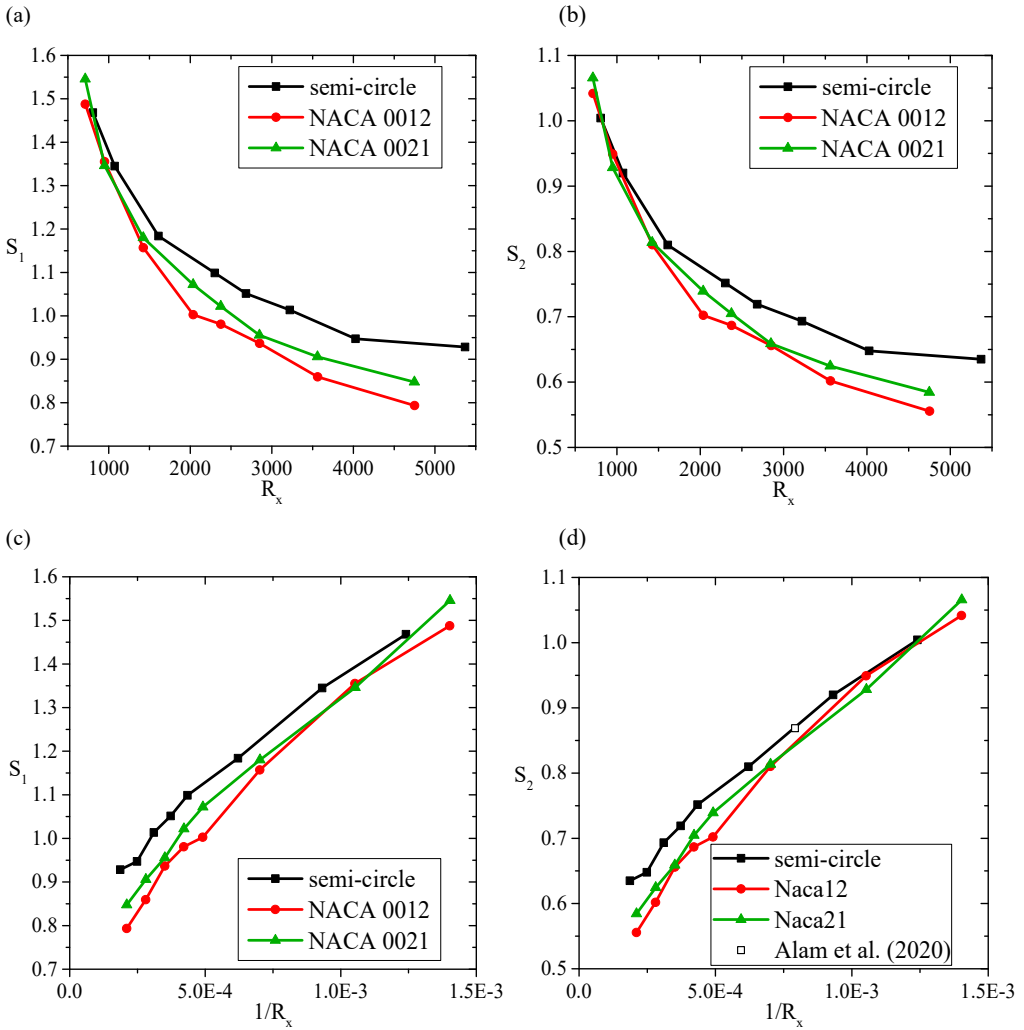


Figure 5-41. Best-fit curves of the drag-thrust transition plotted on different phase spaces: (a)  $S_1 - R_x$ , (b)  $S_2 - R_x$ , (c)  $S_1 - 1/R_x$  and (d)  $S_2 - 1/R_x$

To quantify the influence of the foil profile on the occurrence of drag-thrust transition, several parameters of the body are considered, such as the foil chord length ( $c$ ), maximum thickness ( $D$ ), perimeter ( $L_{pro}$ ) and area ( $a$ ). In fact, they are connected at different levels with the drag and thrust generation. For example, the chord length relates to the foil capability to release vortices from the trailing edge and so to thrust production, in fact the larger  $c$  is the thinner the trailing edge and so the stronger the vortex shedding from this is expected. The maximum thickness relates to the possible flow separation along the body and so pressure-loss drag production, in fact the larger  $D$  is the more pronounced the flow separation is expected. The circumference relates to shear stresses along the foil, in fact the larger  $L_{pro}$  is the higher the frictional drag production. Based on what is said, the nondimensional parameter  $\sqrt{cL_{pro}/a}$

relates to thrust and frictional drag,  $\sqrt{cD/a}$  relates to thrust and pressure drag,  $\sqrt{c^2/a}$  relates to thrust. Using these nondimensional parameters based on the geometrical features of the foils, an attempt was made to identify a proper scaling law for the drag-thrust transition, which properly considered the influence of pressure and friction drag, on one side, and thrust production on the other side. The following laws have been checked: (i)  $Sr_A^* \cdot \sqrt{cL_{pro}/a} = f(Re_c \cdot \sqrt{cD/a})$  and (ii)  $Sr_A^* \cdot \sqrt{c^2/a} = f(Re_c \cdot \sqrt{cD/a})$ . Herein, we define these variables as:  $R_x = Re_c \cdot \sqrt{cD/a}$ ,  $S_1 = Sr_A^* \cdot \sqrt{cL_{pro}/a}$  and  $S_2 = Sr_A^* \cdot \sqrt{c^2/a}$ . Figure 5-41 shows the drag-thrust transition lines for the three examined rigid foils using the aforementioned parameter definitions. The  $R_x$  in Figure 5-41(c) and (d) are represented in the inverse form so that a power law between the critical Strouhal number and Reynolds number is depicted by a straight line. The critical  $Sr_A^*$  from Alam and Muhammad (2020) simulation at  $Re_c = 920$  is also documented in the last plot, and it fits well with the present semi-circle simulation results. The scaling law of  $Sr_A^* \cdot \sqrt{c^2/a} = f(1/[Re_c \cdot \sqrt{cD/a}])$  seems to be the most promising for the examined foils indicating that the pressure drag may play a more relevant role than friction drag in this context. This finding provides an indication that in order to reach a desired speed for a marine vehicle, we can check from the above scaling law what Strouhal number should be implemented for the propulsor according to the Reynolds number.

### 5.4.5 GAMC analysis

In the previous sections the horizontal force was estimated from direct integration. This did not allow clear insights about the relative importance of the flow features near the foil and of those in the wake on the experienced force. Also, it was not obvious to distinguish the differences among the wake structures behind the examined foils for the different profiles, though the detailed estimations provided in Table 5-12 indicate there are slight differences in terms of vorticity intensity, wake width and distance between two alternating vorticities. The spatial accumulation of these differences is suspected to result in the different behaviors of pitching foils, i.e., NACA 0012 foil can generate mean thrust while NACA 0021 foil still experiences drag. This can be done enforcing conservation properties in a control volume. In the following, the generalized added-mass and circulatory (GAMC) force decomposition method for viscous flows (Limacher, 2019) is considered. In the 2D GAMC formulation, the total force can be divided into contributions from the control volume domain, foil surface (which is zero as the no slip boundary condition is applied) and the surfaces of the control volume.

$$\begin{aligned}
 \mathbf{F} = & -\rho \frac{\partial}{\partial t} \int_{V_1} (\mathbf{x} \times \boldsymbol{\omega}) dV - \rho \frac{d}{dt} \oint_{S_b} \mathbf{x} \times (\hat{\mathbf{n}} \times \mathbf{u}) dS \\
 & + \rho \oint_S \left( \frac{1}{2} \hat{\mathbf{n}} (u^2 + v^2) - (\hat{\mathbf{n}} \cdot \mathbf{u}) \mathbf{u} \right) dS - \rho \oint_S (\hat{\mathbf{n}} \cdot (\mathbf{u} - \mathbf{u}_S)) (\mathbf{x} \times \boldsymbol{\omega}) dS \\
 & + \mu \oint_S \left( \mathbf{x} \times \frac{\partial \boldsymbol{\omega}}{\partial n} - \hat{\mathbf{n}} \times \boldsymbol{\omega} \right) dS
 \end{aligned} \tag{5.14}$$

where  $V_1$  is the volume of the control volume bounded by the surface  $S$ , and  $S_b$  is the surface of the body.  $\mathbf{x}$  represents the position vector,  $\boldsymbol{\omega}$  is the vorticity vector, and  $\hat{n}$  is the normal vector pointing outwards from the domain everywhere. The detailed definitions are given in the appendix. There are five terms in the right-hand-side of Eq. (5.14). For the present pitching foil case, the surface integral term along the foil body and the last surface integral (multiplied with the fluid viscosity) along the computational domain boundary are relatively small compared to the total force. As our aim is to investigate the contributions from the vorticity fields of different foils, the first volume integral term is our focus of analysis.

From the definition in Eq. (5.4), it is known that to obtain the value of the time-averaged horizontal force, we should integrate in time the force and this somehow neutralizes the effect of the time derivative in the first term in the right-hand-side of Eq. (5.14). Thus, the vorticity impulse term ( $\int_{V_1} (\mathbf{x} \times \boldsymbol{\omega}) dV$ ) inside such time derivative can, to some extent, represent the contribution to the total time-averaged force. In addition, with this strategy we can avoid the errors associated with numerical estimates of the time derivative as the OpenFOAM results of this vorticity impulse term are not smooth functions with respect to time.

To compare the importance of vorticity field from wake region and foil region, this vorticity impulse term,  $P_{Vx} = -\int_{V_1} y\omega_z dV$ , is calculated in the two regions (foil and wake regions) shown in Figure 5-42.

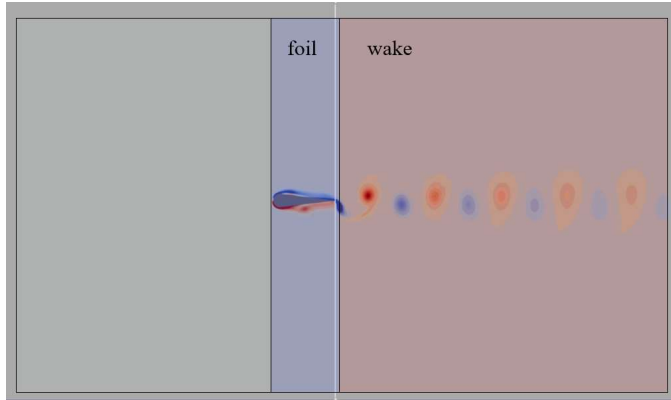


Figure 5-42. Schematic view of the foil and wake regions in the control volume

The results of  $P_{Vx}$  for the semi-circle foil, NACA 0012 foil, NACA 0021 foil and NACA deformable foil with  $\phi = 7\pi/4$  (D15, with the largest thrust) at  $Re_c = 1173$ ,  $f = 2.244 s^{-1}$  and  $\theta_0 = 0.153 rad$  ( $A = 6.25mm$ ) are presented in Figure 5-43. From the comparison of the values in different regions, the wake region plays an overall more important role than the foil region. The foil region causes drag while the wake region creates thrust force, and the region ahead of foil region gives little contribution to the volume integral term. By recalling the flow fields in section 5.4.3, even though the overall wake features for the NACA foils appeared quite similar, the corresponding load contributions shown in top plot of Figure

5-28 indicate clearer differences. Figure 5-43 demonstrates the accumulation of vorticity field distinctions causes important total force differences. The vorticity impulse  $P_{V_x}$  in the foil region confirms qualitatively the largest drag contribution connected with the semi-circle, followed by the NACA 0021 foil, the deformable NACA foil and by the NACA 0012 foil. The vorticity fields in Figure 5-38 show that the flow separation of the semi-circle foil occurs immediately downstream the frontal area, while the flow of other NACA foils would remain attached to the body till the aft part. These flow features indicate the pressure drag may be the main reason for the maximum  $P_{V_x}$  of the semi-circle foil in the foil region. The wake-region results confirm qualitatively the largest thrust contribution connected with the NACA 0012, followed by the semi-circle foil and by the NACA 0021 foil. The deformable NACA foil is between the two rigid NACA foils and is very close to the semi-circle foil. Table 5-12 shows that the vorticity intensity of the wake of the NACA 0021 foil is the second highest (NACA 0012 foil is about 5% smaller than NACA 0021 foil), but its wake width is the smallest (the value of NACA 0012 foil is about 6.5% larger), thus their combination (vorticity impulse) in the wake region gives the least contribution to the thrust force. On the contrary, the NACA 0012 foil has quite low vorticity intensity of the wake but the maximum wake width, and therefore connected with the maximum thrust contribution. The vorticity intensity of the semi-circle foil is larger than that of the deformable NACA foil, but its wake width is smaller than deformable NACA foil, so the  $P_{V_x}$  of the wake region in Figure 5-42 are comparable for these two foils. These discussions demonstrate that the combination of slight differences locally in wake can lead to relatively noticeable differences in total hydrodynamic forces.

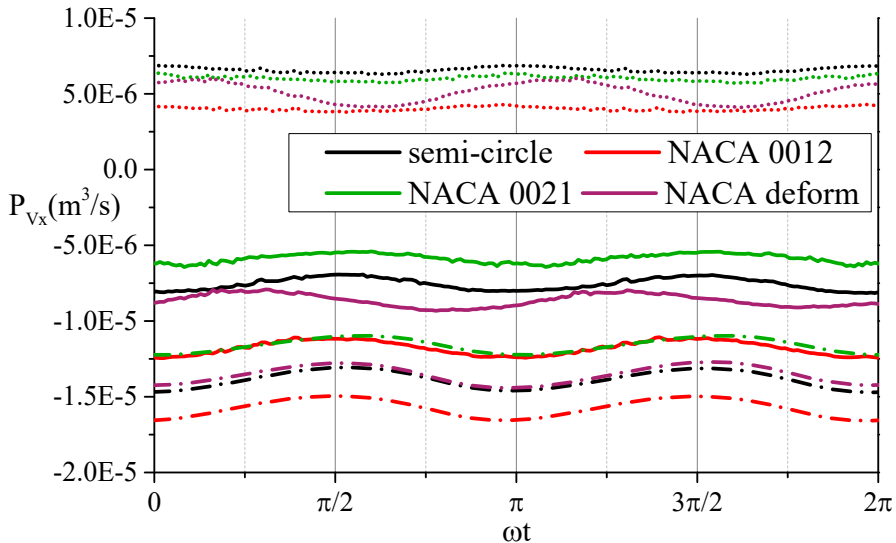


Figure 5-43. Forces contributed by the vorticity field from foil region (... , dot line), wake region (-.-, dashed dot line) and whole control volume region (solid line)

## 5.5 Summary

In this chapter, three rigid foils with different profiles (semi-circle foil, NACA 0012 foil and

NACA 0021 foil) are employed to elucidate the hydrodynamics of pitch motion. They are simulated systematically by varying the Reynolds and Strouhal numbers while keeping the center of rotation fixed.

The numerical results of semi-circle foil have shown good agreement with experimental data, characterizing the key dynamical features relevant to wake vortex systems: the transition from the well-known von Kármán (vK) wake to the reversed vortex street that signals propulsive wakes and the actual drag-thrust transition, which is not expected from inviscid-flow theory, but agrees with many experiments.

From the numerical results of the three foils, it is found that the maximum horizontal force approximately synchronizes with the inflection points of input power history. However, this relationship does not apply for the morphing foils additionally examined, so it might be valid only for rigid pitching foils.

Based on the results of the rigid NACA foils, it was attempted to identify a morphing strategy with the aim of combing the advantages of NACA 0012 and 0021 foils, i.e., generate a thrust similar to that of the NACA 0012 foil while reducing the hydrodynamic torque to a level comparable to that of the NACA 0021 foil. The performances of the deformable NACA foils were investigated by a developed OpenFOAM code. The results illustrate that the maximum thrust and drag force can occur at various instants within one period depending on the phase between morphing and pitching motion, but it makes little differences to the occurrence phases of the input power results. The deformable NACA foil with a morphing phase  $\phi = 7\pi/4$  with respect to the pitching motion can offer a compromise to let the foil have less torque and be robust as NACA 0021 foil while retaining the capability to create large propulsion force. These results are directly relevant for the examined rigid-foil scenario but pave the way for the use of morphing strategies to target optimized behavior between two generic rigid-foil scenarios.

For a given  $Re_c$  there is a unique  $Sr_A^*$ , at which pitch motion produces sufficient thrust to exactly cancel the hydrodynamic drag, making constant-speed self-propulsion possible. The critical  $Sr_A^*$  is a decreasing function of  $Re$  and approaches the range of ( $Sr_A=0.3\pm 0.1$ ) where fish-like swimming and flapping flight occur, suggesting that the conclusions obtained here should be relevant as interpretation tool in the study of natural systems. The 2D GAMC formulation analysis illustrates that the wake vortex plays an important role in creating thrust force.

In addition, a series of CFD sensitivity studies have been performed to investigate the effect of various numerical parameters on local and global phenomena of the pitching foil, including mesh motion methods, the effects of time schemes, grid resolution, overset region size and mesh ratio between overset and background mesh for the overset grid technique. Based on our cost-benefit analysis, the Euler scheme, the overset grid method with overset region having a distance slightly smaller than half foil length, as well as the same mesh size for overset and background grids are considered to be the most efficient numerical set-ups in the present pitching foil studies.

## Chapter 6

# Fish-like swimming foil studies

Most fish undulate their bodies and/or caudal fins (BCF) for cruising and fast start or escape. The movement of a fish body can typically be described as a propulsive wave with an increasing amplitude traveling towards the tail. In this chapter, the hydrodynamics of fish-like swimming foils has been numerically studied. The midline motions of swimming fish are modeled as a streamwise traveling wave. Firstly, viscous flow past traveling wavy foils has been numerically examined to analyze the flow characteristics. Then, the typical locomotion of BCF fish has been investigated using the developed self-propulsion strategy method introduced in chapter 4. The self-propelled fish-like swimming foil has been simulated in both calm water and current flow. In addition, the wall effect of the swim tunnel is studied as well for the fish swimming in currents. The definition of parameters used here without explanation can be found in previous chapters and nomenclature.

### 6.1 Forced fish-like swimming foil

Aquatic animals exhibit a wide variety of designs and propulsion modes. However, the majority of fishes and cetaceans generate propulsion force for cruising, fast-starting and maneuvering, especially at high speeds, by bending their bodies into a backward-traveling wave, i.e., opposite to the swimming direction, that extends to the caudal fin, a type of swimming often classified as body and/or caudal fin (BCF) locomotion (Videler, 1993). With the aim of revealing the fluid mechanisms behind the fishes' extraordinary performances, many researchers from different fields, such as biology, hydrodynamics and engineering, have investigated fish swimming behavior (Fish and Lauder, 2006), measured their metabolic rates (Webb, 1971), proposed hydrodynamic principles and scaling laws (Lighthill, 1960), and built robots replicating the function of fish (Triantafyllou and Triantafyllou, 1995; Sefati et al., 2013).

To better explore propulsive mechanisms involved in this mode of fish swimming, the wave-like swimming motion of the body is usually used as an essential model to deal with the propulsion of fish. Experimental studies were carried out to deal with the drag reduction and flow behavior near a traveling swimming body (Barrett et al., 1999). The wake behind free-swimming fish or organisms were also measured using the digital particle image velocimetry techniques (Nauen and Lauder, 2002). On the other hand, viscous flow past traveling wavy bodies has also been studied numerically. Liu et al. (1997) analyzed the hydrodynamics of an undulatory swimming tadpole and first confirmed that most of the results from the two- and three-dimensional simulations were closely matched with each other. Shen et al. (2003), Dong and Lu (2007) investigated the turbulent flow over a flexible wall undergoing a streamwise traveling wave motion and revealed the hydrodynamic behaviors based on drag reduction and

optimal propulsive efficiency. The numerical simulations of swimming in nature reviewed by Liu (2005) have produced important results and shed light into the hydrodynamics of aquatic swimming. Paniccia et al. (2021a) used the impulse formulation to separate and emphasize the role of the added mass and vorticity release to evaluate in a neat way their specific contributions in the self-propelled aquatic locomotion. It should be noted that all these studies focused on simulating a specific aspect or flow regime of aquatic swimming, and as such systematic parametric investigations of the hydrodynamic performance of various modes of aquatic swimming have yet to be reported in the literature.

As for flapping foils, there are two important non-dimensional parameters that characterize the steady inline undulatory performance of fishes: the Reynolds number of the flow based on the fish length ( $Re_L = UL/\nu$ ) and the Strouhal number ( $St = fA_m/U$ ) of the undulatory body motion. Here  $U$  is the steady inline swimming speed or the free-stream velocity,  $L$  is the chord length of the foil,  $f = 1/T$  is the tail beat frequency, and  $A_m$  is the peak-to-peak amplitude at the trailing edge, i.e., the maximum lateral excursion of the tail over one period, as shown in Figure 6-1. In the present study, a systematic investigation of carangiform swimming over a range of  $Re_L$  and  $St$  is carried out.

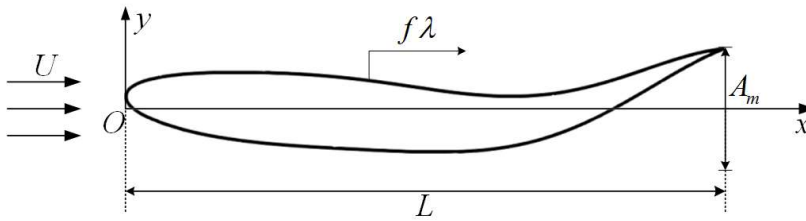


Figure 6-1. Schematic view of the fish model with the leading edge of the body located at  $x = 0$  at rest. An elongated body of length  $L$  undulates in a flow of speed  $U$  with a wave traveling backward at speed  $f\lambda$  and amplitude  $A_m$  at the trailing edge

As found in the Atlantic salmon experiments outlined in chapter 3, fishes with blunter bodies tend to swim slower than slimmer fishes, and they have limited ability to cruise steadily at high velocities. This poses the following research questions: *How much the shape influences the fishes' swimming behavior and its performances? Is bluntness always a negative feature?*

### 6.1.1 Swimming kinematics

In this chapter, the BCF propulsion is investigated with particular focus on carangiform and sub-carangiform swimming motions. In order to capture the main features of this swimming mode while keeping the problem complexity manageable, only the main body of the fish and its caudal fin are taken into the model, i.e., neglecting the other fins or details on the body such as scales, finlets and other protrusions. Besides, in order to make expedient computations, and as the swimmers often bend the body as a plate, i.e., it is quasi-two-dimensional in the oscillation plane, 2D simulations are performed here to investigate the influence of various parameters on the swimming behavior.

To answer the targeted research question, two streamlined symmetric fish-like shapes, i.e., the NACA 0012 and NACA 0021 foils, are chosen as profiles of corresponding undulating foils at their equilibrium position. The leading edge of each body at rest is located at  $x = 0$  (the origin  $O$ ) and its chord length  $L = 1m$  is used to make nondimensional the spatial variables of the problem. The kinematics observed in carangiform swimmers can be resembled in the form of a wave traveling in the streamwise direction. The lateral displacement,  $y$ , of a point located at  $x$  along the foil is given at time  $t$  by:

$$y(x, t) = a(x)\sin(2\pi(x/\lambda - ft)) \quad (6.1)$$

where  $a(x)$  is the envelope of the prescribed backward traveling wave of wavelength  $\lambda$  and frequency  $f$ , which is approximated a quadratic polynomial to reasonably represent the lateral motion of the backbone undulation of fish swimming. This type of analytical expression has been obtained by fitting data from direct fish observations in many previous works (e.g., Videler and Hess, 1984). Among them, the prescribed kinematics of a steadily swimming saithe, a typical carangiform swimmer, is often considered. Based on the experimental observations from marine biologists (Videler 1993), the latter can be modelled as:

$$a(x) = 0.1 - 0.0825(x - 1) + 0.1625(x^2 - 1) \quad (6.2)$$

$$\lambda = 1 \quad (6.3)$$

Here the equation implies a wavelength equal to the fish length. Figure 6-2 shows the prescribed envelope of this carangiform motion.

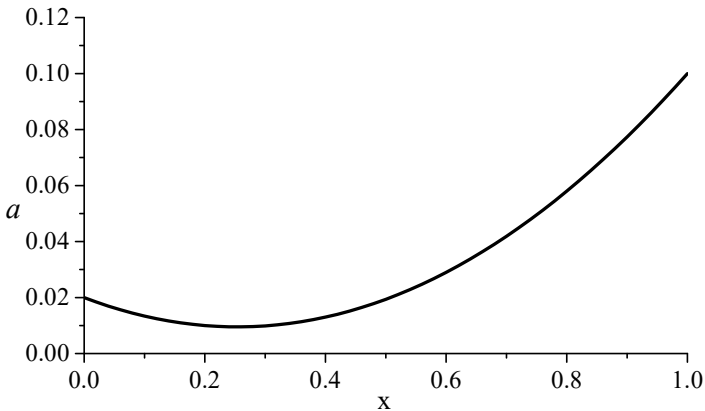


Figure 6-2. Prescribed amplitude envelope of the carangiform motion

To set the kinematic conditions on a deformable body, following the strategy proposed by Liu et al. (1996) and Dong and Lu (2007), the body length  $L$  is assumed to be unchanged during traveling wave and its undulation is purely a lateral compressive motion.

### 6.1.2 Numerical setup

The lateral flexible motion of the fish is prescribed using the overset grid method, which has been described in detail in chapter 4. We have demonstrated the ability of this strategy within



the OpenFOAM platform to simulate accurately the flow around rigid and deformable moving bodies. In order to validate the code for simulating undulating fish-like foils in this study, the force and power resulting from a fully imposed kinematics are compared with results reported in the literature (Dong and Lu, 2007), where the simulations are performed for Reynolds number equal to 5000, which is in the range of intermediate Reynolds numbers for swimming fish, i.e.,  $Re_L \sim 10^3$  (McHenry et al., 2003). Then,  $Re_L$  is varied systematically over the intermediate range to provide some insights into the complex relationship between  $Re_L$  and  $St$  and to explore the energetics of fish with different profiles under controlled conditions with varying governing parameters. In addition, the undulatory frequency  $f$  in the present section is changed from  $0.5s^{-1}$  to  $2.0s^{-1}$  for investigating different flow patterns past the traveling wavy fish-like foil.

In the present numerical simulations, the 2D computational domain around the NACA 0012 foil is defined by a rectangle extending 2 body lengths upstream and 7 body lengths downstream, and the lateral dimension (i.e., in  $y$  direction) is set to  $-3L < y < 3L$ . Boundary conditions for this hydrodynamic problem are shown in Figure 6-3. Similar as in the studies of chapter 5, a no-slip condition is enforced along the deformable foil with prescribed undulatory motions. Zero gradient conditions are applied to the top and bottom domain boundaries, which means the gradients of the velocity and pressure quantities are equal to zero in direction perpendicular to these boundaries ( $y$ -direction in this case), i.e., the actual value is constant from the patch internal field onto the patch faces. A uniform inflow condition is enforced at the inlet while a uniform pressure condition is used at the outlet. Herein, to avoid a break-down at the beginning of the numerical simulations, we adopted a sinusoidal ramp function lasting 1s starting from zero to a desired constant velocity ( $U_c = 1BL/s$  in the study) for the inlet. The boundary conditions in the third direction ( $z$  direction) for all variables are set to be empty as none of them are solved consistently with the two-dimensional flow assumption. For the interpolation layer in the overset mesh, the “overset” boundary condition is applied.

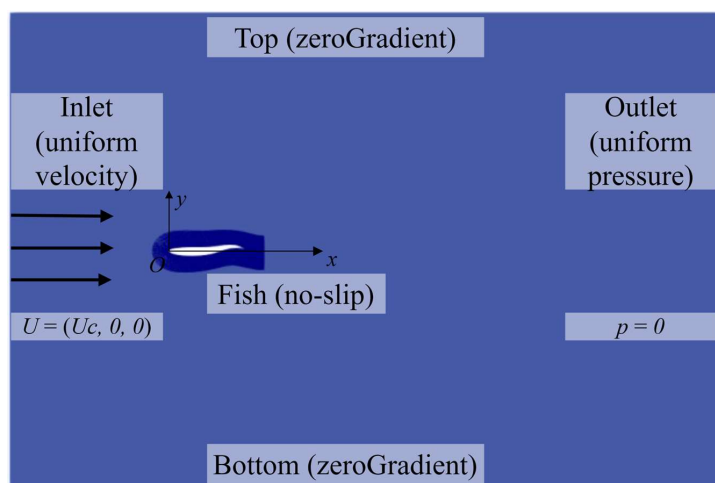


Figure 6-3. Schematic view of the undulating NACA 0012 fish simulation configuration with the reference system

A grid refinement study is carried out for the  $Re_L = 5000$  and  $f = 1.2s^{-1}$  case for both NACA 0012 and NACA 0021 fish-like foils using a series of successively finer meshes. The uniform structured hexahedral cells making up the meshes are given in Table 6-1. We shall refer to the grids of NACA 0012 fish as Grid 1-3, and the grids of NACA 0021 fish as Grid A-C.

Table 6-1. Grid resolutions for the NACA 0012 and NACA 0021 fishes

NACA 0012	Grid 1	Grid 2	Grid 3
Nodes along fish	156	212	294
Cells in BG grid	240000	540000	1071460
NACA 0021	Grid A	Grid B	Grid C
Nodes along fish	110	158	216
Cells in BG grid	135000	240000	540000

To demonstrate the effect of grid refinement on the instantaneous force, the time histories of the horizontal force coefficients (defined as  $C_x = F_x/0.5\rho U^2 L$ ) experienced by the undulatory fishes within one complete cycle are shown in Figure 6-4. It is noted that there are spikes in the force coefficient histories for all the cases. They are reasonably due to the stretch and extrusion of the body-fitted overset grid mesh during fish flexible swimming motion, as well as the linear interpolation between overset and background grid systems in OpenFOAM. This phenomenon can also be observed in previous studies using different numerical methods (see e.g., Borazjani and Sotiropoulos, 2008; Feng et al., 2019) and considered to be mainly resulted from mesh deformation. In spite of the spikes, the numerical results are stable in long-time simulations (not shown here) and the time-averaged values have shown convergence and good consistency with reference data, for instance in Figure 6-5. It is found that Grid A is too coarse for this deformable moving body simulation and causes many large spikes, which are due to interpolation errors associated with the coarse mesh in the vicinity of the overset domain boundary. Though the computed force coefficient histories of the other grids also exhibit spurious high frequency oscillations, the amplitudes of these spikes are seen to become smaller with the grid refinement. The oscillations are drastically reduced on Grid 2 for NACA 0012 fish and Grid C for NACA 0021 fish. Grid 3 has the smoothest force history for NACA 012 fish, but the computational cost for a simulation of  $6s$  ( $t/T = 7.2$ ) is much more expensive (95208s) compared to the Grid 2 (20480s). Therefore, as a compromise between computation accuracy and efficiency, Grid 2 and Grid C are employed for all the further simulations discussed in the present study.

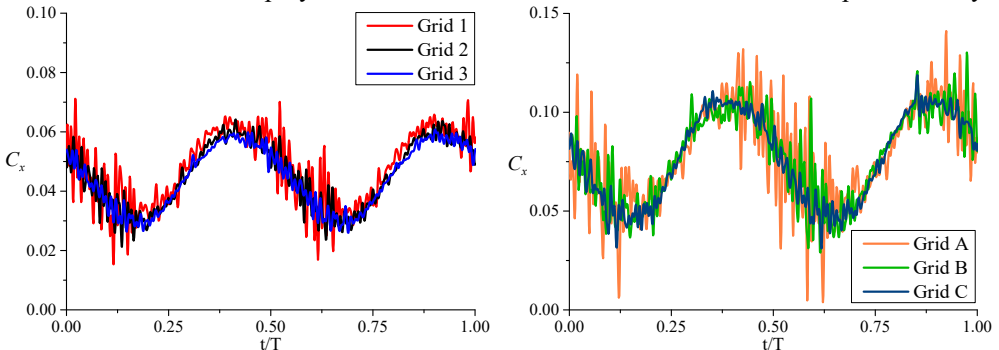


Figure 6-4. Horizontal force coefficient vs. time of different grid resolutions for NACA 0012 (left) and NACA 0021 fish (right). Positive and negative values indicate that the net force is of drag- and thrust-type, respectively

### 6.1.3 Calculation method of swimming forces and efficiency

#### Force and power calculation

Prediction the drag force and the power consumption of the swimming fish is directly relevant to assess fish performances and of great significance to guide a proper design of underwater bio-inspired vehicles. In general, the total force acting on the fish body consists of two components: a pressure force ( $F_{xp}$ ) due to pressure distribution caused by the boundary layer and flow separation, and a friction force ( $F_{xv}$ ) due to tangential stresses along the body surface. Similar as for the flapping-foil case, the pressure and friction components of the horizontal force coefficients are defined as  $C_{xp} = F_{xp}/0.5\rho U^2 L$  and  $C_{xv} = F_{xv}/0.5\rho U^2 L$ .

The total power  $P_T$  required for the propulsive motion of the undulatory fish body also consists of two parts (Dong and Lu, 2005). One is the swimming power  $P_S$  due to the lateral oscillation of the traveling wave motion, which is define as follows:

$$P_S = -\oint (f_{yp} + f_{yv}) \frac{dy_w}{dt} ds \quad (6.4)$$

where  $\oint$  denotes the integration along the entire fish body surface (profile in 2D),  $f_{yp}$  and  $f_{yv}$  are the pressure force and friction force per unit length in  $y$  direction, respectively.  $y_w$  represents the local lateral displacement of the fish body surface (profile), and then its time derivative  $dy_w/dt$  is, in our case, the local velocity due to the lateral undulations.

The second contribution to the total power is the power required to overcome the horizontal force, and it is calculated as:

$$P_D = F_x U \quad (6.5)$$

Thus, the total power is obtained by adding the above two parts, i.e.,  $P_T = P_S + P_D$ . The corresponding nondimensional power coefficients are  $C_{PT} = P_T/\frac{1}{2}\rho U^3 L$ ,  $C_{PS} = P_S/\frac{1}{2}\rho U^3 L$  and  $C_{PD} = P_D/\frac{1}{2}\rho U^3 L$ .

In the numerical simulations performed with our code developed in the OpenFOAM platform and with the employed numerical setup, periodic features of time-dependent forces and powers are typically reached after three to four oscillation cycles. The time-averaged values presented in this section are computed over five undulatory periods in the steady-state conditions.

The verification study of the adopted method has been carried out based on the numerical results from Dong and Lu (2007). Figure 6-5 shows the time-averaged force and power coefficients of the NACA 0012 fish at  $Re_L = 5000$ , compared to the reference values. They have predicted decreasing total force from positive to negative values and a concave upwards total power with the increase of oscillating frequency. Despite slight larger values at the highest frequency, the

comparison illustrates that the present results are in good agreement with the reference data, demonstrating the effectiveness and accuracy of our OpenFOAM code.

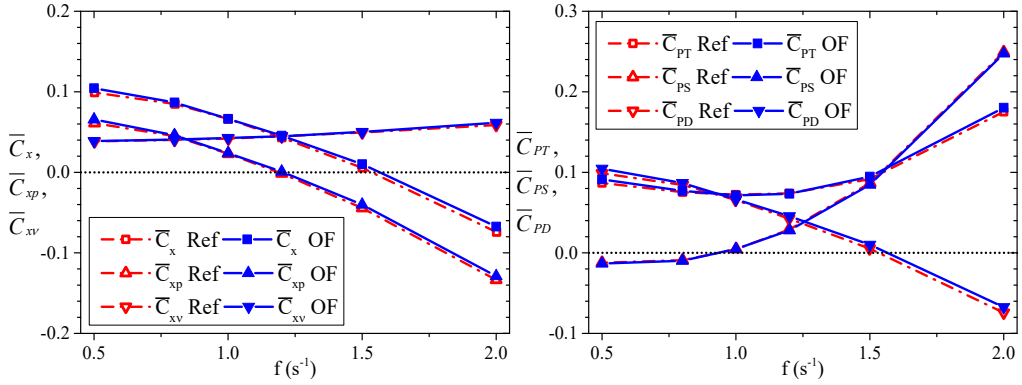


Figure 6-5. Time-averaged horizontal force coefficients (left) and power coefficients (right) for the NACA 0012 fish at  $Re_L = 5000$ . The results are compared with the reference simulations carried out by Dong and Lu (2007)

From the left plot in Figure 6-5, the time-averaged horizontal pressure force coefficient  $\overline{C}_{xp}$  and total force coefficient  $\overline{C}_x$  decrease with the increase of the undulatory frequency, while the friction force coefficient  $\overline{C}_{xv}$  increases almost linearly. Herein, the  $\overline{C}_{xp}$  becomes negative and contributes to the thrust force at  $f > 1.2s^{-1}$ . Due to the increase in friction drag force, the time-averaged total horizontal force turns into a negative value (i.e., thrust force) at higher frequency, approximately at  $f > 1.5s^{-1}$ . This finding is consistent with studies of viscous flow past a streamlined traveling wavy wall (Dong and Lu, 2005).

From the results of the power coefficients, it is found that the time-averaged swimming power  $\overline{C}_{PS}$  rises exponentially with the increase of frequency in order to produce the corresponding lateral undulations of the fish body.  $\overline{C}_{PS}$  is slightly negative before  $f = 1.0s^{-1}$ , and increases to 2.5 around at  $f = 2.0s^{-1}$ . The negative value of  $\overline{C}_{PS}$  indicates that the traveling wave motion of the body can be actuated by the current and thus no power is needed for that. The  $\overline{C}_{PD}$  decreases monotonically as the frequency increases, which is related with the drop of pressure force  $\overline{C}_{xp}$ . Its negative value means that the undulatory fish is propelled by the thrust force, whose energy is provided by the swimming power  $\overline{P}_S$ . As a result, the total power cost by the fish,  $\overline{P}_T$ , is a concave curve upwards with the minimum value around  $f = 1.0s^{-1}$ .

### Drag and thrust decomposition

For the studies on fish swimming performances, the definition of the efficiency, based on the net thrust force and power, is of significance but is also controversial and ambiguous. The main problem results from the fact that for the fish-like swimming, the acquirement of the net thrust force is not straightforward because the propulsor is the fish body itself, and it produces thrust and experiences drag simultaneously. These force contributions have the same average

value in steady free-swimming and the thrust is larger than drag for accelerating fish. Some researchers such as Gray (1936) carried out their studies on fish locomotion based on the possibility to distinguish drag and thrust in steady swimming. Schultz and Webb (2002) claimed the dilemma that sources of drag and thrust are not separable for fish in axial undulatory self-propulsion.

In this work, the approach to calculate the thrust and drag forces proposed by Borazjani and Sotiropoulos (2008) is adopted. According to their description, the horizontal force could contribute to either hydrodynamic thrust  $F_T(t)$  or drag force  $F_D(t)$  depending on whether the horizontal force  $F_x(t)$  is negative or positive. To separate the two contributions the instantaneous force is defined to be decomposed as follows:

$$-F_T = -(F_{Tp} + F_{Tv}) = \frac{1}{2}(F_{xp} - |F_{xp}|) + \frac{1}{2}(F_{xv} - |F_{xv}|) \quad (6.6)$$

$$F_D = F_{Dp} + F_{Dv} = \frac{1}{2}(F_{xp} + |F_{xp}|) + \frac{1}{2}(F_{xv} + |F_{xv}|) \quad (6.7)$$

It is obvious that the thrust  $F_T(t)$  produced by the above force decomposition method will have non-zero values only at the time instants when the instantaneous net horizontal force  $F_x(t)$  is of thrust type. Similarly, the drag  $F_D(t)$  is not zero when  $F_x(t)$  is of drag type.

From the decomposition given by Eqs. (6.6) and (6.7), the net force can be constructed as:

$$F_x(t) = F_D(t) - F_T(t) \quad (6.8)$$

The time-averaged thrust  $\overline{F_T}$  and drag  $\overline{F_D}$  are obtained by taking the mean values of these instantaneous forces over several oscillation periods in the steady-state conditions, respectively.

### Swimming efficiency calculation

The definition of the fish swimming efficiency has been controversial and ambiguous. Among various methods, Froude efficiency is often used by many researchers to analyze fish swimming performances. It is introduced based on the time-averaged zero horizontal forces for steady inline swimming, that is, when the thrust force can exactly balance the drag force. As discussed by Tytell and Lauder (2004), the Froude propulsive efficiency is proposed in terms of the net thrust force at constant inline swimming speed as follows:

$$\eta = \frac{\overline{F_T}U}{\overline{F_T}U + \overline{P_S}} \quad (6.9)$$

This formula indicates the percentage of the total power that is used for the thrust generation. The variables herein are the same as in the last section, i.e.,  $F_T$  and  $P_S$  represent the net hydrodynamic thrust force and the swimming power due to the fish's lateral undulatory motion, respectively.

It has already been known that the thrust force  $F_T$  cannot be measured directly in experiments or simulations, but we can still find alternative ways to calculate them using either a mathematical model, such as Lighthill's elongated body theory (EBT) for steady swimming

(Lighthill, 1971), or directly from the results of the numerical simulation, as introduced by Eq. (6.6). Although the EBT overestimates the efficiency (Cheng and Blickhan, 1994) as it is by itself an inviscid theory, it provides a simple and easy method to measure the efficiency and relate the efficiency with the Reynolds number associated with the real swimming fish. The Froude efficiency based on the EBT is given as:

$$\eta_{EBT} = \frac{1}{2}(1 + \beta) \quad (6.10)$$

where  $\beta = U/V$  is the speed ratio of the swimming speed  $U$  to the wave speed  $V = f\lambda = \omega/k$  of the body undulation. In addition, an improved EBT efficiency approach containing the slope of the amplitude function at the fish tail has been proposed by Cheng and Blickhan (1994), and herein it is denoted as EBT-2 method. Then the Froude efficiency becomes:

$$\eta_{EBT-2} = \frac{1}{2}(1 + \beta) - \frac{1}{2}\alpha^2 \frac{\beta^2}{1+\beta} \quad (6.11)$$

$$\alpha = \frac{\lambda}{2\pi} \frac{a'(L)}{a(L)} \quad (6.12)$$

here  $a(x)$  is the amplitude of the fish traveling wavy motion, and  $a'(L) = \partial a / \partial x|_{x=L}$  is the local slope at the tail.

#### 6.1.4 Results and discussion

Here, the characteristics of the flow over the undulating fish will be examined in terms of local quantities such as the vorticity field, and integrated/global quantities such as the forces, the power consumption, the swimming efficiency as a function of the Strouhal and Reynolds numbers. More in detail, the vortex structures in the wake of the fishes are illustrated and the wake patterns after fishes under various conditions are compared and analyzed.

In the following discussion, the hydrodynamic loads and flow features of the NACA 0012 fish-like foil are firstly examined at  $Re_L = 5000$ , and then followed by the analysis on the influence of the Reynolds number. Subsequently, the simulation results of the NACA 0021 fish-like foil are compared with the NACA 0012 fish to investigate the body shape effect. Then, the swimming efficiency and the influence of Strouhal number are discussed for the NACA 0012 fish-like foil. Lastly, this undulatory deformable foil is compared against the rigid flapping foil under the same oscillating frequency and amplitude to identify which propulsion method can be more efficient.

#### Force and power consumption

Figure 6-6 shows the corresponding instantaneous horizontal force results for all the above cases at  $Re_L = 5000$  within one oscillation period in steady-state conditions as a function of the Strouhal number  $St = fA_m/U$ . As described in the swimming kinematics section, in this case the peak-to-peak amplitude at the trailing edge is  $A_m = 2a(L) = 0.4m$ . In other words, for  $f = 0.5 - 2.0s^{-1}$ , the Strouhal number ranges as  $St = 0.1 - 0.4$ . We should recall that the fish is forced to perform prescribed motions in this section, and thus the net horizontal force

is absorbed by the hypothetical tether that keeps the fish in place. It means that this force would accelerate the fish either forward or backward depending on the sign of the force if the numerical tether is removed. The black solid line in Figure 6-6 is the force coefficient calculated for the case of a rigid body with the same shape as the fish-like foil in its equilibrium configuration and at rest ( $St = 0$ ) at the same Reynolds number, which is a constant value  $C_x \approx 0.054$ .

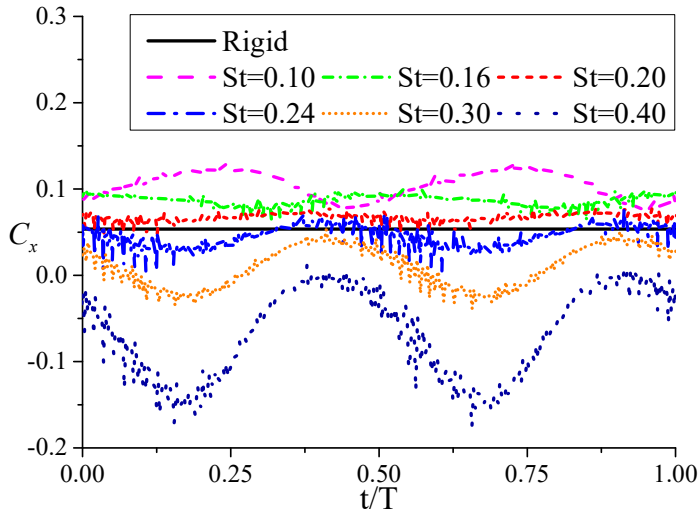


Figure 6-6. Instantaneous horizontal force coefficients within one cycle for the NACA 0012 fish-like foil at  $Re_L = 5000$ . Rigid case represents the body is a static NACA 0012 foil in the flow at zero angle of attack

From the results we can see that for all the examined swimming scenarios of the NACA 0012 fish-like foil, the forces experience two peaks in one oscillation period due to the traveling wavy motion. Surprisingly, the swimming fish even suffers a greater drag force than the still rigid fish at small Strouhal number  $St \leq 0.20$ . Within this range, the lower frequencies of body undulations can cause the larger amplitudes of drag force. The total horizontal force remains a drag throughout the entire period when  $St < 0.24$  and the first excursions into the thrust regime occur at  $St = 0.30$ , in which case the drag-state force has also smaller magnitude due to the faster traveling wavy motion. Further increase of the Strouhal number leads to larger amplitude and longer duration of the force in the thrust regime, and therefore to a total time-averaged thrust force.

To examine more in-depth the behavior of the time dependent horizontal force, the time histories of the three force coefficients within one complete period in steady-state conditions for two cases  $f = 1.0s^{-1}$  and  $f = 1.5s^{-1}$  are shown in Figure 6-7. The friction force  $C_{xv}$  varies little with time, i.e., is approximately constant in both cases, and gets larger at higher frequency. The pressure force  $C_{xp}$  keeps positive (drag force) during one cycle at  $f = 1.0s^{-1}$  while it is always negative at  $f = 1.5s^{-1}$ . It is considered that the pressure force often makes an essential contribution to the propulsion of the undulatory fish with traveling wavy motion. When the negative  $C_{xp}$  is large enough to exceed the positive  $C_{xv}$ , the swimming fish is able to generate thrust force instead of experiencing drag.

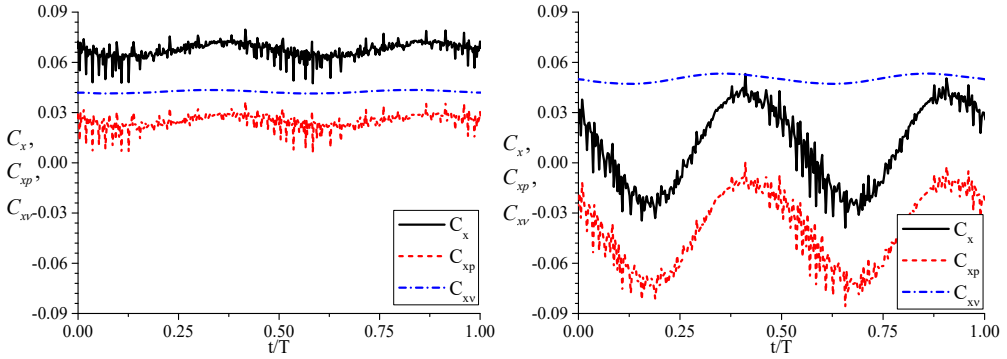


Figure 6-7. Instantaneous horizontal force coefficients for the NACA 0012 fish-like foil within one oscillation period at  $St = 0.2$  (left) and  $St = 0.3$  (right) at  $Re_L = 5000$

The coefficients of the time-averaged thrust  $\overline{F_T}$  and drag  $\overline{F_D}$  (defined in Eqs. (6.6) and (6.7)) for the NACA 0012 fish-like foil at  $Re_L = 5000$  are shown in Figure 6-8. It is found that the swimming fish can generate thrust force when its undulatory frequency is large enough ( $St > 0.20$ ).

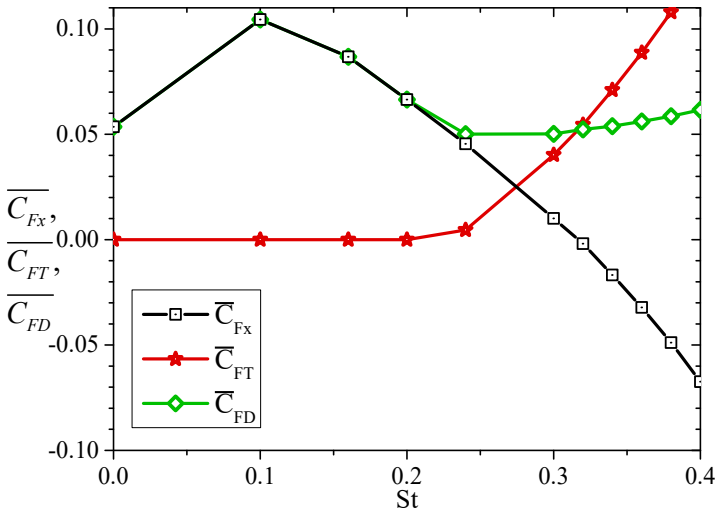


Figure 6-8. Total horizontal force coefficient, thrust and drag components of the NACA 0012 fish-like foil vs. Strouhal number at  $Re_L = 5000$

Many previous researchers have attempted to reveal the mechanism whether the undulatory motion of a swimming fish is drag-reducing or drag-increasing. Barrett et al. (1999) concluded that the undulatory motion is drag-reducing as the upper bound drag estimate was found to be less than that of the corresponding rigid body drag. But Liu and Kawachi (1999) and Anderson et al. (2001) indicated that the friction drag increases due to the undulatory motion in their numerical and experimental studies, respectively. Fish et al. (2014) suggested that the dolphin can produce high thrust without requiring special drag-reducing mechanisms and the pressure drag can increase as the animal swims. The main reason for these contradictory hypotheses is



the inherent difficulty to separate the net thrust and drag forces in experimental and numerical models. By adopting the aforementioned decomposition method, we are able to compute the total drag force  $F_D$  and together with the two drag components ( $F_{Dp}$  and  $F_{Dv}$ ) and thus estimate the impact of the undulatory motion on the different contributions to the hydrodynamic forces.

Figure 6-9 illustrates the averaged drag and thrust forces experienced by the NACA 0012 fish-like foil within the  $St = 0 - 0.40$  at  $Re_L = 5000$ . For easier comparison with the rigid-body case, the results in the plot are normalized by the total horizontal force acting on the still rigid NACA 0012 fish-like foil ( $St = 0$ ). For example, the nondimensional averaged total drag force here is written as  $F_D^* = F_D/F_x(St = 0)$ .

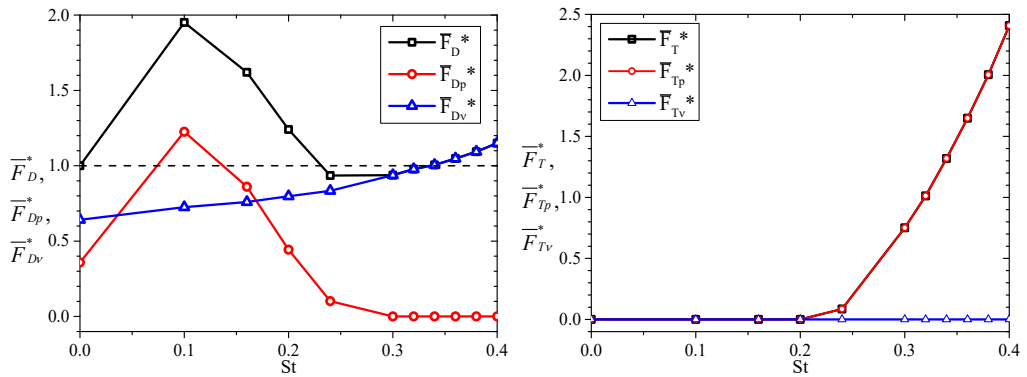


Figure 6-9. Time-averaged total drag, pressure and friction drag (left) and time-averaged total thrust, pressure and friction thrust (right) normalized by the rigid body total drag of the NACA 0012 fish-like foil vs. Strouhal number at  $Re_L = 5000$

From this figure we can see that the total drag force  $\overline{F}_D^*$  of the NACA 0012 foil has a sharp initial increase from 1 to 2 above that of the rigid fish drag up to  $St = 0.10$ . Then the  $\overline{F}_D^*$  starts to decrease with the increase of the Strouhal number, and the value drops below the rigid fish drag around  $St = 0.23$ . However, the total drag force starts increasing again after  $St = 0.30$  and exceeds the rigid fish drag when  $St \geq 0.34$  at this Reynolds number.

The friction drag force  $\overline{F}_{Dv}^*$  increases almost monotonically with  $St$  while the pressure drag force  $\overline{F}_{Dp}^*$  has a similar tendency as the total drag for small Strouhal numbers and then decreases asymptotically toward zero at  $St > 0.30$ . It is obvious that the variation of the  $\overline{F}_D^*$  for this NACA 0012 fish-like foil is dominated by the large variation of the pressure drag (between 0 and 1.23), and the friction drag becomes the major contributor to the total drag force at high Strouhal numbers. The right plot of Figure 6-9 proves that the friction component of the horizontal forces cannot make contributions to the thrust force, which is as expected. The source of the thrust force come from the pressure force.

The above results could provide some insights into the effect of undulatory motion on fish drag force and help reconcile the conflicting suggestions given by previous researchers.

### Vortex structures in the wake

The wake is closely associated with the hydrodynamic characteristics in fish swimming, and the vortex shedding is often discussed in order to understand the mechanisms behind the propulsive performance of a fish with traveling wavy motion. Here, the wake regimes under different conditions are analyzed as a function of the Strouhal number and of the oscillation frequency. This can allow to identify the transition between different regimes and their connection with drag-to-thrust transition.

Figure 6-10 shows the instantaneous spanwise vorticity fields of the NACA 0012 fish-like foil at  $Re_L = 5000$  with various undulatory frequencies. The vorticity contours are obtained at the time instant  $t/T = 0$  after the simulation comes to the steady state.

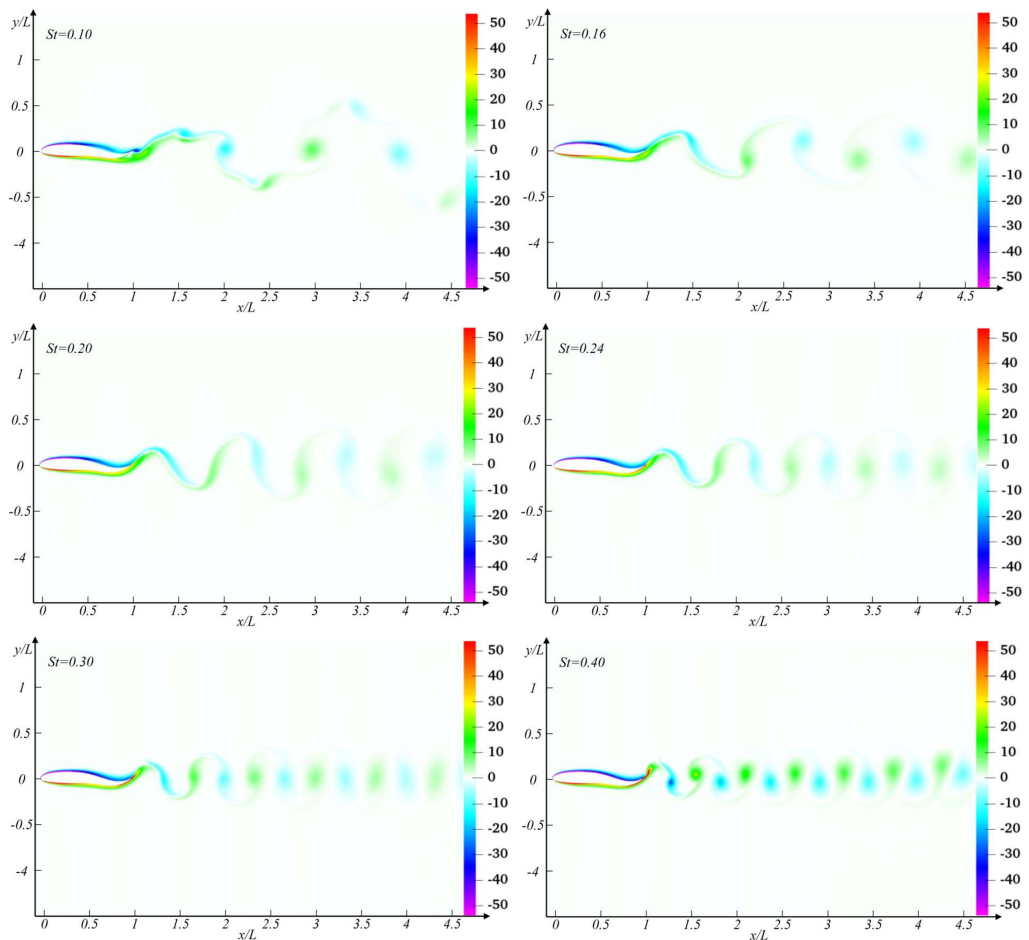


Figure 6-10. Instantaneous spanwise vorticity contours for the NACA 0012 fish at  $Re_L = 5000$  and  $St = 0.10, 0.16, 0.20, 0.24, 0.30, 0.40$

It is found that the wake regimes of the undulatory fish are consistent with the phase diagram of vortex regions observed for the rigid flapping foils illustrated in chapter 5 and reported by

Schnipper et al. (2009). As the swimming amplitude of the NACA 0012 fish-like foil is fixed in this case, the variation of the oscillating frequency is the only cause of the Strouhal number change. The region of  $0.10 < St \leq 0.40$  is dominated by 2-single-vortex shedding per period (2S) wakes, i.e., von Kármán (vK) wake at small frequencies and reverse von Kármán vortex street at large frequencies. In the region with  $St \leq 0.10$ , the wakes behind the fish tail would be more complex and can contain more than two vortices per oscillation period. For the present  $St = 0.10$  case, there are two vortex pairs shed per oscillation period (2P) from the fish tail. The vortex pairs move away from the wake centerline and slowly turn anticlockwise (clockwise) on the lower-hand (upper-hand) side of the centerline. It is interesting to note that though the geometry and kinematics in the present fish swimming problem is different from those of the pitching foils or oscillating cylinders, the boundary between the 2S and 2P regions in our numerical simulations is qualitatively similar to the boundary found by Schnipper et al. (2009) and Williamson and Roshko (1988).

The wake transition from 2P to 2S with increasing oscillation frequency involves a change in the timing of the vortex shedding and in the strength of the vorticity production at the trailing edge and in the side boundary layers. In our first 2S wake case,  $St = 0.16$ , the strong downstream vortex in a pair merge with the same-sign upstream vortex during the shedding at the fish trailing edge, and the wake appears to be a von Kármán type 2S wake. With further increase of the undulatory frequency, the vortex street evolves into the aligned wave scenario where vortices of alternating signs align on the symmetry line of the wake. Followed by this, the wake is transitioned into the reverse von Kármán wake when the Strouhal number is large enough,  $St = 0.30$  for instance. However, the vK-reverse vK transition does not coincide with the force transition from drag to thrust, as known from Figure 6-5 that the total horizontal force at  $St = 0.30$  is still a drag. The force transition would often take place at a slightly larger Strouhal number, as pointed out for the flapping foil.

### **Influence of Reynolds number**

As known from chapter 5, the critical Strouhal number at which the total horizontal force changes from drag to thrust is not universal but depends on the Reynolds number of the flow. To systematically quantify the effect of Reynolds number on the hydrodynamic loads and associated flow patterns of carangiform swimming, a series of numerical investigations have been carried out for various  $Re_L$  and  $St$ . Viscous flow simulations are performed for the NACA 0012 fish-like foil at intermediate Reynolds numbers ranging from  $Re_L = 1250$  to  $Re_L = 9500$ . For this Reynolds number study, the Strouhal number  $St$  is varied from 0.10 to 0.40, consistently with the validation cases at  $Re_L = 5000$ .

The dependence of the time-averaged horizontal force coefficient on the Reynolds number is shown in Figure 6-11. When the Reynolds number  $Re_L$  increases, the total horizontal force coefficient  $\overline{C_x}$  decreases towards negative values, and its variations with  $St$  exhibit essentially qualitative trends as those observed for  $Re_L = 5000$ . For the  $Re_L = 1250$  case, the mean horizontal force is of drag type at all the examined values of  $St$ . As the  $Re_L$  increases, the critical  $St^*$  (where  $\overline{C_x}$  turns negative) decreases, indicating that the force transition is easier to occur for the swimming fish from drag to thrust at higher Reynolds

number. However, this decrease of the  $St^*$  of varying Reynolds numbers becomes much smaller with the increase of  $Re_L$ . From the results of the pressure  $\overline{C_{xp}}$  and friction  $\overline{C_{xv}}$  components, the pressure force  $\overline{C_{xp}}$  remains nearly the same for different  $Re_L$  while, as expected, the friction force  $\overline{C_{xv}}$  is highly dependent on  $Re_L$ .  $\overline{C_{xv}}$  is always positive for the undulating fish-like foil in a current and decreases with the increase of  $Re_L$ , the influence of this parameter seems to become less pronounced near the highest examined values. Thus, for the examined cases the dependence of the total horizontal force on the Reynolds number is mainly because of the change of shear stresses while the pressure contribution is dominated by inviscid effects.

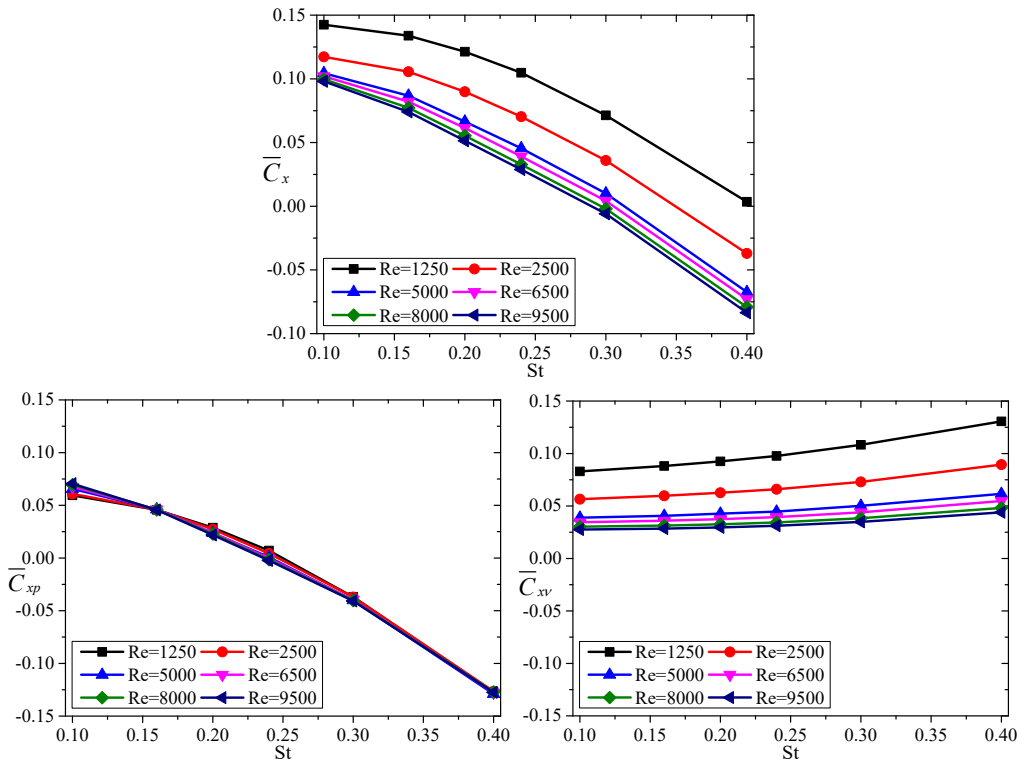


Figure 6-11. Time-averaged horizontal force coefficients of the NACA 0012 fish vs. Strouhal number at different Reynolds numbers

The time-averaged power coefficients at various Reynolds numbers are illustrated in Figure 6-12. It clearly shows that the total power requirement of the fish-like swimming decreases as the  $Re_L$  increases. Because the  $\overline{C_{PD}}$  is linearly connected to the total horizontal force  $\overline{C_x}$  by definition,  $\overline{C_{PD}}$  decreases monotonically with the increase of  $Re_L$  and this decreasing rate becomes less pronounced at higher Reynolds number. However, the time-averaged swimming power  $\overline{C_{PS}}$  changes little with varying  $Re_L$ , indicating that the undulatory fish requires almost the same power in the flow with different viscosities to perform the same lateral oscillations of

the traveling wavy motion, especially at high Strouhal numbers. Therefore, the main reason for the differences of the total power with varying Reynolds number relates to  $\overline{C_{PD}}$ . The total power coefficient  $\overline{C_{PT}}$  decreases to a minimum value around  $St = 0.20$  and increases sharply afterwards. It is noted that this concave trend becomes more obvious at sufficiently high  $Re_L$  keeps similar features if increasing further the value of this parameter. These results confirm that it is of benefit for the undulatory fish to swim around  $St = 0.20 \sim 0.30$  to reduce the input power requirement.

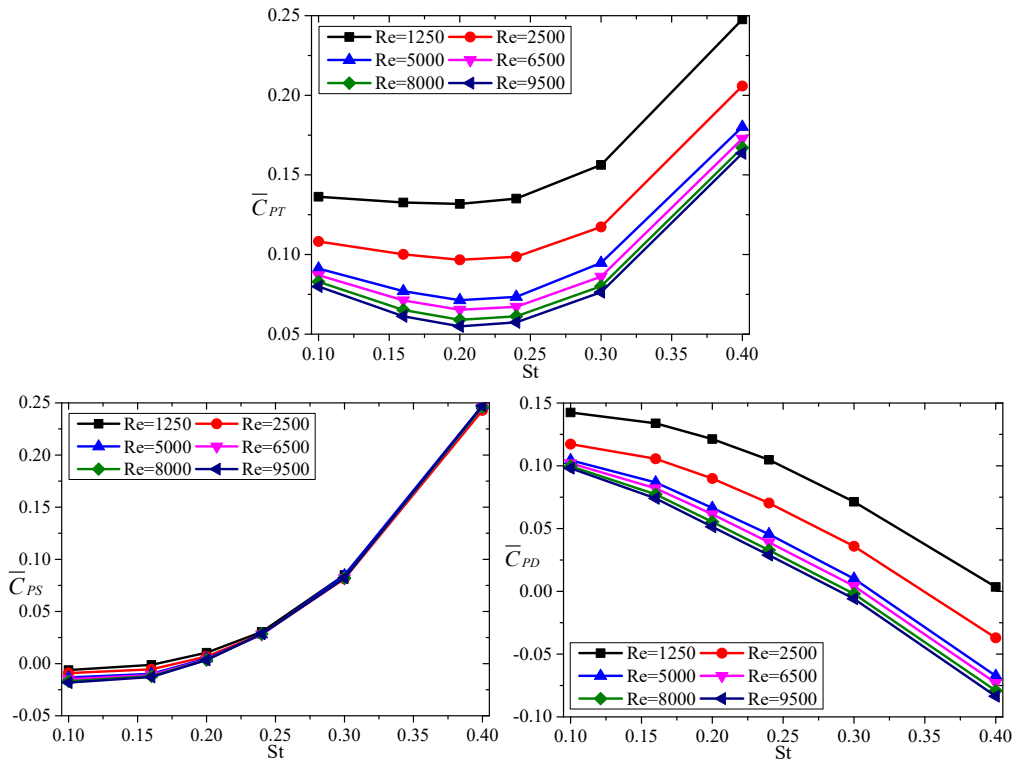


Figure 6-12. Time-averaged power coefficients of the NACA 0012 fish vs. Strouhal number at different Reynolds numbers

To understand the influence of the Reynolds number on the hydrodynamic characteristics of fish-like swimming, the instantaneous spanwise vorticity fields of the NACA 0012 fish-like foil with oscillation frequency  $f = 1.5s^{-1}$  at  $Re_L = 5000$  and  $Re_L = 9500$  are shown in Figure 6-13 at the start phase during one period (time instant  $t/T = 9$ ). In the present two cases, the flow patterns after the fish exhibit similar reverse von Kármán (vK) wakes, but the involved vortical intensity at  $Re_L = 9500$  is clearly stronger. Besides, the reversed vortex pairs have larger lateral distances from the wake centerline at this Reynolds number than at  $Re_L = 5000$ , which suggests larger propulsive forces. The local flow field close to the fish-like body highlights that the shear layer is generated along the body surface and is gradually shed downstream to form concentrated vortices and that the vorticity intensity in the shear layer tends to be higher for the higher Reynolds number case. These qualitative features are also

possessed by the fish undulating at the same frequency and with Reynolds number between 5000 and 9500. However, as known from Figure 5-35 and Figure 6-10, the fish-like foil experiencing drag force always have a von Kármán (vK) wake, thus the fish undulating at  $f = 1.5s^{-1}$  with Reynolds number lower than 5000 has qualitatively different flow patterns.

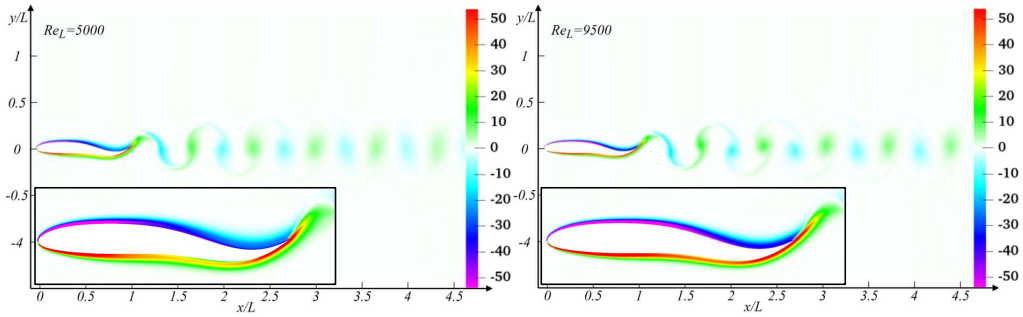


Figure 6-13. Instantaneous spanwise vorticity contours for the NACA 0012 fish at  $St = 0.30$  in the case of (left)  $Re_L = 5000$  and (right)  $Re_L = 9500$

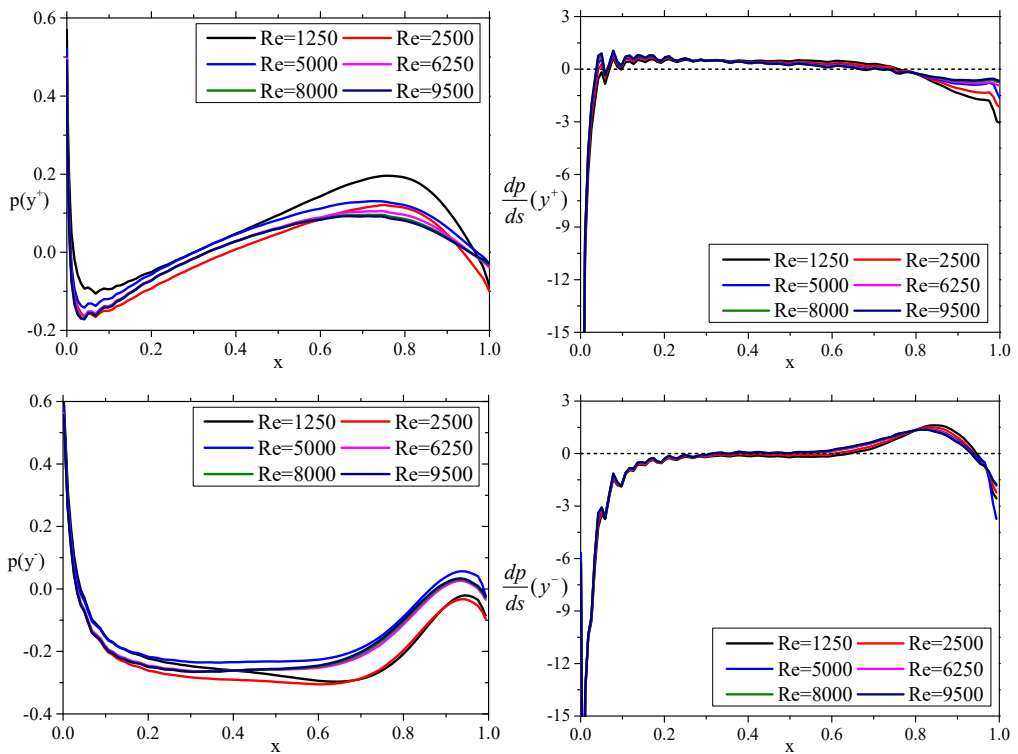


Figure 6-14. Pressure and pressure gradient on the top ( $y^+$ ) and bottom surfaces ( $y^-$ ) for the NACA 0012 fish at  $St = 0.30$  for different Reynolds numbers

However, it is difficult to identify where along the body the flow separation actually starts to occur from Figure 6-13. Based on the boundary-layer theory, Schlichting and Gersten (2015) have pointed out the fact that flow separation in steady inflow occurs only in decelerate flow, i.e., an adverse pressure gradient on the body surface ( $dp/ds > 0$ , where  $s$  represents the curvilinear coordinate along the fish body starting from the leading edge to trailing edge). In our case we also have an undulatory motion of the body but still this condition is relevant for flow detachment. To this purpose, Figure 6-14 provides the pressure and the pressure gradients along the top (+) and bottom (–) sides of the NACA 0012 fish-like foil at various Reynolds numbers at the start phase during one cycle (time instant  $t/T = 9$ ). For the present  $St = 0.30$  case, the flow along the top surface begins to detach from the body around  $x/L = 0.05$ . From the pressure gradient results, it is found that the flow at higher  $Re_L$  tends to separate closer to the leading part of the body. The same thing also happens for the bottom surface, i.e., the adverse pressure gradient starts from about  $x/L = 0.32$  at  $Re_L = 9500$ , and about  $x/L = 0.62$  at  $Re_L = 1250$ . However, due to the traveling wavy body motion, the maximum value of the adverse pressure gradient on the bottom surface decreases with the increase of  $Re_L$ .

To compare the vorticity field in the wake region at different Reynolds numbers, the vorticity impulse term introduced in chapter 5,  $P_{Vx} = - \int_{V_1} y\omega_z dV$ , is calculated in the wake region shown in Figure 6-15.

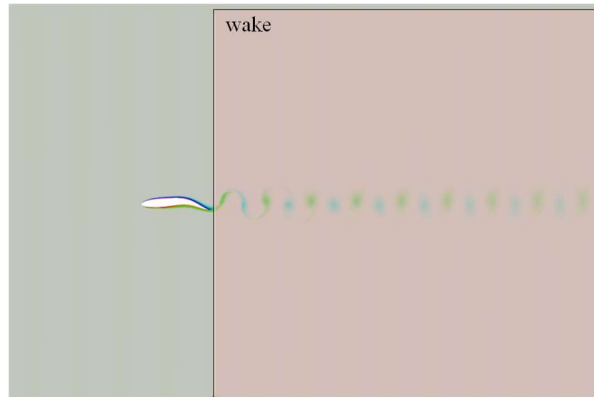


Figure 6-15. Schematic view of the wake region in the control volume

The results of  $P_{Vx}$  for the NACA 0012 fish-like foil at  $St = 0.30$  are presented in Figure 6-16 within one oscillation period, for  $Re_L = 5000$  and  $Re_L = 9500$ . This wake-region computation confirms qualitatively a larger thrust contribution connected with higher Reynolds number, and it is consistent with the flow features of stronger reverse von Kármán wake shown in Figure 6-13.

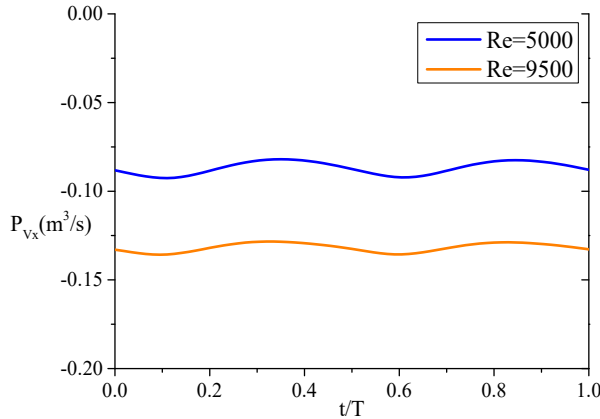


Figure 6-16. The contribution to the vorticity impulse term  $P_{vx}$  (see chapter 5) of the NACA 0012 fish-like foil from the vorticity field in the wake region at different Reynolds numbers

### Influence of fish shape

From the physical and numerical investigations described in the previous chapters, it is known that the fish/foil with different profiles can have different behaviors and performances. In this section, numerical simulations of two NACA fish-like foils are carried out to investigate the effect of body shape on the hydrodynamics of undulatory swimming. The swimmers employed here are the NACA 0012 and NACA 0021 fish-like foils, and the same kinematics is prescribed for them so to highlight the shape effect.

Figure 6-17 shows the time-averaged force and power coefficients of the NACA 0021 fish-like foil at  $Re_L = 5000$ , to be compared to the numerical results of the NACA 0012 fish-like foil in Figure 6-5. One should note that the force coefficients here are defined using the fish body length (i.e., normalized by  $0.5\rho U^2 L$ ). From the results, the NACA 0021 and NACA 0012 fish-like foils are associated with similar friction component  $C_{xv}$ , while the pressure component  $C_{xp}$  of the NACA 0021 fish-like foil is much higher than that of the NACA 0012 fish-like foil. Therefore, the total horizontal force acting on NACA 0021 fish-like foil is larger than the NACA 0012 fish-like foil at all the examined Strouhal numbers, which indicates the NACA 0021 profile experiences larger drag force and has weaker capability to generate propulsion force. The NACA 0021 fish-like foil can only experience the thrust force when the frequency is higher than  $f > 1.8s^{-1}$ . From the plots of the power coefficients, we found that as the undulatory frequency increases, the swimming power  $\overline{C_{PS}}$  of the NACA 0021 fish-like foil increases slower than that of the NACA 0012 fish-like foil, which means that it requires less power to actuate the traveling wavy motion of the NACA 0021 fish. However, the  $\overline{C_{PD}}$  of the NACA 0021 fish-like foil is higher than that of the NACA 0012 fish-like foil in all the examined cases, which is consistent with tendency of the pressure force  $\overline{C_{xp}}$ . Therefore, the time-averaged total power coefficient of the NACA 0021 fish-like foil is overall larger than that of the NACA 0012 fish-like foil. The differences in  $\overline{C_{PT}}$  between the two fishes are the largest at  $f = 0.5s^{-1}$ , and become smaller as the frequency increases. Their values are about the same



at  $f = 2.0s^{-1}$ . The minimum value of the  $\overline{C_{PT}}$  for the NACA 0021 fish-like foil occurs around  $f = 1.2s^{-1}$  ( $St = 0.24$ ).

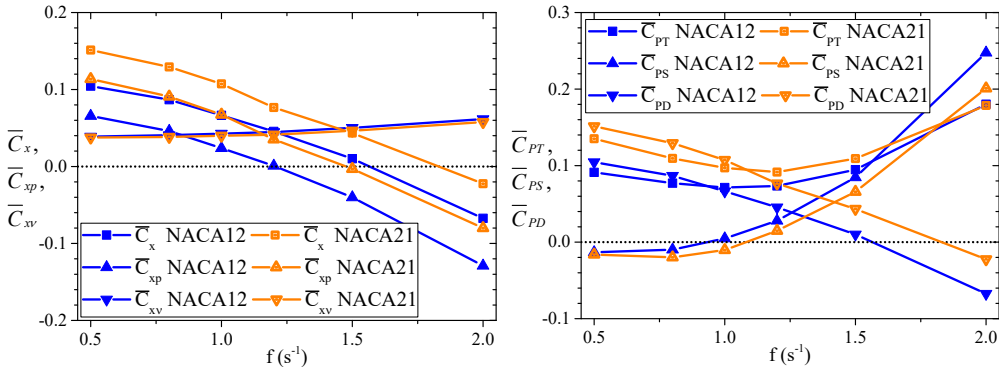


Figure 6-17. Time-averaged horizontal force coefficients (left) and power coefficients (right) for the NACA 0021 fish at  $Re_L = 5000$

Although the force results in Figure 6-17 illustrate that the friction components of the two fishes approximately coincide, it does not necessarily represent that the shear stresses acting on their bodies are the same because the NACA 0021 fish-like foil has apparently blunter body. A more appropriate method for analyzing the friction force is the normalization using the fish profile length, i.e.,  $C_{xv,pro} = F_{xv}/0.5\rho U^2 L_{pro}$ . The perimeter of the NACA 0012 and NACA 0021 fish-like profiles are, respectively,  $L_{pro} = 2.04m$  and  $2.10m$  at the equilibrium position. For the pressure component of the horizontal force, the maximum thickness of the fish would be a more suitable characteristic length (i.e.,  $C_{xp,D} = F_{xp}/0.5\rho U^2 D$ ). From the results in Figure 6-18,  $C_{xv,pro}$  of the NACA 0021 fish is slightly lower. This is different from the finding in chapter 5 that the  $C_{xv,pro}$  of the pitching NACA 0021 foil is larger than that of the pitching NACA 0012 foil, which might be due to larger flow acceleration along the thicker foil body. Owing to the undulatory fish-like motions, it becomes challenging for the flow to remain attached along the body with the increase of the Strouhal number, especially around the trailing part. The blunt body shape of the NACA 0021 fish-like foil is expected to enlarge this flow separation effect, and thus the shear stresses along this fish are smaller than those along the NACA 0012 fish-like foil. This will be illustrated in the later discussion in terms of vorticity fields around the two geometries. The difference in  $C_{xp,D}$  between the two NACA fish-like foils enlarges with the increase of the undulatory frequency. At the smallest examined frequency, the pressure coefficients are similar. Then, the  $C_{xp,D}$  of the NACA 0012 fish-like foil declines sharply towards negative values, which indicates its good capability in generating propulsive forces. On the contrary, the  $C_{xp,D}$  of the NACA 0021 fish-like foil decreases slowly from 0.52 to  $-0.37$ , and only when the frequency is very high its value can exceed the friction force, i.e., about  $f > 1.8s^{-1}$ . It suggests that the body shape can have a greater influence on the  $C_{xp,D}$  as the oscillation frequency increases.

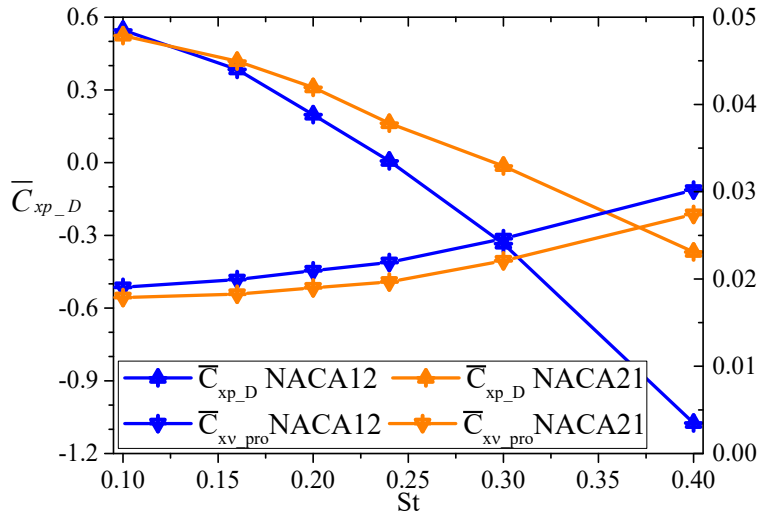


Figure 6-18. Time-averaged pressure and friction force coefficients for the NACA 0021 fish at  $Re_L = 5000$

Figure 6-19 shows the instantaneous spanwise vorticity fields at the start phase during one cycle (instant  $t/T = 9$ ) to illustrate the flow patterns of the NACA 0012 and NACA 0021 fish-like foils at  $Re_L = 5000$  with the oscillation frequency  $f = 1.5s^{-1}$ . As the corresponding Strouhal number is relatively small ( $St = 0.30$ ), the wakes behind the undulatory fishes are advected in the form of an aligned wake, i.e., there are two single vortices shed per oscillation period ( $2S$ ) from the fish-like tail and their distances to the wake centerline are symmetry. By comparing the results, the downstream vortex of the NACA 0021 fish-like foil is slightly stronger, which might be due to larger flow acceleration along its blunter profile. From the local vortical structures close to the body, it looks that the NACA 0021 fish-like foil experiences more severe flow separations in the aft part, thus leading to more pressure loss than for the NACA 0012 fish-like foil.

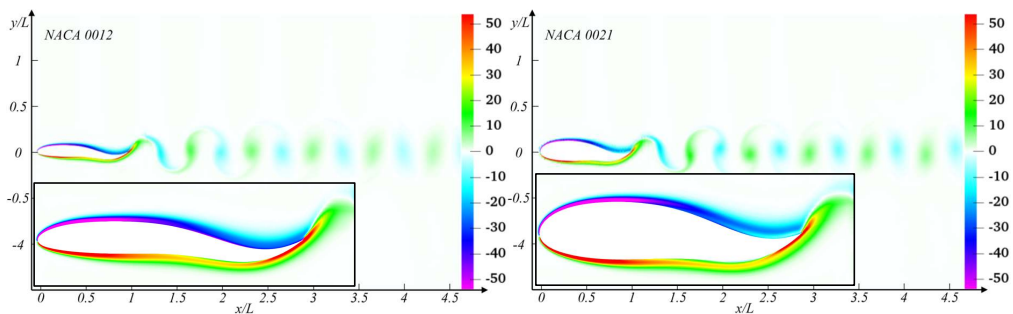


Figure 6-19. Instantaneous spanwise vorticity contours for the NACA 0012 (left) and NACA 0021 (right) fish-like foils at  $Re_L = 5000$  and  $St = 0.30$

To carefully estimate the flow features along the fish-like foils, the pressure and its gradient along the top and bottom sides of these bodies at the start phase during one cycle (time instant  $t/T = 9$ ) are illustrated in Figure 6-20. It is found that the flow past the NACA 0021 fish-like

foil tends to detach from the body around  $x/L = 0.10$ , and it occurs later for the NACA 0012 fish-like foil on both sides. Due to the lateral undulations of the fish-like body, the adverse pressure gradients on the top surface for both fish-like foils remain for a large portion (until  $x/L = 0.80$  for the NACA 0021 fish). Herein, the gradient gradients along the NACA 0021 fish-like foil are larger than those for the NACA 0012 fish-like foil, indicating stronger flow detachment can happen in this region. On the bottom surfaces, the pressure gradient results are similar for the two fish-like foils except that the values of the NACA 0021 fish are slightly larger at some points.

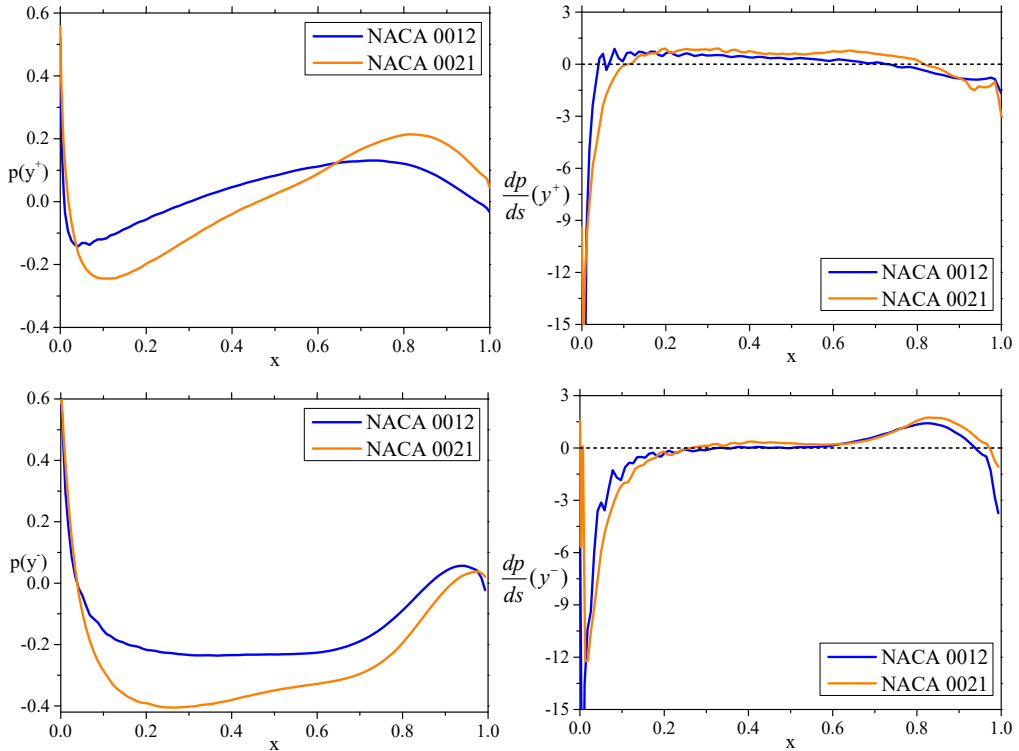


Figure 6-20. Pressure and pressure gradient on the top ( $y^+$ ) and bottom surfaces ( $y^-$ ) for the NACA 0012 and NACA 0021 fish-like foils at  $Re_L = 5000$  and  $St = 0.30$

The coefficients of the time-averaged thrust  $\overline{F_T}$  and drag  $\overline{F_D}$  of the NACA 0021 fish-like foil at  $Re_L = 5000$  are obtained by Eqs. (6.6), (6.7) and (6.8) and documented in Figure 6-21. The simulation results show that the main differences of the forces between the two fish-like foils are drag at low  $St$  and become thrust at high  $St$ . The NACA 0021 fish-like foil starts to generate thrust force at  $St = 0.20$  slightly earlier than the NACA 0012 fish-like foil ( $St > 0.20$ ), but it has limited ability to obtain as large thrust force as the slimmer geometry. As expected, the drag force of the NACA 0021 fish-like foil is much higher due to its blunt profile at small frequencies. After the fish-like foils start to generate larger thrust forces, the differences in the drag forces experienced by the two fishes become smaller. By comparison with the force results in Figure 6-17, we can understand that at  $St = 0.4$ , the drags of the two fishes are

dominated by the friction force, and the pressure components give almost all the contributions to create propulsions. The drag force at high  $St$  is less affected by the shape of the fish body.

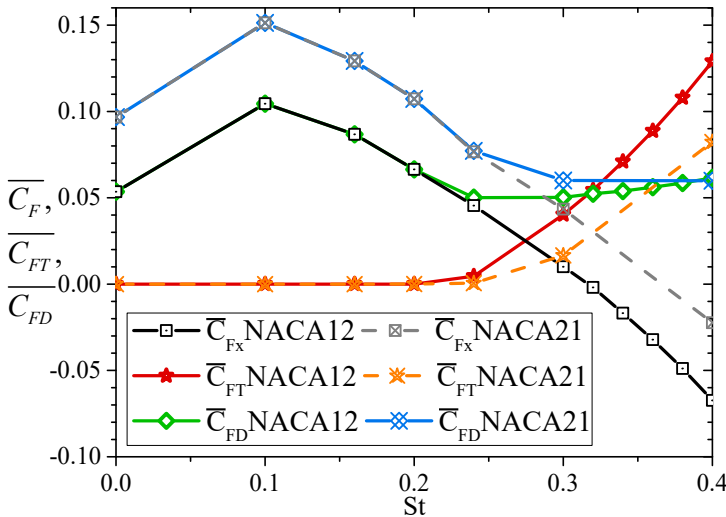


Figure 6-21. Total horizontal force coefficient, thrust and drag components vs. Strouhal number at  $Re_L = 5000$

Viscous flow simulations have been performed for the NACA 0021 fish-like foil also at intermediate Reynolds numbers ranging from  $Re_L = 1250$  to  $Re_L = 9500$ . In this study, the Strouhal number  $St$  is varied from 0.10 to 0.40, consistently with the cases for the NACA 0012 fish-like foil. Though the NACA 0021 fish-like foil has a thicker profile, the dependences of the time-averaged horizontal force coefficients and the power coefficients on the Reynolds number are similar to those for the NACA 0012 fish-like foil, as presented in Figure 6-22. When  $Re_L$  increases, the  $\overline{C_x}$  and  $\overline{C_{pT}}$  are shifted towards smaller values, and they exhibit essentially qualitative trends. The swimming NACA 0021 fish-like foil would require the least power input around  $St = 0.20 \sim 0.30$ .

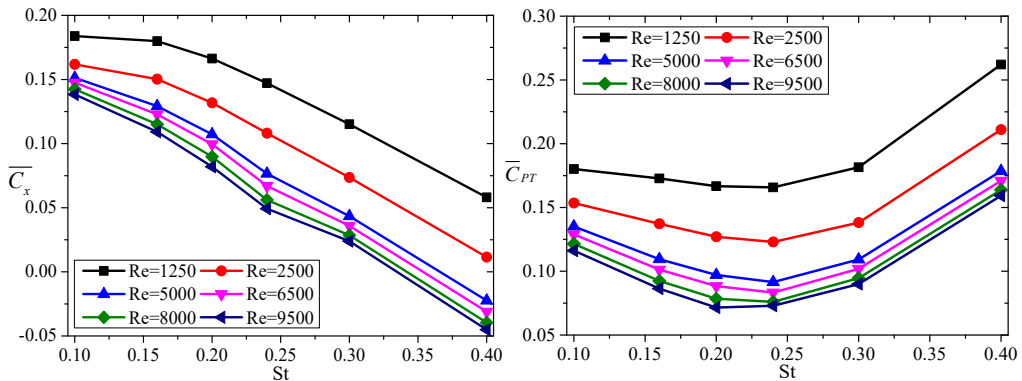


Figure 6-22. Time-averaged horizontal force and power coefficients for the NACA 0021 fish-like foil vs. Strouhal number at different Reynolds numbers

Using the scaling law for the drag-thrust transition introduced in chapter 5, which used the following variables defined as:  $R_x = Re_L \cdot \sqrt{LD/a}$  and  $S_2 = St^* \cdot \sqrt{L^2/a}$ . Figure 6-23 shows the drag-thrust transition lines for the two examined NACA fish-like foils at various Reynolds numbers. The  $R_x$  in the plot is represented in the inverse form so that a power law between the critical Strouhal number and Reynolds number is depicted by a straight line.

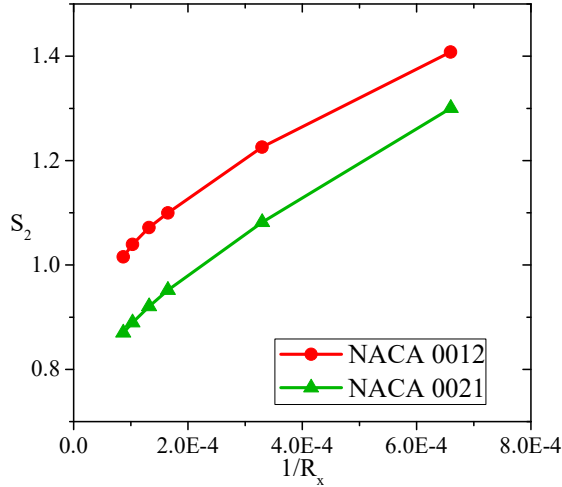


Figure 6-23. Best-fit curves of the drag-thrust transition plotted on the phase spaces of  $S_2 - 1/R_x$

### Swimming efficiency

It is of certain that the Froude propulsive efficiency can also be calculated directly from the results of numerical simulations according to Eq. (6.9) and we refer to it as CFD in the following discussion. Figure 6-24 shows the computation results of the NACA 0012 fish-like foil at  $Re_L = 5000$  by using this CFD approach. The values at small Strouhal numbers are zero because the fish does not have capability to generate thrust by performing very slow undulations, i.e.,  $St \leq 0.20$  under this condition.

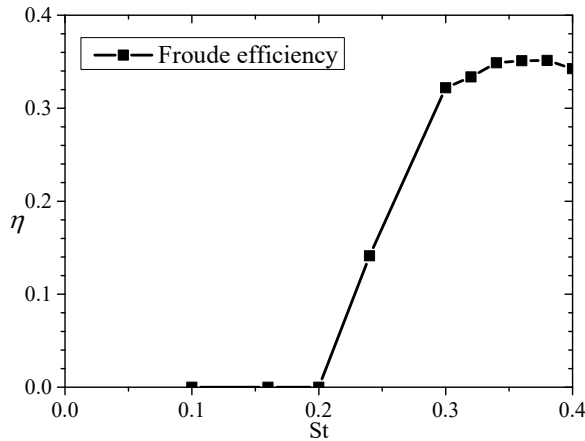


Figure 6-24. Froude efficiency of the NACA 0012 fish-like foil calculated by CFD method vs. Strouhal number at  $Re_L = 5000$

One should note that the calculation of the Froude efficiency formula can only be applied under inline steady swimming when the thrust and drag force counterbalance. If this equilibrium condition is violated, the fish will either accelerate or decelerate. Then the velocity can no longer be a constant value and thus the calculation for Froude efficiency is not meaningful. Therefore, the propulsive efficiency of the fish should be computed at the critical Strouhal number  $St^*$  (drag-thrust transition) for a given Reynolds number, when the fish is assumed to swim steadily at a constant speed. For example, the total horizontal force of the NACA 0012 fish-like foil is zero around  $St = 0.30$  at  $Re_L = 5000$ , and thus the Froude efficiency is only valid around this value of the Strouhal number.

Table 6-2 documents the Froude efficiency of the NACA 0012 fish for different  $Re_L$  at the corresponding value of  $St^*$  using the EBT, EBT-2 and CFD methods. From the results plotted in Figure 6-11 we have found that the critical Strouhal number decreases with the increase of the Reynolds number, which indicates that the fish can achieve constant-speed swimming with lower frequency (wave speed of body undulation) at higher  $Re_L$ . According to the formulas for EBT and EBT-2, it is clear that the swimming efficiency within the range of  $Re_L = 1250 \sim 9500$  is an increasing function of the Reynolds number and these two methods yield similar efficiency values. When it comes to the CFD method, interpolations have been adopted to calculate the thrust force and lateral power loss at the corresponding critical  $St^*$  and this would lead to errors in the efficiency calculations. The results of CFD method differ significantly from the values calculated by the two EBT formulas. This discrepancy is understandable in part because the EBT is an inviscid, slender-body theory, and it is not at all applicable at sufficiently low Reynolds numbers where the viscous forces play an important role. The CFD results do not show an obvious increasing trend of the swimming efficiency within the examined  $Re_L$  range. The propulsive efficiency for the NACA 0012 fish-like foil is around 33% at the intermediate Reynolds numbers (i.e.,  $Re_L \sim 10^3$ ). This is consistent with the numerical computation  $\eta \approx 23\%$  obtained by Borazjani and Sotiropoulos (2008) at  $Re_L = 4000$  for a 3D fish using the same approach. However, it should be considered that the efficiency values obtained by CFD are restricted to  $Re_L \sim 10^3$ , and can be somewhat lower than the swimming efficiencies at larger Reynolds numbers. For example, Borazjani and Sotiropoulos (2008) reported that the Froude efficiency at infinite  $Re_L$  is twice as large as that at  $Re_L = 4000$ . Therefore, it is important to point out that this carangiform swimming mode can become more effective at higher  $Re_L$ , but the Froude efficiency at the intermediate Reynolds number changes little. Moreover, from the previous discussion on Reynolds number influence, the critical  $St^*$  decreases with  $Re_L$ , which implies slower lateral body undulations at higher  $Re_L$ , and thus less swimming power consumption and higher efficiency, as shown in Table 6-2. At  $St^*$  the time-averaged axial power is zero because the mean horizontal force over a period is zero. Therefore, the total power required at  $St^*$  is only the power used to perform traveling wavy motions. Given the aforementioned ambiguities in the definition of a meaningful and objective measure of swimming efficiency, the CFD results suggest that the power requirement might be a better measure for quantifying the efficiency of fish swimming.

Table 6-2. Froude efficiency (%) at critical Strouhal number for the NACA 0012 fish-like foil

$Re_L$	EBT	EBT-2	CFD	$\bar{C}_{PS}$ at $St^*$
1250	75.00	72.61	34.24	0.244
2500	78.57	76.00	33.54	0.162
5000	81.85	79.10	33.08	0.102
6250	82.68	79.89	32.92	0.092
8000	83.69	80.85	32.70	0.079
9500	84.48	81.60	32.29	0.072

### Influence of Strouhal number

To systematically quantify the influence of Strouhal number on the hydrodynamic performance of the carangiform fish swimming, the undulation amplitude is varied while the oscillation frequency remains a constant at  $Re_L = 5000$ . In this section, three fixed frequencies  $f = 1.5s^{-1}$ ,  $f = 1.8s^{-1}$  and  $f = 2.0s^{-1}$  with varying amplitude are examined. In the case of fixed  $f = 1.5s^{-1}$  case, the swimming amplitude is amplified from  $A/L = 0.2$  to  $0.23$ . For the cases with  $f = 1.8s^{-1}$  and  $f = 2.0s^{-1}$ , the swimming amplitude is decreased from  $A/L = 0.2$  to  $0.1$ . The resulting time-averaged horizontal force coefficients for the NACA 0012 fish-like foil are shown in Figure 6-25 and should be compared to the values of the cases with fixed amplitude and changing frequency, i.e., the cases studied for the NACA 0012 fish-like foil in Figure 6-5.

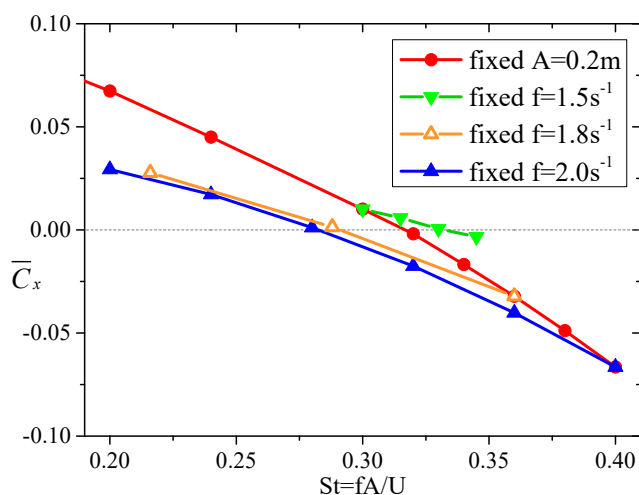


Figure 6-25. Time-averaged horizontal force coefficient for the NACA 0012 fish-like foil vs. Strouhal number at  $Re_L = 5000$

The results show that the critical Strouhal number  $St^*$  at the drag-thrust transition is not exactly the same and suggest that the undulating frequency and amplitude can affect the fish swimming performance using different mechanisms. This is consistent with the phase diagrams we have plotted in chapter 5 and the experiments carried out by previous researchers. For the

fixed amplitude with varying frequency cases, the net force is zero at frequency approximately  $f = 1.57s^{-1}$ . From the results of fixed  $f = 1.8s^{-1}$  and  $f = 2.0s^{-1}$  cases we find that when the fish applies smaller amplitude of swimming pattern and larger frequency, the critical  $St^*$  reduces, and larger amplitude with smaller frequency leads to higher critical  $St^*$ . This shows that the  $St$  is not the only parameter that affects the fish-like swimming behavior.

The Froude efficiency results calculated using CFD method are given in Figure 6-26. Because strictly speaking the Froude efficiency formula makes sense only at the equilibrium condition, its value for the different cases examined in Figure 6-26 is documented in Table 6-3 with the corresponding values of the critical Strouhal number.

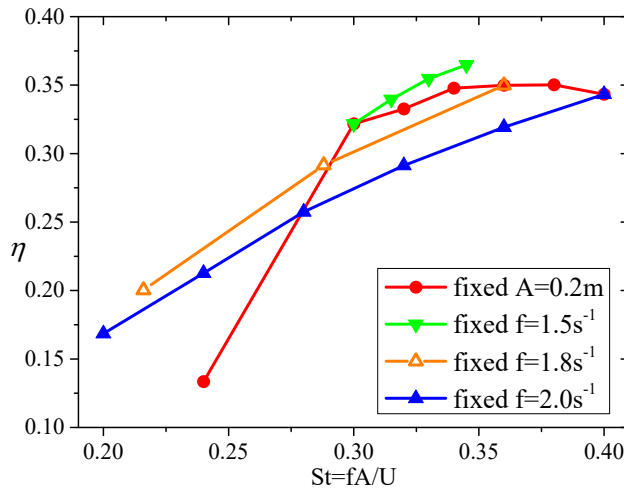


Figure 6-26. Swimming efficiency calculated by Eq. (6.9) vs. Strouhal number at  $Re_L = 5000$

Table 6-3. Froude efficiency (%) at critical Strouhal number for the NACA 0012 fish

case	$St^*$	corresponding $f$ or $A$	$\eta$
Fixed $A = 0.2m$	0.31	$f = 1.57s^{-1}$	33.08
Fixed $f = 1.5s^{-1}$	0.33	$A = 0.22m$	35.47
Fixed $f = 1.8s^{-1}$	0.29	$A = 0.16m$	29.15
Fixed $f = 2.0s^{-1}$	0.28	$A = 0.14m$	25.74

In these examined cases, the Froude efficiency grows with the increasing amplitude and decreasing frequency. It suggests that within the examined Strouhal number range at  $Re_L = 5000$ , the fish may undulate at lower frequency with larger amplitude to achieve higher swimming efficiency. The limit of the amplitude is supposed to be related with its body physiology and the fish in natural has made its own best selection.

## 6.2 Self-propelled fish-like swimming foil

It has always been attractive for biologists, hydrodynamicists and engineers to observe and understand the fish locomotion in water. As aforementioned, there have been a large number of



papers experimentally and numerically studying a deformable body fixed in its position in a uniform current or tethered with the opposite velocity in a quiescent fluid. However, apart from the assigned stream in the forward direction, the fish body can also experience either lateral or angular motions, perceived as recoil motions (Paniccia et al., 2021b). Some investigations pointed out that the recoil effects induced by the fluid interaction with the deformable fish can be significant and this can affect the resulting fish locomotion (Maertens et al., 2017). Therefore, it is important to study the hydrodynamic behavior of a self-propelled fish with/without constrained gaits in water both physically and numerically.

As a matter of fact, investigating the performance of carangiform fish with different shapes and under various swimming conditions, could however pose challenges to experimental studies. It may be difficult to impose experimental control over live fish, such as searching for a fish of desired body shape or let the fish swim constantly at certain tail-beat frequency. Another challenge is to obtain the detailed flow fields around the live fish, which are always important for analyzing fish propulsion performance. It is particularly difficult because most of particle image velocimetry (PIV) techniques can only provide the flow measurements in 2D planes (Tytell, 2007) or in a restricted 3D volume smaller than fish swimming space (Raffel et al., 2018). Meanwhile, with the increase of computational capability, the computational fluid dynamics (CFD) method has become an attractive alternative approach to study the fish swimming performance and to convey detailed flow images. In addition, it is also a powerful complement to real-fish experiments while it allows wide parametric studies through systematic changes in the body geometry and/or the swimming kinematics. Therefore, free-swimming fish-like foils under various flow conditions are numerically examined here by using the solvers described in chapter 4. One should also note that, because steady-state self-propelled conditions correspond to zero mean horizontal force, the resulting Strouhal number is always the critical Strouhal number.

### 6.2.1 Self-propelled foil in calm water and current

The purpose of the present section is to systematically investigate the hydrodynamic performance of a self-propelled carangiform swimmer in different hydrodynamic environments. As main results, the time-averaged forward swimming speed, the fish locomotion and the wake patterns are obtained and discussed for fishes in different flow conditions. Herein, the effect of the fish shape is also examined by comparing the results of two different fish-like geometries.

For a proper comparison with the undulatory swimming fishes fixed in current, as discussed in section 6.1, we continue to select the NACA 0012 and NACA 0021 foil profiles as the fish model at rest. They are placed in the viscous fluid and start undulating their bodies in the carangiform swimming pattern, but they are free to accelerate or decelerate depending on the experienced hydrodynamic loads. For the self-propelled fish, there is no tether to absorb the excess force acting on the fish body. When the fish starts to perform periodic lateral undulatory motions, the body would generate a thrust-type force, which initially leads to a time-averaged acceleration to the swimmer. The swimming speed continues to increase until the mean force during one oscillating cycle becomes zero, and then the fish reaches a steady state that can be characterized by constant swimming speed  $U$ , Reynolds number  $Re_L$  and Strouhal number

*St*. The present work will analyze the swimming performance of the self-propelled fish with focus on the asymptotic steady state condition in terms of various performance metrics, such as locomotion velocity, power consumption, swimming efficiency, etc. The wake structure associated with the fish is also investigated at the asymptotic steady state.

### Numerical setup

The locomotion of the undulatory fish is obtained by coupling the body dynamics and the fluid dynamic actions, and the corresponding self-propulsion strategy is developed in the OpenFOAM toolbox as introduced in section 4.5. The effectiveness and accuracy of this strategy has been verified by correctly predicting the horizontal motions of various heaving elliptic foils. As for the tethered undulatory fish-like foils, the deformation of the fish is handled by the overset grid method, and the governing Navier-Stokes equations are solved in a 2D computational domain including the fish-like body, defined by a rectangle of  $-2L < x < 7L$  in  $x$  direction and  $-3L < y < 3L$  in  $y$  direction, as shown in Figure 6-3. The boundary conditions in this study should be appropriately set under different flow conditions. A no-slip condition is enforced along the deformable swimming fish. Zero gradient conditions are applied to the top and bottom domain boundaries. For the self-propelled fish swimming in open-water current, a uniform inflow condition is enforced at the inlet while a uniform pressure condition is used at the outlet. A sinusoidal ramp function is employed for the inlet velocity to avoid a break-down at the beginning of the numerical simulations. For the calm-water case, the fluid velocity at the inlet boundary is set as zero. The boundary conditions in the third direction ( $z$  direction) for all variables are set to be empty as none of them are solved consistently with the two-dimensional flow assumption. For the interpolation layer in the overset mesh, the “overset” boundary condition is applied.

As basic study, the self-propelled fish is restricted to swim freely only along the streamwise direction. The lateral undulatory motion of the self-propelled fish coincides with the swimming mode used in the forced fish-like foil simulations, as prescribed in Eqs. (6.1-6.3). The simulations are continued until the asymptotic steady state is reached, i.e., the mean swimming speed  $U$  approaches a constant value. This speed during the steady swimming depends on the fish oscillating frequency, and consequently,  $Re_L$  and  $St$  also depend on the frequency  $f$  due to their relationship with  $U$ . Therefore, the fish swimming frequency should be carefully selected in order to obtain the steady state  $Re_L$  in a desired range. To accomplish this, the results of the forced fish-like swimming foils from the precious section 6.1 can be used herein as guidance. For example, the critical Strouhal number  $St^*$  is found to be about 0.31 for the NACA 0012 fish-like foil at  $Re_L = 5000$ , which means that the swimmer could self-propel itself at a constant speed equal to the corresponding velocity of the inlet current. On the contrary, the simulations of a free-swimming fish can be considered as a sort of inverse problem of the forced undulatory fish case, as we now fix the oscillating frequency and aim to find the resulting free-swimming speed  $U$  at steady state. Therefore, if the self-propelled fish performs undulations at the frequency corresponding to the value of  $St^*$  for the tethered fish, the free-swimming speed  $U$  at the steady state is expected to be the same as the current velocity in the tethered case, with the assumption of the same fluid viscosity. And if the self-propelled fish oscillates itself at another frequency, the final swimming speed would become a different value.

As described in chapter 4, the self-propulsion strategy moves the body boundary to the new positions according to the calculated displacement, and the mesh surrounding the body should also be moved together in order to maintain its good quality. In this numerical study, the *displacementLaplacian* solver is employed to handle the mesh motion and deformation within the body-fitted overset grid. As the self-propelled fish in calm water will swim forward at the speed corresponding to the current velocity of the critical  $St^*$  for the tethered fish, the body-fixed grid will also follow the fish motion. A practical technique for using the aforementioned numerical solver is to avoid the mesh being overstretched during simulation, and the cells with low aspect ratio can help the grid to remain in good quality during movement. A grid refinement study is carried out for both NACA 0012 and NACA 0021 fishes swimming at  $f = 1.0s^{-1}$  in a fluid with kinematic viscosity  $\nu = 2 \times 10^{-4} m^2/s$  (same as that in the tethered fish case at  $Re_L = 5000$ ). The uniform structured hexahedral cells forming the meshes are given in Table 6-4. We shall refer to the grids of NACA 0012 fish as Grid 4-6, and the grids of NACA 0021 fish as Grid D-F.

Table 6-4. Grid resolutions for the NACA 0012 and NACA 0021 fishes

<b>NACA 0012</b>	Grid 4	Grid 5	Grid 6
Nodes along fish	114	154	198
Cells in BG grid	135000	240000	540000
<b>NACA 0021</b>	Grid D	Grid E	Grid F
Nodes along fish	114	160	222
Cells in BG grid	135000	240000	540000

The locomotion of the swimming fish along the  $x$ -axis is calculated by setting the fish model to be neutrally buoyant, i.e., the body density equals to the fluid density ( $\rho_b/\rho_f = 1$ ). In the convergence study, the mass of the 2D NACA 0012 fish is around  $0.082 kg/m$  and the one of the 2D NACA 0021 fish is around  $0.143 kg/m$ . The time step is  $0.002s$  to ensure that the maximum Courant number is less than 1 for the dynamic simulations. From the force results in Figure 6-17, it is known that both fishes still generate drag forces at the oscillation frequency  $f = 1.0s^{-1}$  with inlet flow  $U_c = 1 m/s$ , indicating that they cannot speed up to this velocity when the tether is removed. Here, the NACA 0012 and 0021 fishes are released in currents with income flow velocity being  $U_c = 0.5 m/s$  and  $U_c = 0.3 m/s$ , respectively. In this scenario, the actual (total) swimming fish speed is the sum of the velocity obtained by solving the surgemotion equation and the opposite of the current velocity, i.e.,  $U_t = U_r - U_c$ . The calculated total swimming velocity histories of the two NACA fishes using different grids are shown in Figure 6-27. Negative values of the velocity indicate that the fish is swimming towards the negative  $x$ -axis, i.e., to the upstream direction in this study, as shown in Figure 6-1. It can be observed from the figures that the NACA 0012 and 0021 fishes reach the asymptotic steady state after about 15 and 20 cycles, respectively. There are obvious differences between Grid 4 and 5 for the NACA 0012 fish and between Grid D and E for the NACA 0021fish, that might be because Grid 4 and Grid D are too coarse for the self-propulsion simulations. The computed total speed histories of finest grids (Grid 6 and Grid F) also exhibit slightly smaller absolute values than the medium grids (Grid 5 and Grid E), but the differences between them are very small compared to the coarsest grids, demonstrating a good level of convergence. Though the

finest grids are expected to predict more accurate results, the computational cost for a simulation of  $t/T = (0:55)$  is much more expensive: Grid 6 takes 92908s ( $\approx 26h$ ) compared to Grid 5 (23523s  $\approx 6.5h$ ) while Grid F takes 89049s ( $\approx 25h$ ) compared to Grid E (22706s  $\approx 6.3h$ ). Therefore, as a compromise between accuracy and efficiency, Grid 5 and Grid E are employed for all the further self-propelled fish simulations.

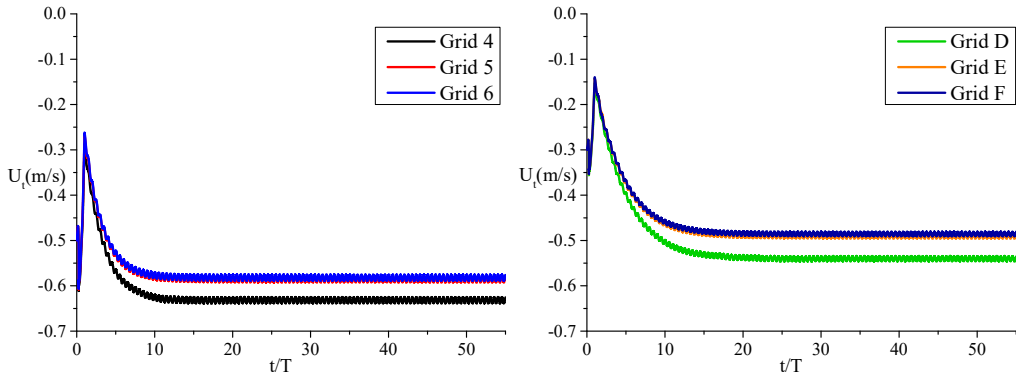


Figure 6-27. Time history of the total speed for self-propelled NACA 0012 (left) and NACA 0021 fish (right) swimming at  $f = 1.0s^{-1}$  in current with three different grid resolutions

### Comparison between calm water and current scenarios

The swimming performances of the NACA 0012 fish are examined under two different hydrodynamic environments: in calm water and in open-water current. For the calm-water case, the fish is released from the equilibrium position in still water and starts the undulatory motion with a constant oscillation frequency until a steady swimming speed  $U_t$  is reached; for the open-water current case, the total fish-swimming speed is  $U_t = U_r - U_c$ . The results for the NACA 0012 fish under these two hydrodynamic conditions at oscillation frequency  $f = 1.0s^{-1}$  and  $f = 1.5s^{-1}$  are shown in Figure 6-28. Herein, the values of the inflow velocity  $U_c$  are set as  $0.5 m/s$  and  $0.9 m/s$  in the two current cases, respectively.

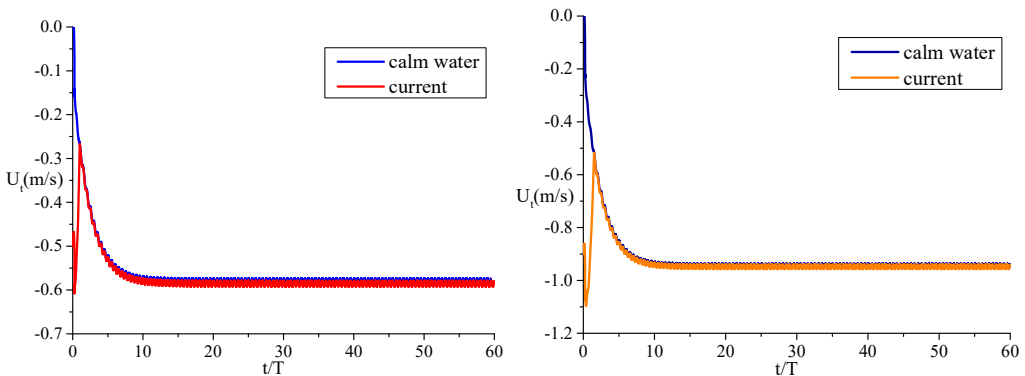


Figure 6-28. Time history of the total fish-swimming speed for self-propelled NACA 0012 swimming at  $f = 1.0s^{-1}$  (left) and  $f = 1.5s^{-1}$  (right) in calm water and current

It can be observed from the results that the swimmer reaches the asymptotic steady state after same cycles in both calm water and current regardless of the swimming frequency. The final steady-state swimming speeds in calm water and current exhibit little differences in the plots. This is documented quantitatively by table 6-5 in terms of the time-averaged values. The forward speed of the NACA 0012 fish at steady state is slightly faster in current than that in calm water, which may be caused by larger mesh motion/deformation of the overset grids fitted to the fish body.

Table 6-5. Time-averaged steady-state swimming speed of the NACA 0012 fish in calm water and current

$U_t$	Calm water (m/s)	Current (m/s)	Error
$f = 1.0s^{-1}$	-0.580	-0.586	0.89%
$f = 1.5s^{-1}$	-0.945	-0.948	0.34%

Figure 6-29 shows the instantaneous spanwise vorticity fields of the NACA 0012 fish swimming at the above four conditions. The vorticity contours are obtained at the time instant  $t/T = 60$ , i.e., after the simulation has reached the steady state. The parameters with superscript ' in the figure represent the body-fixed reference frame with the origin located at the fish leading edge of the equilibrium position.

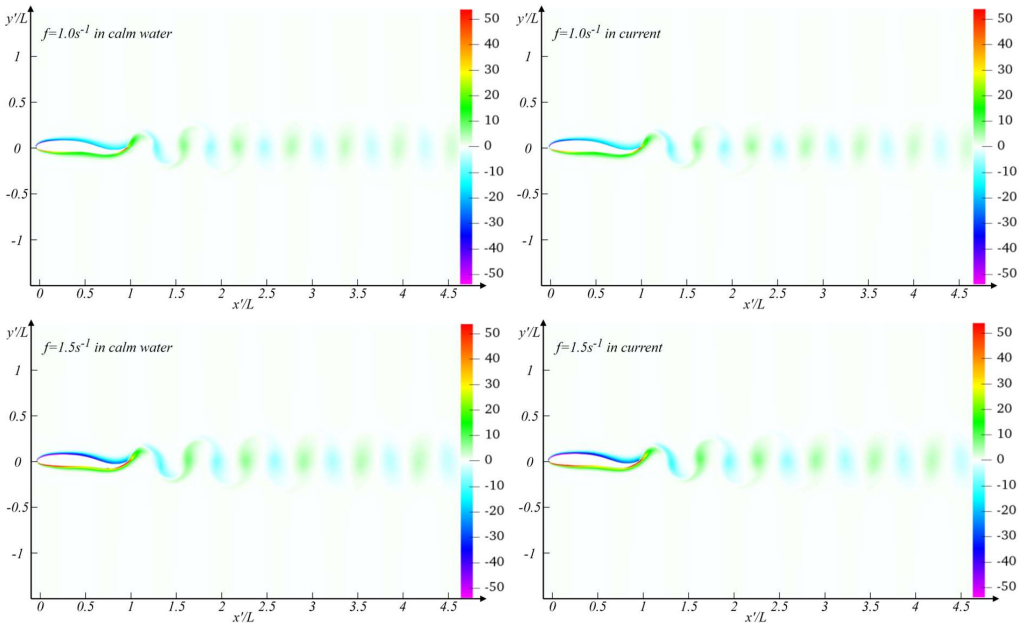


Figure 6-29. Instantaneous spanwise vorticity contours for the NACA 0012 fish swimming at  $f = 1.0s^{-1}$  (top) and  $f = 1.5s^{-1}$  (bottom) in calm water (left) and current (right)

The simulations in calm water and current conditions predict approximately the same asymptotic state for the self-propelled fish swimming along the streamwise direction. As the grids in current cases can retain better original mesh structure and quality, the fish swimming in currents are studied in the following analysis.

### Effect of tail-beat frequency

As discussed in section 6.1, the undulatory motions performed by the tethered NACA 0012 fish in current can lead to different drag-/thrust-type force depending on the oscillation frequency. Here, the fishes are released to self-propelling themselves with the same examined frequencies as in Figure 6-5 to compare occurrence and features of free-swimming scenarios in the two numerical set-ups. The corresponding instantaneous spanwise vorticity fields of the NACA 0012 fish are shown Figure 6-30. The vorticity contours are obtained at the time instant  $t/T = 60$ , i.e., after the simulation has reached the steady state.

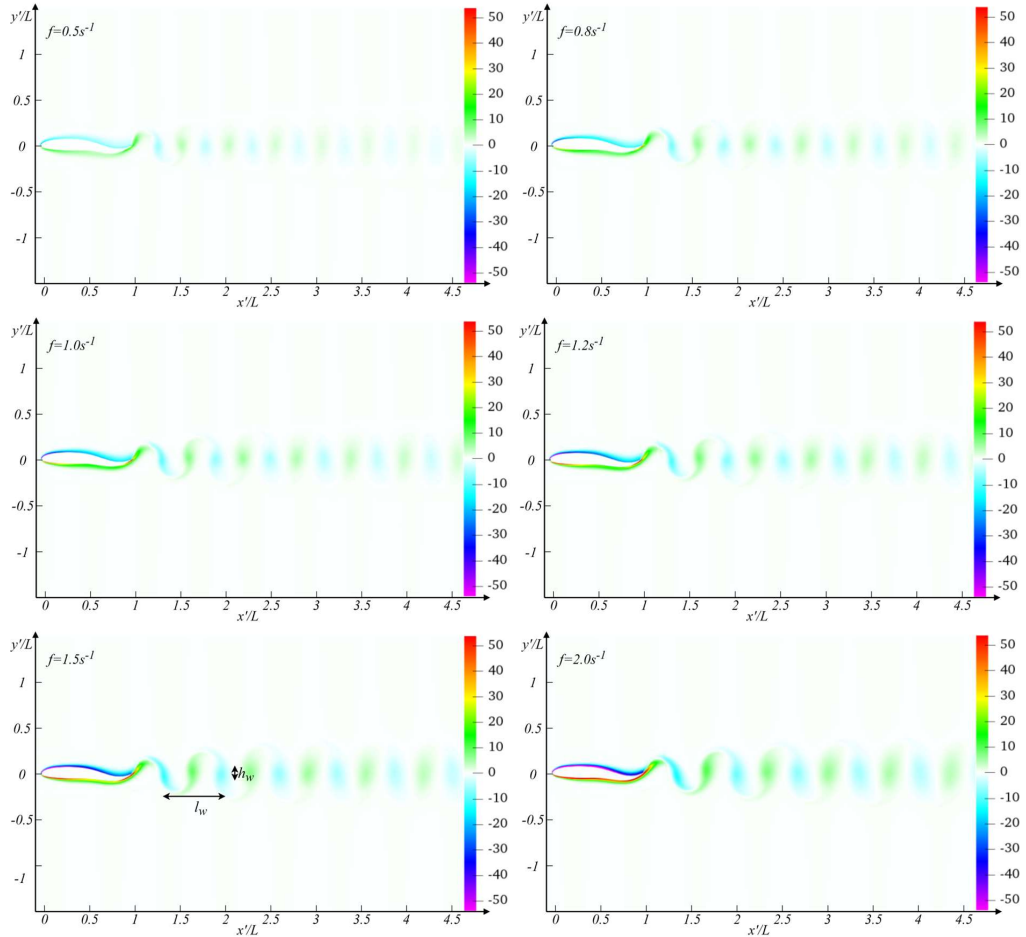


Figure 6-30. Instantaneous spanwise vorticity contours for the NACA 0012 fish swimming in currents at different frequencies

It can be found from the plots that the wakes are of similar reverse-vK pattern for all the self-propelled fishes. These reversed shedding vortex streets are associated with the propulsive performance of the undulatory fishes. As the horizontal hydrodynamic forces experienced by the fishes at the asymptotic steady state are averagely zero, corresponding to the drag-thrust transition in the forced swimming foil cases, the reversed vK configurations in the figures do not exhibit very large wake widths.

For the forced fish-like swimming foil, the critical frequency for the drag-thrust transition in a current with velocity  $U_c = 1 \text{ m/s}$  is estimated to be approximately  $f = 1.57 \text{ s}^{-1}$ . Therefore, the self-propelled fish swimming at this frequency is also simulated for comparison.

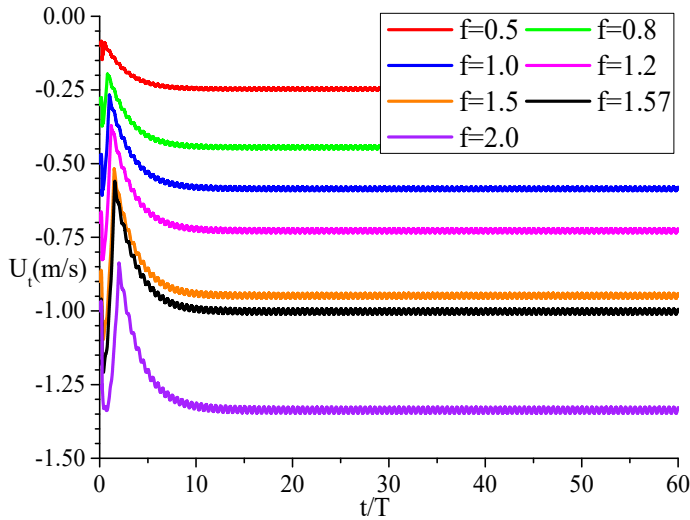


Figure 6-31. Time history of the total speed for self-propelled NACA 0012 foil swimming at different frequencies in currents

Figure 6-31 shows the time histories of the total forward swimming speed of the NACA 0012 fish for the examined oscillation frequencies. As expected, the fish with larger oscillation frequency is able to reach higher forward speed. Besides, it is found that the fish reaches the asymptotic steady state after slightly more cycles at larger  $f$ . The time-averaged values of the fish swimming speeds for all the examined frequencies are documented in Table 6-6. Here, the phase velocity  $\omega/k = f\lambda$  is often used to normalize the swimming speed of the fish,  $U^* = U_t/f\lambda$ . The results of this nondimensional speed also exhibit an increasing tendency with the undulatory frequency. In order to better identify the relationship between the fish swimming speed and frequency, two other characteristic lengths are selected and examined: the wake width ( $h_w$ ) and the distance between two vortices in the same row ( $l_w$ , as shown in the fifth contour of Figure 6-30). It should be noted that the estimate of these wake features from the contours are not absolutely accurate, but they can give some insights to investigate the relationship.

Table 6-6. Time-averaged steady-state swimming speed of the NACA 0012 fish

$f$ ( $\text{s}^{-1}$ )	0.5	0.8	1.0	1.2	1.5	1.57	2.0
$\bar{U}_t$ (m/s)	-0.247	-0.445	-0.586	-0.728	-0.948	-1.002	-1.337
$U^* = U_t/f\lambda$	-0.494	-0.556	-0.586	-0.606	-0.632	-0.638	-0.668
$h_w$ (m)	0.015	0.015	0.03	0.03	0.045	0.045	0.06
$\bar{U}_h^* = U_t/fh_w$	-32.92	-37.07	-19.52	-20.21	-14.04	-14.18	-11.13
$l_w$ (m)	0.525	0.570	0.585	0.615	0.630	0.630	0.660
$\bar{U}_l^* = U_t/fl_w$	-0.941	-0.975	-1.001	-0.986	-1.003	-1.013	-1.012

Figure 6-32 illustrates the relationships between these fish swimming speeds and oscillation frequency. From the results of  $\overline{U}_t$ , it is seen that the time-averaged dimensional forward speed is approximately proportional to the swimming frequency. The nondimensional speed  $\overline{U}^*$  becomes larger at higher frequencies, indicating that the increase rate of the fish forward velocity is larger than that of the frequency. As the shedding vorticities at the asymptotic steady state for all the examined cases exhibit similar reverse-vK wake patterns and do not have sharp differences from the aligned vortex streets, the estimated wake widths are relatively small compared to the fish thickness ( $D = 0.12m$ ). The speed normalized by  $h_w$  shows an overall decline tendency with the increase of frequency. From the plot of  $\overline{U}_l^*$ , we observed that the fish forward speed  $U_t$  is equal to the product of the oscillation frequency  $f$  and characteristic wake length  $l_w$ , indicating that for the NACA 0012 fish, the vortex street shed from the fish body is dominant by the convection by inflow.

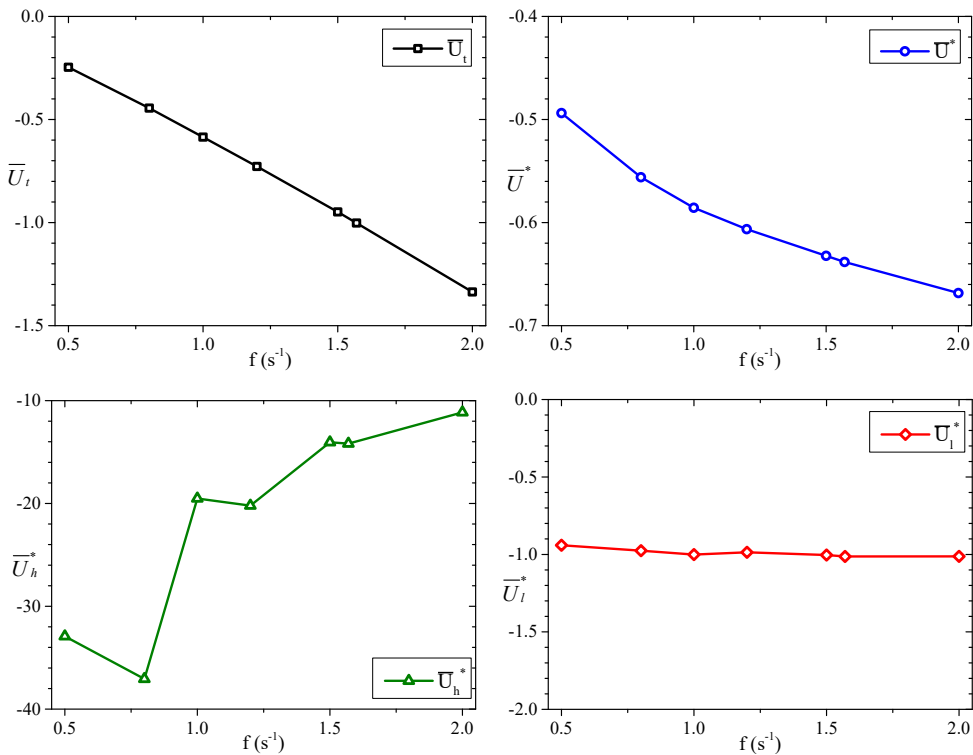


Figure 6-32. Relationship between the forward speed of self-propelled NACA 0012 and swimming frequency

Above discussions focused on the fish swimming speeds at various oscillation frequencies without considering the corresponding power requirement to reach the steady-state condition. The thrust force defined by Eq. (6.6) and the swimming power defined by Eq. (6.4) are calculated during simulations. Figure 6-33 illustrates the time histories of the nondimensional coefficients,  $C_{FT} = F_T / \frac{1}{2} \rho U_1^2 L$  and  $C_{PS} = P_S / \frac{1}{2} \rho U_1^3 L$ , where  $U_1 = 1BL/s$  (the current velocity in the forced swimming foil study). Based on the adopted thrust definition,  $C_{FT1}$  and



$C_{FTt}$  are always positive, while a positive value of  $C_{PS1}$  or  $C_{PS}$  indicates that the fish needs to consume energy to perform undulatory motions during swimming cycle. With the increase of the fish oscillation frequency, both  $C_{FT}$  and  $C_{PS}$  show increasing fluctuation amplitudes, indicating that the NACA 0012 fish can generate larger thrust force at higher frequency, but it also requires larger power input to remain in a steady swimming motion. As last note,  $C_{FT}$  and  $C_{PS}$  of the fishes with different undulating frequencies exhibit their minima and maxima at the same time phases during the cycle.

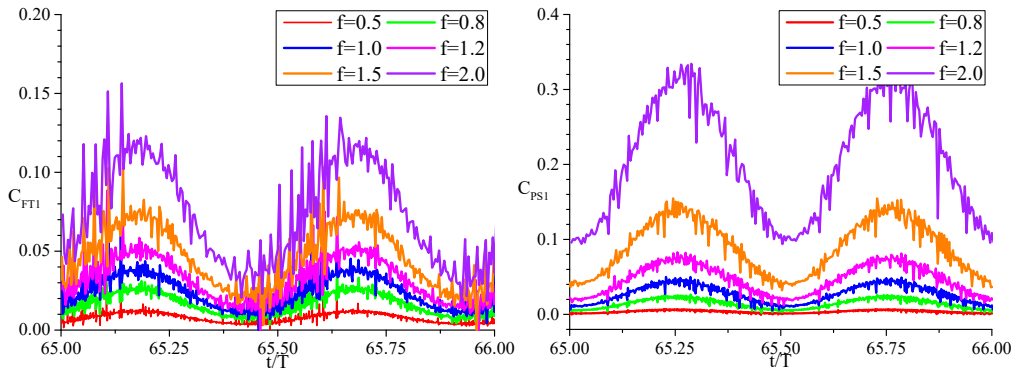


Figure 6-33. Thrust force and swimming power coefficients of self-propelled NACA 0012 swimming at different frequencies in currents

It has been found that the NACA 0012 fish swimming at larger frequency can reach higher forward speed, generate larger propulsion force, but also needs larger input power. Being able to swim faster is not necessarily associated with higher efficiency and more quantitative analysis should be carried out to identify the swimming efficiency. Table 6-7 documents the time-averaged values of the NACA 0012 fish thrust force and swimming power for all the examined frequencies. In addition, for the self-propelled fish with certain kinematics, there should be a unique Strouhal number and Reynolds number corresponding to the steady-state forward speed, and their values are provided as well in the table. The swimming efficiency is calculated using the CFD method according to Eq. (6.9). As presented in the forced swimming foil section, the NACA 0012 fish with  $f = 1.57s^{-1}$  experiences the drag-thrust transition, and here, the results of the self-propelled fish at  $f = 1.50s^{-1}$  are comparable to those of the tethered fish. The critical  $St$  is a decreasing function of  $Re_L$ , similarly as for forced swimming fishes. Although the Reynolds number for all the examined cases varies a lot, the corresponding Strouhal numbers stay in a range of  $0.25 \sim 0.35$ , which agrees with the most cruising aquatic animals in nature. The self-propelled fish swimming kinematics get closer to this range of Strouhal number as  $Re_L$  increases. The values of the Froude efficiency of the NACA 0012 fish are around 0.3 for  $Re_L \sim 10^3$ , also consistently with those of the tethered fishes swimming at different Reynolds numbers reported in Table 6-2. However, it should be noted that as thrust and drag counterbalance during the steady-state self-propelled motion, the Froude efficiency is not a proper measure of the actual swimming performance in this case. Therefore, the mechanical cost of transport (COT), defined as the ratio between the expended energy and the travelled distance of fish, i.e.,  $COT = \bar{P}_S / \bar{U}_T$ , has been adopted by many researchers in the last decade

(see e.g., Paniccia et al., 2021a). This is also used for the following analysis in a dimensionless form, as described by Bale et al. (2014), i.e.:

$$COT^* = COT \frac{\lambda}{\rho f^2 A_m^3 A_p} \quad (6.13)$$

Here  $A_p$  is the projected area (length in 2D case) of the swimmer's body in the lateral direction.  $COT^*$  quantifies the energy consumption during propulsion, and therefore a lower value is desirable because it indicates greater mechanical efficiency to move for a unit distance. The nondimensional COT results documented in Table 6-7 show that the self-propelled NACA 0012 fish require less COT with the increase of the examined frequency, i.e., it has the most efficient swimming performance at Strouhal number 0.299 in the present study.

Table 6-7. Time-averaged steady-state results of the NACA 0012 fish

$f$ ( $s^{-1}$ )	0.5	0.8	1.0	1.2	1.5	2.0
$Re_L = U_t L / \nu$	1235	2224	2928	3639	4742	6684
$St^* = f A_m / U_t$	0.405	0.360	0.342	0.330	0.316	0.299
$C_{FT1}$	0.0078	0.0168	0.0241	0.0324	0.0464	0.0737
$C_{PS1}$	0.0036	0.0141	0.0271	0.0464	0.0894	0.2057
$\eta$	0.349	0.347	0.343	0.337	0.330	0.324
$COT^*$	3.657	3.089	2.889	2.767	2.618	2.404

### Effect of body mass

Biomimetic studies and observations of fishes have obtained a wide array of information on the kinematics for the propulsive performance, and these findings can guide towards green and novel solutions of underwater robots for marine applications. Though the fish in water is often neutrally buoyant, the biomimicking robots can either have same density as fluid or be heavier. The body mass of the NACA 0012 fish is thus changed to understand its influence on the self-propelled behavior. Here, three values are selected: a 2D fish body with the same density as the fluid, leading to a mass  $m = 0.0082kg$ , a 2D body with density 10 times larger, leading to  $m = 0.082kg$ , and a much heavier body with  $m = 0.2kg$ . Figure 6-34 shows the time histories of their total swimming speeds in the same inflow current. From the plots we can see that the heavier NACA 0012 fishes are not easy to be swept downstream when they are released in the current as the neutrally buoyant one, but they do have limited capability to accelerate rapidly. The 10-time-density fish requires about 30 more cycles with respect to the lightest one to reach the steady-state swimming motion, while the heaviest fish cannot achieve steady motion even after 90 cycles, and it is still slowly going towards the asymptotic steady state. Besides, it can be found that the velocity fluctuations during swimming are much smaller for the fish with larger mass. However, as expected the time-averaged total swimming speeds of the fish with  $m = 0.0082kg$  and  $m = 0.082kg$  are approximately same at the asymptotic steady-state, equal to  $\bar{U}_t = -0.948 m/s$  and  $\bar{U}_t = -0.950 m/s$ , respectively.

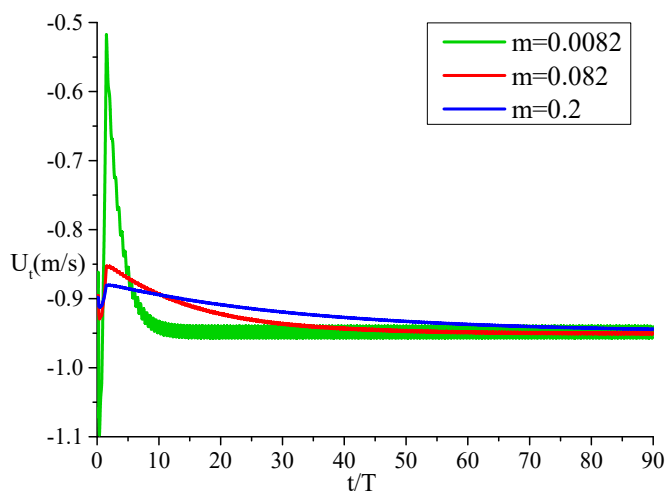


Figure 6-34. Time history of the total speed for self-propelled NACA 0012 swimming at  $f = 1.5s^{-1}$  with different mass

During the numerical simulation, the smaller acceleration of the heavier fish leads to lower mesh movement following the fish body, and therefore the overset grid can maintain a good structure and quality as at the initial state. Figure 6-35 shows the instantaneous spanwise vorticity fields of the NACA 0012 fish with larger solid densities at time instant  $t/T = 90$ . The wakes exhibit similar patterns, but the vorticity intensity of the  $m = 0.082kg$  case is slightly larger than that of the  $m = 0.2kg$  case.

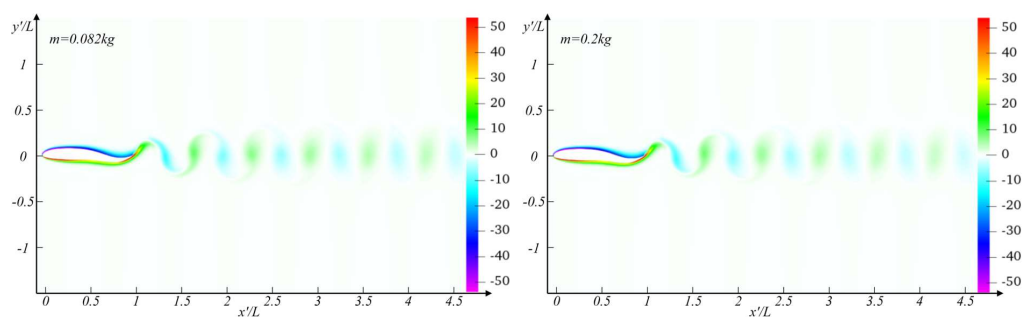


Figure 6-35. Instantaneous spanwise vorticity contours for the NACA 0012 fish-like foil of different mass swimming in currents at different frequencies

### Body shape effect

To investigate the influence of body shape on the hydrodynamics of carangiform swimming behavior, two fishes with different profiles are studied with the same kinematics. Here, the NACA 0021 fish is chosen to be compared with the NACA 0012 fish. The NACA 0021 fish is released to swim freely in streamwise direction in the same current condition as the NACA 0012 fish. Figure 6-36 shows the time histories of the total swimming speed  $U_t$  for the two fishes with oscillation frequency  $f = 1.0s^{-1}$  and  $f = 1.5s^{-1}$ . As known from the previous discussion in the forced-swimming case, the NACA 0021 fish always experiences larger drag

forces than the NACA 0012 one under the same lateral motion and inflow conditions. Therefore, it is expected that the NACA 0021 fish cannot swim as fast as the NACA 0012 fish when the same flexible motion and hydrodynamic environment are considered. The results in Figure 6-36 confirm this.

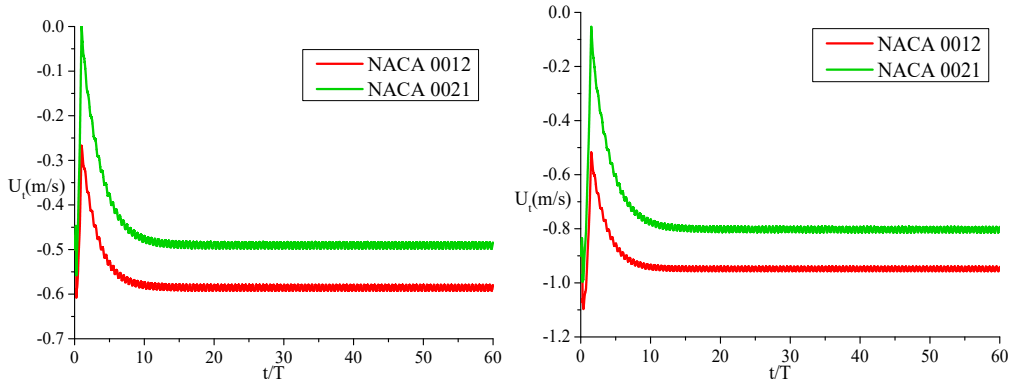


Figure 6-36. Time histories of the total speeds for self-propelled NACA 0012 and 0021 fishes swimming in the same current at  $f = 1.0s^{-1}$  (left) and  $f = 1.5s^{-1}$  (right)

The corresponding instantaneous spanwise vorticity fields of the NACA 0012 and 0021 fishes in the above cases are shown in Figure 6-37. The vorticity contours are obtained at the time instant  $t/T = 60$  during the steady-state swimming. From the figures we find that the wakes after the NACA 0021 fish are also of the reverse-vK wake type. Its vorticity intensity is stronger than that of the NACA 0012 fish, but its wake length and width are smaller.

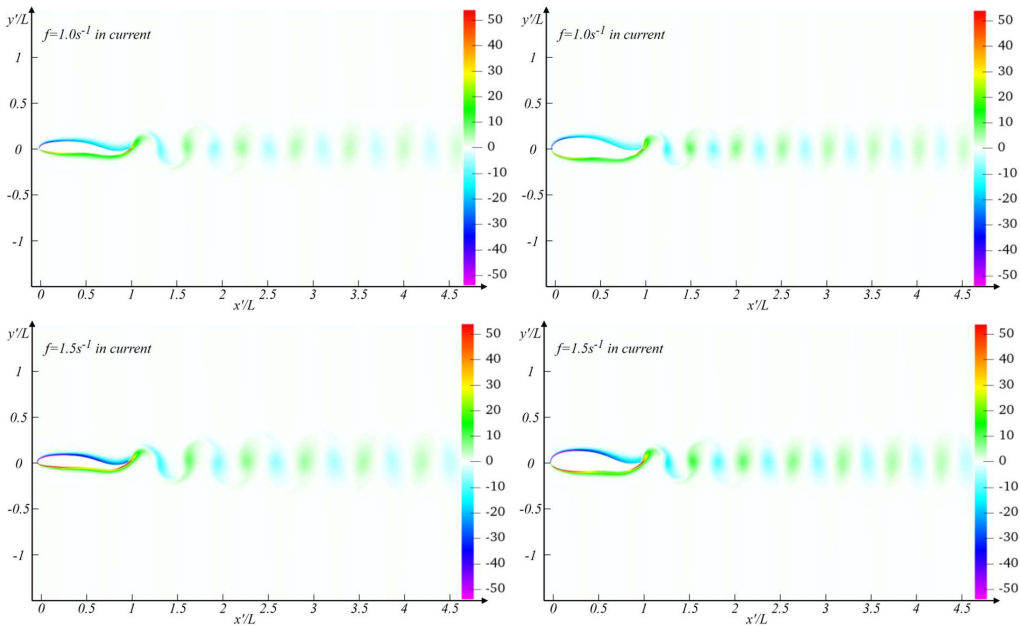


Figure 6-37. Instantaneous spanwise vorticity contours for the NACA 0012 (left) and 0021 (right) fishes swimming at  $f = 1.0s^{-1}$  (top) and  $f = 1.5s^{-1}$  (bottom)

The greater vorticity intensity of the NACA 0021 fish-like foil might be associated with larger horizontal force oscillation amplitude, as illustrated in the left plot of Figure 6-38. The right figure shows that the friction drag for the NACA 0012 fish is higher than that of the NACA 0021 fish, which could be due to the flow would remain attached in a larger portion of the foil, but the absolute values of the pressure force are overall larger for the NACA 0012 fish compared to the NACA 0021 fish, leading to stronger thrust generation capability of the NACA 0012 fish.

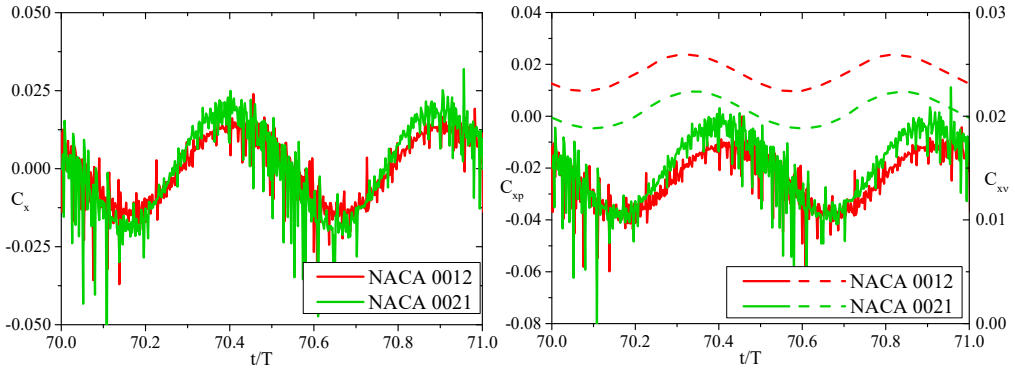


Figure 6-38. Non-dimensional horizontal force (left) and the pressure (solid line) and friction (dash line) components (right) of self-propelled NACA 0012 and 0021 fishes

The time-averaged values of the fish swimming speeds at various frequencies are documented in Table 6-8. Similar as for the NACA 0012 fish, the total swimming speed  $\bar{U}_t$  and its nondimensional value  $\bar{U}^*$  are increasing functions with respect to the undulatory frequency. As the widths of the wakes ( $h_w$ ) after the NACA 0021 fish tail are even smaller than those of the NACA 0012 fish, thus making it more difficult for estimation from vorticity contours. The values of wake length  $l_w$  prove that they are smaller than those of the NACA 0012 fish, consistently with results in Figure 6-37.

Table 6-8. Time-averaged steady-state swimming speed of the NACA 0021 fish

$f$ ( $s^{-1}$ )	0.5	0.8	1.0	1.2	1.5	1.8	2.0
$\bar{U}_t$ (m/s)	-0.206	-0.373	-0.491	-0.613	-0.804	-0.993	-1.137
$\bar{U}^*$	-0.413	-0.466	-0.491	-0.511	-0.536	-0.552	-0.569
$l_w$ (m)	0.450	0.495	0.510	0.540	0.555	0.555	0.570
$\bar{U}_t^* = U_t/f l_w$	-0.917	-0.942	-0.962	-0.946	-0.966	-0.994	-0.998

Figure 6-39 illustrates the relationship between the fish swimming speed ( $\bar{U}_t$  and  $\bar{U}_t^*$ ) and the oscillation frequency. From the left plot we can see that the total swimming speed of the NACA 0021 fish is also proportional to the frequency, but its increasing rate is lower than that of the NACA 0012 fish, which suggests that the NACA 0021 fish has limited propulsive capability especially at higher frequencies. The right plot illustrates that the forward speed  $U_t$  of the NACA 0021 fish also approximately equals to the product of the oscillation frequency  $f$  and characteristic wake length  $l_w$ , but its values are slightly smaller than those of the NACA 0012 fish. However, it should be noted that the measurement of the wake features of the NACA 0021

fish may contain larger errors as the values are smaller than those of the NACA 0012 fish. It indicates that the wake shedding from the NACA 0021 fish body is dominant by the convection of the inflow as well.

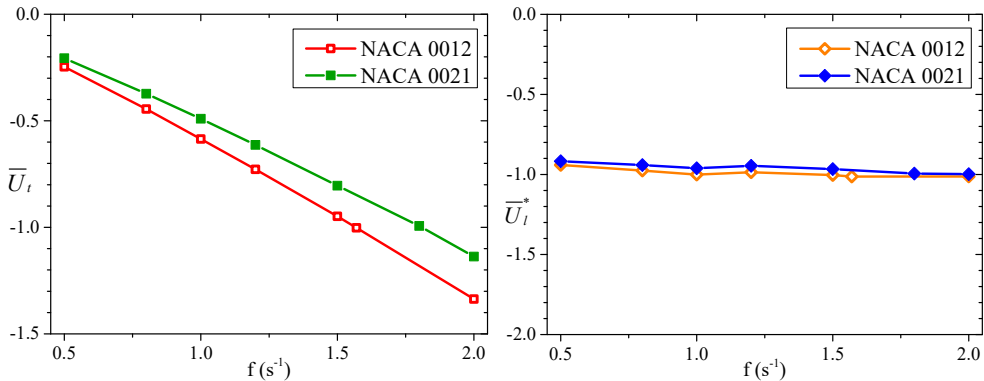


Figure 6-39. Relationship between the swimming speed and frequency of self-propelled NACA 0012 and 0021 fishes

The NACA 0012 fish is found to swim faster with the increase of the oscillation frequency, but it also uses larger thrust force and requires more input power to perform the corresponding undulatory motions at higher frequencies. Figure 6-40 shows the comparisons of the thrust force and swimming power coefficients,  $C_{FT}$  and  $C_{PS1}$ , between the NACA 0012 and 0021 fishes with different frequencies. The results illustrate that the NACA 0021 fish generates less thrust force than the NACA 0012 fish, and the difference between them become larger with the increase of swimming frequency. However, the swimming power required by the self-propelled NACA 0021 fish coincides with that of the NACA 0012 fish at all the examined frequencies, because it is consumed to perform the undulatory motions of the same kinematics. The lower thrust generation, the lower fish swimming speed, and the same power consumption suggest that the NACA fish with thicker body profile is less efficient than the thinner fish, as reported later.

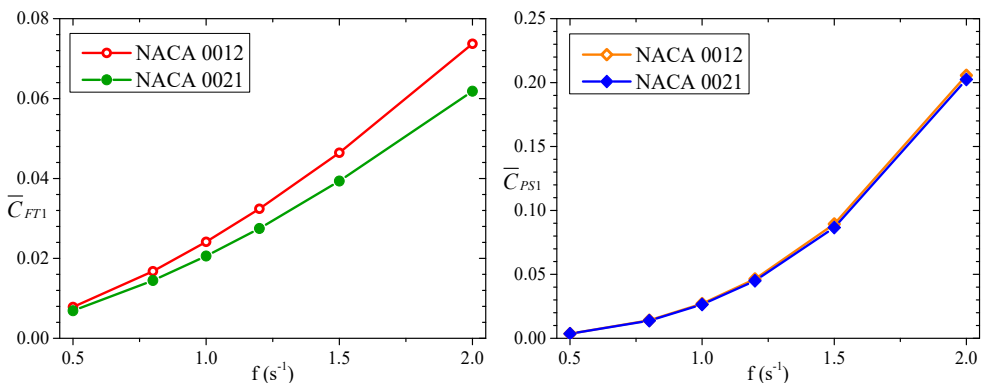


Figure 6-40. Time-averaged thrust force and swimming power coefficients of self-propelled NACA 0012 and 0021 fishes swimming at different frequencies in currents

Table 6-9 reports the Reynolds number, the critical Strouhal number and the nondimensional COT of the NACA 0021 fish during the steady-state swimming motion, together with the corresponding values for the NACA 0012 fish. The critical  $St$  of the NACA 0021 fish is also a decreasing function of  $Re_L$ . Due to smaller swimming speed achieved by the NACA 0021 fish, the Reynolds number of the self-propelled fish is lower than that of the NACA 0012 fish at all the examined frequencies. On the contrary, the critical Strouhal number of the free swimming NACA 0021 fish is much higher with respect to the NACA 0012 fish. In addition, the  $COT^*$  required by the self-propelled NACA 0021 fish is about 16~19% higher than that of the NACA 0012 fish. The results also indicate that the efficiency of the NACA 0021 fish improves at larger Reynolds number and smaller Strouhal number. It is known that most of the real fishes choose to swim within the Strouhal number range of 0.25~0.35 with the aim of efficient cruising, and this study on fish-shape effect may help to explain why the wild carangiform swimmers tend to have slender, streamlined instead of blunt bodies from the hydrodynamic point of view.

Table 6-9. Critical Strouhal, Reynolds number and COT of the self-propelled NACA 0021 fish

	$f$ ( $s^{-1}$ )	0.5	0.8	1.0	1.2	1.5	2.0
NACA 0012	$Re_L$	1235	2224	2928	3639	4742	6684
	$St^*$	0.405	0.360	0.342	0.330	0.316	0.299
	$COT^*$	3.657	3.089	2.889	2.767	2.618	2.404
NACA 0021	$Re_L$	1032	1864	2451	3065	4022	5687
	$St^*$	0.485	0.429	0.408	0.391	0.373	0.352
	$COT^*$	4.358	3.621	3.370	3.188	2.990	2.782

### Recoil effect

Apart from the fish locomotion in the longitudinal direction, the oscillatory lateral and angular velocities, identified as the recoil motions, can also make a significant influence on the swimming performance. To evaluate the recoil effect for a free-swimming fish in open water, the simulations of the self-propelled 2D fish with the prescribed undulatory motion are carried out with/without various constrained motions, i.e., some recoil reactions are prohibited in the corresponding cases. As a primary result, the locomotion speed, oscillating recoil velocities and swimming efficiency are measured for the fish under different constrained gaits.

Same as the method for calculating fish locomotion, the recoil motions are numerically solved by coupling the dynamics of the fish body and of the surrounding fluid. At each time step, the fluid and the fish kinematics are updated sequentially. As the lateral forces and hydrodynamic torques experienced by the fish body are relatively large during undulatory motion, the corresponding accelerations at the center of mass can be quite large. In order to ensure the convergence to a solution, two types of under-relaxation are used in the recoil cases, explicit and inertial. The explicit under-relaxation method employed in OpenFOAM uses the *accelerationRelaxation* parameter to control the change in the body motion state at an intermediate iteration. The inertial under-relaxation method is based on approaches as those

described, for example, by Sun and Faltinsen (2011), in which the added mass effect is considered to stabilize the numerical solver. It inserts an estimate of the added mass force to both left and right-hand-sides of the motion equation, i.e., on the left-hand-side the effective mass of the system is increased with an estimate of the added mass, and on the right-hand-side an additional added mass force is used by multiplying the same estimated added mass with the body acceleration approximated with a value known from the previous time instant. In the simulations of the self-propelled NACA 0012 fish recoil cases, the *accelerationRelaxation* value of the explicit method is set to 0.1, and the added mass value of the inertial method is  $0.78 \text{ kg/m}$  according to Korotkin (2008). In addition, a sinusoidal ramp function within the first second has been used for the fish swimming motion starting from equilibrium position to the described amplitude in Eq. (6.2), in order to avoid a break-down at the beginning of the numerical simulations. The comparison of the two under-relaxation methods showed good consistency in predicting the locomotion speeds of fish swimming at  $f = 1.0 \text{ s}^{-1}$ , as illustrated in Figure 6-41. The inertial under-relaxation method is applied for the recoil studies in the following work.

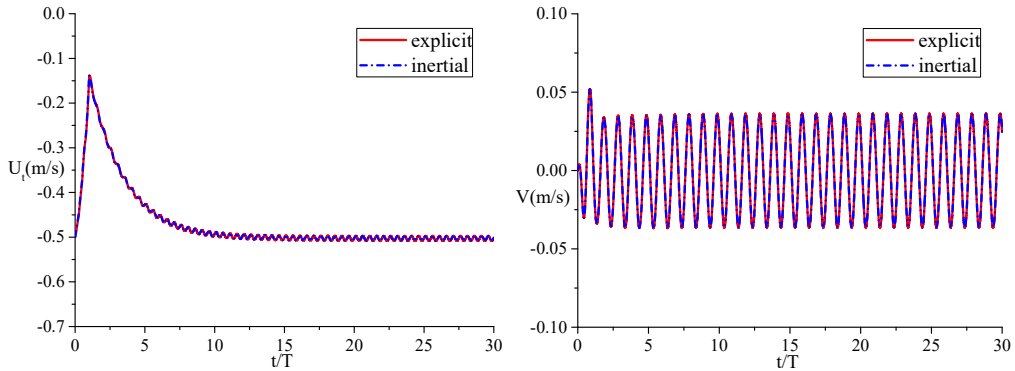


Figure 6-41. Time history of the forward (left) and lateral (right) speeds for self-propelled NACA 0012 fish swimming at  $f = 1.0 \text{ s}^{-1}$  in current with angular constraint using different under-relaxation methods

To evaluate the effect of the recoil motions accompanying the fish locomotion generated by body undulations, the comparisons between a fish whose lateral recoil is allowed and a fish who is free only in streamwise direction are shown in Figure 6-42. The instantaneous spanwise vorticity fields for the two cases are presented in Figure 6-43 at the time instant  $t/T = 60$ . The contours do not document substantial difference in terms of wake structure; the locomotion results indicate that, for the swimming frequency  $f = 1.0 \text{ s}^{-1}$ , the fish free in streamwise and lateral directions has a lateral recoil velocity oscillating at the same frequency as the undulatory motion and would reach 14% lower forward speed than a fish only free in streamwise direction. As the propulsive force for the fish locomotion comes from the fish swimming power due to the fish prescribed undulatory motion, it is suspected that for a fish free in both streamwise and lateral directions, the fish has spent less power into the forward motion and thus achieving a lower forward swimming speed. However, one must note that the numerical inviscid studies by Paniccia et al. (2021b) suggested the fish free in streamwise and lateral directions would swim faster. This poses a research question about the relevance of viscosity in this framework. It is



apparent that the recoil can significantly affect the fish swimming behavior, and a more in-depth analysis on recoil effect under various motion constraints should be carried out. This is left as recommendation for future studies.

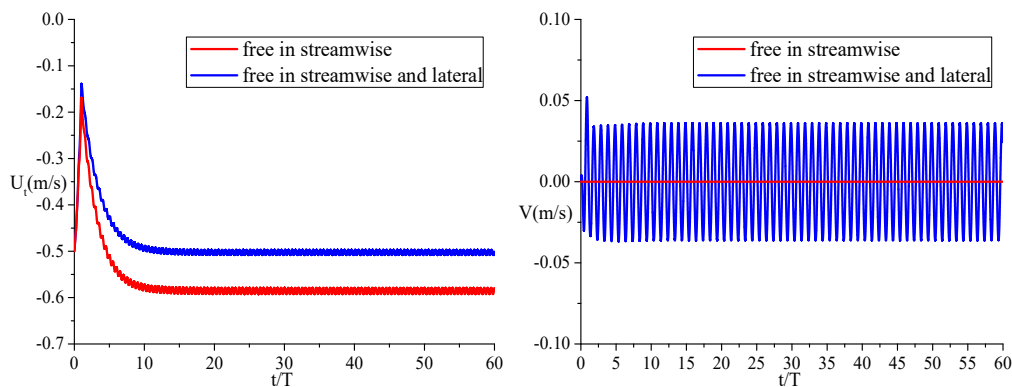


Figure 6-42. Time history of the forward (left) and lateral (right) speeds for self-propelled NACA 0012 fish swimming at  $f = 1.0s^{-1}$  in current with different constraints

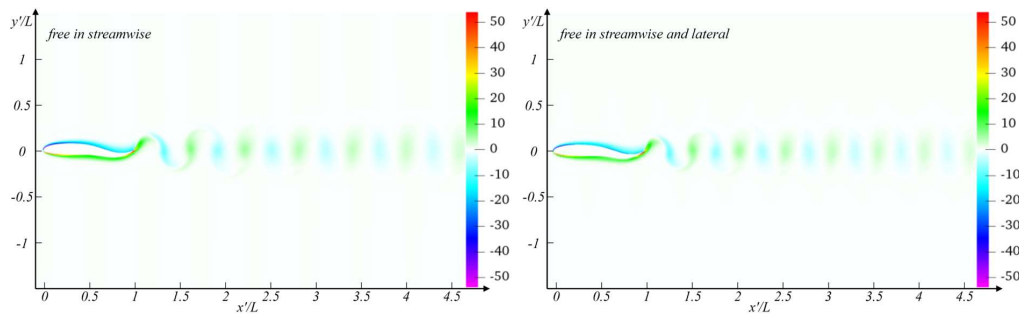


Figure 6-43. Instantaneous spanwise vorticity contours for the NACA 0012 fish swimming at  $f = 1.0s^{-1}$  free in streamwise (left) and streamwise and lateral directions (right) at time instant  $t/T = 60$

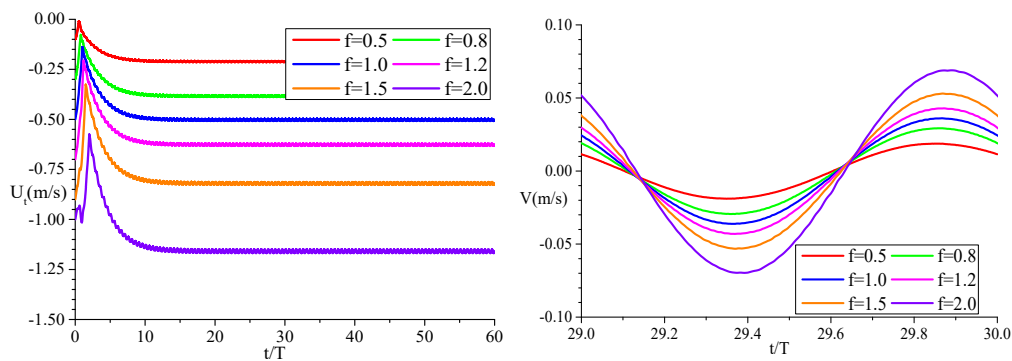


Figure 6-44. Instantaneous forward (left) and lateral (right) speeds for self-propelled NACA 0012 fish free in streamwise and lateral directions at different frequencies in currents

Figure 6-44 shows the instantaneous total forward swimming speed and lateral speed of the self-propelled NACA 0012 fish, free to swim in both streamwise and lateral directions, under different undulatory frequencies. The results illustrate that the fish-like foil can achieve higher forward and lateral speeds with larger oscillation frequency. Compared to the swimming speed of the self-propelled NACA 0012 fish that only moves in streamwise direction, as shown in Figure 6-31, the total forward speed of the fish free in both streamwise and lateral directions is smaller at all the examined frequencies.

Table 6-10 documents the time-averaged values of the forward swimming speed for the self-propelled NACA 0012 fish with different frequencies. The calculations indicate that in all the examined cases, the forward speed of the fish-like foil swimming freely in streamwise and lateral directions (referred as  $X + Y$  in Table 6-10) is about 14% lower than that of a fish only free in streamwise direction (referred as  $X$ ). As the traditional Froude efficiency is not a suitable efficiency measure for steady-state self-propelled swimming, the cost of transport is applied here to quantify the fish propulsive efficiency. The results show that the NACA 0012 fish with lateral recoil motions consumed less energy by 14~17% than the fish only free in the streamwise direction. This finding of COT reduction for fish with recoil motions is consistent with the fish COT results reported by Paniccia et al. (2021b).

Table 6-10. Time-averaged steady-state swimming speed  $\bar{U}_t$  and COT of the self-propelled NACA 0012 fish with different constraints

$f$ ( $s^{-1}$ )	0.5	0.8	1.0	1.2	1.5	2.0
$\bar{U}_t(X)$	-0.247	-0.445	-0.586	-0.728	-0.948	-1.337
$\bar{U}_t(X + Y)$	-0.211	-0.384	-0.503	-0.627	-0.820	-1.159
Reduction	14.49%	13.77%	14.15%	13.89%	13.49%	13.27%
$COT^*(X)$	3.657	3.089	2.889	2.767	2.618	2.404
$COT^*(X + Y)$	3.141	2.590	2.421	2.296	2.162	2.006
Reduction	14.10%	16.14%	16.19%	16.99%	17.41%	16.58%

## 6.2.2 Self-propelled foil in a tunnel

The investigation on the fish swimming behaviour and performance has been undertaken by many researchers from biology and hydrodynamics, and a wealth of data has been provided from these studies from physical experiments. Different types of swim tunnels have been designed and developed by biologists with the focus on estimating metabolic parameters. In such respirometer tanks, the tunnel volume is often set to be less than 200 times the fish volume with the aim of obtaining more accurate measurement of oxygen level from the water inside. It results in limited space for a swimming fish and this might affect the fish behaviour both mentally and physically. Besides, the fish is often smart enough to swim close to the bottom and side boundaries in order to find a place with lower current velocity and save energy for swimming. Both aspects indicate potential wall effects on fish swimming performance, which is of significance for hydrodynamic analysis and biological underwater vehicle development. Moreover, the metabolic parameters measured could not either correspond to the actual values for a fish in open-water conditions. This section will investigate the wall effect on the hydrodynamic behavior of a self-propelled swimming fish in tunnels.

The maximum thickness of the NACA 0012 fish is  $D = 0.12m$ , and here it is used to normalize the width of the swim tunnel  $h_t$ . Here, the swim tunnel size is varied systematically from  $h_t = 6m$  (i.e.,  $h_t/D = 50$ ) to  $h_t = 0.72m$  ( $h_t/D = 6$ ), and the NACA 0012 fish is released to perform self-propelled motion in these tunnels at oscillation frequency  $f = 1.0s^{-1}$  and  $f = 1.5s^{-1}$  in the currents with inflow velocity  $U_c = 0.5 m/s$  and  $U_c = 0.9 m/s$ , respectively. It should be noted that for a self-propelled fish in infinite domain, the fish can achieve the same total steady-state swimming speed despite of the value of the enforced current velocity, as proved by comparison between the cases of calm water and currents. However, when the fish swims in a laterally restricted fluid domain, the current also interacts with the wall boundary, leading to boundary-layer effects. This fact and the interaction of the fish itself with the walls result into different final swimming states of the fish in different inflow conditions. In the following, the numerical simulations examine a fixed current velocity while investigating the wall effect of the swim tunnel on the fish behavior.

Figure 6-45 shows the time histories of the total swimming speed  $U_t$  for the fish with two different undulatory frequencies. The case labelled  $h_t/D = \infty$  represents the fish swimming in an infinite fluid domain without boundary effects, i.e., open-water current cases in previous sections. It can be found from the results that when the tunnel is 50 times wide of the fish thickness, there are little differences between the swimming speed in the tunnel and in infinite domain. As the swim tunnel becomes narrower, the self-propelled fish experiences stronger decrease in the swimming speed, especially when the tunnel width  $h_t/D < 10$ .

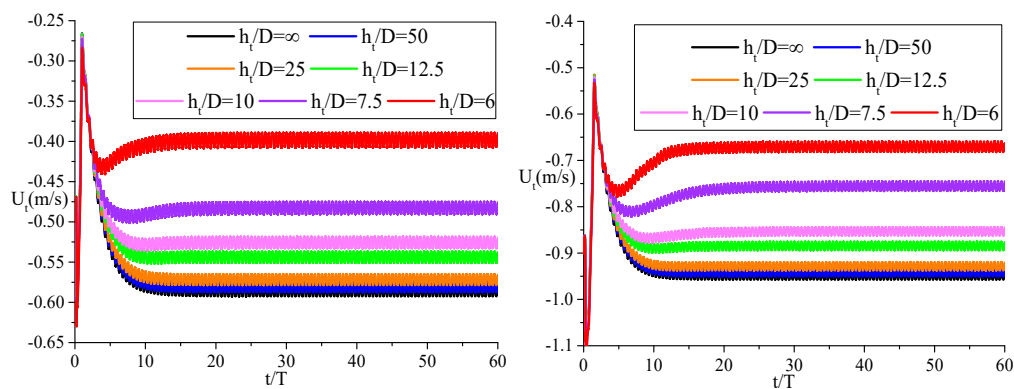


Figure 6-45. Time history of the total speed for self-propelled NACA 0012 fish swimming at  $f = 1.0s^{-1}$  and  $f = 1.5s^{-1}$  in tunnels with different widths

Table 6-11 documents the time-averaged values of the fish swimming speed for all the examined tunnel widths and the corresponding speed drop with respect to the fish swimming in the infinite domain. These quantities demonstrate that when the distance between the fish body and the tunnel boundary is large enough, i.e.,  $h_t/D \approx 50$  in this NACA 0012 fish case, the tunnel wall has little influence on the fish swimming performance. As the tunnel width decreases to  $h_t/D = 10$ , the swimming speed becomes 10% lower than the fish speed in infinite domain. Below this tunnel size, a small decrease of the tunnel width can lead to a big reduction of the total fish forward speed. This tendency is more obvious for the self-propelled fish swimming with larger undulatory frequency.

Table 6-11. Time-averaged steady-state swimming speed  $\bar{U}_t$  of the NACA 0012 fish

$h_t$ (m)	$\infty$	6.0	3.0	1.5	1.2	0.9	0.72
$h_t/D$	$\infty$	50	25	12.5	10	7.5	6
$f = 1.0s^{-1}$	-0.586	-0.581	-0.572	-0.544	-0.526	-0.482	-0.432
Reduction	–	0.87%	2.37%	7.14%	10.24%	17.62%	26.25%
$f = 1.5s^{-1}$	-0.948	-0.942	-0.928	-0.885	-0.853	-0.756	-0.670
Reduction		0.71%	2.10%	6.73%	10.06%	20.33%	29.33%

Figure 6-46 illustrates the relationship between the nondimensional swimming speed and the tunnel width. The left plot explicitly shows a sharp drop of the fish speed when the tunnel is very narrow ( $h_t < 1.5m$ , i.e.,  $h_t/D < 12.5$ ). The figure on the right indicates that the fish swimming speed can be nonlinearly associated with the tunnel size.

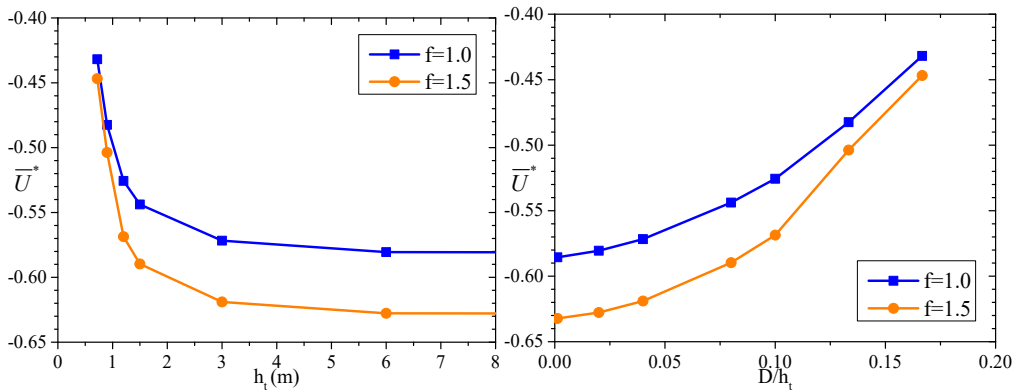


Figure 6-46. Relationship between the swimming speed of the self-propelled NACA 0012 and tunnel width

The instantaneous spanwise vorticity fields at the time instant  $t/T = 60$  of the NACA 0012 fish swimming in tunnels at  $f = 1.0s^{-1}$  are shown in Figure 6-47. Little difference can be seen from the comparison between the wake in the case of  $h_t/D = 50$  and the wake in the infinite domain case (see the first contour in Figures 6-37). It can be observed from the figures that when the width of the swim tunnel decreases, the fish wake structures have similar configurations, i.e., the wake length and width are approximately the same, but the vorticity intensity becomes stronger. As the fish total swimming speed is reduced in narrower tunnels, it is found that the total speed  $\bar{U}_t$  is no longer proportional to the characteristic wake length  $l_w$ . Instead, the shedding vortex seems to be still dominated by the inlet current velocity regardless of the fish swimming behavior in tunnels. When  $h_t/D < 10$ , the side walls get so close to the undulatory fish that the boundaries begin to have significant interaction with the wake. From the last two contours of Figure 6-47, the wake width increases as the tunnel width decreases, and the vortex street shows an apparent reverse-vK type, indicating that the fish may struggle to generate larger thrust force in order to balance a larger drag force.

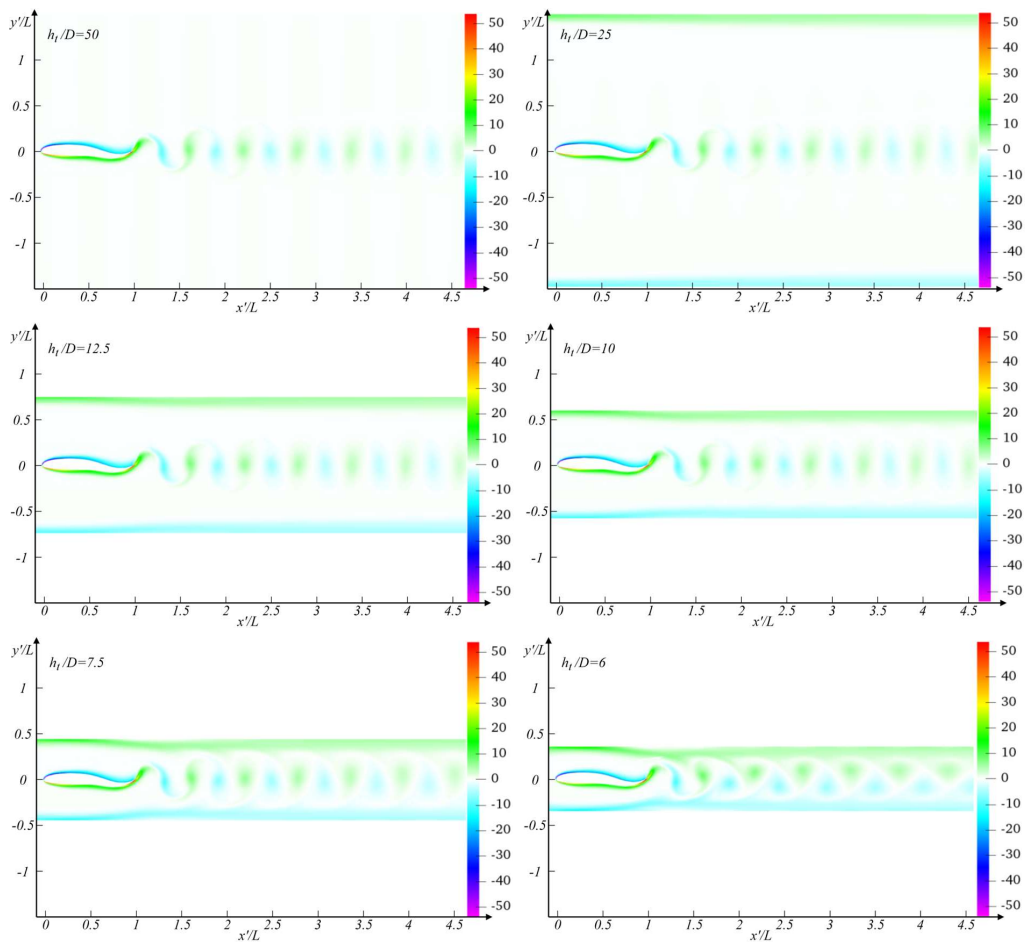


Figure 6-47. Instantaneous spanwise vorticity contours for the NACA 0012 fish swimming at  $f = 1.0s^{-1}$  in tunnels with different widths

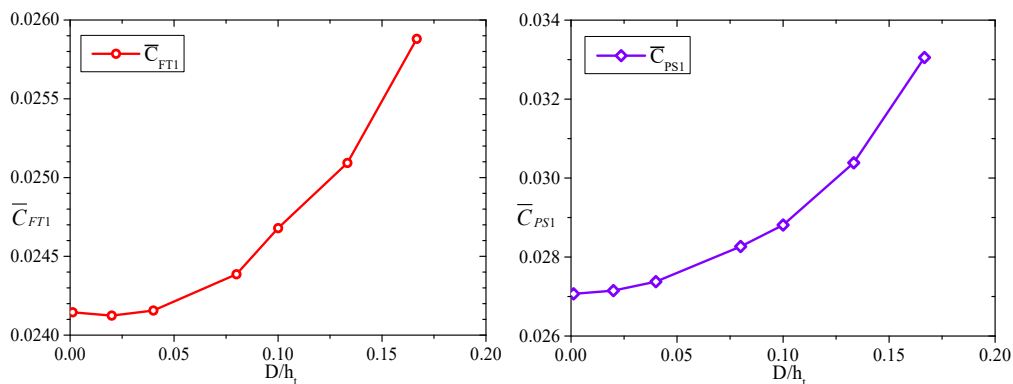


Figure 6-48. Time-averaged thrust force and swimming power coefficients of self-propelled NACA 0012 fish swimming at  $f = 1.0s^{-1}$  in tunnels with different widths

To elucidate the influence of the tunnel size on the hydrodynamics of self-propelled swimming fish, Figure 6-48 shows the calculated thrust force and swimming power coefficients of the NACA 0012 fish swimming at  $f = 1.0s^{-1}$  in tunnels with different widths. As the size of the tunnel becomes smaller, i.e., the value of  $D/h_t$  gets larger, both the thrust force and swimming power consumption increase, while the total swimming speed reduces. It represents that the swimming fish experiences larger thrust/drag forces, at lower total forward speed in narrower tunnel, and requires more power input to perform the self-propelled undulatory motion with the same kinematics.

The Reynolds number, the critical Strouhal number, and the nondimensional COT of the self-propelled NACA 0012 fish in the examined swim tunnels are documented in Table 6-12 and Figure 6-49. The results show that when the fish swims in a tunnel with smaller width, it requires higher Strouhal number than the fish in a larger domain, and the critical  $St$  of the NACA 0012 fish is inversely related with  $Re_L$ . The right plot illustrates that the energy consumption coefficient of the NACA 0012 fish increases with the decrease of the tunnel width. It means that the self-propelled fish swims less efficiently in restricted water domain. Based on these 2D laminar-flow findings, it is suspected that the biological respirometer tank can have an influence on the swimming fish behavior and the performance investigated in labs might be less efficient than the fishes in nature. Therefore, swim tunnels should be designed suitably wide to minimize the boundary effects for more accurate hydrodynamic studies.

Table 6-12. Asymptotic steady-state results of the NACA 0012 fish with  $f = 1.0s^{-1}$  in tunnels

$h_t/D$	$\infty$	50	25	12.5	10	7.5	6
$Re_L$	2928	2903	2859	2719	2628	2412	2159
$St^*$	0.342	0.345	0.350	0.368	0.380	0.415	0.463
$COT^*$	2.889	2.921	2.991	3.249	3.426	3.937	4.783

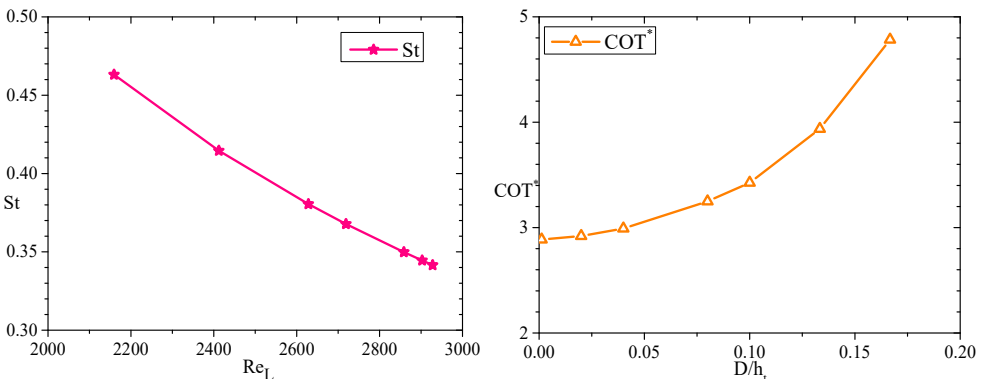


Figure 6-49. Strouhal number vs. Reynolds number and nondimensional COT of the self-propelled NACA 0012 fish swimming at  $f = 1.0s^{-1}$  in tunnels with different widths

The effect of recoil has also been evaluated for the self-propelled NACA 0012 fish swimming in tunnels with different widths, and the predicted forward and lateral speeds for fish with angular constraint swimming at  $f = 1.0s^{-1}$  are shown in Figure 6-50. The results of  $U_t$

exhibited similar qualitative dependence on the tunnel width as that of the self-propelled fish only moving in streamwise direction (Figure 6-45). When the tunnel width is 50 times of the fish thickness, there are little differences between the swimming speed in the tunnel and in infinite domain, but the swimming speed drops rapidly with the decrease of the tunnel width, especially at  $h_t/D < 10$ . However, the values of  $U_t$  for the recoil cases are smaller than those in the left plot of Figure 6-45 under the same swim tunnel environments. For the lateral swimming speeds of the self-propelled NACA 0012 fish, the tunnel width is found to have little influence. It is therefore suspected that the lateral swimming speed depends primarily on the prescribed undulatory motion of the fish body.

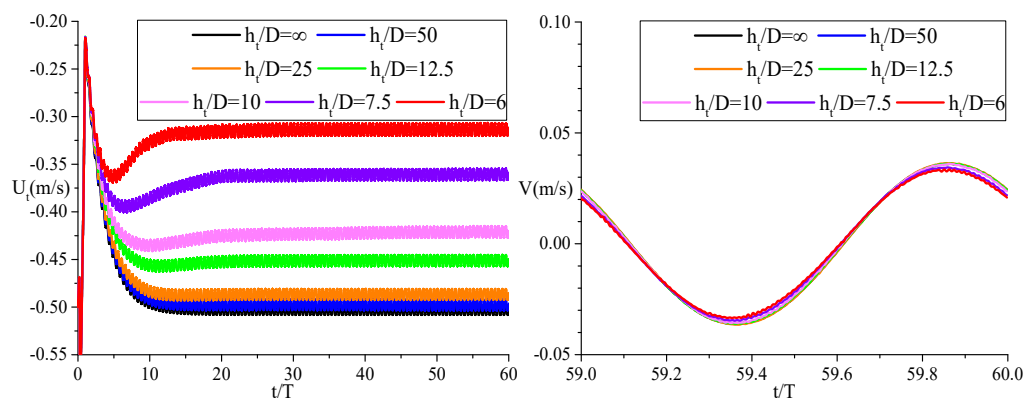


Figure 6-50. Time history of the forward (left) and lateral (right) speeds for self-propelled NACA 0012 fish with angular constraint swimming at  $f = 1.0s^{-1}$  in tunnels with different widths

Table 6-13 documents the time-averaged values of the forward swimming speed for the self-propelled NACA 0012 fish in different swim tunnels and the reduction of  $U_t$  for fish with lateral recoil motions ( $X + Y$ ) compared to the fish only moving in streamwise direction ( $X$ ). For the cases at  $h_t/D > 25$ ,  $U_t$  of the fish free in streamwise and lateral directions remains about 14% smaller than that of a fish only free in streamwise direction, demonstrating that the tunnel wall has little influence on the fish swimming performance when the distance between the fish body and the tunnel boundary is large enough. As the tunnel width decreases, the differences of the fish swimming speed between  $X + Y$  and  $X$  cases become larger. The results indicate that the boundary walls close to the fish body could have an influence on the hydrodynamics of fish swimming. Moreover, compared with the open-water scenario discussed in the previous section, the effect of recoil on fish locomotion speed seems to be enhanced in a narrow swim tunnel.

Table 6-13. Time-averaged steady-state swimming speed  $\bar{U}_t$  of the NACA 0012 fish at  $f = 1.0s^{-1}$

$h_t$ (m)	$\infty$	6.0	3.0	1.5	1.2	0.9	0.72
$h_t/D$	$\infty$	50	25	12.5	10	7.5	6
$\bar{U}_t$ (X)	-0.586	-0.581	-0.572	-0.544	-0.526	-0.482	-0.432
$\bar{U}_t$ (X + Y)	-0.503	-0.498	-0.487	-0.451	-0.422	-0.361	-0.314
Reduction	14.21%	14.28%	14.91%	17.01%	19.69%	25.15%	27.32%

The instantaneous spanwise vorticity fields at the time instant  $t/T = 60$  for the NACA 0012 fish with lateral recoil motions and swimming at  $f = 1.0s^{-1}$  in the two narrowest tunnels are shown in Figure 6-51. It can be observed from the figures that the wake structures have a strong interaction with the tunnel boundaries and present an apparent reverse-vK type of wake, as compared to the wake in the infinite water domain in Figure 6-43 where the vortex streets are almost aligned. The wake width increases with the decrease of tunnel width. By comparing the last two contours of Figure 6-47, the wake length and width for the fish free in both streamwise and lateral directions are smaller than those of the fish only free along streamwise direction, which could be associated with smaller thrust force of fish with recoil motions.

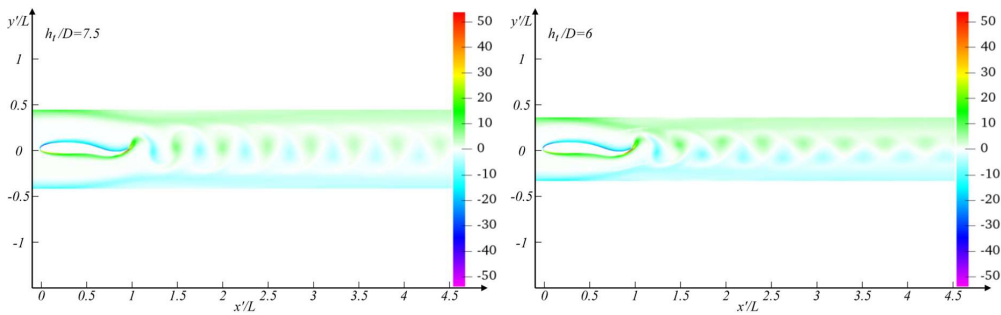


Figure 6-51. Instantaneous spanwise vorticity contours for the NACA 0012 fish swimming at  $f = 1.0s^{-1}$  free in both streamwise and lateral directions in tunnels with different widths

Figure 6-52 illustrates the calculated thrust force coefficient, swimming power coefficient, COT, critical Strouhal number and Reynolds number of the NACA 0012 fish with lateral recoils swimming at  $f = 1.0s^{-1}$  in different tunnels. With the decrease of the tunnel size, i.e., the value of  $D/h_t$  gets larger, both the thrust force and swimming power consumption increase, and the values for the fish free in streamwise and lateral directions are always lower than those of the fish free in streamwise direction. The cost of transport results indicate that the self-propelled fish with lateral recoil has better swimming efficiency than the fish only free in streamwise direction in all the examined swim tunnels, but as the distance between tunnel boundaries and fish body becomes very small, the COT of the fish with lateral recoil motions rises rapidly and gets closer to that of the fish only free in streamwise direction, demonstrating that a self-propelled fish experiences a severe efficiency drop in restricted water domain and the hydrodynamic advantage of recoil seems to be reduced. The last plot of Figure 6-52 shows that the critical  $St$  of the NACA 0012 fish is inversely related with  $Re_L$ . It has already been documented in Tables 6-11 and 6-13 that in a swim tunnel with smaller width, the self-propelled fish experiences always smaller locomotion speed, indicating smaller Reynolds number. The relationship between  $St$  and  $Re_L$  confirms that the self-propelled fish with lateral directions requires higher Strouhal number in a narrow water domain. It is interesting to note that, even though the fish would achieve different swimming speeds without and with lateral recoil in the same tunnel, it follows the same relationship between  $St$  and  $Re_L$ . The above findings suggest the effect and recoil and boundary wall can have a large influence on the hydrodynamics of self-propelled swimming fish. It is suspected that the respirometer tanks could reduce the fish propulsive efficiency and speed, and the experimental data might underestimate fish critical



swimming speed and maximum metabolic rate. Therefore, swim tunnels should be designed suitably wide to minimize the boundary effects for more accurate hydrodynamic studies. One should note that these findings are based on 2D flow conditions; confirmations from 3D investigations are desirable and are left as recommendations for future studies.

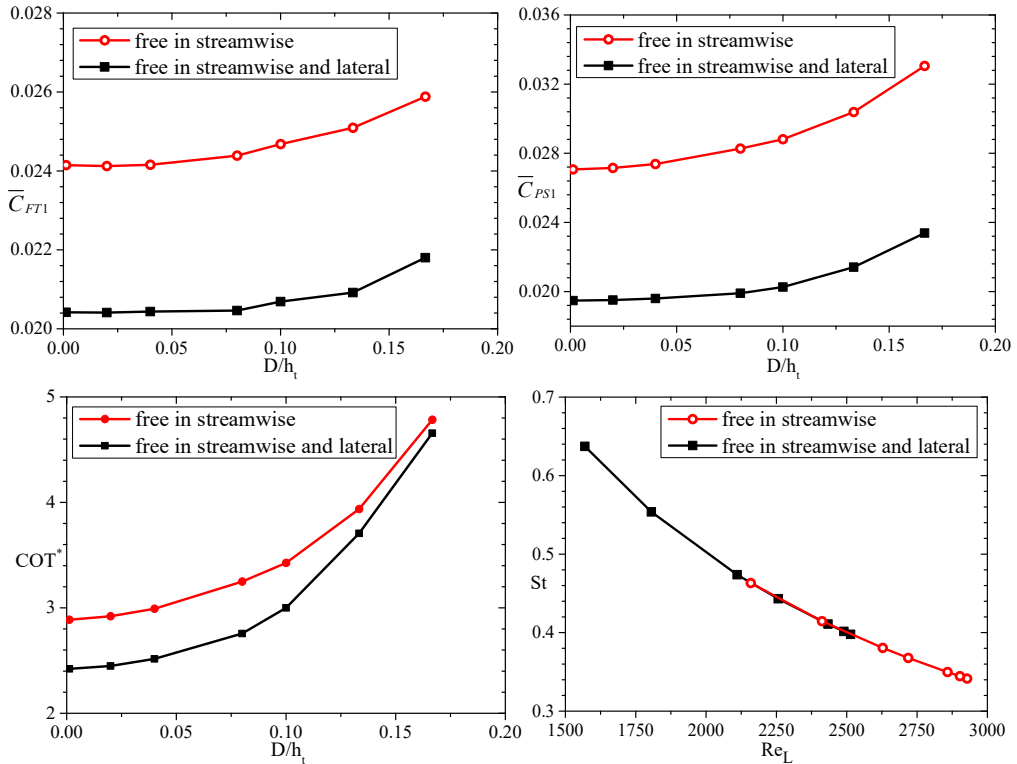


Figure 6-52. Time-averaged thrust force and swimming power coefficients,  $COT$  and  $St$  vs.  $Re_L$  of self-propelled NACA 0012 fish swimming at  $f = 1.0s^{-1}$  in tunnels with different widths

### 6.3 Summary

In this chapter, the fish-like foils with carangiform swimming mode have been numerically studied to understand the hydrodynamic mechanisms of their propulsive performance. They are simulated in two different scenarios. One is the fish-like foil being held in a fixed position under an incoming uniform stream, and the other one is the fish self-propelling itself in the fluid.

For the first scenario, the simulations of the forced fish-like swimming foil have been verified by good agreement with previous numerical data in reference papers in terms of hydrodynamic forces and powers. The thrust and drag forces experienced by the fish is decomposed according to the method proposed by Borazjani and Sotiropoulos (2008). For the forced swimming NACA 0012 fish with  $Re_L = 5000$ , it can generate thrust force only when its undulatory frequency is large enough ( $St > 0.20$ ), and the source of the thrust comes from the pressure component.

The wake regimes of the forced swimming fish are consistent with the phase diagram of vortex regions observed for the rigid flapping foils illustrated in chapter 5 and reported by previous researchers. The wake transits from complex paired vortex shedding (2P) to von Kármán wake, aligned wake and reverse-vK wake with the increase of the Strouhal number, and the drag-thrust transition occurs within the reverse-vK wake regime. In addition, the effect of the Reynolds number is studied for the forced fish-like swimming foils. It is found that the force transition occurs at smaller Strouhal numbers at higher Reynolds number, and the reason is mainly that the shear stress decreases while the pressure force changes little. The study of the body shape effect shows that the blunt fish-like foil experiences larger drag force and generates less thrust than the slim swimming foil. Besides, the propulsive performance of the undulatory fish-like foil is compared against the rigid pitching foil with the same oscillation amplitude and frequency, it indicates that undulatory propulsion mode can be more efficient under the examined conditions.

In the second scenario, the fish is released to perform self-propelled locomotion in water using the developed self-propulsion strategy introduced in chapter 4. For a fish free to move in the streamline direction, the predicted swimming speed under different conditions is consistent with the velocity in the force transition case obtained from the forced swimming foils. In order to reach higher swimming speed, the fish needs to undulate with higher frequency. The wake patterns are of the similar reverse-vK regime at the steady-state swimming as the horizontal force experienced by the fish is time-averaged zero. The body mass of the fish can slow down its acceleration process but have little influence on the final swimming speed. In order to explain the effect of body shape on the swimming behavior from the hydrodynamic perspective, the self-propelled NACA 0012 and 0021 fishes are simulated and compared. It is found that the blunt NACA 0021 fish cannot achieve as high speed as the slim NACA 0012 fish with the same kinematic conditions. The fish with a thicker body generates less thrust force but requires the same mechanical power input for undulations, thus leading to less efficient swimming performance. The effect of lateral recoil motion has been examined and the swimming efficiency, measured by cost of transport, indicates that the fish free in both streamwise and lateral directions has better propulsive efficiency than the fish only moving in streamwise direction.

It is important to notice that a lot of data in terms of fish swimming kinematics and wake flow observations are obtained from the experiments in respirometer tanks, where the boundaries of the tunnel are often close to the fish body. From the hydrodynamic point of view, the wall effect is too important to be ignored for the study of fish swimming motion. Here, the self-propelled NACA 0012 fish is released to swim along the centerline of the tunnel. The decrease of the tunnel width results in the decrease of the fish swimming speed. The boundary layers along the tunnel walls have stronger interaction with the wakes after the fish tail, especially when the tunnel width is less than 10 times of the thickness of the NACA 0012 fish in our examined cases. Both the drag force and power consumption increase for fish in a narrow tunnel. The swimming efficiency calculation indicates that the fish may swim less efficient in the tanks than in the wild. Therefore, a swim tunnel with enough space is suggested for the hydrodynamic investigation on a swimming fish.



# Chapter 7

## Conclusions and further work

The swimming behaviors of two different fish species have been investigated experimentally, and the propulsive performance of various fish-like foils have been examined numerically. Herein, both rigid and deformable foil scenarios have been studied. The main purpose of the work has been to observe fish kinematic features under different swimming speeds and to understand the fluid mechanisms behind their extraordinary propulsive performances by means of systematical numerical simulations. The investigated physical phenomena were quantified and compared with findings from previous research, and the numerical predictions were validated and verified with reference data. The influence of several parameters on fish-like foil propulsion have been analyzed to shed light on the improvements of bio-inspired underwater vehicles and real-fish experimental setups. A morphing strategy has been proposed and optimized based on the studies of foil shape effect to enhance foil propulsion performance.

This final chapter concludes the thesis work by summarizing the main activities and findings and presents recommendations where further work can be pursued.

### 7.1 Conclusions

The main findings from the real-fish observation experiments are summarized in Section 7.1.1, while main results for the investigation of various fish-like foil propulsive performance are presented in Section 7.1.2.

#### 7.1.1 Physical investigations

Fish swimming modes can be classified into two generic categories based on their locomotion features: one is body and caudal fin swimming (BCF), and the other is median and paired fin swimming (MPF). In the present study, observation experiments were carried out on two different fish species, one BCF swimmer and one MPF swimmer, to investigate their swimming performance and behaviors under different conditions.

##### **Labriform swimmer**

A series of experiments were performed on shiner perch (*Cymatogaster aggregate*), a labriform swimmer using primarily pectoral fins and assisted by the caudal fin at high speed, in a Steffensen-type swimming tunnel. Fish were randomly assigned to one of the three experimental scenarios: a solitary fish (Single), a schooling pair of fish (Pair), and a false pair where a single fish swims alongside a video of a conspecific fish (False pair). The swimming

performances of the fish, including swimming speed, pectoral fin beat frequency and amplitude, gait transition and metabolic rate, in current with various inflow velocities were compared and analyzed to examine the hydrodynamic and behavioral advantages during fish schooling.

The kinematic analysis of the experiments showed that the pectoral fin beat frequency increased with fish swimming speed almost linearly in all scenarios, indicating that the fish consumed more energy to keep up with the increasing inflow velocity. It was found that the back fish in a real Pair treatment used apparently lower fin beat frequencies than the front fish and the ones in other scenarios during steady swimming state, i.e., before gait transition speed. This demonstrates that there are hydrodynamic advantages in being the back fish in a swimming school, and that the back fish does not use as much energy for swimming as the front fish or as it would if it was alone. Another important observation was that at higher swimming speeds (around and above gait transition speed), the fin beat frequency of the fish in False Pair was noticeably lower than that in other treatments. This may be due to the “fake friend” on the computer monitor displayed steady swimming performance. It indicated that the fish in the experiments were sensitive to the visual stimuli and there was hypothesized to be a calming effect of swimming together with another steady individual when high speeds were involved.

The metabolic rates of the examined fish were analyzed with respect to the swimming speed using a hydrodynamic-based power function model. The results demonstrated that the average metabolic cost of the real fish school was always smaller than that of the single swimming fish. Besides, the fish with a fake friend were found to have lower oxygen consumption relative to the single fish from speed  $3.5 BL/s$  and higher, which suggested that the presence of an accompany "fake" fish remaining always steady may calm down the real fish that was struggling to maintain swimming.

It was concluded that schooling confers both hydrodynamic and behavioral advantages over swimming alone for a gregarious fish, but that the relative contribution of the two influences depends on the speed of swimming. At low speeds hydrodynamic effects outweigh behavioral effects, but at high speeds when an individual may start to struggle with the effort required to maintain swimming, the presence of another fish who remains calm may have a calming effect on the fish that is struggling.

### **Sub-carangiform swimmer**

Observation experiments were carried out on Atlantic salmon *Salmo salar* post-smolts, a typical sub-carangiform swimmer propelling itself by bending its body into a backward-moving propulsive wave that extends to its caudal fin, in a Blazka-type swim tunnel. The current velocity inside the tunnel was controlled to increase incrementally with the focus on investigating the salmon behavior and kinematics at different swimming speeds. The swimming performance of the hatchery-reared fish in the flume was recorded over the entire trials. The influence of salmon body size, current velocity and tunnel boundary walls were analyzed to identify important factors affecting the fish swimming capability.

Individual swimming salmon in the swim tunnel produced a significantly lower critical

swimming speed compared to biological data of wild fish and fish swimming in larger flumes. The tail beat frequency of the fish increased almost linearly with the swimming speed. Both critical swimming speed and tail beat frequency of the examined salmon tended to decrease with the fish size. One possible reason for these observations could be the blunt body shape of the hatchery-reared fish, which caused larger hydrodynamic loads acting on the fish body. The side-wall effect of the swim tunnel should be another important reason to explain these behaviors of fish. The hydrodynamic interaction between fish swimming motion and boundary walls in a narrow swim tunnel may lead to the underestimate of fish critical swimming speed. The analysis on the boundary wall effect of swim tunnel suggested that fish swimming performance could be compromised in restricted water space. Therefore, the fish experimental setup should be improved to be suitably large for more accurate hydrodynamic studies.

### 7.1.2 Numerical simulations

In order to understand the mechanisms behind high propulsive performance of fish, especially the ones with sub-carangiform swimming mode, a series of hydrodynamic scenarios has been examined by CFD simulations using OpenFOAM. As the fish appendages are of secondary importance in this study, the fish body is modelled as a rigid or deforming foil interacting with a current or advancing in otherwise calm water without the presence of a free surface.

A numerical method capable of simulating self-propelled rigid and/or flexible bodies with periodic lateral motions has been proposed. The implemented self-propulsion strategy in OpenFOAM, verified to be numerically accurate and efficient through an oscillating elliptic foil case, is adopted to predict the swimming locomotion of a carangiform fish-like body. Convergence for spatial and temporal discretizations was demonstrated. The use of dynamic morphing and overset mesh methods was analyzed for moving bodies/boundaries. A detailed study was performed for examining the influence of time discretization method, overset region size, as well as mesh ratio between overset and background mesh. This analysis helps to guide researchers in proper selection of numerical parameters in OpenFOAM. The employment of overset grid proved to be useful to handle the large flapping and swimming motions of fish-like foils. Reasonable agreement was observed for both hydrodynamic loads and flow features in the pitching and swimming foil cases compared to previous experimental and numerical findings.

#### Rigid foils and morphing strategies

Though the kinematics and dynamics of swimming fish are complex, some key propulsion characteristics of fish tail and fins can be obtained from a simplified model of flapping foils. The propulsive performances of three rigid pitching foils with the same chord length but different fish-like profiles: the tear-shaped semi-circle foil, NACA 0012 foil and NACA 0021 foil, were systematically examined with varying Reynolds (500: 4000) and flapping amplitude-based Strouhal numbers (0.036: 1.07). The trailing edge of NACA 0012 foil is as sharp as the semi-circle foil, but its maximum thickness is much smaller. In contrast, the NACA 0021 foil has the same maximum thickness as the semi-circle foil, but it is thicker in the aft part. As previous experimental research revealed that a quasi-2D mechanism often contains key

dynamical elements of most flapping foil systems, the numerical simulations in this study were carried out in two-dimensional conditions. The results of the semi-circle foil were validated against reference experimental data in terms of hydrodynamic forces and wake characteristics.

Detailed investigations and comparisons of the three different foils were performed with the focus on thrust force, required power and wake features. It was found that for these rigid pitching foils, their instantaneous horizontal forces and input powers had the extreme values nearly at the same phases, respectively, and that both the maximum thrust and the maximum drag force approximately synchronized with the inflection points of input power history. However, the body shape of flapping foil made a big difference on the values of the hydrodynamic loads. The oscillation amplitude of the instantaneous horizontal force was found to be associated with the trailing edge shape and the value increased for sharper geometries. The maximum drag force of the NACA 0021 and semi-circle foils were similar, occurring slightly after the foil passed its mean position, while the value for the slimmer NACA 0012 was smaller. It confirmed the primary role of the maximum thickness in the front part of the foil. The input power histories showed that the results of the semi-circle foil and NACA 0012 foil practically coincided, while the maximum required power of the NACA 0021 foil was smaller. It confirmed the importance of the trailing edge shape for the hydrodynamic torque acting on pitching foils and indicated that a thicker trailing edge could lead to lower input power requirement. Besides, the pressure and friction force decomposition showed that friction-force component depended highly on the forepart of foil profile and the possible vortex shedding occurring there; the main features of the pressure-force component depended on the trailing-edge shape and the resulting shedding vortex.

In addition, the numerical results of the three examined flapping foils demonstrated that the drag-thrust force transition occurred after the transition from the well-known von Kármán (vK) wake to the reversed-vK vortex street, which is not expected from inviscid-flow theory, but agrees with many experiments.

Based on the results of the rigid NACA foils, it was attempted to identify a morphing strategy, involving volume change of the foil, with the aim of combining the advantages of the rigid foils with different profiles, i.e., to maximize the thrust similarly to that of the NACA 0012 foil while minimizing the required input power to a level comparable to that of the NACA 0021 foil. The performances of deformable NACA foils were investigated by a developed OpenFOAM code. The results illustrated that as the phase between morphing and pitching motion changes, the maximum thrust and drag force can occur at different instants within one pitching period, but the extreme values of the input power results still occur at similar phases as the rigid foils. The numerical simulations proved that the proposed morphing strategy could serve to our scope, and the deformable NACA foil morphing with a phase  $\phi = 7\pi/4$  with respect to the pitching motion was identified as the optimal morphing strategy in terms of the parameter  $\phi$ . In fact, it resulted in a foil subjected to a limited torque and robust as NACA 0021 foil while retaining the capability to create large propulsion force. These results, directly relevant for the examined rigid-foil scenario, can pave the way for the use of morphing strategies to target optimized behavior between two generic rigid-foil scenarios.

For a foil flapping at a given Reynolds number, there should be a unique Strouhal number, at which oscillatory motion produces sufficient thrust to exactly cancel the hydrodynamic drag, making constant-speed self-propulsion possible. The relationship between the critical Strouhal number at the drag-thrust transition and the Reynolds number was therefore investigated. The critical Strouhal number was found to be a decreasing function of the Reynolds number and lay mostly in the range of (0.2:0.4) where fish-like swimming and flapping flight often occur, suggesting that the conclusions obtained here should be relevant as interpretation tools in the study of natural systems.

### **Fish-like swimming foils**

The swimming performance of fish-like foils with carangiform swimming mode were numerically studied to understand the hydrodynamic mechanisms of their propulsive performance. The numerical simulations were performed in two different scenarios. One is the fish-like foil, with prescribed undulatory deformations and restrained rigid motions, under an incoming uniform stream, and the other one is the fish self-propelling itself in the fluid.

For the first scenario where the forced fish-like swimming foil was examined, the simulation results were verified by good agreement with reference numerical data in terms of the hydrodynamic force and power. It was shown that as the foil undulatory frequency increased, the horizontal force experienced by the fish body changed linearly from drag to thrust, while the required power input was a concave curve. A force decomposition method was employed to distinguish thrust from drag. The results illustrated that the forced swimming NACA 0012 fish was able to generate thrust force only when its oscillating frequency is large enough ( $St > 0.20$  at  $Re_L = 5000$ ), and this thrust came from the pressure force component. The wake regimes and the pattern transitions were consistent with the phase diagram of vortex regions obtained from the flapping foils. In addition, a series of simulations were performed to investigate the influence of Reynolds number. It was seen that the force transition occurred at smaller Strouhal numbers for higher Reynolds number, and the reason was mainly that the shear stress decreased while the pressure force varied little. The hydrodynamic performance of NACA 0021 fish was compared with that of the NACA 0012 fish to examine the body shape effect, which demonstrated that the blunt fish-like foil experienced larger drag force and had more limited capability to generate thrust than the slim swimming foil with sharper trailing edge.

In the second scenario, the locomotion of the self-propelled swimming fish-like foil was investigated using the developed self-propulsion strategy method. For a fish free to move in the streamline direction, the predicted swimming speed was found to be consistent with the velocity in the drag-thrust force transition case obtained from the forced swimming foils. As expected, the fish undulating its body with higher frequency was able to reach higher swimming speed. The wake patterns at the steady-state swimming were of the reverse-vK regime, which was reasonable as the horizontal force acting on the fish body is time-averagely zero. The body mass of the fish could slow down its acceleration process but has little influence on the final swimming speed. Through the body-shape effect study, it was found that the blunt NACA 0021 fish cannot achieve as high speed as the slim NACA 0012 fish under the same kinematic conditions. The fish with a thicker body generated less thrust force but required the same



mechanical power input for undulations, thus leading to less efficient swimming performance. This finding could help to explain why the hatchery-reared fish which were out of shape in our salmon experiments swam noticeably slower than the wild slim fish.

Given the fact that many real-fish experiments were carried out in respirometer tanks, where the boundaries of the tunnel were often close to the fish body, the hydrodynamic influence of side walls on the fish swimming performance was examined through systematic simulations with varying swim tunnel width and assuming 2D flow conditions. The numerical results predicted that the fish swimming speed decreased rapidly as the tunnel became narrower. The boundary layers along the tunnel walls had stronger interaction with the vortex shedding of the fish, especially when the tunnel width was less than 10 times of the thickness of the examined NACA 0012 fish. Both the drag force and power consumption increased with the decrease of tunnel width. The swimming efficiency calculation indicated that the fish may swim less efficiently in the tanks than in the wild. Therefore, a swim tunnel with enough space is suggested for both biological and hydrodynamic investigations on a swimming fish. For instance, the ratio between the tunnel width and fish body width should be at least larger than 10.

## 7.2 Recommendations for further work

The present studies can be pursued further in many different aspects and several topics that deserve additional attention are presented here:

- In the salmon observation experiments, the fish swimming performance under different current velocity conditions was recorded by multi-cameras. The videos of all the examined fish can be further analyzed to delicately calibrate the kinematic model of Atlantic salmon post-smolts as well as determine the values of oscillation frequency and amplitude at various swimming speeds, which could provide as background and theoretical support for numerical predictions of fish propulsive performance.
- The labriform swimmer uses primarily pectoral fins for cruising, but it should be noted that it transits into the body-caudal fin swimming mode at high speeds and burst swimming. The experimental data obtained after gait-transition can be analyzed to identify its kinematic model, and then compared against that of the BCF swimmers to reveal their similarity and difference. It could help to understand and find out the optimal swimming motion for underwater-vehicle propulsion based on the values of relevant locomotion parameters.
- The investigation experiments on real fishes were carried out in respirometer tanks, which provided limited space for fish movement. The boundary layer along the tunnel walls can make a big difference on the hydrodynamic loads acting on the fish body and therefore the fish swimming performance. It is of great importance to perform real-fish experiments in swim tunnels of different sizes and investigate the influence of boundary walls on fish swimming behaviors. In this context, another important aspect to be ensured is the quality of the inflow in the flume.

- The recoil effects induced by the fluid interaction with the deformable fish can be significant and affect the resulting fish locomotion. The lateral recoil motion of a fish in a tunnel could be more complex due to the wall effect.
- The natural swimming behaviors of the fish are likely to be compromised in the present physical investigations due to the narrow space within the tunnel. It means that the fish oscillation amplitudes reported in experiments can be different from those in an open-water domain. A correction factor is suggested to be identified for reasonable use of experimental data.
- With the requirement of developing and improving bio-inspired underwater vehicles, an optimal multi-joint strategy can be assessed to better represent the flexible swimming behavior, i.e., to assess if a minimum number of rigid body sections and joints exists above which high propulsive and maneuvering performances of the biological fish-like locomotion can be realized and if it can be comparable to that of soft control strategies.
- It is demonstrated that fish can enjoy hydrodynamic advantages during schooling and their swimming can become more efficient. The propulsive performances of fish schooling should be carried out physically and/or numerically to form a map on their swimming behavior at different speeds, and these findings can be compared with individual swimming fish to quantify the improvement of propulsion efficiency and the reduction of consumed energy.
- The effectiveness of visual stimuli as fish calming mechanism and improving swimming performance especially at high speeds should be examined as auxiliary tool to support fish welfare in aquaculture systems designed for offshore environments.
- Numerical studies in this work were carried out at in the range of intermediate Reynolds numbers ( $\sim 10^3$ ) with the assumption of viscous flow and without turbulence-flow model because the previous experiments support a quasi-2D mechanism and the flow is laminar close to the oscillating foil while transition to turbulence is expected to happen in the far field. The next research step can examine the role of turbulent-flow effect and capture the evolution features of vortex shedding in 3D.
- The critical Strouhal number at drag-thrust force transition of a flapping foil is found to be inversely related to the Reynolds number. A universal scaling law, quantifying the influence of foil profile, is recommended to be further identified for a better prediction of the propulsive performance, i.e., regardless of foil geometries.
- A thickness-varying morphing foil strategy is proposed in this study to maximize thrust generation and minimize the required input power. We can also develop other methods for morphing foil design, and one simple way is to change the position of the maximum thickness. Moreover, depending on the application, the 3D effect should also be considered in the real case. Offshore wind turbines represent a possible scenario of a morphing foil strategy as bio-inspired solution for improving green-energy production. For instance, it could be targeted to lower cut-in and rated velocity of wind turbines in Mediterranean Sea

and increase the cut-out speed for wind turbines in North Sea. Therefore, morphing foil strategies can be useful and give some insight into novel wind turbine blade's shape design to reach these targets.

- CFD simulations in 3D are computationally more expensive and require special attention to ensure accurate prediction, however, they are important to highlight similarities and differences with respect to simplified 2D fish-like foil scenarios. Moreover, reliable 3D predictions represent a crucial option when experiments are not directly available or feasible. The simulations on 3D fish swimming motion can help to study local flow behavior around the moving body and the complex turbulence-flow features under different conditions; in addition, it can shed light on the proper design of bio-inspired underwater robotics. In this context, reliability of the simulations represents the major challenge.
- Fluid-structure interaction studies, where the structure is the fish body, can help more detailed understanding of fish propulsive motion. In this regard, OpenFOAM seems to be a very attractive numerical tool and the fluid solvers can be coupled with many solid body models within the extended OpenFOAM platform or some commercial structural software.
- The studies demonstrated the influence of water environment on the fish swimming behaviors; on the other hand, the fish swimming motions can also change the surrounding fluid. A practical example is given by closed fish farms where fish can reduce the internal current velocity and impose pressures on the boundaries of the cage. Performing fluid-structure interaction analysis is therefore of significance for the aquaculture industry.

# References

- Abrahams, M. V., & Colgan, P. W. (1987). Fish schools and their hydrodynamic function: a reanalysis. *Environmental Biology of Fishes*, 20(1), 79-80.
- Alam, M. M., & Muhammad, Z. (2020). Dynamics of flow around a pitching hydrofoil. *Journal of Fluids and Structures*, 99, 103151.
- Alben, S., Witt, C., Baker, T. V., Anderson, E., & Lauder, G. V. (2012). Dynamics of freely swimming flexible foils. *Physics of Fluids*, 24(5), 051901.
- Algarín-Pinto, J. A., Garza-Castañón, L. E., Vargas-Martínez, A., & Minchala-Ávila, L. I. (2021). Dynamic modeling and control of a parallel mechanism used in the propulsion system of a biomimetic underwater vehicle. *Applied Sciences*, 11(11), 4909.
- Altman, D. G., & Bland, J. M. (2005). Standard deviations and standard errors. *Bmj*, 331(7521), 903.
- Andersen, A., Bohr, T., Schnipper, T., & Walther, J. H. (2017). Wake structure and thrust generation of a flapping foil in two-dimensional flow. *Journal of Fluid Mechanics*, 812.
- Anderson, E. J., Mcgillis, W. R., & Grosenbaugh, M. A. (2001). The boundary layer of swimming fish. *Journal of Experimental Biology*, 204(1), 81-102.
- Anderson, J. M., & Chhabra, N. K. (2002). Maneuvering and stability performance of a robotic tuna. *Integrative and comparative biology*, 42(1), 118-126.
- Anderson, J. M., Streitlien, K., Barrett, D. S., & Triantafyllou, M. S. (1998). Oscillating foils of high propulsive efficiency. *Journal of Fluid mechanics*, 360, 41-72.
- Ansys, ICEM. (2005). version 10.0.1, user manual.
- Bainbridge, R. (1958). The speed of swimming of fish as related to size and to the frequency and amplitude of the tail beat. *Journal of experimental biology*, 35(1), 109-133.
- Bale, R., Hao, M., Bhalla, A. P. S., & Patankar, N. A. (2014). Energy efficiency and allometry of movement of swimming and flying animals. *Proceedings of the National Academy of Sciences*, 111(21), 7517-7521.
- Bandyopadhyay, P. R. (2005). Trends in biorobotic autonomous undersea vehicles. *IEEE Journal of Oceanic Engineering*, 30(1), 109-139.
- Barrett, D. S., Triantafyllou, M. S., Yue, D. K. P., Grosenbaugh, M. A., & Wolfgang, M. (1999). Drag reduction in fish-like locomotion. *Journal of Fluid Mechanics*, 392, 183-212.
- Bayat, B., Crespi, A., & Ijspeert, A. (2016, November). Envirobot: A bio-inspired environmental monitoring platform. In *2016 IEEE/OES Autonomous Underwater Vehicles (AUV)* (pp. 381-386). Ieee.
- Bayraktar, E., Mierka, O., & Turek, S. (2012). Benchmark computations of 3D laminar flow around a cylinder with CFX, OpenFOAM and FeatFlow. *International Journal of Computational Science and Engineering*, 7(3), 253-266.
- Beamish, FW (1978). Swimming capacity. *Fish physiology* , 7 , 101-187.
- Bell, WH, & Terhune, LDB (1970). Water tunnel design for fisheries research . Fisheries Research Board of Canada, Biological Station.
- Birnbaum, W. (1924). Der Schlagflügelpropeller und die kleinen Schwingungen elastisch befestigter Tragflügel. *Zeitschrift für Flugtechnik und Motorluftschiffahrt*, 15(11), 128-134.
- Bjelland, H. V., Føre, M., Lader, P., Kristiansen, D., Holmen, I. M., Fredheim, A., ... & Schjøberg, I. (2015, October). Exposed aquaculture in Norway. In *OCEANS 2015-MTS/IEEE Washington*

- (pp. 1-10). IEEE.
- Bone, Q., & Moore, R. (2008). *Biology of fishes*. Taylor & Francis.
- Booth, R. K., McKinley, R. S., Økland, F., & Sisak, M. M. (1997). In situ measurement of swimming performance of wild Atlantic salmon (*Salmo salar*) using radio transmitted electromyogram signals. *Aquatic Living Resources*, 10(4), 213-219.
- Borazjani, I., & Sotiropoulos, F. (2008). Numerical investigation of the hydrodynamics of carangiform swimming in the transitional and inertial flow regimes. *Journal of experimental biology*, 211(10), 1541-1558.
- Borazjani, I., & Sotiropoulos, F. (2010). On the role of form and kinematics on the hydrodynamics of self-propelled body/caudal fin swimming. *Journal of Experimental Biology*, 213(1), 89-107.
- Bowker, J. A., Townsend, N. C., Tan, M., & Sheno, R. A. (2016, September). Experimental analysis of submerged flapping foils; implications for autonomous surface vehicles (ASVs). In *OCEANS 2016 MTS/IEEE Monterey* (pp. 1-10). IEEE.
- Bratt, J. B. (1950). Flow patterns in the wake of an oscillating aerofoil. *Aeronautical Research Council, R&M*, p. 2773.
- Breder Jr, C. M. (1926). The locomotion of fishes. *Zoologica*, 4, 159-291.
- Breder Jr, C. M. (1967). On the survival value of fish schools. *Zoologica*, 52(2), 25-40.
- Brett, J. R. (1964). The respiratory metabolism and swimming performance of young sockeye salmon. *Journal of the Fisheries Board of Canada*, 21(5), 1183-1226.
- Brown, A. M. (2005). A new software for carrying out one-way ANOVA post hoc tests. *Computer methods and programs in biomedicine*, 79(1), 89-95.
- Böckmann, E., & Steen, S. (2016). Model test and simulation of a ship with wavefoils. *Applied Ocean Research*, 57, 8-18.
- Chabot, D., Steffensen, J. F., & Farrell, A. P. (2016). The determination of standard metabolic rate in fishes. *Journal of Fish Biology*, 88(1), 81-121.
- Chao, L. M., Pan, G., Zhang, D., & Yan, G. X. (2019). On the drag–thrust transition of a pitching foil. *Ocean Engineering*, 192, 106564.
- Chen, H., Qian, L., Ma, Z., Bai, W., Li, Y., Causon, D., & Mingham, C. (2019). Application of an overset mesh based numerical wave tank for modelling realistic free-surface hydrodynamic problems. *Ocean Engineering*, 176, 97-117.
- Chen, Y., Zhan, J., Wu, J., & Wu, J. (2017). A fully-activated flapping foil in wind gust: Energy harvesting performance investigation. *Ocean Engineering*, 138, 112-122.
- Chen, Z., Um, T. I., & Bart-Smith, H. (2012). Bio-inspired robotic manta ray powered by ionic polymer–metal composite artificial muscles. *International Journal of Smart and Nano Materials*, 3(4), 296-308.
- Cheng, J. Y., & Blickhan, R. (1994). Note on the calculation of propeller efficiency using elongated body theory. *The Journal of experimental biology*, 192(1), 169-177.
- Childress, S. (1981). *Mechanics of swimming and flying* (No. 2). Cambridge University Press.
- Clapham, R. J., & Hu, H. (2015). iSplash: Realizing fast carangiform swimming to outperform a real fish. In *Robot Fish* (pp. 193-218). Springer, Berlin, Heidelberg.
- Cognetti, L. (2019). Low Reynolds number flow characterization around an heaving airfoil by the use of the novel Generalized Harmonic Polynomial Cell method. Master degree thesis in Aeronautical Engineer: Univ. of Rome “La Sapienza”.
- Colicchio, G., Landrini, M., & Chaplin, J. R. (2005). Level-set computations of free surface rotational

- flows. *Journal of Fluids Engineering*;127(6):1111–1121.
- Crespi, A., & Ijspeert, A. J. (2009). Salamandra robotica: a biologically inspired amphibious robot that swims and walks. In *Artificial life models in hardware* (pp. 35-64). Springer, London.
- Cui, W., Hu, Y., & Guo, W. (2017). Chinese journey to the challenger deep: The development and first phase of sea trial of an 11,000-m Rainbowfish ARV. *Marine Technology Society Journal*, 51(3), 23-35.
- Cui, Z., Yang, Z., Shen, L., & Jiang, H. Z. (2018). Complex modal analysis of the movements of swimming fish propelled by body and/or caudal fin. *Wave motion*, 78, 83-97.
- De Greef, A., Lambert, P., & Delchambre, A. (2009). Towards flexible medical instruments: Review of flexible fluidic actuators. *Precision engineering*, 33(4), 311-321.
- Deng, J., & Caulfield, C. P. (2015). Three-dimensional transition after wake deflection behind a flapping foil. *Physical Review E*, 91(4), 043017.
- Deslauriers, D., & Kieffer, J. D. (2011). The influence of flume length and group size on swimming performance in shortnose sturgeon *Acipenser brevirostrum*. *Journal of Fish Biology*, 79(5), 1146-1155.
- Dewey, P. A., Boschitsch, B. M., Moored, K. W., Stone, H. A., & Smits, A. J. (2013). Scaling laws for the thrust production of flexible pitching panels. *Journal of Fluid Mechanics*, 732, 29-46.
- Dewey, P. A., Carriou, A., & Smits, A. J. (2012). On the relationship between efficiency and wake structure of a batoid-inspired oscillating fin. *Journal of fluid mechanics*, 691, 245-266.
- Donea, J., Huerta, A., Ponthot, J. P., & Rodríguez-Ferran, A. (2004). Arbitrary Lagrangian-Eulerian Methods. *Encyclopedia of computational mechanics*.
- Dong, G. J., & Lu, X. Y. (2005). Numerical analysis on the propulsive performance and vortex shedding of fish - like travelling wavy plate. *International Journal for Numerical Methods in Fluids*, 48(12), 1351-1373.
- Dong, G. J., & Lu, X. Y. (2007). Characteristics of flow over traveling wavy foils in a side-by-side arrangement. *Physics of fluids*, 19(5), 057107.
- Donley, J. M., Sepulveda, C. A., Konstantinidis, P., Gemballa, S., & Shadwick, R. E. (2004). Convergent evolution in mechanical design of lamnid sharks and tunas. *Nature*, 429(6987), 61-65.
- Drucker, E., & Jensen, J. (1996). Pectoral fin locomotion in the striped surperch. II. Scaling swimming kinematics and performance at a gait transition. *The Journal of experimental biology*, 199(10), 2243-2252.
- Eloy, C. (2012). Optimal Strouhal number for swimming animals. *Journal of Fluids and Structures*, 30, 205-218.
- Engbretsen, M. A., Gjerden, K. S., Utbjoe, Ø. B., & Våge, A. (2019). Autonomous Navigation, Mapping, and Exploration for Underwater Robots (Master's thesis, NTNU).
- Esposito, C. J., Tangorra, J. L., Flammang, B. E., & Lauder, G. V. (2012). A robotic fish caudal fin: effects of stiffness and motor program on locomotor performance. *Journal of Experimental Biology*, 215(1), 56-67.
- Fan, D., Yang, L., Wang, Z., Triantafyllou, M. S., & Karniadakis, G. E. (2020). Reinforcement learning for bluff body active flow control in experiments and simulations. *Proceedings of the National Academy of Sciences*, 117(42), 26091-26098.
- Fattah, S. A., Abedin, F., Ansary, M. N., Rokib, M. A., Saha, N., & Shahnaz, C. (2016, November). R3Diver: Remote robotic rescue diver for rapid underwater search and rescue operation. In 2016 IEEE Region 10 Conference (TENCON) (pp. 3280-3283). IEEE.

- Feng, H., Wang, Z., Todd, P. A., & Lee, H. P. (2019). Simulations of self-propelled anguilliform swimming using the immersed boundary method in OpenFOAM. *Engineering Applications of Computational Fluid Mechanics*, 13(1), 438-452.
- Fish, F. E. (1993). Power output and propulsive efficiency of swimming bottlenose dolphins (*Tursiops truncatus*). *Journal of Experimental Biology*, 185(1), 179-193.
- Fish, F. E. (2020). Advantages of aquatic animals as models for bio-inspired drones over present AUV technology. *Bioinspiration & biomimetics*, 15(2), 025001.
- Fish, F. E., & Lauder, G. V. (2006). Passive and active flow control by swimming fishes and mammals. *Annu. Rev. Fluid Mech.*, 38, 193-224.
- Fish, F. E., Legac, P., Williams, T. M., & Wei, T. (2014). Measurement of hydrodynamic force generation by swimming dolphins using bubble DPIV. *Journal of Experimental Biology*, 217(2), 252-260.
- Floryan, D., Van Buren, T., Rowley, C. W., & Smits, A. J. (2017). Scaling the propulsive performance of heaving and pitching foils. *Journal of Fluid Mechanics*, 822, 386-397.
- Føre, M., Svendsen, E., Økland, F., Gräns, A., Alfredsen, J. A., Finstad, B., ... & Uglem, I. (2021). Heart rate and swimming activity as indicators of post-surgical recovery time of Atlantic salmon (*Salmo salar*). *Animal Biotelemetry*, 9(1), 1-13.
- Gagnon, L. (2019). OpenFOAM-moving-wall-slip. Github.
- Garrick, I. E. (1936). Propulsion of a flapping and oscillating airfoil. NACA report 567, 419-427.
- Godoy-Diana, R., Aider, J. L., & Wesfreid, J. E. (2008). Transitions in the wake of a flapping foil. *Physical Review E*, 77(1), 016308.
- Gray, J. (1936). Studies in animal locomotion. *Journal of Experimental Biology*, 13(2), 192-199.
- Hayashida, K., Nii, H., Tsuji, T., Miyoshi, K., Hamamoto, S., & Ueda, H. (2013). Effects of anesthesia and surgery on U crit performance and MO2 in chum salmon, *Oncorhynchus keta*. *Fish physiology and biochemistry*, 39(4), 907-915.
- Herskin, J., & Steffensen, J. F. (1998). Energy savings in sea bass swimming in a school: measurements of tail beat frequency and oxygen consumption at different swimming speeds. *Journal of Fish Biology*, 53(2), 366-376.
- Horlock, J. H. (1978). Actuator disk theory-Discontinuities in thermo-fluid dynamics. New York.
- Horreo, J. L., Machado-Schiaffino, G., Griffiths, A. M., Bright, D., Stevens, J. R., & Garcia-Vazquez, E. (2011). Atlantic salmon at risk: apparent rapid declines in effective population size in southern European populations. *Transactions of the American Fisheries Society*, 140(3), 605-610.
- Hu, H., Liu, J., Dukes, I., & Francis, G. (2006, October). Design of 3D swim patterns for autonomous robotic fish. In 2006 IEEE/RSJ International Conference on Intelligent Robots and Systems (pp. 2406-2411). IEEE.
- Hunter, J. R. (1971). Swimming speed, tail beat frequency, tail beat amplitude and size in jack mackerel, *Trachurus symmetricus*, and other fishes. *Fish. Bull.*, 69, 253-266.
- Hvas, M., Folkedal, O., Imsland, A., & Oppedal, F. (2017). The effect of thermal acclimation on aerobic scope and critical swimming speed in Atlantic salmon, *Salmo salar*. *Journal of Experimental Biology*, 220(15), 2757-2764.
- Hvas, M., Folkedal, O., & Oppedal, F. (2019). Sea-based farming - how much water flow can salmon and cleaner fish tolerate? - fish welfare and limit values. Report from marine research.
- Hvas, M., & Oppedal, F. (2019). Influence of experimental set-up and methodology for measurements of metabolic rates and critical swimming speed in Atlantic salmon *Salmo salar*. *Journal of Fish Biology*, 95(3), 893-902.

- Jasak, H. (2009a, January). Dynamic mesh handling in OpenFOAM. In 47th AIAA aerospace sciences meeting including the new horizons forum and aerospace exposition (p. 341).
- Jasak, H. (2009b). OpenFOAM: open source CFD in research and industry. *International Journal of Naval Architecture and Ocean Engineering*, 1(2), 89-94.
- Jasak, H., & Tukovic, Z. (2006). Automatic mesh motion for the unstructured finite volume method. *Transactions of FAMENA*, 30(2), 1-20.
- Johansen, J. L., Vaknin, R., Steffensen, J. F., & Domenici, P. (2010). Kinematics and energetic benefits of schooling in the labriform fish, striped surfperch *Embiotoca lateralis*. *Marine Ecology Progress Series*, 420, 221-229.
- Kane, T. R. (1988). Communications: Length-Weight Relationship of Hatchery-Reared Atlantic Salmon. *The Progressive Fish-Culturist*, 50(1), 28-30.
- Katz, Y., Tunström, K., Ioannou, C. C., Huepe, C., & Couzin, I. D. (2011). Inferring the structure and dynamics of interactions in schooling fish. *Proceedings of the National Academy of Sciences*, 108(46), 18720-18725.
- Katz, J., & Weihs, D. (1978). Hydrodynamic propulsion by large amplitude oscillation of an airfoil with chordwise flexibility. *Journal of Fluid Mechanics*, 88(3), 485-497.
- Katzmayr, R. (1922). Effect of periodic changes of angle of attack on behavior of airfoils (No. NACA-TM-147).
- Klyashtorin, LV, & Salikzyanov, RF (1981). A change in metabolic rate over time and the influence of the group effect. *Journal of Ichthyology*, 20, 132-137.
- Koochesfahani, M. M. (1989). Vortical patterns in the wake of an oscillating airfoil. *AIAA journal*, 27(9), 1200-1205.
- Korotkin, A. I. (2008). *Added masses of ship structures* (Vol. 88). Springer Science & Business Media.
- Kovač, M. (2014). The bioinspiration design paradigm: A perspective for soft robotics. *Soft Robotics*, 1(1), 28-37.
- Kurtulus, D. F. (2015). On the unsteady behavior of the flow around NACA 0012 airfoil with steady external conditions at  $Re = 1000$ . *International journal of micro air vehicles*, 7(3), 301-326.
- Lagopoulos, N. S., Weymouth, G. D., & Ganapathisubramani, B. (2019). Universal scaling law for drag-to-thrust wake transition in flapping foils. *Journal of Fluid Mechanics*, 872.
- Lefrançois, C., Ferrari, R. S., Moreira Da Silva, J., & Domenici, P. (2009). The effect of progressive hypoxia on spontaneous activity in single and shoaling golden grey mullet *Liza aurata*. *Journal of Fish Biology*, 75(7), 1615-1625.
- Li, D., Zhao, S., Da Ronch, A., Xiang, J., Drofelnik, J., Li, Y., ... & De Breuker, R. (2018). A review of modelling and analysis of morphing wings. *Progress in Aerospace Sciences*, 100, 46-62.
- Li, G., Chen, X., Zhou, F., Liang, Y., Xiao, Y., Cao, X., ... & Yang, W. (2021). Self-powered soft robot in the Mariana Trench. *Nature*, 591(7848), 66-71.
- Li, Y., Xu, Y., Wu, Z., Ma, L., Guo, M., Li, Z., & Li, Y. (2022). A comprehensive review on fish-inspired robots. *International Journal of Advanced Robotic Systems*, 19(3), 17298806221103707.
- Liao, J. C., Beal, D. N., Lauder, G. V., & Triantafyllou, M. S. (2003). Fish exploiting vortices decrease muscle activity. *Science*, 302(5650), 1566-1569.
- Lighthill, M. J. (1960). Note on the swimming of slender fish. *Journal of fluid Mechanics*, 9(2), 305-317.
- Lighthill, M. J. (1969). Hydromechanics of aquatic animal propulsion. *Annual review of fluid mechanics*, 1(1), 413-446.
- Lighthill, M. J. (1971). Large-amplitude elongated-body theory of fish locomotion. *Proceedings of the*



- Royal Society of London. Series B. Biological Sciences, 179(1055), 125-138.
- Lighthill, M. J. (1975). *Mathematical biofluidynamics*. Society for Industrial and Applied Mathematics, Philadelphia.
- Liljebäck, P., & Mills, R. (2017, June). Eelume: A flexible and subsea resident IMR vehicle. In *Oceans 2017-Aberdeen* (pp. 1-4). IEEE.
- Limacher, E. J. (2019). *Added mass and vortical impulse: theory and experiment*. PhD thesis, University of Calgary (CA).
- Lindsey, C. C. (1978). Form, function and locomotory habits in fish. *Fish Physiology*, vol 2: Locomotion.
- Liu, H. (2005). Simulation-based biological fluid dynamics in animal locomotion. *Applied Mechanics Reviews*, 58(4), 269–282.
- Liu, H., & Kawachi, K. (1999). A numerical study of undulatory swimming. *Journal of Computational Physics*, 155(2), 223-247.
- Liu, H., Wassersug, R., & Kawachi, K. (1996). A computational fluid dynamics study of tadpole swimming. *The Journal of Experimental Biology*, 199(6), 1245-1260.
- Liu, H., Wassersug, R., & Kawachi, K. (1997). The three-dimensional hydrodynamics of tadpole locomotion. *The Journal of experimental biology*, 200(22), 2807-2819.
- Liu, J., & Hu, H. (2004). A 3D simulator for autonomous robotic fish. *International Journal of automation and computing*, 1(1), 42-50.
- Liu, W., Xiao, Q., & Cheng, F. (2013). A bio-inspired study on tidal energy extraction with flexible flapping wings. *Bioinspiration & biomimetics*, 8(3), 036011.
- Low, K. H., Zhou, C., Seet, G., Bi, S., & Cai, Y. (2011, December). Improvement and testing of a robotic manta ray (RoMan-III). In *2011 IEEE International Conference on Robotics and Biomimetics* (pp. 1730-1735). IEEE.
- Mackowski, A. W., & Williamson, C. H. K. (2015). Direct measurement of thrust and efficiency of an airfoil undergoing pure pitching. *Journal of Fluid Mechanics*, 765, 524-543.
- Maertens, A. P., Gao, A., & Triantafyllou, M. S. (2017). Optimal undulatory swimming for a single fish-like body and for a pair of interacting swimmers. *Journal of Fluid Mechanics*, 813, 301-345.
- Marais, C., Thiria, B., Wesfreid, J. E., & Godoy-Diana, R. (2012). Stabilizing effect of flexibility in the wake of a flapping foil. *Journal of Fluid Mechanics*, 710, 659-669.
- Marras, S., Killen, S. S., Lindström, J., McKenzie, D. J., Steffensen, J. F., & Domenici, P. (2015). Fish swimming in schools save energy regardless of their spatial position. *Behavioral ecology and sociobiology*, 69(2), 219-226.
- McClure, J., & Yarusevych, S. (2019). Planar momentum balance in three-dimensional flows: applications to load estimation. *Experiments in Fluids*, 60(3), 1-15.
- McHenry, M. J., Azizi, E., & Strother, J. A. (2003). The hydrodynamics of locomotion at intermediate Reynolds numbers: undulatory swimming in ascidian larvae (*Botrylloides* sp.). *Journal of Experimental Biology*, 206(2), 327-343.
- Methling, C., Tudorache, C., Skov, P. V., & Steffensen, J. F. (2011). Pop up satellite tags impair swimming performance and energetics of the European eel (*Anguilla anguilla*). *PLoS one*, 6(6), e20797.
- Miao, J. M., & Ho, M. H. (2006). Effect of flexure on aerodynamic propulsive efficiency of flapping flexible airfoil. *Journal of Fluids and Structures*, 22(3), 401-419.
- Miklosovic, D. S., Murray, M. M., Howle, L. E., & Fish, F. E. (2004). Leading-edge tubercles delay stall on humpback whale (*Megaptera novaeangliae*) flippers. *Physics of fluids*, 16(5), L39-L42.
- Miller, S. T., Campbell, R. L., Elsworth, C. W., Pitt, J. S., & Boger, D. A. (2014). An overset grid method

- for fluid-structure interaction. *World Journal of Mechanics*, 2014.
- Montgomery, J., Coombs, S., & Halstead, M. (1995). Biology of the mechanosensory lateral line in fishes. *Reviews in Fish Biology and Fisheries*, 5(4), 399-416.
- Moored, K. W., Dewey, P. A., Smits, A. J., & Haj-Hariri, H. (2012). Hydrodynamic wake resonance as an underlying principle of efficient unsteady propulsion. *Journal of Fluid Mechanics*, 708, 329-348.
- Moriche, M., Flores, O., & García-Villalba, M. (2016). Three-dimensional instabilities in the wake of a flapping wing at low Reynolds number. *International Journal of Heat and Fluid Flow*, 62, 44-55.
- Mu, X., Cao, P., Gong, L., Baiyin, B., & Li, X. (2019). A classification method for fish swimming behaviors under incremental water velocity for fishway hydraulic design. *Water*, 11(10), 2131.
- Muller, U. K., van den Boogaart, J. G., & van Leeuwen, J. L. (2008). Flow patterns of larval fish: undulatory swimming in the intermediate flow regime. *Journal of Experimental Biology*, 211(2), 196-205.
- Mussi, M., Summers, A. P., & Domenici, P. (2002). Gait transition speed, pectoral fin-beat frequency and amplitude in *Cymatogaster aggregata*, *Embiotoca lateralis* and *Damalichthys vacca*. *Journal of Fish Biology*, 61(5), 1282-1293.
- Nadler, L. E., Killen, S. S., McClure, E. C., Munday, P. L., & McCormick, M. I. (2016). Shoaling reduces metabolic rate in a gregarious coral reef fish species. *Journal of Experimental Biology*, 219(18), 2802-2805.
- Nauen, J. C., & Lauder, G. V. (2001). Locomotion in scombrid fishes: visualization of flow around the caudal peduncle and finlets of the chub mackerel *Scomber japonicus*. *Journal of Experimental Biology*, 204(13), 2251-2263.
- Neogi, I., Shah, V. N., Singh, P. D., & Joshi, V. (2022). Propulsive performance of morphing and heaving foil. arXiv preprint arXiv:2201.03352.
- Norin, T., & Clark, T. D. (2016). Measurement and relevance of maximum metabolic rate in fishes. *Journal of Fish Biology*, 88(1), 122-151.
- Paniccia, D. (2018). Vortex shedding around a deformable wing profile in unsteady condition. Master degree thesis in Aeronautical Engineer: Univ. of Rome "La Sapienza".
- Paniccia, D., Graziani, G., Lugni, C., & Piva, R. (2021a). On the role of added mass and vorticity release for self-propelled aquatic locomotion. *Journal of Fluid Mechanics*, 918.
- Paniccia, D., Graziani, G., Lugni, C., & Piva, R. (2021b). The relevance of recoil and free swimming in aquatic locomotion. *Journal of Fluids and Structures*, 103, 103290.
- Parker Jr, F. R. (1973). Reduced metabolic rates in fishes as a result of induced schooling. *Transactions of the American Fisheries Society*, 102(1), 125-131.
- Parrish, J. K., & Edelman-Keshet, L. (1999). Complexity, pattern, and evolutionary trade-offs in animal aggregation. *Science*, 284(5411), 99-101.
- Partridge, B. L., & Pitcher, T. J. (1979). Evidence against a hydrodynamic function for fish schools. *Nature*, 279(5712), 418-419.
- Pavlov, D. S., & Kasumyan, A. O. (2000). Patterns and mechanisms of schooling behavior in fish: a review. *Journal of Ichthyology*, 40(2), S163.
- Quinn, D. B., Lauder, G. V., & Smits, A. J. (2014). Scaling the propulsive performance of heaving flexible panels. *Journal of fluid mechanics*, 738, 250-267.
- Raffel, M., Willert, C. E., Scarano, F., Kähler, C. J., Wereley, S. T., & Kompenhans, J. (2018). Techniques

- for 3D-PIV. In *Particle Image Velocimetry* (pp. 309-365). Springer, Cham.
- Read, D. A., Hover, F. S., & Triantafyllou, M. S. (2003). Forces on oscillating foils for propulsion and maneuvering. *Journal of Fluids and Structures*, 17(1), 163-183.
- Reid, J. T., & Hunsaker, D. F. (2017). Implementation of OpenFOAM for Inviscid Incompressible Aerodynamic Flows.
- Remen, M., Solstorm, F., Bui, S., Klebert, P., Vågseth, T., Solstorm, D., ... & Oppedal, F. (2016). Critical swimming speed in groups of Atlantic salmon *Salmo salar*. *Aquaculture Environment Interactions*, 8, 659-664.
- Richards, A. J., & Oshkai, P. (2015). Effect of the stiffness, inertia and oscillation kinematics on the thrust generation and efficiency of an oscillating-foil propulsion system. *Journal of Fluids and Structures*, 57, 357-374.
- Riggs, P., Bowyer, A., & Vincent, J. (2010). Advantages of a biomimetic stiffness profile in pitching flexible fin propulsion. *Journal of Bionic Engineering*, 7(2), 113-119.
- Ross, R. M., Backman, T. W., & Limburg, K. E. (1992). Group-size-mediated metabolic rate reduction in American shad. *Transactions of the American Fisheries Society*, 121(3), 385-390.
- Salehi, S., Nilsson, H., Lillberg, E., & Edh, N. (2021, June). Development of a novel numerical framework in OpenFOAM to simulate Kaplan turbine transients. In *IOP Conference Series: Earth and Environmental Science* (Vol. 774, No. 1, p. 012058). IOP Publishing.
- Schlichting, H., & Gersten, K. (2015). *Boundary layer theory* (p. 573). New York: McGraw-Hill.
- Schnipper, T., Andersen, A., & Bohr, T. (2009). Vortex wakes of a flapping foil. *Journal of Fluid Mechanics*, 633, 411-423.
- Schouveiler, L., Hover, F. S., & Triantafyllou, M. S. (2005). Performance of flapping foil propulsion. *Journal of fluids and structures*, 20(7), 949-959.
- Schultz, W. W., & Webb, P. W. (2002). Power requirements of swimming: do new methods resolve old questions?. *Integrative and Comparative Biology*, 42(5), 1018-1025.
- Schurmann, H., & Steffensen, J. F. (1997). Effects of temperature, hypoxia and activity on the metabolism of juvenile Atlantic cod. *Journal of fish biology*, 50(6), 1166-1180.
- Sefati, S., Neveln, I. D., Roth, E., Mitchell, T. R., Snyder, J. B., MacIver, M. A., ... & Cowan, N. J. (2013). Mutually opposing forces during locomotion can eliminate the tradeoff between maneuverability and stability. *Proceedings of the National Academy of Sciences*, 110(47), 18798-18803.
- Sfakiotakis, M., Lane, D. M., & Davies, J. B. C. (1999). Review of fish swimming modes for aquatic locomotion. *IEEE Journal of oceanic engineering*, 24(2), 237-252.
- Shaw, E. (1978). Schooling fishes: the school, a truly egalitarian form of organization in which all members of the group are alike in influence, offers substantial benefits to its participants. *American Scientist*, 66(2), 166-175.
- Shen, H., Xiao, Q., Zhou, J., Su, Y., & Bi, X. (2022). Design of hydrofoil for the resistance improvement of planing boat based on CFD technology. *Ocean Engineering*, 255, 111413.
- Shen, L., Zhang, X., Yue, D. K., & Triantafyllou, M. S. (2003). Turbulent flow over a flexible wall undergoing a streamwise travelling wave motion. *Journal of Fluid Mechanics*, 484, 197-221.
- Shin, S., Bae, S. Y., Kim, I. C., & Kim, Y. J. (2009). Effects of flexibility on propulsive force acting on a heaving foil. *Ocean Engineering*, 36(3-4), 285-294.
- Siddiqui, M. A., Xu, H. L., Greco, M., & Colicchio, G. (2020, August). Analysis of Open-Source CFD Tools for Simulating Complex Hydrodynamic Problems. In *International Conference on*

- Offshore Mechanics and Arctic Engineering (Vol. 84409, p. V008T08A036). American Society of Mechanical Engineers.
- Sil'va, A., & Saburenkov, Y. N. (1979). " Verkhovka", *Leucaspius delineatus*. *Journal of Ichthyology*, 18(1-3), 513.
- Stefanini, C., Orofino, S., Manfredi, L., Mintchev, S., Marrazza, S., Assaf, T., ... & Dario, P. (2012, May). A compliant bioinspired swimming robot with neuro-inspired control and autonomous behavior. In *2012 IEEE International Conference on Robotics and Automation* (pp. 5094-5098). IEEE.
- Sun, B., Li, W., Wang, Z., Zhu, Y., He, Q., Guan, X., ... & Fan, D. (2022). Recent Progress in Modeling and Control of Bio-Inspired Fish Robots. *Journal of Marine Science and Engineering*, 10(6), 773.
- Sun, H., & Faltinsen, O. M. (2011). Predictions of porpoising inception for planing vessels. *Journal of marine science and technology*, 16(3), 270-282.
- Sutton, S. G., Bult, T. P., & Haedrich, R. L. (2000). Relationships among fat weight, body weight, water weight, and condition factors in wild Atlantic salmon parr. *Transactions of the American Fisheries Society*, 129(2), 527-538.
- Svendsen, E., Føre, M., Randeberg, L. L., & Alfredsen, J. A. (2021). Design of a novel biosensor implant for farmed Atlantic salmon (*Salmo salar*). In *2021 IEEE Sensors* (pp. 1-4). IEEE.
- Søvik, E. (2022). Systematic analysis of experiments on sub-carangiform fish hydrodynamics. Master thesis: Norwegian University of Science and Technology.
- Taylor, G. K., Nudds, R. L., & Thomas, A. L. (2003). Flying and swimming animals cruise at a Strouhal number tuned for high power efficiency. *Nature*, 425(6959), 707-711.
- Techet, A. H., Hover, F. S., & Triantafyllou, M. S. (2003). Separation and turbulence control in biomimetic flows. *Flow, Turbulence and Combustion*, 71(1), 105-118.
- Teng, N. H. (1987). The Development of a Computer Code (U2DIIF) for the Numerical Solution of Unsteady, Inviscid and Incompressible Flow Over an Airfoil. *NAVAL POSTGRADUATE SCHOOL MONTEREY CA*.
- Triantafyllou, G. S., Triantafyllou, M. S., & Grosenbaugh, M. A. (1993). Optimal thrust development in oscillating foils with application to fish propulsion. *Journal of Fluids and Structures*, 7(2), 205-224.
- Triantafyllou, M. S., Techet, A. H., & Hover, F. S. (2004). Review of experimental work in biomimetic foils. *IEEE Journal of Oceanic Engineering*, 29(3), 585-594.
- Triantafyllou, M. S., Techet, A. H., Zhu, Q., Beal, D. N., Hover, F. S., & Yue, D. K. P. (2002). Vorticity control in fish-like propulsion and maneuvering. *Integrative and comparative biology*, 42(5), 1026-1031.
- Triantafyllou, M. S., & Triantafyllou, G. S. (1995). An efficient swimming machine. *Scientific american*, 272(3), 64-70.
- Triantafyllou, M. S., Triantafyllou, G. S., & Yue, D. K. P. (2000). Hydrodynamics of fishlike swimming. *Annual review of fluid mechanics*, 32(1), 33-53.
- Triantafyllou, M. S., Weymouth, G. D., & Miao, J. (2016). Biomimetic survival hydrodynamics and flow sensing. *Annual Review of Fluid Mechanics*, 48(1).
- Triantafyllou, M. S., Winey, N., Trakht, Y., Elhassid, R., & Yoerger, D. (2020). Biomimetic design of dorsal fins for AUVs to enhance maneuverability. *Bioinspiration & biomimetics*, 15(3), 035003.
- Tucker, V. A. (1970). Energetic cost of locomotion in animals. *Comparative Biochemistry and Physiology*, 34, 841-846.

- Tudorache, C., O'Keefe, R. A., & Benfey, T. J. (2010). Flume length and post - exercise impingement affect anaerobic metabolism in brook charr *Salvelinus fontinalis*. *Journal of Fish Biology*, 76(3), 729-733.
- Tytell, E. D. (2010). Do trout swim better than eels? Challenges for estimating performance based on the wake of self-propelled bodies. In *Animal Locomotion* (pp. 63-74). Springer, Berlin, Heidelberg.
- Tytell, E. D., & Lauder, G. V. (2004). The hydrodynamics of eel swimming: I. Wake structure. *Journal of Experimental Biology*, 207(11), 1825-1841.
- Tytler, P. (1969). Relationship between oxygen consumption and swimming speed in the haddock, *Melanogrammus aeglefinus*. *Nature*, 221(5177), 274-275.
- Ullmann, J. F., Gallagher, T., Hart, N. S., Barnes, A. C., Smullen, R. P., Collin, S. P., & Temple, S. E. (2011). Tank color increases growth, and alters color preference and spectral sensitivity, in barramundi (*Lates calcarifer*). *Aquaculture*, 322, 235-240.
- Verheijen, F. J. (1956). Transmission of a flight reaction amongst a school of fish and the underlying sensory mechanisms. *Experientia*, 12(5), 202-204.
- Versteeg, H. K., & Malalasekera, W. (2007). *An introduction to computational fluid dynamics: the finite volume method*. Pearson education.
- Videler, J. J. (1993). *Fish swimming* (Vol. 10). Springer Science & Business Media.
- Videler, J. J., & Hess, F. (1984). Fast continuous swimming of two pelagic predators, saithe (*Pollachius virens*) and mackerel (*Scomber scombrus*): a kinematic analysis. *Journal of experimental biology*, 109(1), 209-228.
- Van Buren, T., Floryan, D., & Smits, A. J. (2019). Scaling and performance of simultaneously heaving and pitching foils. *AIAA Journal*, 57(9), 3666-3677.
- Van Den Thillart, G. E. E. J., Van Ginneken, V., Körner, F., Heijmans, R., Van der Linden, R., & Gluvers, A. (2004). Endurance swimming of European eel. *Journal of Fish Biology*, 65(2), 312-318.
- von Kármán, T., Burgers, J.M. (1943). General aerodynamic theory-perfect fluids. In: Durand, W.F., Division, E. (Eds.), *Aerodynamic theory*, vol. 2. Julius-Springer, Berlin, p. 308.
- Walker, J., & Westneat, M. (1997). Labriform propulsion in fishes: kinematics of flapping aquatic flight in the bird wrasse *Gomphosus varius* (Labridae). *The Journal of experimental biology*, 200(11), 1549-1569.
- Wang, P., Tian, X., Lu, W., Hu, Z., & Luo, Y. (2019). Dynamic modeling and simulations of the wave glider. *Applied Mathematical Modelling*, 66, 77-96.
- Watanabe, Y. Y., Lydersen, C., Fisk, A. T., & Kovacs, K. M. (2012). The slowest fish: swim speed and tail-beat frequency of Greenland sharks. *Journal of Experimental Marine Biology and Ecology*, 426, 5-11.
- Webb, P. W. (1971). The swimming energetics of trout: II. Oxygen consumption and swimming efficiency. *Journal of Experimental Biology*, 55(2), 521-540.
- Webb, P. W. (1984). Body form, locomotion and foraging in aquatic vertebrates. *American zoologist*, 24(1), 107-120.
- Webb, P. W. (1993). The effect of solid and porous channel walls on steady swimming of steelhead trout *Oncorhynchus mykiss*. *Journal of Experimental Biology*, 178(1), 97-108.
- Webb, P. W., Kostecki, P. T., & Stevens, E. D. (1984). The effect of size and swimming speed on locomotor kinematics of rainbow trout. *Journal of Experimental Biology*, 109(MAR), 77-95.
- Weih, D. (1973). Hydromechanics of fish schooling. *Nature*, 241(5387), 290-291.
- Wen, L., Wang, T., Wu, G., & Liang, J. (2012). Quantitative thrust efficiency of a self-propulsive robotic

- fish: Experimental method and hydrodynamic investigation. *IEEE/Asme Transactions on Mechatronics*, 18(3), 1027-1038.
- Weymouth, G. D., & Triantafyllou, M. S. (2013). Ultra-fast escape of a deformable jet-propelled body. *Journal of Fluid Mechanics*, 721, 367-385.
- Williams, S. B., Newman, P., Rosenblatt, J., Dissanayake, G., & Durrant-Whyte, H. (2001). Autonomous underwater navigation and control. *Robotica*, 19(5), 481-496.
- Williamson, C. H., & Roshko, A. (1988). Vortex formation in the wake of an oscillating cylinder. *Journal of fluids and structures*, 2(4), 355-381.
- Wiwchar, L. D., Gilbert, M. J., Kasurak, A. V., & Tierney, K. B. (2018). Schooling improves critical swimming performance in zebrafish (*Danio rerio*). *Canadian Journal of Fisheries and Aquatic Sciences*, 75(4), 653-661.
- Wu, T. Y. T. (1961). Swimming of a waving plate. *Journal of Fluid Mechanics*, 10(3), 321-344.
- Xiao, Q., & Zhu, Q. (2014). A review on flow energy harvesters based on flapping foils. *Journal of fluids and structures*, 46, 174-191.
- Xie, F., Zuo, Q., Chen, Q., Fang, H., He, K., Du, R., ... & Li, Z. (2021). Designs of the biomimetic robotic fishes performing body and/or caudal fin (BCF) swimming locomotion: a review. *Journal of Intelligent & Robotic Systems*, 102(1), 1-19.
- Xu, H. L., Greco, M., & Lugni, C. (2021, June). 2D Numerical Study on Wake Scenarios for a Flapping Foil. In *International Conference on Offshore Mechanics and Arctic Engineering* (Vol. 85185, p. V008T08A033). American Society of Mechanical Engineers.
- Yu, J., Ding, R., Yang, Q., Tan, M., Wang, W., & Zhang, J. (2011). On a bio-inspired amphibious robot capable of multimodal motion. *IEEE/ASME Transactions On Mechatronics*, 17(5), 847-856.
- Yu, J., Tan, M., Wang, S., & Chen, E. (2004). Development of a biomimetic robotic fish and its control algorithm. *IEEE Transactions on Systems, Man, and Cybernetics, Part B (Cybernetics)*, 34(4), 1798-1810.
- Yu, J., Wang, K., Tan, M., & Zhang, J. (2014). Design and control of an embedded vision guided robotic fish with multiple control surfaces. *The Scientific World Journal*, 2014.
- Yu, J., Wang, M., Dong, H., Zhang, Y., & Wu, Z. (2018). Motion control and motion coordination of bionic robotic fish: A review. *Journal of Bionic Engineering*, 15(4), 579-598.
- Zhang, X., Ni, S., Wang, S., & He, G. (2009). Effects of geometric shape on the hydrodynamics of a self-propelled flapping foil. *Physics of Fluids*, 21(10), 103302.
- Zhu, Q., Wolfgang, M. J., Yue, D. K. P., & Triantafyllou, M. S. (2002). Three-dimensional flow structures and vorticity control in fish-like swimming. *Journal of Fluid Mechanics*, 468, 1-28.



## Appendix A

### Mean pressure distribution along NACA 0012 foil at $AOA=15^\circ$ and $Re=1000$

To verify the effectiveness and accuracy of overset grid method within OpenFOAM, numerical simulations have been performed for a stationary NACA 0012 foil at  $AOA = 15^\circ$  and  $Re = 1000$  in a uniform current. With grid and time refinement studies, the numerical simulations converged to the time-averaged horizontal-force coefficient  $\overline{C_x} = 0.287$  and lift-force coefficient  $\overline{C_y} = 0.701$ . The time-averaged pressure coefficients around the NACA 0012 foil are presented and compared to the reference values from Kurtulus (2015) and the results from Cognetti (2019) using different computational domain size, as shown in Figure A-1. The results from OpenFOAM show an overall good agreement with the reference data. The predicted pressure coefficients around the foil leading edge are consistent with the results from Cognetti (2019), and the values at the trailing edge agree better with the data from Kurtulus (2015).

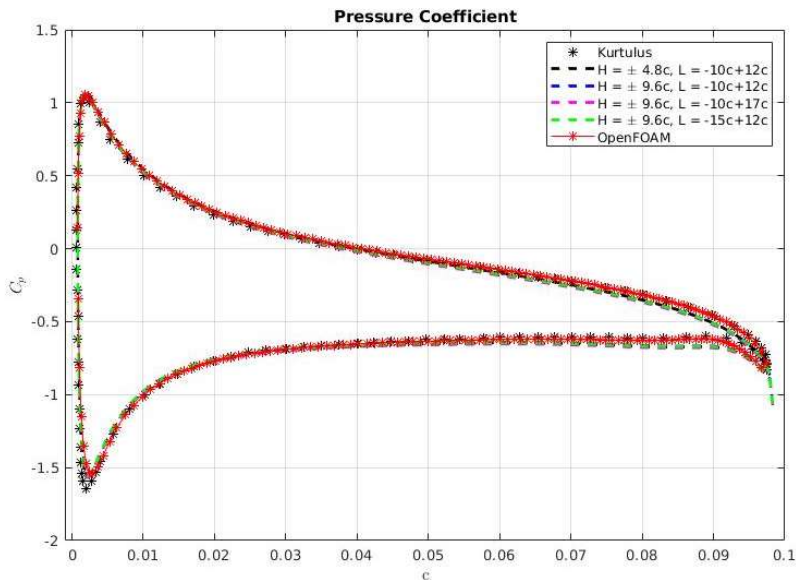


Figure A-1. Time-averaged pressure coefficient along a stationary NACA 0012 foil at  $AOA = 15^\circ$  and  $Re = 1000$





## Appendix B

### Force calculation using conservation of fluid momentum

The hydrodynamic forces on a foil can be obtained by conservation of fluid momentum (CFM) in a closed control volume surrounding the body. This offers the opportunity to cross-check the accuracy of numerical results in terms of integrated loads predictions.

The formulation of CFM for a stationary, non-deforming control volume (CV) encompassing a stationary body, described for example by McClure and Yarusevych (2019), is written as:

$$\mathbf{F} = -\frac{d}{dt} \left( \int_V \rho \mathbf{u} dV \right) - \int_S \rho \mathbf{u} (\mathbf{u} \cdot \mathbf{n}) dS - \int_S p \mathbf{n} dS + \int_S (\boldsymbol{\tau} \cdot \mathbf{n}) dS \quad (\text{B.1})$$

where  $\mathbf{F}$  denotes the force vector acting on the body,  $V$  and  $S$  denote CV and the outer boundary of the CV, respectively. The local quantities inside the integrals are defined as follows:  $\rho$  is the fluid density,  $\mathbf{u}$  the fluid velocity,  $\mathbf{n}$  the outward-facing normal on  $S$ , and  $\boldsymbol{\tau}$  the viscous stress tensor field.

In the present work, the formulation for a moving CV is considered, which reads:

$$\mathbf{F} = -\frac{d}{dt} \left( \int_V \rho \mathbf{u} dV \right) - \int_S \rho \mathbf{u} [(\mathbf{u} - \mathbf{u}_S) \cdot \mathbf{n}] dS - \int_S p \mathbf{n} dS + \int_S (\boldsymbol{\tau} \cdot \mathbf{n}) dS \quad (\text{B.2})$$

where  $\mathbf{u}_S$  denotes the local velocity of  $S$ .

In numerical simulations where the overset grid method is employed, Eq. (B.1) is useful for a control volume extending outside the time-dependent overset grid and fixed to the background grid, while Eq. (B.2) can be used within the region of the overset grid and assuming a control volume changing in time consistently with this grid. For cases where the overset grid is stationary, Eqs. (B.1) and (B.2) should coincide.

### Numerical examples for CFM calculation

#### Stationary NACA 0012 foil at $AOA = 10^\circ$

For a stationary NACA 0012 foil placed at  $AOA = 10^\circ$  and  $Re = 1000$  in a uniform current, the hydrodynamic force can be calculated by the CFM method using Eq. (B.1). In the foil cases employing overset grid method, there are two grid systems. The control

volume can be therefore selected as a large region within the background grid or as a small region within the overset grid. Figure B-1 shows the estimated instantaneous lift force coefficients using three approaches:

- 1) Direct integration (DI) method of OpenFOAM;
- 2) CFM method with a large CV within the background grid (CFM background);
- 3) CFM method with a small CV within the overset grid (CFM overset).

The results computed by CFM overset are in good agreement with DI except for slightly smaller values. The curve of CFM background is not as smooth as those from the other two methods, which is due to the linear interpolation used for information exchange between background and overset grids. The time-averaged lift coefficients of the three methods are documented in Table B-1. They are all consistent with the reference data reported in Kurtulus (2015), and the errors between each other are not larger than 0.39%. However, it is suggested to adopt DI method or CFM in the overset grid around a stationary body to ensure the accuracy of instantaneous hydrodynamic force prediction.

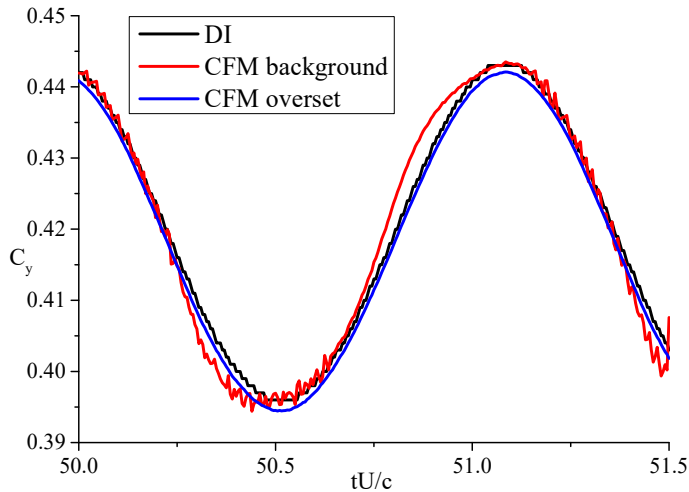


Figure B-1. Instantaneous force estimated by different methods for a stationary NACA 0012 foil at  $AOA = 10^\circ$  and  $Re = 1000$

Table B-1. Time-averaged lift force coefficients calculated by DI and CFM

Reference	DI	CFM background	CFM overset
0.417~0.423	0.4197	0.4201	0.4184

### Pitching semi-circle foil

Force estimation is carried out for the rigid semi-circle foil pitching at  $Sr = 0.22$ ,  $A_D = 1.77$  and  $Re_c = 1173$ . The details of the numerical setup are introduced in Chapter 5. In this flapping foil case, the hydrodynamic force can be calculated by Eq. (B.1) in a stationary CV in background grid or calculated by Eq. (B.2) in a body-fixed

CV in the overset grid. Figure B-2 illustrates the CV employed in the latter method, which is selected as the inner half of the overset region.

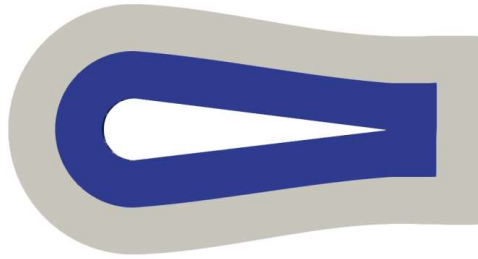


Figure B-2. Schematics showing the control volume (CV, blue) inside the overset grid (grey) around a pitching foil

The instantaneous horizontal forces within one pitch period measured by CFM method in different control volumes are compared with the results of DI method, as shown in Figure B-3. The values of CFM overset curve are slightly larger than those of DI results, while the CFM background curve exhibits large noise during the whole pitch period. This error mainly comes from the interpolation values of fringe cells within the background grid.

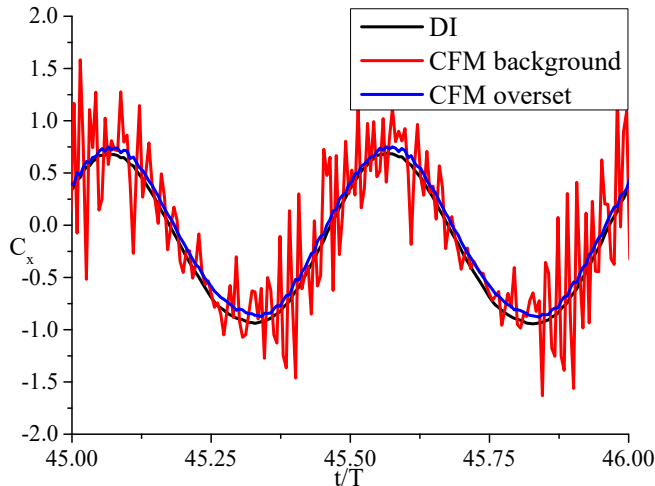


Figure B-3. Instantaneous horizontal force coefficients estimated by different methods for a semi-circle foil pitching at  $Sr = 0.22$ ,  $A_D = 1.77$  and  $Re_c = 1173$

The time-averaged horizontal force coefficients estimated by the three approaches are documented in Table B-2. The mean thrust force predicted by DI is larger than that of CFM method. In chapter 5, the DI results have been compared with the experimental data and showed consistency with the force transition map, as presented in Figure 5-29. It should be noted that a grid convergence test has not been carried out for the results of the CFM methods. Therefore, it is suggested to perform an in-depth numerical-

convergence study for applying the CFM method in hydrodynamic problems where the overset grid method is employed within OpenFOAM platform.

Table B-2. Time-averaged horizontal force coefficients calculated by DI and CFM

DI	CFM background	CFM overset
-0.171	-0.102	-0.096

## Appendix C

### Free-slip boundary condition on a moving body

In problems where fluid forces and moments on a moving body are required, the *movingWallVelocity* boundary condition is a standard boundary condition provided in OpenFOAM library. It sets the velocity to the desired value for moving walls when employed in moving mesh cases and is equivalent to *noSlip* boundary conditions when employed in a stationary mesh case. However, if we want to calculate the hydrodynamic loads under inviscid flow assumption, i.e., to set a free-slip boundary condition on moving walls, a user-defined library should be implemented. In this work, a *slipMovingWallVelocity* boundary condition is attempted using the method reported by Gagnon (2019) and has been examined by the following cases.

#### Stationary NACA 0012 foil at $AOA = 5^\circ$

In the case of a stationary body, the implemented *slipMovingWallVelocity* boundary condition should coincide with the *slip* boundary condition in OpenFOAM. The lift coefficient of a symmetric NACA 0012 foil has been calculated using the two boundary conditions at  $AOA = 5^\circ$ . It is possible to notice that for small values of AOA in the inviscid flow or high Reynolds number ( $\sim 10^6$ ), the ratio of analytical lift force coefficient to AOA should be almost equal to  $2\pi$ . As OpenFOAM does not have an explicitly inviscid solver for incompressible flow, the NACA 0012 foil has been simulated at the Reynolds number of one million, which could be the upper limit of numerical convergence for OpenFOAM simulations, as reported by Reid and Hunsaker (2017). The estimated mean lift-force coefficients using the two, *slip* and *slipMovingWallVelocity* boundary conditions are documented in Table C-1 and confirm their consistency.

Table C-1. Time-averaged horizontal force coefficients calculated by DI and CFM

$\bar{C}_y$	Analytical	<i>slip</i>	<i>slipMovingWallVelocity</i>
$AOA = 5^\circ$	0.548	0.527	0.525
Error	–	3.72%	4.10%

#### Pitching von Mises foil

The 8.4% von Mises airfoil has been adopted to examine the *slipMovingWallVelocity* boundary condition under harmonic pitch motion. The detailed parameters are introduced in the work of Paniccia (2018) and Teng (1987). The foil has been

numerically studied under two conditions:

1) at a low amplitude ( $\theta_0 = 0.01rad$ ) oscillation and a rather high reduced frequency ( $k = \omega c/U = 20$ ) about the leading edge.

2) a lower reduced frequency ( $k = 0.8$ ) and a larger amplitude ( $\theta_0 = 0.3973rad$ ) about the chord's mid-point.

One should note that the frequencies and amplitudes in the present cases are outside the parameter ranges used by the pitching foils in chapter 5, i.e.,  $k = (2.89: 14.43)$  and  $\theta_0 = (0.04: 0.27)$ .

The drag and lift force coefficients of the von Mises airfoil under two pitching conditions are shown in Figure C-1. The data from Paniccia (2018) are indicated as UPC in the figures, and the present *slipMovingWallVelocity* boundary condition cases are indicated as OF. In the high frequency pitching foil case, the hydrodynamic forces are consistent with the reference results, but there are large discrepancies for the lift force prediction in the low frequency case.

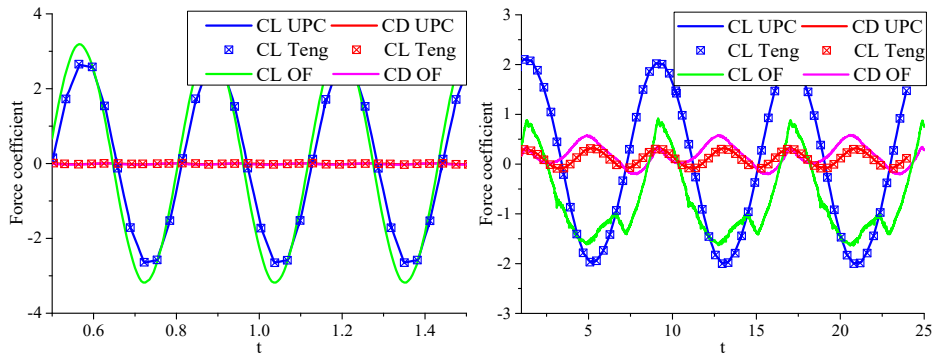


Figure C-1. Drag and lift force coefficients of the von Mises airfoil pitch at high frequency (left) and low frequency (right)

The instantaneous spanwise vorticity fields of the two cases are shown in Figure C-2. The wake behind the von Mises airfoil in the left contour is a well-organized reverse- $\nu$ K vortex street owing to the high oscillation frequency. However, when the foil pitches at low frequency, the vortex shedding from the foil leading edge plays an important role, which could be the main reason of large discrepancies in predicting the hydrodynamic forces because in the infinite Reynolds-number prediction by Paniccia (2018) the vortex shedding can only occur at the trailing edge. In order to carry out accurate simulations of moving bodies with slip boundary conditions, further development should be carried out in OpenFOAM library.

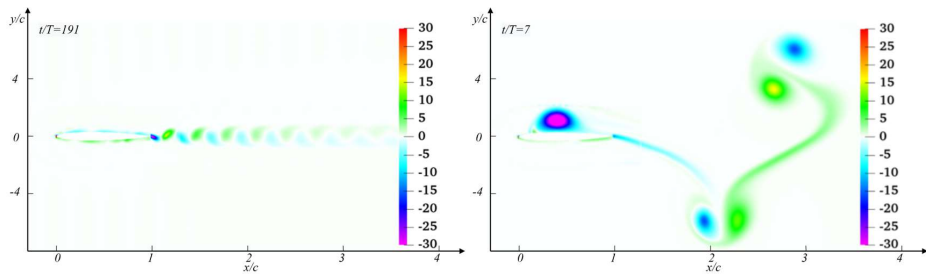


Figure C-2. Instantaneous spanwise vorticity contours for the von Mises airfoil pitch at high frequency (left) and low frequency (right)





**Previous PhD theses published at the Department of Marine Technology  
(earlier: Faculty of Marine Technology)  
NORWEGIAN UNIVERSITY OF SCIENCE AND TECHNOLOGY**

<b>Report No.</b>	<b>Author</b>	<b>Title</b>
	Kavlie, Dag	Optimization of Plane Elastic Grillages, 1967
	Hansen, Hans R.	Man-Machine Communication and Data-Storage Methods in Ship Structural Design, 1971
	Gisvold, Kaare M.	A Method for non-linear mixed -integer programming and its Application to Design Problems, 1971
	Lund, Sverre	Tanker Frame Optimalization by means of SUMT-Transformation and Behaviour Models, 1971
	Vinje, Tor	On Vibration of Spherical Shells Interacting with Fluid, 1972
	Lorentz, Jan D.	Tank Arrangement for Crude Oil Carriers in Accordance with the new Anti-Pollution Regulations, 1975
	Carlsen, Carl A.	Computer-Aided Design of Tanker Structures, 1975
	Larsen, Carl M.	Static and Dynamic Analysis of Offshore Pipelines during Installation, 1976
UR-79-01	Brigt Hatlestad, MK	The finite element method used in a fatigue evaluation of fixed offshore platforms. (Dr.Ing. Thesis)
UR-79-02	Erik Pettersen, MK	Analysis and design of cellular structures. (Dr.Ing. Thesis)
UR-79-03	Sverre Valsgård, MK	Finite difference and finite element methods applied to nonlinear analysis of plated structures. (Dr.Ing. Thesis)
UR-79-04	Nils T. Nordsve, MK	Finite element collapse analysis of structural members considering imperfections and stresses due to fabrication. (Dr.Ing. Thesis)
UR-79-05	Ivar J. Fylling, MK	Analysis of towline forces in ocean towing systems. (Dr.Ing. Thesis)
UR-79- x	Finn Gunnar Nielsen, MH	Hydrodynamic problems related to oil barriers for offshore application
UR-80-06	Nils Sandsmark, MM	Analysis of Stationary and Transient Heat Conduction by the Use of the Finite Element Method. (Dr.Ing. Thesis)
UR-80-09	Sverre Haver, MK	Analysis of uncertainties related to the stochastic modeling of ocean waves. (Dr.Ing. Thesis)

UR-81-15	Odland, Jonas	On the Strength of welded Ring stiffened cylindrical Shells primarily subjected to axial Compression
UR-82-17	Engesvik, Knut	Analysis of Uncertainties in the fatigue Capacity of Welded Joints
UR-82-18	Rye, Henrik	Ocean wave groups
UR-83-30	Eide, Oddvar Inge	On Cumulative Fatigue Damage in Steel Welded Joints
UR-83-33	Mo, Olav	Stochastic Time Domain Analysis of Slender Offshore Structures
UR-83-34	Amdahl, Jørgen	Energy absorption in Ship-platform impacts
UR-84-37	Mørch, Morten	Motions and mooring forces of semi submersibles as determined by full-scale measurements and theoretical analysis
UR-84-38	Soares, C. Guedes	Probabilistic models for load effects in ship structures
UR-84-39	Aarsnes, Jan V.	Current forces on ships
UR-84-40	Czujko, Jerzy	Collapse Analysis of Plates subjected to Biaxial Compression and Lateral Load
UR-85-46	Alf G. Engseth, MK	Finite element collapse analysis of tubular steel offshore structures. (Dr.Ing. Thesis)
UR-86-47	Dengody Sheshappa, MP	A Computer Design Model for Optimizing Fishing Vessel Designs Based on Techno-Economic Analysis. (Dr.Ing. Thesis)
UR-86-48	Vidar Aanesland, MH	A Theoretical and Numerical Study of Ship Wave Resistance. (Dr.Ing. Thesis)
UR-86-49	Heinz-Joachim Wessel, MK	Fracture Mechanics Analysis of Crack Growth in Plate Girders. (Dr.Ing. Thesis)
UR-86-50	Jon Taby, MK	Ultimate and Post-ultimate Strength of Dented Tubular Members. (Dr.Ing. Thesis)
UR-86-51	Walter Lian, MH	A Numerical Study of Two-Dimensional Separated Flow Past Bluff Bodies at Moderate KC-Numbers. (Dr.Ing. Thesis)
UR-86-52	Bjørn Sortland, MH	Force Measurements in Oscillating Flow on Ship Sections and Circular Cylinders in a U-Tube Water Tank. (Dr.Ing. Thesis)
UR-86-53	Kurt Strand, MM	A System Dynamic Approach to One-dimensional Fluid Flow. (Dr.Ing. Thesis)
UR-86-54	Arne Edvin Løken, MH	Three Dimensional Second Order Hydrodynamic Effects on Ocean Structures in Waves. (Dr.Ing. Thesis)
UR-86-55	Sigurd Falch, MH	A Numerical Study of Slamming of Two-

		Dimensional Bodies. (Dr.Ing. Thesis)
UR-87-56	Arne Braathen, MH	Application of a Vortex Tracking Method to the Prediction of Roll Damping of a Two-Dimension Floating Body. (Dr.Ing. Thesis)
UR-87-57	Bernt Leira, MK	Gaussian Vector Processes for Reliability Analysis involving Wave-Induced Load Effects. (Dr.Ing. Thesis)
UR-87-58	Magnus Småvik, MM	Thermal Load and Process Characteristics in a Two-Stroke Diesel Engine with Thermal Barriers (in Norwegian). (Dr.Ing. Thesis)
MTA-88-59	Bernt Arild Bremdal, MP	An Investigation of Marine Installation Processes – A Knowledge - Based Planning Approach. (Dr.Ing. Thesis)
MTA-88-60	Xu Jun, MK	Non-linear Dynamic Analysis of Space-framed Offshore Structures. (Dr.Ing. Thesis)
MTA-89-61	Gang Miao, MH	Hydrodynamic Forces and Dynamic Responses of Circular Cylinders in Wave Zones. (Dr.Ing. Thesis)
MTA-89-62	Martin Greenhow, MH	Linear and Non-Linear Studies of Waves and Floating Bodies. Part I and Part II. (Dr.Techn. Thesis)
MTA-89-63	Chang Li, MH	Force Coefficients of Spheres and Cubes in Oscillatory Flow with and without Current. (Dr.Ing. Thesis)
MTA-89-64	Hu Ying, MP	A Study of Marketing and Design in Development of Marine Transport Systems. (Dr.Ing. Thesis)
MTA-89-65	Arild Jæger, MH	Seakeeping, Dynamic Stability and Performance of a Wedge Shaped Planing Hull. (Dr.Ing. Thesis)
MTA-89-66	Chan Siu Hung, MM	The dynamic characteristics of tilting-pad bearings
MTA-89-67	Kim Wikstrøm, MP	Analysis av projekteringen for ett offshore projekt. (Licenciat-avhandling)
MTA-89-68	Jiao Guoyang, MK	Reliability Analysis of Crack Growth under Random Loading, considering Model Updating. (Dr.Ing. Thesis)
MTA-89-69	Arnt Olufsen, MK	Uncertainty and Reliability Analysis of Fixed Offshore Structures. (Dr.Ing. Thesis)
MTA-89-70	Wu Yu-Lin, MR	System Reliability Analyses of Offshore Structures using improved Truss and Beam Models. (Dr.Ing. Thesis)
MTA-90-71	Jan Roger Hoff, MH	Three-dimensional Green function of a vessel with forward speed in waves. (Dr.Ing. Thesis)
MTA-90-72	Rong Zhao, MH	Slow-Drift Motions of a Moored Two-Dimensional Body in Irregular Waves. (Dr.Ing. Thesis)
MTA-90-73	Atle Minsaas, MP	Economical Risk Analysis. (Dr.Ing. Thesis)

MTA-90-74	Knut-Aril Farnes, MK	Long-term Statistics of Response in Non-linear Marine Structures. (Dr.Ing. Thesis)
MTA-90-75	Torbjørn Sotberg, MK	Application of Reliability Methods for Safety Assessment of Submarine Pipelines. (Dr.Ing. Thesis)
MTA-90-76	Zeuthen, Steffen, MP	SEAMAID. A computational model of the design process in a constraint-based logic programming environment. An example from the offshore domain. (Dr.Ing. Thesis)
MTA-91-77	Haagensen, Sven, MM	Fuel Dependant Cyclic Variability in a Spark Ignition Engine - An Optical Approach. (Dr.Ing. Thesis)
MTA-91-78	Løland, Geir, MH	Current forces on and flow through fish farms. (Dr.Ing. Thesis)
MTA-91-79	Hoen, Christopher, MK	System Identification of Structures Excited by Stochastic Load Processes. (Dr.Ing. Thesis)
MTA-91-80	Haugen, Stein, MK	Probabilistic Evaluation of Frequency of Collision between Ships and Offshore Platforms. (Dr.Ing. Thesis)
MTA-91-81	Sødahl, Nils, MK	Methods for Design and Analysis of Flexible Risers. (Dr.Ing. Thesis)
MTA-91-82	Ormberg, Harald, MK	Non-linear Response Analysis of Floating Fish Farm Systems. (Dr.Ing. Thesis)
MTA-91-83	Marley, Mark J., MK	Time Variant Reliability under Fatigue Degradation. (Dr.Ing. Thesis)
MTA-91-84	Krokstad, Jørgen R., MH	Second-order Loads in Multidirectional Seas. (Dr.Ing. Thesis)
MTA-91-85	Molteberg, Gunnar A., MM	The Application of System Identification Techniques to Performance Monitoring of Four Stroke Turbocharged Diesel Engines. (Dr.Ing. Thesis)
MTA-92-86	Mørch, Hans Jørgen Bjelke, MH	Aspects of Hydrofoil Design: with Emphasis on Hydrofoil Interaction in Calm Water. (Dr.Ing. Thesis)
MTA-92-87	Chan Siu Hung, MM	Nonlinear Analysis of Rotordynamic Instabilities in Highspeed Turbomachinery. (Dr.Ing. Thesis)
MTA-92-88	Bessason, Bjarni, MK	Assessment of Earthquake Loading and Response of Seismically Isolated Bridges. (Dr.Ing. Thesis)
MTA-92-89	Langli, Geir, MP	Improving Operational Safety through exploitation of Design Knowledge - an investigation of offshore platform safety. (Dr.Ing. Thesis)
MTA-92-90	Sævik, Svein, MK	On Stresses and Fatigue in Flexible Pipes. (Dr.Ing. Thesis)
MTA-92-91	Ask, Tor Ø., MM	Ignition and Flame Growth in Lean Gas-Air Mixtures. An Experimental Study with a Schlieren

		System. (Dr.Ing. Thesis)
MTA-86-92	Hessen, Gunnar, MK	Fracture Mechanics Analysis of Stiffened Tubular Members. (Dr.Ing. Thesis)
MTA-93-93	Steinebach, Christian, MM	Knowledge Based Systems for Diagnosis of Rotating Machinery. (Dr.Ing. Thesis)
MTA-93-94	Dalane, Jan Inge, MK	System Reliability in Design and Maintenance of Fixed Offshore Structures. (Dr.Ing. Thesis)
MTA-93-95	Steen, Sverre, MH	Cobblestone Effect on SES. (Dr.Ing. Thesis)
MTA-93-96	Karunakaran, Daniel, MK	Nonlinear Dynamic Response and Reliability Analysis of Drag-dominated Offshore Platforms. (Dr.Ing. Thesis)
MTA-93-97	Hagen, Arnulf, MP	The Framework of a Design Process Language. (Dr.Ing. Thesis)
MTA-93-98	Nordrik, Rune, MM	Investigation of Spark Ignition and Autoignition in Methane and Air Using Computational Fluid Dynamics and Chemical Reaction Kinetics. A Numerical Study of Ignition Processes in Internal Combustion Engines. (Dr.Ing. Thesis)
MTA-94-99	Passano, Elizabeth, MK	Efficient Analysis of Nonlinear Slender Marine Structures. (Dr.Ing. Thesis)
MTA-94-100	Kvålsvold, Jan, MH	Hydroelastic Modelling of Wetdeck Slamming on Multihull Vessels. (Dr.Ing. Thesis)
MTA-94-102	Bech, Sidsel M., MK	Experimental and Numerical Determination of Stiffness and Strength of GRP/PVC Sandwich Structures. (Dr.Ing. Thesis)
MTA-95-103	Paulsen, Hallvard, MM	A Study of Transient Jet and Spray using a Schlieren Method and Digital Image Processing. (Dr.Ing. Thesis)
MTA-95-104	Hovde, Geir Olav, MK	Fatigue and Overload Reliability of Offshore Structural Systems, Considering the Effect of Inspection and Repair. (Dr.Ing. Thesis)
MTA-95-105	Wang, Xiaozhi, MK	Reliability Analysis of Production Ships with Emphasis on Load Combination and Ultimate Strength. (Dr.Ing. Thesis)
MTA-95-106	Ulstein, Tore, MH	Nonlinear Effects of a Flexible Stern Seal Bag on Cobblestone Oscillations of an SES. (Dr.Ing. Thesis)
MTA-95-107	Solaas, Frøydis, MH	Analytical and Numerical Studies of Sloshing in Tanks. (Dr.Ing. Thesis)
MTA-95-108	Hellan, Øyvind, MK	Nonlinear Pushover and Cyclic Analyses in Ultimate Limit State Design and Reassessment of Tubular Steel Offshore Structures. (Dr.Ing. Thesis)
MTA-95-109	Hermundstad, Ole A., MK	Theoretical and Experimental Hydroelastic Analysis of High Speed Vessels. (Dr.Ing. Thesis)

MTA-96-110	Bratland, Anne K., MH	Wave-Current Interaction Effects on Large-Volume Bodies in Water of Finite Depth. (Dr.Ing. Thesis)
MTA-96-111	Herfjord, Kjell, MH	A Study of Two-dimensional Separated Flow by a Combination of the Finite Element Method and Navier-Stokes Equations. (Dr.Ing. Thesis)
MTA-96-112	Æsøy, Vilmar, MM	Hot Surface Assisted Compression Ignition in a Direct Injection Natural Gas Engine. (Dr.Ing. Thesis)
MTA-96-113	Eknes, Monika L., MK	Escalation Scenarios Initiated by Gas Explosions on Offshore Installations. (Dr.Ing. Thesis)
MTA-96-114	Erikstad, Stein O., MP	A Decision Support Model for Preliminary Ship Design. (Dr.Ing. Thesis)
MTA-96-115	Pedersen, Egil, MH	A Nautical Study of Towed Marine Seismic Streamer Cable Configurations. (Dr.Ing. Thesis)
MTA-97-116	Moksnes, Paul O., MM	Modelling Two-Phase Thermo-Fluid Systems Using Bond Graphs. (Dr.Ing. Thesis)
MTA-97-117	Halse, Karl H., MK	On Vortex Shedding and Prediction of Vortex-Induced Vibrations of Circular Cylinders. (Dr.Ing. Thesis)
MTA-97-118	Igland, Ragnar T., MK	Reliability Analysis of Pipelines during Laying, considering Ultimate Strength under Combined Loads. (Dr.Ing. Thesis)
MTA-97-119	Pedersen, Hans-P., MP	Levendefiskteknologi for fiskefartøy. (Dr.Ing. Thesis)
MTA-98-120	Vikestad, Kyrre, MK	Multi-Frequency Response of a Cylinder Subjected to Vortex Shedding and Support Motions. (Dr.Ing. Thesis)
MTA-98-121	Azadi, Mohammad R. E., MK	Analysis of Static and Dynamic Pile-Soil-Jacket Behaviour. (Dr.Ing. Thesis)
MTA-98-122	Ulltang, Terje, MP	A Communication Model for Product Information. (Dr.Ing. Thesis)
MTA-98-123	Torbergsen, Erik, MM	Impeller/Diffuser Interaction Forces in Centrifugal Pumps. (Dr.Ing. Thesis)
MTA-98-124	Hansen, Edmond, MH	A Discrete Element Model to Study Marginal Ice Zone Dynamics and the Behaviour of Vessels Moored in Broken Ice. (Dr.Ing. Thesis)
MTA-98-125	Videiro, Paulo M., MK	Reliability Based Design of Marine Structures. (Dr.Ing. Thesis)
MTA-99-126	Mainçon, Philippe, MK	Fatigue Reliability of Long Welds Application to Titanium Risers. (Dr.Ing. Thesis)
MTA-99-127	Haugen, Elin M., MH	Hydroelastic Analysis of Slamming on Stiffened Plates with Application to Catamaran Wetdecks. (Dr.Ing. Thesis)
MTA-99-	Langhelle, Nina K., MK	Experimental Validation and Calibration of

128		Nonlinear Finite Element Models for Use in Design of Aluminium Structures Exposed to Fire. (Dr.Ing. Thesis)
MTA-99-129	Berstad, Are J., MK	Calculation of Fatigue Damage in Ship Structures. (Dr.Ing. Thesis)
MTA-99-130	Andersen, Trond M., MM	Short Term Maintenance Planning. (Dr.Ing. Thesis)
MTA-99-131	Tveiten, Bård Wathne, MK	Fatigue Assessment of Welded Aluminium Ship Details. (Dr.Ing. Thesis)
MTA-99-132	Søreide, Fredrik, MP	Applications of underwater technology in deep water archaeology. Principles and practice. (Dr.Ing. Thesis)
MTA-99-133	Tønnessen, Rune, MH	A Finite Element Method Applied to Unsteady Viscous Flow Around 2D Blunt Bodies With Sharp Corners. (Dr.Ing. Thesis)
MTA-99-134	Elvekrok, Dag R., MP	Engineering Integration in Field Development Projects in the Norwegian Oil and Gas Industry. The Supplier Management of Norne. (Dr.Ing. Thesis)
MTA-99-135	Fagerholt, Kjetil, MP	Optimeringsbaserte Metoder for Ruteplanlegging innen skipsfart. (Dr.Ing. Thesis)
MTA-99-136	Bysveen, Marie, MM	Visualization in Two Directions on a Dynamic Combustion Rig for Studies of Fuel Quality. (Dr.Ing. Thesis)
MTA-2000-137	Storteig, Eskild, MM	Dynamic characteristics and leakage performance of liquid annular seals in centrifugal pumps. (Dr.Ing. Thesis)
MTA-2000-138	Sagli, Gro, MK	Model uncertainty and simplified estimates of long term extremes of hull girder loads in ships. (Dr.Ing. Thesis)
MTA-2000-139	Tronstad, Harald, MK	Nonlinear analysis and design of cable net structures like fishing gear based on the finite element method. (Dr.Ing. Thesis)
MTA-2000-140	Kroneberg, André, MP	Innovation in shipping by using scenarios. (Dr.Ing. Thesis)
MTA-2000-141	Haslum, Herbjørn Alf, MH	Simplified methods applied to nonlinear motion of spar platforms. (Dr.Ing. Thesis)
MTA-2001-142	Samdal, Ole Johan, MM	Modelling of Degradation Mechanisms and Stressor Interaction on Static Mechanical Equipment Residual Lifetime. (Dr.Ing. Thesis)
MTA-2001-143	Baarholm, Rolf Jarle, MH	Theoretical and experimental studies of wave impact underneath decks of offshore platforms. (Dr.Ing. Thesis)
MTA-2001-144	Wang, Lihua, MK	Probabilistic Analysis of Nonlinear Wave-induced Loads on Ships. (Dr.Ing. Thesis)
MTA-2001-145	Kristensen, Odd H. Holt, MK	Ultimate Capacity of Aluminium Plates under Multiple Loads, Considering HAZ Properties.



(Dr.Ing. Thesis)

MTA-2001-146	Greco, Marilena, MH	A Two-Dimensional Study of Green-Water Loading. (Dr.Ing. Thesis)
MTA-2001-147	Heggelund, Svein E., MK	Calculation of Global Design Loads and Load Effects in Large High Speed Catamarans. (Dr.Ing. Thesis)
MTA-2001-148	Babalola, Olusegun T., MK	Fatigue Strength of Titanium Risers – Defect Sensitivity. (Dr.Ing. Thesis)
MTA-2001-149	Mohammed, Abuu K., MK	Nonlinear Shell Finite Elements for Ultimate Strength and Collapse Analysis of Ship Structures. (Dr.Ing. Thesis)
MTA-2002-150	Holmedal, Lars E., MH	Wave-current interactions in the vicinity of the sea bed. (Dr.Ing. Thesis)
MTA-2002-151	Rognebakke, Olav F., MH	Sloshing in rectangular tanks and interaction with ship motions. (Dr.Ing. Thesis)
MTA-2002-152	Lader, Pål Furset, MH	Geometry and Kinematics of Breaking Waves. (Dr.Ing. Thesis)
MTA-2002-153	Yang, Qinzhen, MH	Wash and wave resistance of ships in finite water depth. (Dr.Ing. Thesis)
MTA-2002-154	Melhus, Øyvind, MM	Utilization of VOC in Diesel Engines. Ignition and combustion of VOC released by crude oil tankers. (Dr.Ing. Thesis)
MTA-2002-155	Ronæss, Marit, MH	Wave Induced Motions of Two Ships Advancing on Parallel Course. (Dr.Ing. Thesis)
MTA-2002-156	Økland, Ole D., MK	Numerical and experimental investigation of whipping in twin hull vessels exposed to severe wet deck slamming. (Dr.Ing. Thesis)
MTA-2002-157	Ge, Chunhua, MK	Global Hydroelastic Response of Catamarans due to Wet Deck Slamming. (Dr.Ing. Thesis)
MTA-2002-158	Byklum, Eirik, MK	Nonlinear Shell Finite Elements for Ultimate Strength and Collapse Analysis of Ship Structures. (Dr.Ing. Thesis)
IMT-2003-1	Chen, Haibo, MK	Probabilistic Evaluation of FPSO-Tanker Collision in Tandem Offloading Operation. (Dr.Ing. Thesis)
IMT-2003-2	Skaugset, Kjetil Bjørn, MK	On the Suppression of Vortex Induced Vibrations of Circular Cylinders by Radial Water Jets. (Dr.Ing. Thesis)
IMT-2003-3	Chezian, Muthu	Three-Dimensional Analysis of Slamming. (Dr.Ing. Thesis)
IMT-2003-4	Buhaug, Øyvind	Deposit Formation on Cylinder Liner Surfaces in Medium Speed Engines. (Dr.Ing. Thesis)
IMT-2003-5	Tregde, Vidar	Aspects of Ship Design: Optimization of Aft Hull with Inverse Geometry Design. (Dr.Ing. Thesis)

IMT-2003-6	Wist, Hanne Therese	Statistical Properties of Successive Ocean Wave Parameters. (Dr.Ing. Thesis)
IMT-2004-7	Ransau, Samuel	Numerical Methods for Flows with Evolving Interfaces. (Dr.Ing. Thesis)
IMT-2004-8	Soma, Torkel	Blue-Chip or Sub-Standard. A data interrogation approach of identity safety characteristics of shipping organization. (Dr.Ing. Thesis)
IMT-2004-9	Ersdal, Svein	An experimental study of hydrodynamic forces on cylinders and cables in near axial flow. (Dr.Ing. Thesis)
IMT-2005-10	Brodtkorb, Per Andreas	The Probability of Occurrence of Dangerous Wave Situations at Sea. (Dr.Ing. Thesis)
IMT-2005-11	Yttervik, Rune	Ocean current variability in relation to offshore engineering. (Dr.Ing. Thesis)
IMT-2005-12	Fredheim, Arne	Current Forces on Net-Structures. (Dr.Ing. Thesis)
IMT-2005-13	Heggemes, Kjetil	Flow around marine structures. (Dr.Ing. Thesis)
IMT-2005-14	Fouques, Sebastien	Lagrangian Modelling of Ocean Surface Waves and Synthetic Aperture Radar Wave Measurements. (Dr.Ing. Thesis)
IMT-2006-15	Holm, Håvard	Numerical calculation of viscous free surface flow around marine structures. (Dr.Ing. Thesis)
IMT-2006-16	Bjørheim, Lars G.	Failure Assessment of Long Through Thickness Fatigue Cracks in Ship Hulls. (Dr.Ing. Thesis)
IMT-2006-17	Hansson, Lisbeth	Safety Management for Prevention of Occupational Accidents. (Dr.Ing. Thesis)
IMT-2006-18	Zhu, Xinying	Application of the CIP Method to Strongly Nonlinear Wave-Body Interaction Problems. (Dr.Ing. Thesis)
IMT-2006-19	Reite, Karl Johan	Modelling and Control of Trawl Systems. (Dr.Ing. Thesis)
IMT-2006-20	Smogeli, Øyvind Notland	Control of Marine Propellers. From Normal to Extreme Conditions. (Dr.Ing. Thesis)
IMT-2007-21	Storhaug, Gaute	Experimental Investigation of Wave Induced Vibrations and Their Effect on the Fatigue Loading of Ships. (Dr.Ing. Thesis)
IMT-2007-22	Sun, Hui	A Boundary Element Method Applied to Strongly Nonlinear Wave-Body Interaction Problems. (PhD Thesis, CeSOS)
IMT-2007-23	Rustad, Anne Marthine	Modelling and Control of Top Tensioned Risers. (PhD Thesis, CeSOS)
IMT-2007-24	Johansen, Vegar	Modelling flexible slender system for real-time

simulations and control applications

IMT-2007-25	Wroldsen, Anders Sunde	Modelling and control of tensegrity structures. (PhD Thesis, CeSOS)
IMT-2007-26	Aronsen, Kristoffer Høy	An experimental investigation of in-line and combined inline and cross flow vortex induced vibrations. (Dr. avhandling, IMT)
IMT-2007-27	Gao, Zhen	Stochastic Response Analysis of Mooring Systems with Emphasis on Frequency-domain Analysis of Fatigue due to Wide-band Response Processes (PhD Thesis, CeSOS)
IMT-2007-28	Thorstensen, Tom Anders	Lifetime Profit Modelling of Ageing Systems Utilizing Information about Technical Condition. (Dr.ing. thesis, IMT)
IMT-2008-29	Refsnes, Jon Erling Gorset	Nonlinear Model-Based Control of Slender Body AUVs (PhD Thesis, IMT)
IMT-2008-30	Berntsen, Per Ivar B.	Structural Reliability Based Position Mooring. (PhD-Thesis, IMT)
IMT-2008-31	Ye, Naiquan	Fatigue Assessment of Aluminium Welded Box-stiffener Joints in Ships (Dr.ing. thesis, IMT)
IMT-2008-32	Radan, Damir	Integrated Control of Marine Electrical Power Systems. (PhD-Thesis, IMT)
IMT-2008-33	Thomassen, Paul	Methods for Dynamic Response Analysis and Fatigue Life Estimation of Floating Fish Cages. (Dr.ing. thesis, IMT)
IMT-2008-34	Pákozdi, Csaba	A Smoothed Particle Hydrodynamics Study of Two-dimensional Nonlinear Sloshing in Rectangular Tanks. (Dr.ing.thesis, IMT/ CeSOS)
IMT-2007-35	Grytøy, Guttorm	A Higher-Order Boundary Element Method and Applications to Marine Hydrodynamics. (Dr.ing.thesis, IMT)
IMT-2008-36	Drummen, Ingo	Experimental and Numerical Investigation of Nonlinear Wave-Induced Load Effects in Containerships considering Hydroelasticity. (PhD thesis, CeSOS)
IMT-2008-37	Skejic, Renato	Maneuvering and Seakeeping of a Singel Ship and of Two Ships in Interaction. (PhD-Thesis, CeSOS)
IMT-2008-38	Harlem, Alf	An Age-Based Replacement Model for Repairable Systems with Attention to High-Speed Marine Diesel Engines. (PhD-Thesis, IMT)
IMT-2008-39	Alsos, Hagbart S.	Ship Grounding. Analysis of Ductile Fracture, Bottom Damage and Hull Girder Response. (PhD-thesis, IMT)
IMT-2008-40	Graczyk, Mateusz	Experimental Investigation of Sloshing Loading and Load Effects in Membrane LNG Tanks Subjected to Random Excitation. (PhD-thesis, CeSOS)

IMT-2008-41	Taghipour, Reza	Efficient Prediction of Dynamic Response for Flexible and Multi-body Marine Structures. (PhD-thesis, CeSOS)
IMT-2008-42	Ruth, Eivind	Propulsion control and thrust allocation on marine vessels. (PhD thesis, CeSOS)
IMT-2008-43	Nystad, Bent Helge	Technical Condition Indexes and Remaining Useful Life of Aggregated Systems. PhD thesis, IMT
IMT-2008-44	Soni, Prashant Kumar	Hydrodynamic Coefficients for Vortex Induced Vibrations of Flexible Beams, PhD thesis, CeSOS
IMT-2009-45	Amlashi, Hadi K.K.	Ultimate Strength and Reliability-based Design of Ship Hulls with Emphasis on Combined Global and Local Loads. PhD Thesis, IMT
IMT-2009-46	Pedersen, Tom Arne	Bond Graph Modelling of Marine Power Systems. PhD Thesis, IMT
IMT-2009-47	Kristiansen, Trygve	Two-Dimensional Numerical and Experimental Studies of Piston-Mode Resonance. PhD-Thesis, CeSOS
IMT-2009-48	Ong, Muk Chen	Applications of a Standard High Reynolds Number Model and a Stochastic Scour Prediction Model for Marine Structures. PhD-thesis, IMT
IMT-2009-49	Hong, Lin	Simplified Analysis and Design of Ships subjected to Collision and Grounding. PhD-thesis, IMT
IMT-2009-50	Koushan, Kamran	Vortex Induced Vibrations of Free Span Pipelines, PhD thesis, IMT
IMT-2009-51	Korsvik, Jarl Eirik	Heuristic Methods for Ship Routing and Scheduling. PhD-thesis, IMT
IMT-2009-52	Lee, Jihoon	Experimental Investigation and Numerical in Analyzing the Ocean Current Displacement of Longlines. Ph.d.-Thesis, IMT.
IMT-2009-53	Vestbøstad, Tone Gran	A Numerical Study of Wave-in-Deck Impact using a Two-Dimensional Constrained Interpolation Profile Method, Ph.d.thesis, CeSOS.
IMT-2009-54	Bruun, Kristine	Bond Graph Modelling of Fuel Cells for Marine Power Plants. Ph.d.-thesis, IMT
IMT-2009-55	Holstad, Anders	Numerical Investigation of Turbulence in a Skewed Three-Dimensional Channel Flow, Ph.d.-thesis, IMT.
IMT-2009-56	Ayala-Uraga, Efrén	Reliability-Based Assessment of Deteriorating Ship-shaped Offshore Structures, Ph.d.-thesis, IMT
IMT-2009-57	Kong, Xiangjun	A Numerical Study of a Damaged Ship in Beam Sea Waves. Ph.d.-thesis, IMT/CeSOS.
IMT-2010-58	Kristiansen, David	Wave Induced Effects on Floaters of Aquaculture Plants, Ph.d.-thesis, CeSOS.

IMT 2010-59	Ludvigsen, Martin	An ROV-Toolbox for Optical and Acoustic Scientific Seabed Investigation. Ph.d.-thesis IMT.
IMT 2010-60	Hals, Jørgen	Modelling and Phase Control of Wave-Energy Converters. Ph.d.thesis, CeSOS.
IMT 2010- 61	Shu, Zhi	Uncertainty Assessment of Wave Loads and Ultimate Strength of Tankers and Bulk Carriers in a Reliability Framework. Ph.d. Thesis, IMT/ CeSOS
IMT 2010-62	Shao, Yanlin	Numerical Potential-Flow Studies on Weakly-Nonlinear Wave-Body Interactions with/without Small Forward Speed, Ph.d.thesis,CeSOS.
IMT 2010-63	Califano, Andrea	Dynamic Loads on Marine Propellers due to Intermittent Ventilation. Ph.d.thesis, IMT.
IMT 2010-64	El Khoury, George	Numerical Simulations of Massively Separated Turbulent Flows, Ph.d.-thesis, IMT
IMT 2010-65	Seim, Knut Sponheim	Mixing Process in Dense Overflows with Emphasis on the Faroe Bank Channel Overflow. Ph.d.thesis, IMT
IMT 2010-66	Jia, Huirong	Structural Analysis of Intact and Damaged Ships in a Collision Risk Analysis Perspective. Ph.d.thesis CeSoS.
IMT 2010-67	Jiao, Linlin	Wave-Induced Effects on a Pontoon-type Very Large Floating Structures (VLFS). Ph.D.-thesis, CeSOS.
IMT 2010-68	Abrahamsen, Bjørn Christian	Sloshing Induced Tank Roof with Entrapped Air Pocket. Ph.d.thesis, CeSOS.
IMT 2011-69	Karimirad, Madjid	Stochastic Dynamic Response Analysis of Spar-Type Wind Turbines with Catenary or Taut Mooring Systems. Ph.d.-thesis, CeSOS.
IMT - 2011-70	Erlend Meland	Condition Monitoring of Safety Critical Valves. Ph.d.-thesis, IMT.
IMT – 2011-71	Yang, Limin	Stochastic Dynamic System Analysis of Wave Energy Converter with Hydraulic Power Take-Off, with Particular Reference to Wear Damage Analysis, Ph.d. Thesis, CeSOS.
IMT – 2011-72	Visscher, Jan	Application of Particle Image Velocimetry on Turbulent Marine Flows, Ph.d.Thesis, IMT.
IMT – 2011-73	Su, Biao	Numerical Predictions of Global and Local Ice Loads on Ships. Ph.d.Thesis, CeSOS.
IMT – 2011-74	Liu, Zhenhui	Analytical and Numerical Analysis of Iceberg Collision with Ship Structures. Ph.d.Thesis, IMT.
IMT – 2011-75	Aarsæther, Karl Gunnar	Modeling and Analysis of Ship Traffic by Observation and Numerical Simulation. Ph.d.Thesis, IMT.

Imt – 2011-76	Wu, Jie	Hydrodynamic Force Identification from Stochastic Vortex Induced Vibration Experiments with Slender Beams. Ph.d.Thesis, IMT.
Imt – 2011-77	Amini, Hamid	Azimuth Propulsors in Off-design Conditions. Ph.d.Thesis, IMT.
IMT – 2011-78	Nguyen, Tan-Hoi	Toward a System of Real-Time Prediction and Monitoring of Bottom Damage Conditions During Ship Grounding. Ph.d.thesis, IMT.
IMT- 2011-79	Tavakoli, Mohammad T.	Assessment of Oil Spill in Ship Collision and Grounding, Ph.d.thesis, IMT.
IMT- 2011-80	Guo, Bingjie	Numerical and Experimental Investigation of Added Resistance in Waves. Ph.d.Thesis, IMT.
IMT- 2011-81	Chen, Qiaofeng	Ultimate Strength of Aluminium Panels, considering HAZ Effects, IMT
IMT- 2012-82	Kota, Ravikiran S.	Wave Loads on Decks of Offshore Structures in Random Seas, CeSOS.
IMT- 2012-83	Sten, Ronny	Dynamic Simulation of Deep Water Drilling Risers with Heave Compensating System, IMT.
IMT- 2012-84	Berle, Øyvind	Risk and resilience in global maritime supply chains, IMT.
IMT- 2012-85	Fang, Shaoji	Fault Tolerant Position Mooring Control Based on Structural Reliability, CeSOS.
IMT- 2012-86	You, Jikun	Numerical studies on wave forces and moored ship motions in intermediate and shallow water, CeSOS.
IMT- 2012-87	Xiang ,Xu	Maneuvering of two interacting ships in waves, CeSOS
IMT- 2012-88	Dong, Wenbin	Time-domain fatigue response and reliability analysis of offshore wind turbines with emphasis on welded tubular joints and gear components, CeSOS
IMT- 2012-89	Zhu, Suji	Investigation of Wave-Induced Nonlinear Load Effects in Open Ships considering Hull Girder Vibrations in Bending and Torsion, CeSOS
IMT- 2012-90	Zhou, Li	Numerical and Experimental Investigation of Station-keeping in Level Ice, CeSOS
IMT- 2012-91	Ushakov, Sergey	Particulate matter emission characteristics from diesel engines operating on conventional and alternative marine fuels, IMT
IMT- 2013-1	Yin, Decao	Experimental and Numerical Analysis of Combined In-line and Cross-flow Vortex Induced Vibrations, CeSOS

IMT-2013-2	Kurniawan, Adi	Modelling and geometry optimisation of wave energy converters, CeSOS
IMT-2013-3	Al Ryati, Nabil	Technical condition indexes doe auxiliary marine diesel engines, IMT
IMT-2013-4	Firoozkoohi, Reza	Experimental, numerical and analytical investigation of the effect of screens on sloshing, CeSOS
IMT-2013-5	Ommani, Babak	Potential-Flow Predictions of a Semi-Displacement Vessel Including Applications to Calm Water Broaching, CeSOS
IMT-2013-6	Xing, Yihan	Modelling and analysis of the gearbox in a floating spar-type wind turbine, CeSOS
IMT-7-2013	Balland, Océane	Optimization models for reducing air emissions from ships, IMT
IMT-8-2013	Yang, Dan	Transitional wake flow behind an inclined flat plate----Computation and analysis, IMT
IMT-9-2013	Abdillah, Suyuthi	Prediction of Extreme Loads and Fatigue Damage for a Ship Hull due to Ice Action, IMT
IMT-10-2013	Ramirez, Pedro Agustin Pérez	Ageing management and life extension of technical systems- Concepts and methods applied to oil and gas facilities, IMT
IMT-11-2013	Chuang, Zhenju	Experimental and Numerical Investigation of Speed Loss due to Seakeeping and Maneuvering. IMT
IMT-12-2013	Etemaddar, Mahmoud	Load and Response Analysis of Wind Turbines under Atmospheric Icing and Controller System Faults with Emphasis on Spar Type Floating Wind Turbines, IMT
IMT-13-2013	Lindstad, Haakon	Strategies and measures for reducing maritime CO2 emissons, IMT
IMT-14-2013	Haris, Sabril	Damage interaction analysis of ship collisions, IMT
IMT-15-2013	Shainee, Mohamed	Conceptual Design, Numerical and Experimental Investigation of a SPM Cage Concept for Offshore Mariculture, IMT
IMT-16-2013	Gansel, Lars	Flow past porous cylinders and effects of biofouling and fish behavior on the flow in and around Atlantic salmon net cages, IMT
IMT-17-2013	Gaspar, Henrique	Handling Aspects of Complexity in Conceptual Ship Design, IMT
IMT-18-2013	Thys, Maxime	Theoretical and Experimental Investigation of a Free Running Fishing Vessel at Small Frequency of Encounter, CeSOS
IMT-19-2013	Aglen, Ida	VIV in Free Spanning Pipelines, CeSOS

IMT-1-2014	Song, An	Theoretical and experimental studies of wave diffraction and radiation loads on a horizontally submerged perforated plate, CeSOS
IMT-2-2014	Rogne, Øyvind Ygre	Numerical and Experimental Investigation of a Hinged 5-body Wave Energy Converter, CeSOS
IMT-3-2014	Dai, Lijuan	Safe and efficient operation and maintenance of offshore wind farms ,IMT
IMT-4-2014	Bachynski, Erin Elizabeth	Design and Dynamic Analysis of Tension Leg Platform Wind Turbines, CeSOS
IMT-5-2014	Wang, Jingbo	Water Entry of Freefall Wedged – Wedge motions and Cavity Dynamics, CeSOS
IMT-6-2014	Kim, Ekaterina	Experimental and numerical studies related to the coupled behavior of ice mass and steel structures during accidental collisions, IMT
IMT-7-2014	Tan, Xiang	Numerical investigation of ship's continuous- mode icebreaking in level ice, CeSOS
IMT-8-2014	Muliawan, Made Jaya	Design and Analysis of Combined Floating Wave and Wind Power Facilities, with Emphasis on Extreme Load Effects of the Mooring System, CeSOS
IMT-9-2014	Jiang, Zhiyu	Long-term response analysis of wind turbines with an emphasis on fault and shutdown conditions, IMT
IMT-10-2014	Dukan, Fredrik	ROV Motion Control Systems, IMT
IMT-11-2014	Grimsmo, Nils I.	Dynamic simulations of hydraulic cylinder for heave compensation of deep water drilling risers, IMT
IMT-12-2014	Kvittem, Marit I.	Modelling and response analysis for fatigue design of a semisubmersible wind turbine, CeSOS
IMT-13-2014	Akhtar, Juned	The Effects of Human Fatigue on Risk at Sea, IMT
IMT-14-2014	Syahroni, Nur	Fatigue Assessment of Welded Joints Taking into Account Effects of Residual Stress, IMT
IMT-1-2015	Böckmann, Eirik	Wave Propulsion of ships, IMT
IMT-2-2015	Wang, Kai	Modelling and dynamic analysis of a semi-submersible floating vertical axis wind turbine, CeSOS
IMT-3-2015	Fredriksen, Arnt Gunvald	A numerical and experimental study of a two-dimensional body with moonpool in waves and current, CeSOS
IMT-4-2015	Jose Patricio Gallardo Canabes	Numerical studies of viscous flow around bluff bodies, IMT



IMT-5-2015	Vegard Longva	Formulation and application of finite element techniques for slender marine structures subjected to contact interactions, IMT
IMT-6-2015	Jacobus De Vaal	Aerodynamic modelling of floating wind turbines, CeSOS
IMT-7-2015	Fachri Nasution	Fatigue Performance of Copper Power Conductors, IMT
IMT-8-2015	Oleh I Karpa	Development of bivariate extreme value distributions for applications in marine technology, CeSOS
IMT-9-2015	Daniel de Almeida Fernandes	An output feedback motion control system for ROVs, AMOS
IMT-10-2015	Bo Zhao	Particle Filter for Fault Diagnosis: Application to Dynamic Positioning Vessel and Underwater Robotics, CeSOS
IMT-11-2015	Wenting Zhu	Impact of emission allocation in maritime transportation, IMT
IMT-12-2015	Amir Rasekhi Nejad	Dynamic Analysis and Design of Gearboxes in Offshore Wind Turbines in a Structural Reliability Perspective, CeSOS
IMT-13-2015	Arturo Jesús Ortega Malca	Dynamic Response of Flexibles Risers due to Unsteady Slug Flow, CeSOS
IMT-14-2015	Dagfinn Husjord	Guidance and decision-support system for safe navigation of ships operating in close proximity, IMT
IMT-15-2015	Anirban Bhattacharyya	Ducted Propellers: Behaviour in Waves and Scale Effects, IMT
IMT-16-2015	Qin Zhang	Image Processing for Ice Parameter Identification in Ice Management, IMT
IMT-1-2016	Vincentius Rumawas	Human Factors in Ship Design and Operation: An Experiential Learning, IMT
IMT-2-2016	Martin Storheim	Structural response in ship-platform and ship-ice collisions, IMT
IMT-3-2016	Mia Abrahamsen Prsic	Numerical Simulations of the Flow around single and Tandem Circular Cylinders Close to a Plane Wall, IMT
IMT-4-2016	Tufan Arslan	Large-eddy simulations of cross-flow around ship sections, IMT

IMT-5-2016	Pierre Yves-Henry	Parametrisation of aquatic vegetation in hydraulic and coastal research,IMT
IMT-6-2016	Lin Li	Dynamic Analysis of the Instalation of Monopiles for Offshore Wind Turbines, CeSOS
IMT-7-2016	Øivind Kåre Kjerstad	Dynamic Positioning of Marine Vessels in Ice, IMT
IMT-8-2016	Xiaopeng Wu	Numerical Analysis of Anchor Handling and Fish Trawling Operations in a Safety Perspective, CeSOS
IMT-9-2016	Zhengshun Cheng	Integrated Dynamic Analysis of Floating Vertical Axis Wind Turbines, CeSOS
IMT-10-2016	Ling Wan	Experimental and Numerical Study of a Combined Offshore Wind and Wave Energy Converter Concept
IMT-11-2016	Wei Chai	Stochastic dynamic analysis and reliability evaluation of the roll motion for ships in random seas, CeSOS
IMT-12-2016	Øyvind Selnes Patricksson	Decision support for conceptual ship design with focus on a changing life cycle and future uncertainty, IMT
IMT-13-2016	Mats Jørgen Thorsen	Time domain analysis of vortex-induced vibrations, IMT
IMT-14-2016	Edgar McGuinness	Safety in the Norwegian Fishing Fleet – Analysis and measures for improvement, IMT
IMT-15-2016	Sepideh Jafarzadeh	Energy efficiency and emission abatement in the fishing fleet, IMT
IMT-16-2016	Wilson Ivan Guachamin Acero	Assessment of marine operations for offshore wind turbine installation with emphasis on response-based operational limits, IMT
IMT-17-2016	Mauro Candeloro	Tools and Methods for Autonomous Operations on Seabed and Water Coumn using Underwater Vehicles, IMT
IMT-18-2016	Valentin Chabaud	Real-Time Hybrid Model Testing of Floating Wind Tubines, IMT
IMT-1-2017	Mohammad Saud Afzal	Three-dimensional streaming in a sea bed boundary layer
IMT-2-2017	Peng Li	A Theoretical and Experimental Study of Wave-induced Hydroelastic Response of a Circular Floating Collar
IMT-3-2017	Martin Bergström	A simulation-based design method for arctic maritime transport systems

IMT-4-2017	Bhushan Taskar	The effect of waves on marine propellers and propulsion
IMT-5-2017	Mohsen Bardestani	A two-dimensional numerical and experimental study of a floater with net and sinker tube in waves and current
IMT-6-2017	Fatemeh Hoseini Dadmarzi	Direct Numerical Simulation of turbulent wakes behind different plate configurations
IMT-7-2017	Michel R. Miyazaki	Modeling and control of hybrid marine power plants
IMT-8-2017	Giri Rajasekhar Gunnu	Safety and efficiency enhancement of anchor handling operations with particular emphasis on the stability of anchor handling vessels
IMT-9-2017	Kevin Koosup Yum	Transient Performance and Emissions of a Turbocharged Diesel Engine for Marine Power Plants
IMT-10-2017	Zhaolong Yu	Hydrodynamic and structural aspects of ship collisions
IMT-11-2017	Martin Hassel	Risk Analysis and Modelling of Allisions between Passing Vessels and Offshore Installations
IMT-12-2017	Astrid H. Brodtkorb	Hybrid Control of Marine Vessels – Dynamic Positioning in Varying Conditions
IMT-13-2017	Kjersti Bruslerud	Simultaneous stochastic model of waves and current for prediction of structural design loads
IMT-14-2017	Finn-Idar Grøtta Giske	Long-Term Extreme Response Analysis of Marine Structures Using Inverse Reliability Methods
IMT-15-2017	Stian Skjong	Modeling and Simulation of Maritime Systems and Operations for Virtual Prototyping using co-Simulations
IMT-1-2018	Yingguang Chu	Virtual Prototyping for Marine Crane Design and Operations
IMT-2-2018	Sergey Gavrilin	Validation of ship manoeuvring simulation models
IMT-3-2018	Jeevith Hegde	Tools and methods to manage risk in autonomous subsea inspection, maintenance and repair operations
IMT-4-2018	Ida M. Strand	Sea Loads on Closed Flexible Fish Cages
IMT-5-2018	Erlend Kvinge Jørgensen	Navigation and Control of Underwater Robotic Vehicles

IMT-6-2018	Bård Stovner	Aided Inertial Navigation of Underwater Vehicles
IMT-7-2018	Erlend Liavåg Grotle	Thermodynamic Response Enhanced by Sloshing in Marine LNG Fuel Tanks
IMT-8-2018	Børge Rokseth	Safety and Verification of Advanced Maritime Vessels
IMT-9-2018	Jan Vidar Ulveseter	Advances in Semi-Empirical Time Domain Modelling of Vortex-Induced Vibrations
IMT-10-2018	Chenyu Luan	Design and analysis for a steel braceless semi-submersible hull for supporting a 5-MW horizontal axis wind turbine
IMT-11-2018	Carl Fredrik Rehn	Ship Design under Uncertainty
IMT-12-2018	Øyvind Ødegård	Towards Autonomous Operations and Systems in Marine Archaeology
IMT-13-2018	Stein Melvær Nornes	Guidance and Control of Marine Robotics for Ocean Mapping and Monitoring
IMT-14-2018	Petter Norgren	Autonomous Underwater Vehicles in Arctic Marine Operations: Arctic marine research and ice monitoring
IMT-15-2018	Minjoo Choi	Modular Adaptable Ship Design for Handling Uncertainty in the Future Operating Context
MT-16-2018	Ole Alexander Eidsvik	Dynamics of Remotely Operated Underwater Vehicle Systems
IMT-17-2018	Mahdi Ghane	Fault Diagnosis of Floating Wind Turbine Drivetrain- Methodologies and Applications
IMT-18-2018	Christoph Alexander Thieme	Risk Analysis and Modelling of Autonomous Marine Systems
IMT-19-2018	Yugao Shen	Operational limits for floating-collar fish farms in waves and current, without and with well-boat presence
IMT-20-2018	Tianjiao Dai	Investigations of Shear Interaction and Stresses in Flexible Pipes and Umbilicals
IMT-21-2018	Sigurd Solheim Pettersen	Resilience by Latent Capabilities in Marine Systems
IMT-22-2018	Thomas Sauder	Fidelity of Cyber-physical Empirical Methods. Application to the Active Truncation of Slender Marine Structures
IMT-23-2018	Jan-Tore Horn	Statistical and Modelling Uncertainties in the Design of Offshore Wind Turbines

IMT-24-2018	Anna Swider	Data Mining Methods for the Analysis of Power Systems of Vessels
IMT-1-2019	Zhao He	Hydrodynamic study of a moored fish farming cage with fish influence
IMT-2-2019	Isar Ghamari	Numerical and Experimental Study on the Ship Parametric Roll Resonance and the Effect of Anti-Roll Tank
IMT-3-2019	Håkon Strandenes	Turbulent Flow Simulations at Higher Reynolds Numbers
IMT-4-2019	Siri Mariane Holen	Safety in Norwegian Fish Farming – Concepts and Methods for Improvement
IMT-5-2019	Ping Fu	Reliability Analysis of Wake-Induced Riser Collision
IMT-6-2019	Vladimir Krivopolianskii	Experimental Investigation of Injection and Combustion Processes in Marine Gas Engines using Constant Volume Rig
IMT-7-2019	Anna Maria Kozłowska	Hydrodynamic Loads on Marine Propellers Subject to Ventilation and out of Water Condition.
IMT-8-2019	Hans-Martin Heyn	Motion Sensing on Vessels Operating in Sea Ice: A Local Ice Monitoring System for Transit and Stationkeeping Operations under the Influence of Sea Ice
IMT-9-2019	Stefan Vilsen	Method for Real-Time Hybrid Model Testing of Ocean Structures – Case on Slender Marine Systems
IMT-10-2019	Finn-Christian W. Hanssen	Non-Linear Wave-Body Interaction in Severe Waves
IMT-11-2019	Trygve Olav Fossum	Adaptive Sampling for Marine Robotics
IMT-12-2019	Jørgen Bremnes Nielsen	Modeling and Simulation for Design Evaluation
IMT-13-2019	Yuna Zhao	Numerical modelling and dynamic analysis of offshore wind turbine blade installation
IMT-14-2019	Daniela Myland	Experimental and Theoretical Investigations on the Ship Resistance in Level Ice
IMT-15-2019	Zhengru Ren	Advanced control algorithms to support automated offshore wind turbine installation
IMT-16-2019	Drazen Polic	Ice-propeller impact analysis using an inverse propulsion machinery simulation approach
IMT-17-2019	Endre Sandvik	Sea passage scenario simulation for ship system performance evaluation

IMT-18-2019	Loup Suja-Thauvin	Response of Monopile Wind Turbines to Higher Order Wave Loads
IMT-19-2019	Emil Smilden	Structural control of offshore wind turbines – Increasing the role of control design in offshore wind farm development
IMT-20-2019	Aleksandar-Sasa Milakovic	On equivalent ice thickness and machine learning in ship ice transit simulations
IMT-1-2020	Amrit Shankar Verma	Modelling, Analysis and Response-based Operability Assessment of Offshore Wind Turbine Blade Installation with Emphasis on Impact Damages
IMT-2-2020	Bent Oddvar Arnesen Haugalokken	Autonomous Technology for Inspection, Maintenance and Repair Operations in the Norwegian Aquaculture
IMT-3-2020	Seongpil Cho	Model-based fault detection and diagnosis of a blade pitch system in floating wind turbines
IMT-4-2020	Jose Jorge Garcia Agis	Effectiveness in Decision-Making in Ship Design under Uncertainty
IMT-5-2020	Thomas H. Viuff	Uncertainty Assessment of Wave-and Current-induced Global Response of Floating Bridges
IMT-6-2020	Fredrik Mentzoni	Hydrodynamic Loads on Complex Structures in the Wave Zone
IMT-7-2020	Senthuran Ravinthrakumar	Numerical and Experimental Studies of Resonant Flow in Moonpools in Operational Conditions
IMT-8-2020	Stian Skaalvik Sandøy	Acoustic-based Probabilistic Localization and Mapping using Unmanned Underwater Vehicles for Aquaculture Operations
IMT-9-2020	Kun Xu	Design and Analysis of Mooring System for Semi-submersible Floating Wind Turbine in Shallow Water
IMT-10-2020	Jianxun Zhu	Cavity Flows and Wake Behind an Elliptic Cylinder Translating Above the Wall
IMT-11-2020	Sandra Hogenboom	Decision-making within Dynamic Positioning Operations in the Offshore Industry – A Human Factors based Approach
IMT-12-2020	Woongshik Nam	Structural Resistance of Ship and Offshore Structures Exposed to the Risk of Brittle Failure
IMT-13-2020	Svenn Are Tutturen Værnø	Transient Performance in Dynamic Positioning of Ships: Investigation of Residual Load Models and Control Methods for Effective Compensation
IMT-14-2020	Mohd Atif Siddiqui	Experimental and Numerical Hydrodynamic Analysis of a Damaged Ship in Waves
IMT-15-2020	John Marius Hegseth	Efficient Modelling and Design Optimization of Large Floating Wind Turbines

IMT-16-2020	Asle Natskår	Reliability-based Assessment of Marine Operations with Emphasis on Sea Transport on Barges
IMT-17-2020	Shi Deng	Experimental and Numerical Study of Hydrodynamic Responses of a Twin-Tube Submerged Floating Tunnel Considering Vortex-Induced Vibration
IMT-18-2020	Jone Torsvik	Dynamic Analysis in Design and Operation of Large Floating Offshore Wind Turbine Drivetrains
IMT-1-2021	Ali Ebrahimi	Handling Complexity to Improve Ship Design Competitiveness
IMT-2-2021	Davide Proserpio	Isogeometric Phase-Field Methods for Modeling Fracture in Shell Structures
IMT-3-2021	Cai Tian	Numerical Studies of Viscous Flow Around Step Cylinders
IMT-4-2021	Farid Khazaeli Moghadam	Vibration-based Condition Monitoring of Large Offshore Wind Turbines in a Digital Twin Perspective
IMT-5-2021	Shuashuai Wang	Design and Dynamic Analysis of a 10-MW Medium-Speed Drivetrain in Offshore Wind Turbines
IMT-6-2021	Sadi Tavakoli	Ship Propulsion Dynamics and Emissions
IMT-7-2021	Haoran Li	Nonlinear wave loads, and resulting global response statistics of a semi-submersible wind turbine platform with heave plates
IMT-8-2021	Einar Skiftestad Ueland	Load Control for Real-Time Hybrid Model Testing using Cable-Driven Parallel Robots
IMT-9-2021	Mengning Wu	Uncertainty of machine learning-based methods for wave forecast and its effect on installation of offshore wind turbines
IMT-10-2021	Xu Han	Onboard Tuning and Uncertainty Estimation of Vessel Seakeeping Model Parameters
IMT-01-2022	Ingunn Marie Holmen	Safety in Exposed Aquaculture Operations
IMT-02-2022	Prateek Gupta	Ship Performance Monitoring using In-service Measurements and Big Data Analysis Methods
IMT-03-2022	Sangwoo Kim	Non-linear time domain analysis of deepwater riser vortex-induced vibrations
IMT-04-2022	Jarle Vinje Kramer	Hydrodynamic Aspects of Sail-Assisted Merchant Vessels
IMT-05-2022	Øyvind Rabliås	Numerical and Experimental Studies of Maneuvering in Regular and Irregular Waves

IMT-06-2022	Pramod Ghimire	Simulation-Based Ship Hybrid Power System Conspect Studies and Performance Analyses
IMT-07-2022	Carlos Eduardo Silva de Souza	Structural modelling, coupled dynamics, and design of large floating wind turbines
IMT-08-2022	Lorenzo Balestra	Design of hybrid fuel cell & battery systems for maritime vessels
IMT-09-2022	Sharmin Sultana	Process safety and risk management using system perspectives – A contribution to the chemical process and petroleum industry
IMT-10-2022	Øystein Sture	Autonomous Exploration for Marine Minerals
IMT-11-2022	Tiantian Zhu	Information and Decision-making for Major Accident Prevention – A concept of information- based strategies for accident prevention
IMT-12-2022	Siamak Karimi	Shore-to-Ship Charging Systems for Battery- Electric Ships
IMT-01-2023	Huili Xu	Fish-inspired Propulsion Study: Numerical Hydrodynamics of Rigid/Flexible/Morphing Foils and Observations on Real Fish



